Carbon Molecular Sieves for Air Separation

Harnit Kaur Chagger
B.Sc. (Delhi University), M.Sc. (Leeds University)

Thesis submitted in fulfilment of the requirements for the degree of Doctor of Philosophy

The University of Newcastle upon Tyne
(1994)

For my family

Acknowledgements

I would first like to thank my research supervisor Dr. K.M. Thomas, for his kind support and invaluable tutelage throughout the course of this study. I will cherish my association with him.

My thanks are also due to my collaborative supervisor, Dr. J. Armor, for his constant encouragement and to Dr. M.L. Sykes for his help in organising the experiments and critical reading of the thesis. I thank Dr. I.A.S. Edwards for generously providing some of the diagrams presented in Chapter 1 of thesis besides critical reading the manuscript of the thesis. The financial support provided by Air Products and Chemicals Inc., and SERC is gratefully acknowledged.

I thank my colleagues in NCRL for their help with special mention to Dr. Ana Gonzales, Dr. Jenny Lewis and Miss Bridget Clow. My friends Hanan, Mariama, Popi, Francis, John, Aileen, Pravir and Anjula have been helpful in many ways and I thank them for the same.

Finally, I would like to thank my family, my parents and brother, for their unfailing support and encouragement throughout my stay at Newcastle.

Contents

Contents

CHAPTER TWO

ACTIVATED CARBONS AND CARBON MOLECULAR SIEVES

CHAPTER THREE

OBJECTIVES

CHAPTER FOUR

EXPERIMENTAL

CHAPTER FIVE

RESULTS

CHAPTER SIX

DISCUSSION

CHAPTER SEVEN

CONCLUSIONS

Chapter 1

Structure of carbons

1.1 Introduction

Carbon is one of the naturally occurring elements and has an atomic weight 12.01 atomic mass units (amu) and atomic number 6. It has six electrons and has an electronic configuration of: $1s^2\ 2s^2\ 2p^2$ in the ground state. This element exists in different crystalline forms-diamond, graphite, buckminsterfullerene[1] and carbyne[2]. Carbon also has the ability of catenation via formation of σ and π bonds.

1.2 Allotropes of Carbon

1.2.1 Fullerene

Stable carbon cage compounds based on five and six rings have been identified[1]. The most stable of these, C_{60} has a molar mass of 720 amu which corresponds to a cluster of carbon atoms having a spherical structure like a football based on a combination of six and five membered rings. C_{60} contains 60 vertices and 32 faces, 12 of which are pentagonal and 20 hexagonal. Recent work suggests the existence of many fullerenes based on an even number of carbon atoms within the fullerene class of isomers. The main species are C_{60} (shown in Figure 1.1) and C_{70} but there are many possible cage-like isomers of other fullerenes; for example, C_{76}.

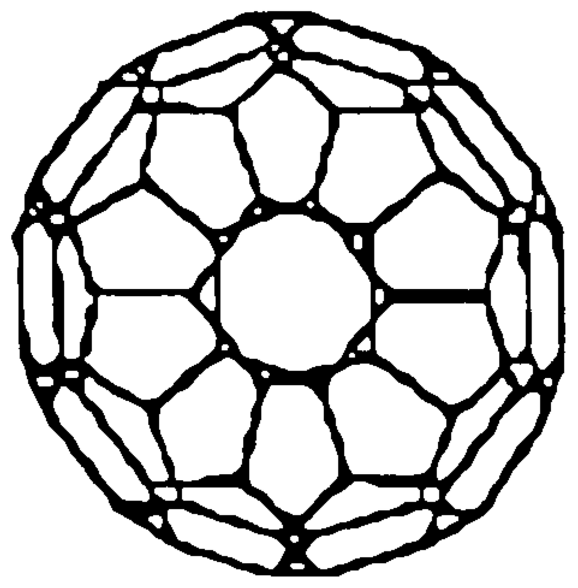

Figure 1.1 Buckminster fullerene - C_{60}[1]

1.2.2 Diamond

The structure of diamond is shown in Figure 1.2. The diamond lattice consists of sp^3 bonds with tetrahedral bond angles linking C-C single bond.

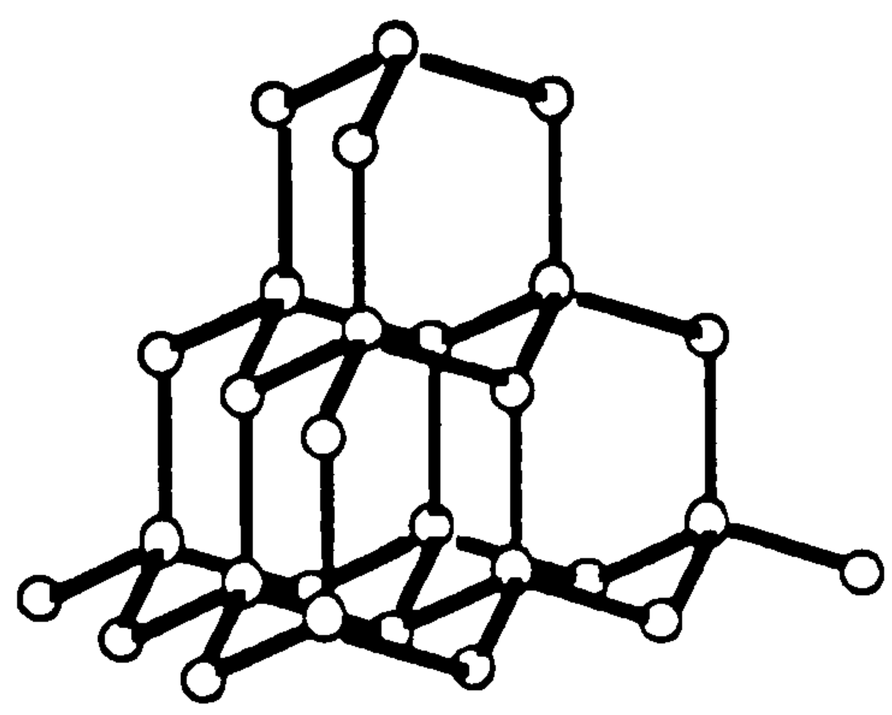

Figure 1.2 Diamond structure.

The structure of fullerenes and diamond will not be discussed in detail in this thesis since the basic structural units in carbons are based on ***'graphene'*** layers which are related to the graphite structure[3].

1.2.3 Structure in graphite

Debye and Scherrer[4] carried out structural analysis of graphite using X-ray diffraction. Hull[5] and Bernal[6] suggested that the adjacent layers are translated by bond length, but alternative layers have identical projections A-B-A-B sequence with unit cells of the hexagonal lattice. The basal layers are held together by van der Waals forces. The spacing between the layers is 0.335 nm, bond length 0.142 nm and crystal density 2.266 g cm^{-3}. Lipton and Stokes[7] observed lines in X-ray diffractograms which could not be attributed to the hexagonal lattice. Thus, these lines were attributed to about 10% of A-B-C-A-B-C sequence, i.e. rhombohedral graphite as shown in Figure 1.3. This lattice form is thermally less stable and reverts to a hexagonal graphite on heat treatment between 1173 and 3273 K[8]. The weak forces and delocalization of π electrons between the planes contribute good electrical conductivity and lubrication properties in graphite. However perfect graphite is a rare form of carbon but, the so-called single crystal graphite also invariably contains defects and structural faults as well as vacancies and interstitial defects[9].

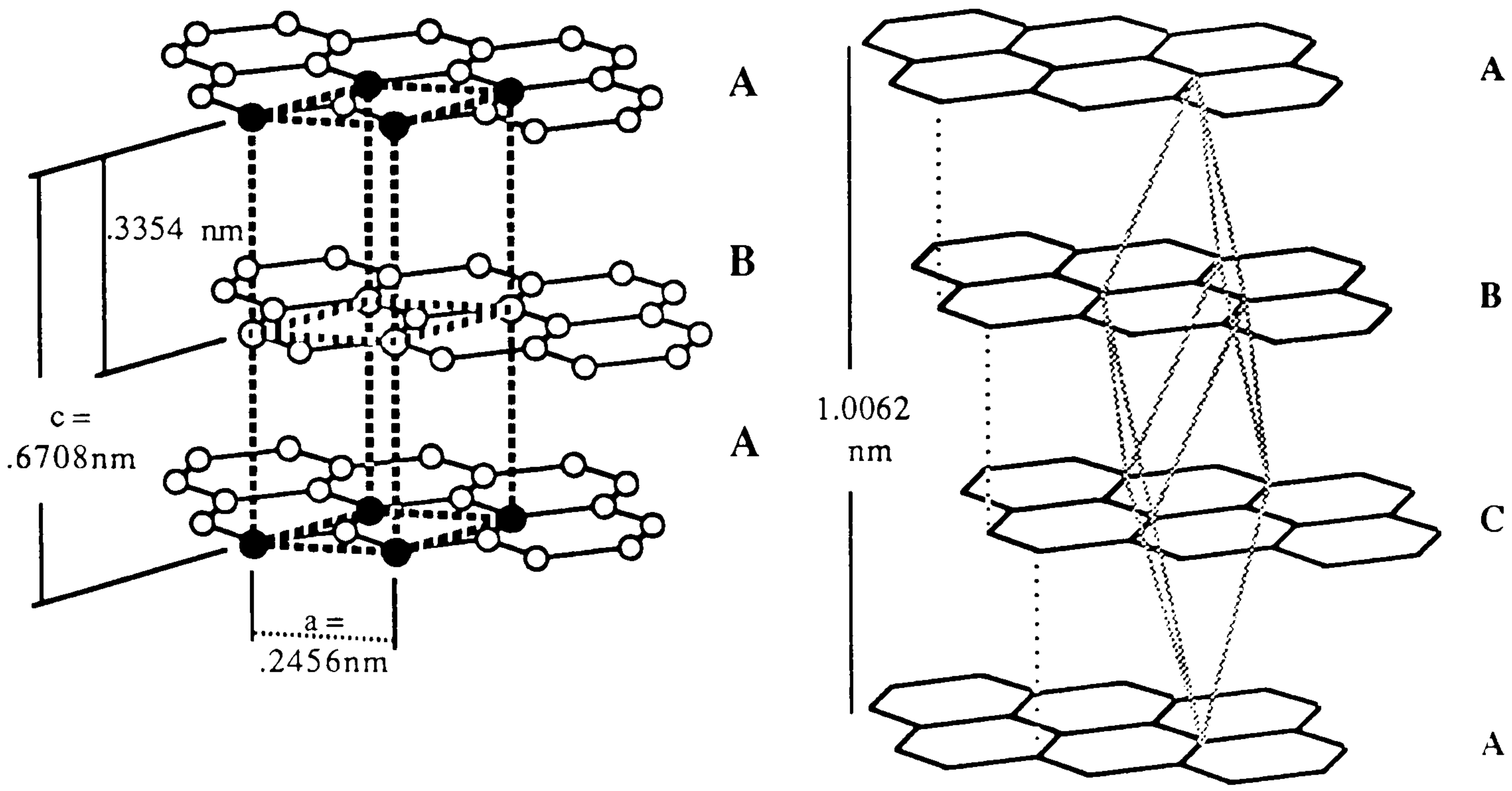

Figure 1.3 Graphite structure[5,7]

The structure of active carbons is less ordered than that of graphite. Riley[10] proposed two different types of structures of active carbons on the basis of X-ray analysis. The first structure consists of the elementary crystallites, which are two-dimensional analogous to graphite being composed of parallel layers of hexagonally ordered carbon atoms. The structure differs from that of graphite as the parallel planes are not perfectly oriented with respect to their perpendicular axis and the angular displacement of one layer with respect to another is random, overlapping each other irregularly. This arrangement has been termed as ***'turbostratic structure'***. The mutual orientation of the elementary basal planes relative to each other is completely random, and their dimensions depend upon the temperature of carbonisation. The following values are typical: crystallite height, L_c from 0.9-1.2 nm; crystallite width, L_a 2.0 - 2.3 nm. The second type of structure was described as a disordered cross-linked space lattice of carbon hexagons.

Detailed X-ray investigations carried out by Franklin[11] contributed to a better understanding of crystallites of carbonaceous materials. She divided all carbonaceous materials, except diamond into two categories: graphitizing (soft) and non-graphitizing (hard) as shown in Figure 1.4. Figure 1.4 also shows the structure of a partially graphitizing carbon.

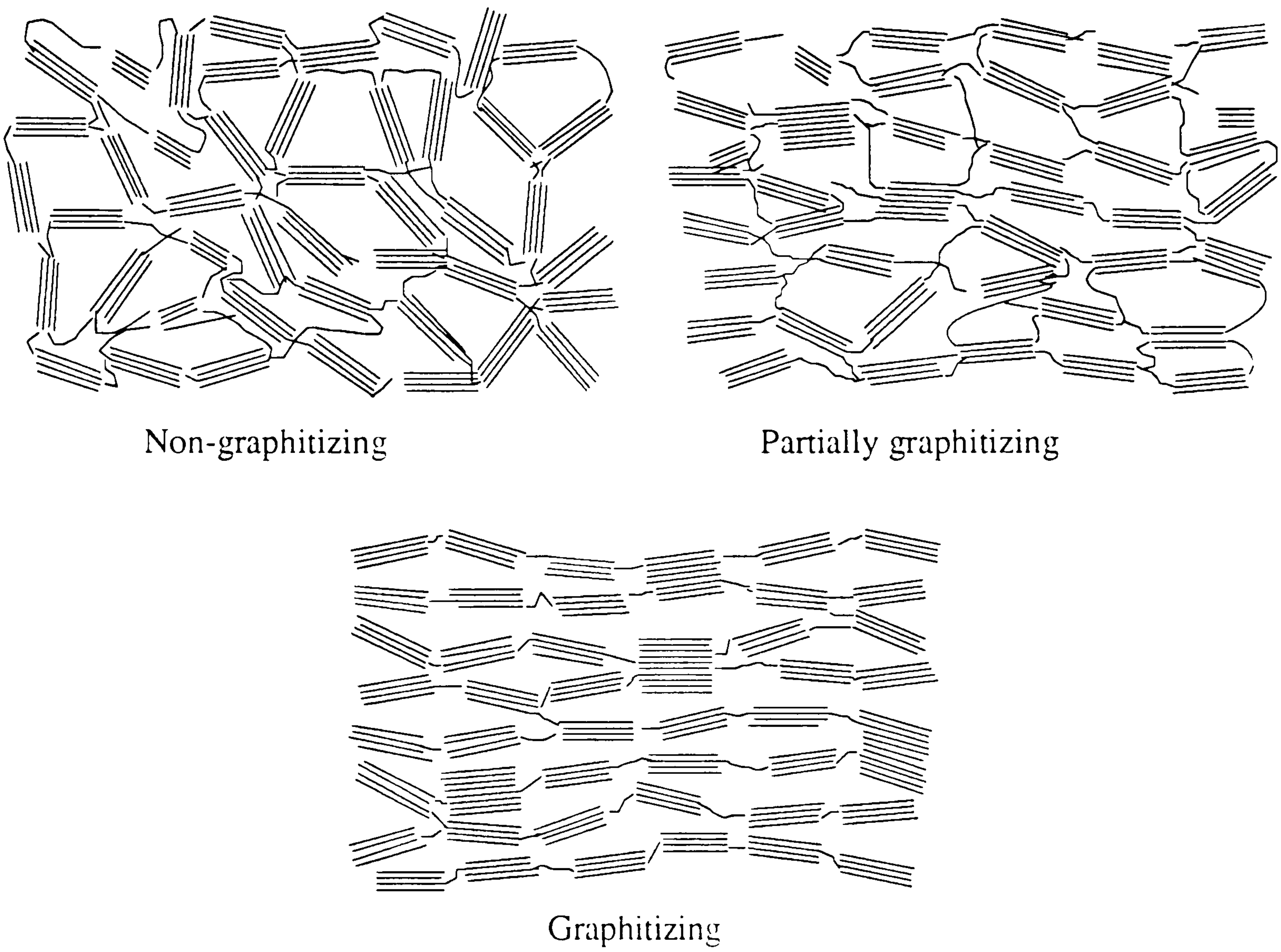

Figure 1.4 Franklin's models of carbon structures[11]

During heat treatment certain non-graphitic carbons show a gradual change from a ***'random layer structure'***[12] towards the ordered structure of crystalline graphite depending on the nature of the precursor. These carbons are referred to as graphitizing carbons, whereas other non-graphitic carbons show no evidence for the development of three-dimensional order even after heating to 3273 K. During carbonisation rearrangement of non-organised carbons occurs in the temperature range 1273 to 2273 K, which results in an increase in the degree of order in the ***'graphene'*** like layers in the elementary crystallites. Experiments conducted by Franklin showed that polyvinylidene chloride (PVDC) carbonised under 1273 K contained about thirty-five percent of disordered carbon, and the diameter of its graphitic-like layer was found to be approximately 1.6 nm. After being heat treated to 2273 K the disordered carbon became less than ten percent and the diameter of layers increased to 2.2 nm. The height of the elementary crystallites (i.e. the number of parallel graphitic like layers) in this temperature range was found to be small, whereas with polyvinyl chloride (PVC) prepared at low temperatures, the number of layers increased considerably, indicating the formation of a graphitic structure. Thus, PVDC was classified as a non-graphitizing material and PVC as a graphitizing material. The reasons suggested for PVDC not graphitizing were that during carbonisation of PVDC strong cross-linking develops between the neighbouring randomly oriented elementary crystallites, which results in a rigid, immobile mass, whereas with PVC the elementary crystallites were mobile and cross linking between them was difficult. Thus, PVC produced a relatively soft, less porous structure of crystallites containing large numbers of parallel graphitic layers. Also the formation of a non-graphitizable structure with strong cross-linking is promoted by the presence of oxygen or an insufficiency of hydrogen in the original material. Carbonisation of PVDC - $(C_2H_3Cl_3)_n$ results in the liberation of gaseous hydrogen chloride during carbonisation, which gives highly porous coke. On the other hand, PVC having a stoichiometric formula - $(C_2H_3Cl)_n$ contains more hydrogen than chlorine thus forming a considerable amount of tar during carbonisation while smaller amounts of hydrogen chloride are liberated. Hence, the carbonisation product remains viscous up to a temperature of 723 K and develops anisotropic structures. The resulting PVDC char showed a microporous structure and the diameter of largest graphitic layer did not exceed 7.0 nm and the elementary layer was found to be 10-12 condensed aromatic rings stacked in layers of two or three. During the formation of graphitizable carbons there is no general organization of these units except a possible preferred local orientation[13]. Between 1273 K and 1873 K the extent of parallel orientation increases, hence graphitization can begin: two-dimensional growth of aromatic layers is followed by orientation of aromatic layers in the hexagonal graphite structure at temperatures greater than 2200 K. The minimum diameter, L_a value, required for the onset of this first stage has been estimated as 8.0-15.0 nm[14,15]. Roosky[16] observed a decrease in inter-layer spacing which was accompanied by increasing graphitization and this inter-layer spacing was later measured by Bacon[17]. Among the non-graphitic carbons in which graphitic structure is as yet undeveloped, the interlayer spacing was found to be constant at 0.344 nm which is very different from that in graphite 0.335 nm. Intermediate values were observed for all partially graphitic carbons and the spacing tends to decrease as the degree of graphitization increases, which is directly related to degree of mutual orientation of the layers[18]. Several workers[19,20] demonstrated that the presence of surplus oxygen hindered the growth of graphitic layers in elementary crystallites.

Carbon can be classified into either non-graphitizable or graphitizable, which refers to the convertibility to a three-dimensional graphitic structure on heating to 3273 K. However, there is a continuous range of materials between graphitizable and non-graphitizable carbon. The differences between these types of carbons are discussed in the following section.

1.3 Origin of Carbons

1.3.1 Formation of graphitizable carbons

The graphitizable carbons are ***'cokes'*** formed by carbonisation of coal tar and petroleum pitches as well as from the fusion of bituminous coals (caking and coking) organic compounds, example decacyclene, anthracene, acenapthylene. Certain thermoplastic polymers like PVC also form graphitizable carbons. The graphitizable carbons owe their inherent embryonic graphitic structure to the formation of - discotic (disc-like), nematic, aromatic liquid crystals, i.e. ***'mesophase'*** within the isotropic melt of coal or pitch during carbonisation.

1.3.1.1 Mesophase

Brooks and Taylor[21] described mesophase as a nematic discotic liquid crystal, which can be distinguished from other forms of liquid crystals on the basis of the molecular stacking, i.e. their constituent molecules are stacked approximately parallel to each other rather than smectic or cholestric crystal as shown in Figure 1.5.

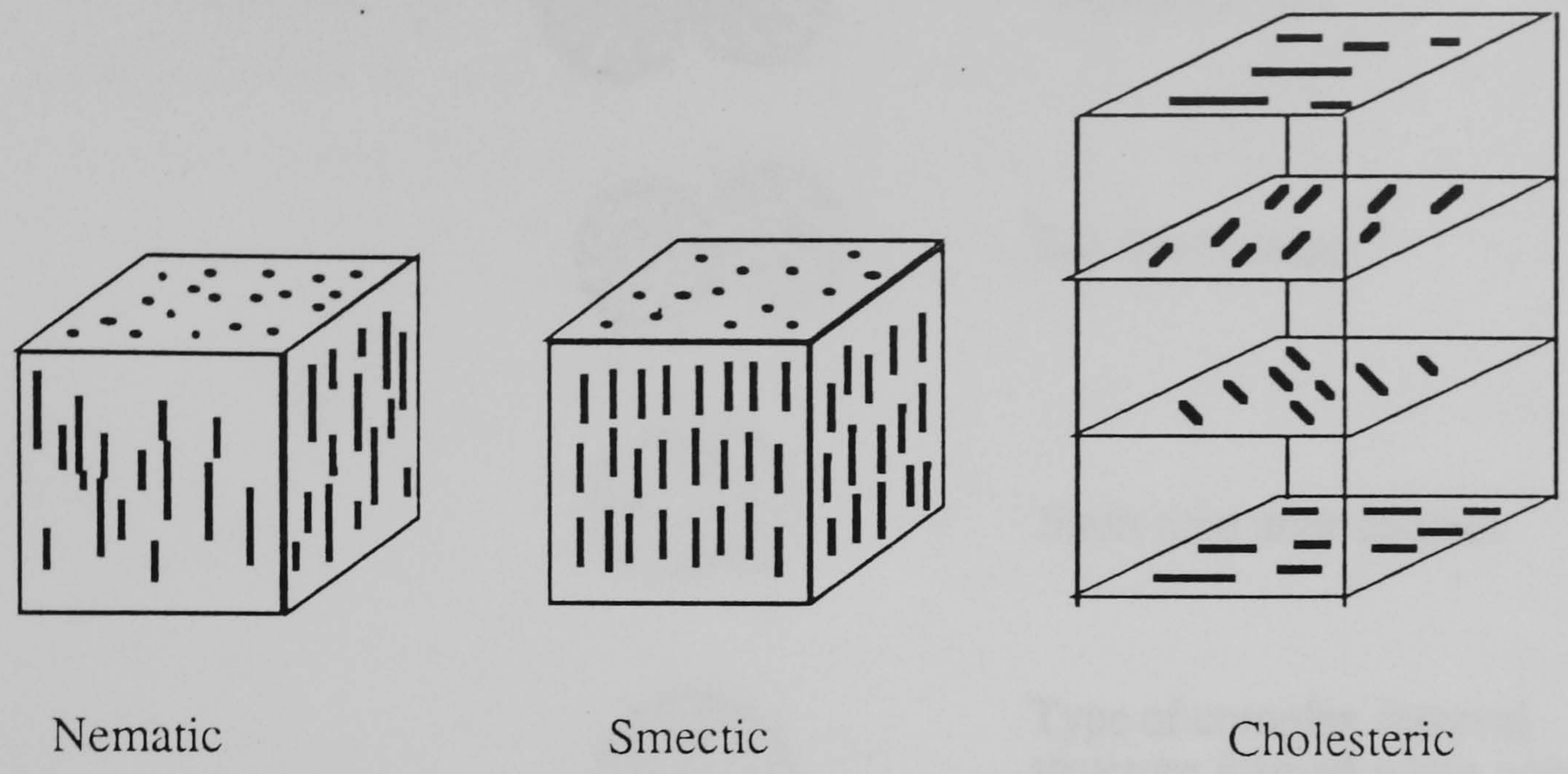

Figure 1.5 Structure of liquid crystals[22]

These polyaromatic molecules possess properties of mobility within the fluid phase and dynamic, reversible associations can occur[23]. During the pyrolysis, small molecules and side chains of functional groups are lost as volatiles like oxygen, nitrogen etc. and C-H, C-C produce free radicals, ring closure and condensation reactions leading to the formation of large polyaromatic molecules. When the molar mass of polyaromatic compounds is high (around ~ 600-900 amu) at about 673 K, they possess the required cohensive energy via van der Waals forces of attraction to overcome their kinetic energy becoming aligned parallel and adopting a spherical shape due to the requirements of minimum surface energy. These spheres grow in size at the expense of the surrounding isotropic fluid and, on contact with another sphere, immediate coalescence occurs resulting in the reorientation of the material to form a new, larger sphere as shown in Figure 1.6.

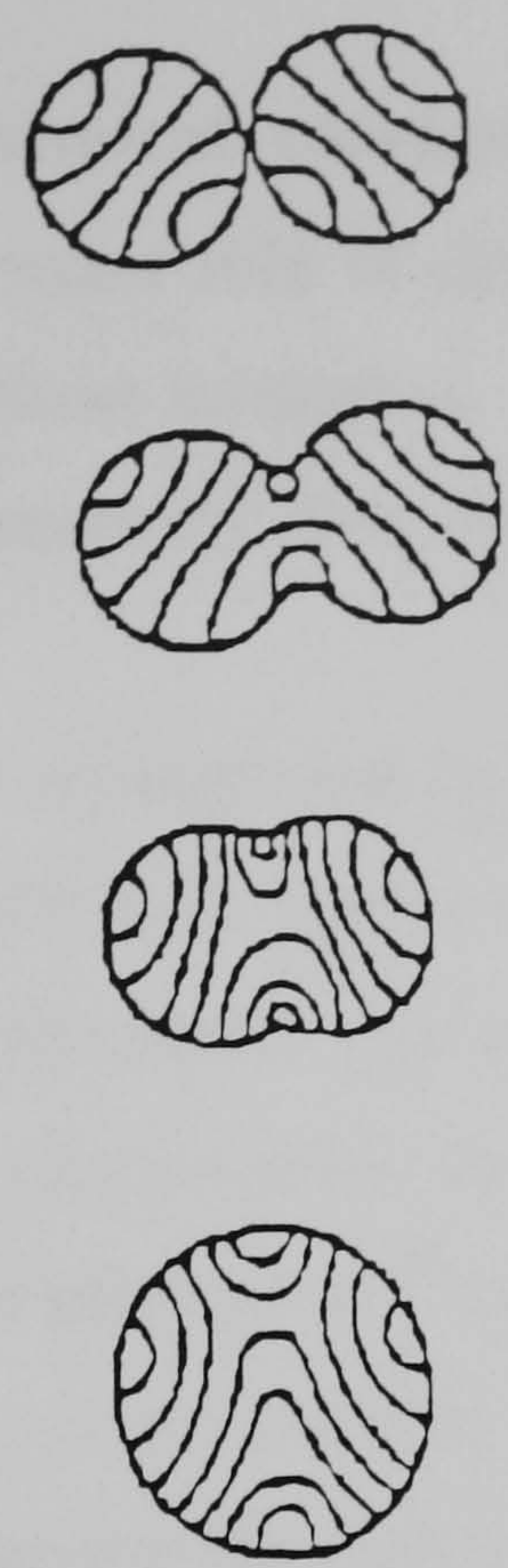

Figure 1.6 Showing different stages of coalescence[21]

This process continues until all pitch matrix has been converted into mesophase of approximately 1~5 μ diameter. These units interlock, but the extent of coalescence and re-orientation which occurs depends upon the viscosity of the mesophase. The molar mass increases with time and temperature and reaches a point where the cohesion energy increases. This leads to a higher order in the liquid crystal phase, resulting in the creation of planar macromolecules consisting of sheets of hexagonally linked carbon atoms[24] within the isotropic pyrolysate as shown in Figures 1.7 and 1.8.

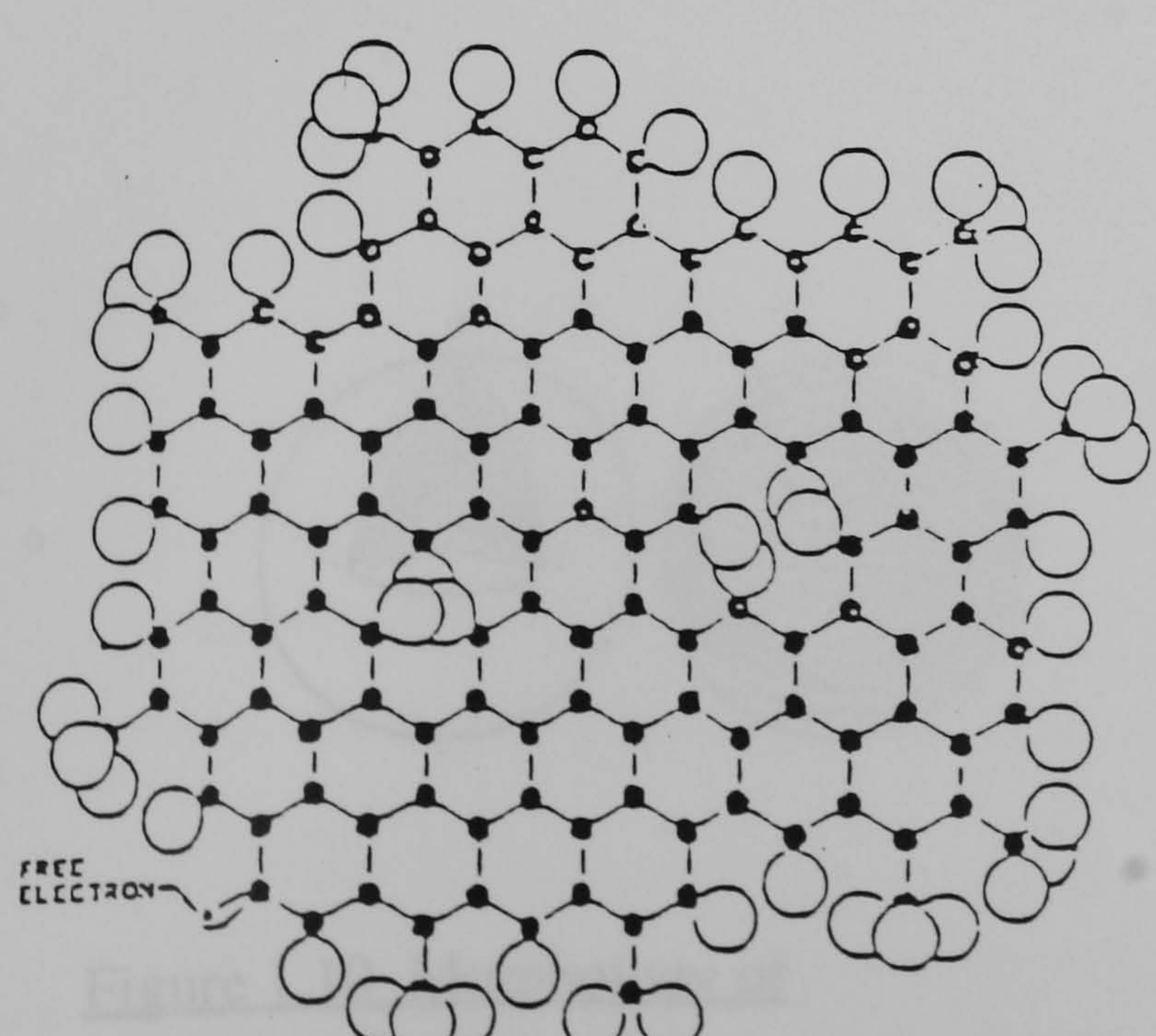

Figure 1.7 Model of a planar aromatic stable free radical that forms nematic liquid crystal.

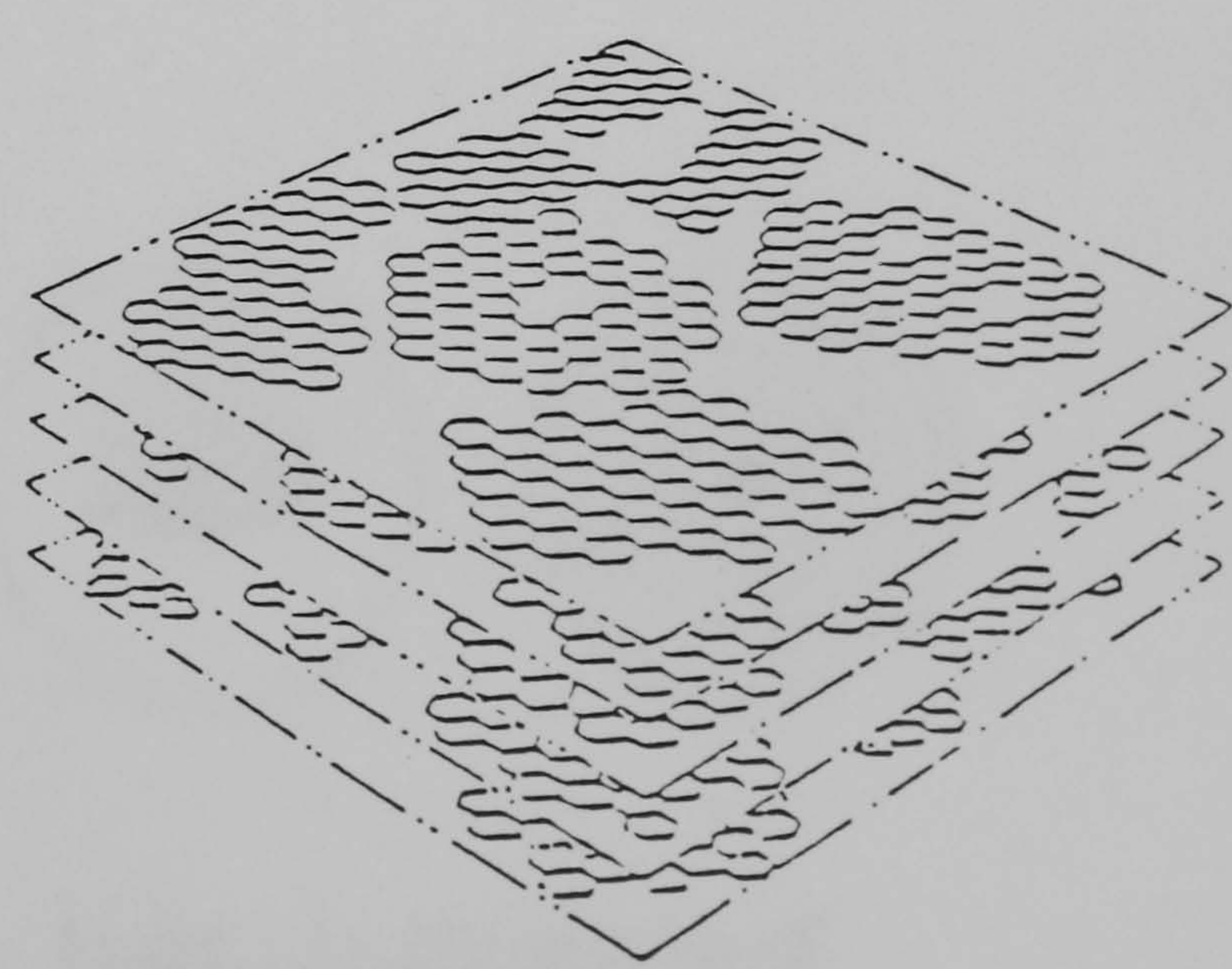

Figure 1.8 Stacking of lamellae in nematic liquid crystal.

However, the chemical characteristics of the environment (reducing or oxidising) plays an important role in determining long term effects on the carbon, particularly during mesophase formation. The action of oxygen leads to the prevention of graphitizablility of the resulting coke; hydrogenation has the opposite effect.

The morphology represented by Brooks and Taylor[21] represents the most commonly found mesophase as shown in Figure 1.9. The lamellae molecules are stacked parallel to an equatorial plane. Alternatively less common mesophase morphologies have been proposed by, for example, Kovac and Lewis[25] (Figure 1.10). Work carried out by Huttinger *et al.*[26] on co-carbonization pitch with carbon black indicated a special type of mesophase. Its lamellae molecules were found to be arranged concentrically around the carbon black particles giving rise to an 'onion-skin' morphology as shown in Figure 1.11.

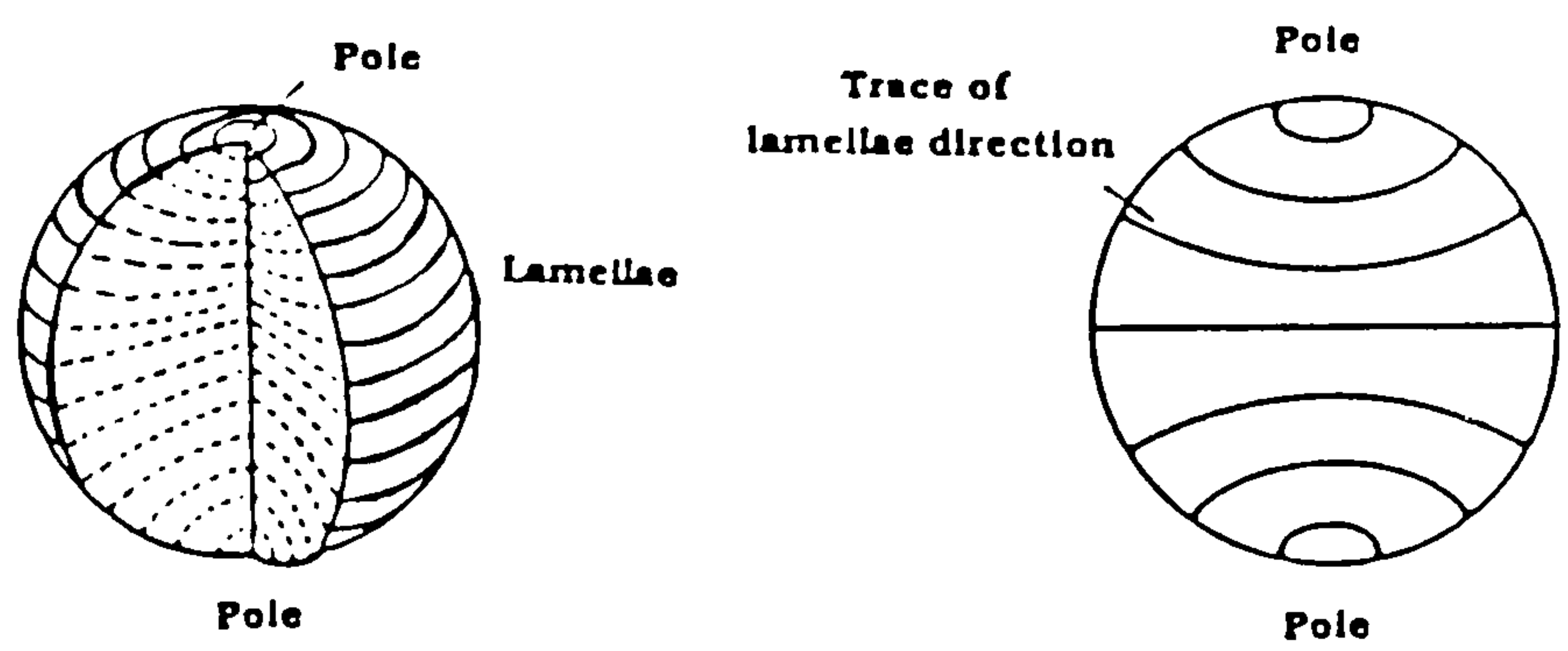

Figure 1.9 Morphology of mesophase spheres (Brooks and Taylor[21])

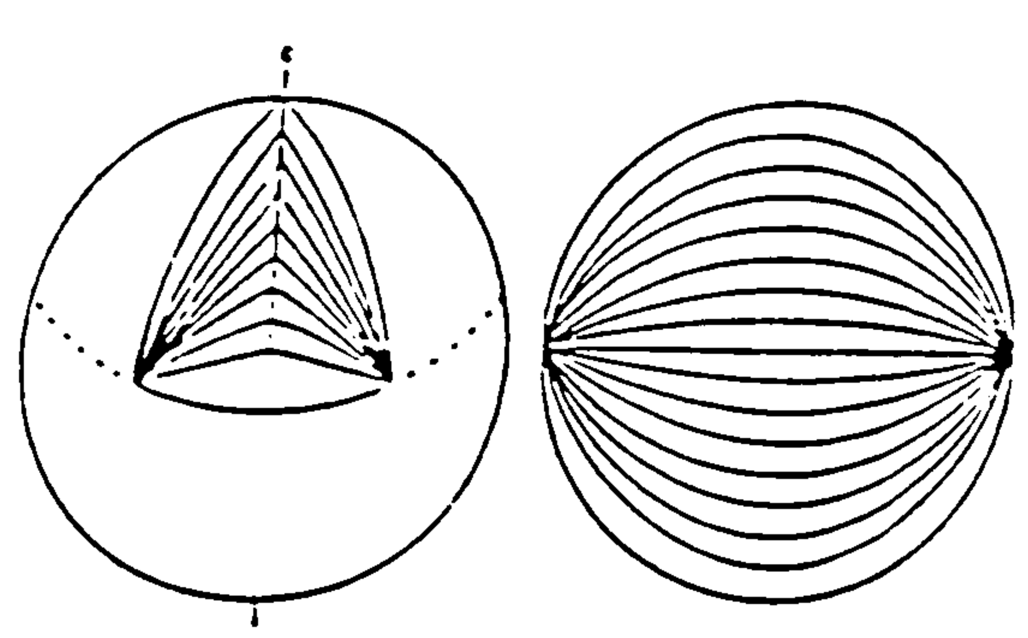

Figure 1.10 Morphology of mesophase spheres (Kovac and Lewis[25])

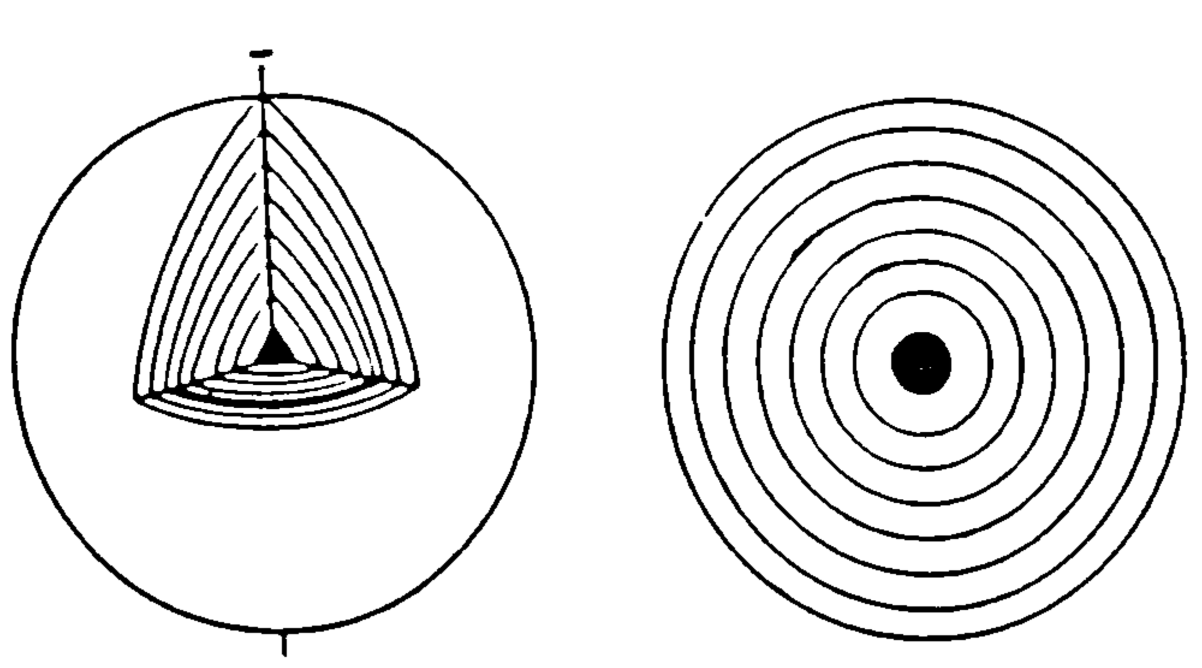

Figure 1.11 Morphology of mesophase spheres (Huttinger[26])

The formation of graphitizable carbons has been explained on the basis of Marchand's[13] model which considers the initial anisotropic carbonaceous material (i.e. mesophase) to be composed of small ***'structural units'*** (SU) below 873 K. The SU comprise of molecules of less than 10-12 condensed aromatic rings; their size is of order 0.8-1.0 nm and they are stacked in groups of two or three as shown in (stage 1) Figure 1.12. There is no general organisation but a possible preferred orientation, which could extend throughout the solid. During the carbonisation process the SU coalesce to form larger regions of local molecular orientation (LMO). The ability to graphitize is predetermined by the size of LMO (i.e. domains). The smaller the LMO in a carbon the less likely it is to graphitize. Around temperatures of 873-1773 K, very few heteroatoms are left and most of them are bound laterally to the aromatic molecules characterised by distorted columns (Stage 2). Above temperature 1773 K the distorted columns coalesce to form wrinkled layers (stage 3). This two-dimensional structure occurs at the expense of the gradual removal of various defects (heteroatoms, sp^3 bonds, twists and dislocations) located at the periphery of the SU. The continuous elimination of defects results in the growth of rigid two-dimensional parallel graphitic layers at temperatures > 2273 K (as shown in stage 3). The two-dimensional structure is generally referred to as ***'graphenes'*** in order to avoid confusion with ***'true graphite'***. The graphenes do not possess a three-dimensional organization of stacking and might be quite parallel to a certain degree of perfection, but they undergo arbitrary changes relative to each other, i.e. translated or rotated. Hence, there is no fixed relationship between the position of two carbon atoms belonging to adjacent graphenes. This kind of structure is referred to as ***'turbostratic'***. The next step comprises of having order in this turbostratic stacking. There is dewrinkling of layers and development of three-dimensional order by elimination of in-plane structural defects to form stiff, structurally perfect layers (stage 4); this is referred to as the graphitization stage. Non-graphitizing carbons do not graphitize because of structural factors such as cross-linking, small grain sizes etc. Temperature and pressure both play an important role in the transformation of three-dimensional growth of aromatic layers into orientations of aromatic layers in the hexagonal graphitic structure.

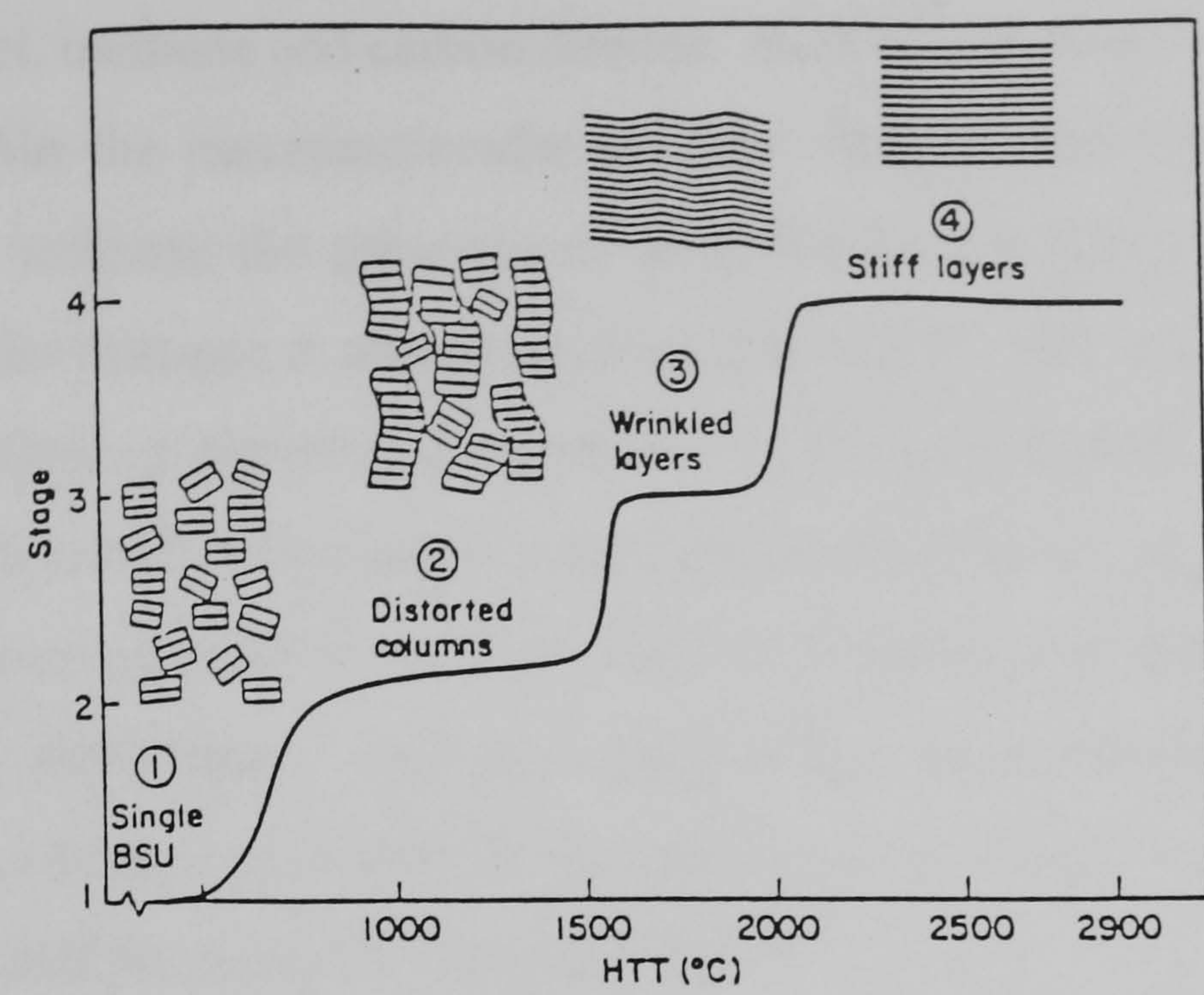

Figure 1.12 Schematic building of graphitic structure[13]

1.3.2 Formation of non-graphitizable carbons

Non-graphitizable isotropic carbons are essentially ***chars*** obtained from materials which decompose during carbonisation without passing through a plastic stage. The majority of non-graphitizable carbons originate from wood, cellulose or lignin, nut shells or specific cross-linked structures of (C-O-C bonding) of low rank coals, peats, lignites, synthetic resins like phenolic resins, polyfurfuryl alcohol and polyvinylidene chloride

It is the polymeric cellulose or lignin within the natural-occurring materials such as wood, nut shells etc. which is pyrolysed. These polymers lose heteroatoms during carbonisation by pyrolytic decomposition leaving behind the basic skeleton of polymer which eventually cross-links thus preventing fusing. The voidage created by loss of small molecules, including hydrogen, carbon dioxide, water and carbon monoxide (1273 K) constitutes porosity and high surface areas within the carbon[27,28]. The detail of the collapse of macromolecules during carbonization is not fully understood. However, Mrozowski[29] showed that the early stage of carbonisation involves the cleavages of bonds within the macromolecular system to give free radicals. Electron spin resonance (ESR) studies show a rapid increase in free radical concentration around the HTT of 973 K. The early stages also involve release of volatiles in the form of water, methanol, methane and carbon dioxide. Such elimination causes fissures, cracks or spaces within the macromolecular system. Fourier transform infra-red (FTIR) investigations indicate the presence of aromatic lamellae when Phenadur resin is carbonised under nitrogen at temperatures around 623 K. The aliphatic side-chains are linked to developing aromatic domains by mixtures of ketonic and ether linkages. During the process of carbonisation simultaneous elimination of small molecules and subsequent re-arrangement of the carbon atoms to form six membered rings of carbon lamellae, albeit imperfectly. Aliphatic carbon groups are removed in the form of tars at around 823 K, and at around 1073 K the specimen is no longer transparent to Infra-red (IR) radiation and the carbon has been formed[30].

1.4 Carbon Characterisation

Several techniques are available for the analysis of the structure of isotropic and anisotropic carbons. Some of these techniques are discussed briefly below but more stress is laid upon the fundamental principles of adsorption which is the basis of the adsorptive gas separation processes operating in the carbon molecular sieve materials and it is this which falls within the context of this thesis. The fundamental principles of adsorption are discussed separately under section 1.5.

1.4.1 X-ray diffraction

This technique is used to determine the average bulk structure of carbon material. This technique provides a measure of the amount of ordered material present and can be used to give an indication of the size of crystallites in the ordered structure. The X-ray diffraction pattern is recorded in terms of angle of scattering and interpreted in terms of positions and widths. The parameters usually quoted from X-ray diffraction experiments are as follows:

d_{002} - interlayer spacing; L_c - apparent stack or crystallite height; L_a - apparent stack or crystallite width.

In general, the d_{002} distance is the average spacing between two adjacent basal plane carbon - carbon layers (0.3354 nm in graphite). L_a represents an apparent crystallite dimension in the case of disordered carbons caused by the wrinkling of layers.

This technique has drawbacks and there are limitations to the information obtained for developing a model of structure in carbons. This is basically for two reasons. Firstly, the broadening of diffraction lines of graphitic carbons is a result of two structural phenomena - small notional crystallite size and strain within the lattice resulting from defects. The size broadening can not be separated from strain broadening hence diffraction is interpreted in terms of sizes of notional crystallite, L_c and L_a. Secondly, X-ray diffractions result from those parts which show Debye diffraction conditions. A part of the structure may be highly disordered and therefore not contribute to the X-ray diffraction data. This structural aspect is not included in the model.

1.4.2 Electron microscopy

X-ray diffraction is unsuitable to distinguish clearly between non-graphitizable and graphitizable carbons in the range of HTT up to 1273 K. Electron diffraction makes it possible to resolve the more complex crystalline components of graphitizable carbons by making use of dark-field imaging. In this technique the more ordered regions of graphitizable carbons show up as bright spots on the microscope screen. The high resolution fringe imaging enables a clear distinction between non-graphitizable isotropic carbons with a quite random arrangement of constitute lamellae as in the porous active carbons. Oblerlin's[31] review on electron microscope observations related to carbonisation and graphitization of a wide range of carbonaceous precursors is summarised below:

(1) The initial carbonaceous material which can graphitize i.e. mesophase, must be made up of small basic structural units (BSU) less than 1 nm in size.

(2) These BSUs must align approximately parallel in large areas (elemental domains of bulk mesophase) before the semi-coke stage (brittle solid stage). In all cases, the leading parameter seems to be the ziz-zag texture which allows defect mobility. either interstitial or in-plane defects, with a minimum energy.

(3) Various carbons studied showed a continuous process, as explained in Marchand's model in section 1.3.1, for formation of graphitizable carbons. All the possible intermediates were found between the coarse mosaic domains ($\geq 1\ \mu m$) forming the bulk mesophase of graphitizing carbons and small domains (less than 5.0 nm in size) forming the bulk mesophase of non-graphitizing carbons, with only the first showing anisotropic domains in optical microscopy images. This implies two groups of carbon - graphitizable or non-graphitizable and represents extremes of continuous availability of carbons in terms of graphitization properties.

1.4.3 Raman microprobe spectroscopy

The use of Raman microprobe spectroscopy is based on the vibrational characteristics of carbonaceous lamellae. The advantage being that it is a microscopic measurement capable of a spatial resolution of a few square micrometers and can identify structural heterogeneity within the sample. Raman spectroscopy of graphite and various carbon materials has been reported by various investigators[32]. The Raman spectrum for crystalline hexagonal graphite displays lines at 1580 cm^{-1} (G), 2245 cm^{-1} and 3248 cm^{-1}. For carbons with structural disorder, additional lines appear at 1360 cm^{-1} (D), 1620 cm^{-1} (D) and 2960 cm^{-1}. The 1360 cm^{-1} and 1620 cm^{-1} bands increase in intensity with increasing structural disorder while the 2710 cm^{-1} band shows the opposite trend. The band centred at 2710 cm^{-1} becomes a doublet at 2735 cm^{-1} and 2685 cm^{-1} when a high degree of structural order is developed. This occurs below a d_{002} spacing of 0.338 nm.

1.4.4 Optical properties

Optical microscopy is used to study the optical texture of the carbon structure. The specimen to be studied is mounted in a resin block and the surface polished using alumina. This sample is examined by reflected light microscopy using a half wave retarder plate between the specimen and the analyser[33], as shown in Figure 1.13. Under this microscope configuration the polished surface may give rise to interference colours due to orientation of the graphitic lamella at the surface. The polished anisotropic carbon surfaces appear with various colours from yellow, blue to purple of different sizes and shapes whereas the isotropic carbon is independent of the angle of rotation of the specimen stage. Isotropic carbons appear purple under the optical microscope under all orientations; this is due to the lack of structural anisotropy created by the surface which is optically inactive. The characterisation of appearance of anisotropic or isotropic carbon in terms of size, isochromatic areas and orientation of stacking of lamellae relative to polarized texture of carbons is classified into different sizes as shown in Table 1.1. By point counting the individual components on the entire surface, optical textures can be identified. The optical texture index is the sum of the percentage of each class of optical texture multiplied by its own optical index factor. This number gives an empirical measure of the overall anisotropy of the carbon.

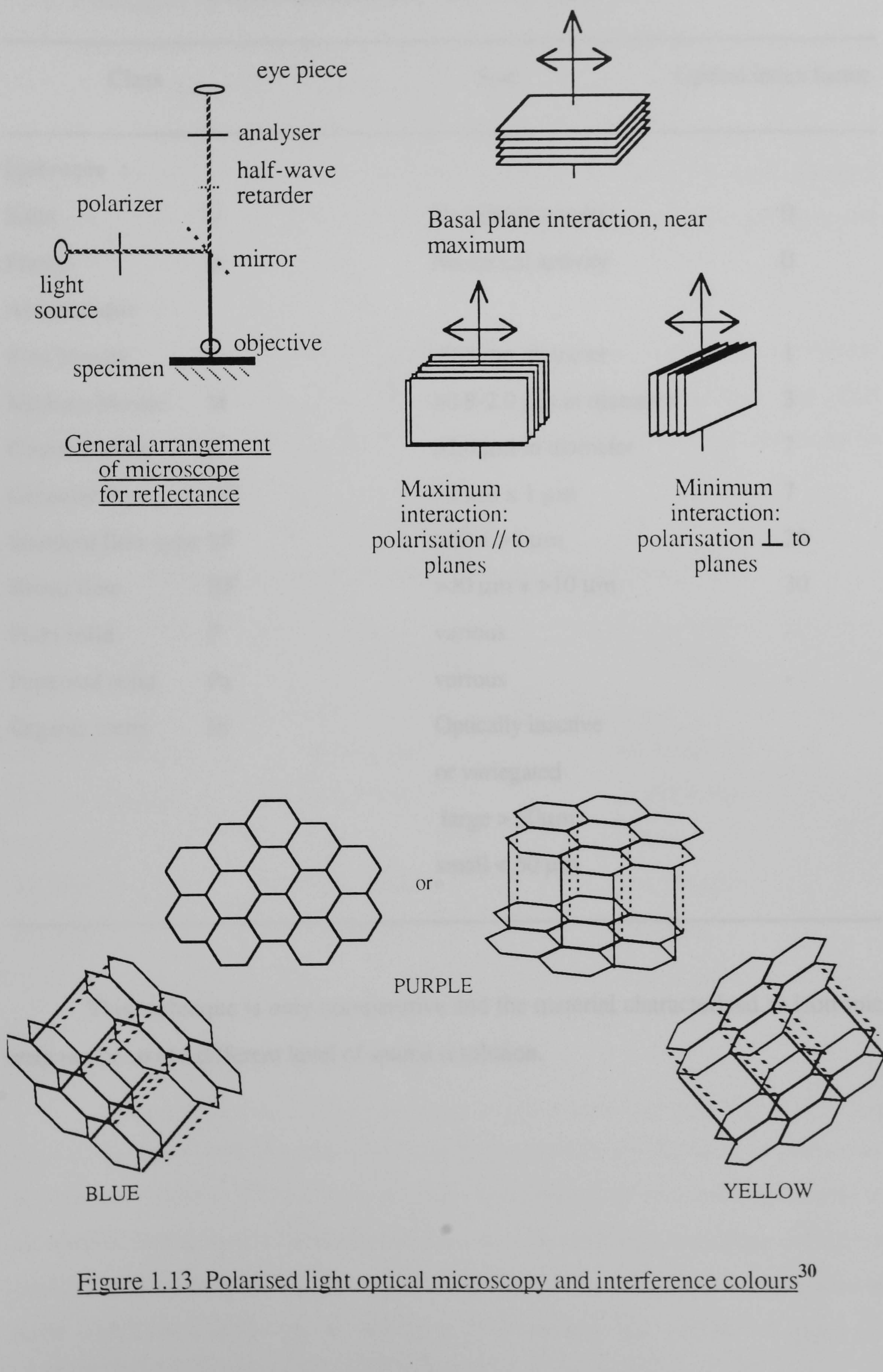

Figure 1.13 Polarised light optical microscopy and interference colours[30]

Table 1.1

Nomenclature used to describe optical texture[33]

Class		Size	Optical index factor
Isotropic :			
Solid	Is	No optical activity	0
Plastic	Ip	No optical activity	0
Anisotropic :			
Fine Mosaic	F	<0.8 μm diameter	1
Medium Mosaic	M	>0.8-2.0 μm in diameter	3
Coarse Mosaic	C	>2.0 μm in diameter	7
Granular flow	GF	>2 μm x 1 μm	7
Standard flow type	SF	>20 x >2 μm	20
Broad flow	BF	>20 μm x >10 μm	30
Plain solid	P	various	-
Patterned solid	Pa	various	-
Organic inerts	In	Optically inactive or variegated large > 50μm small < 50 μm	

This technique is only comparative and the material characterised as isotropic may not be so at a different level of spatial resolution.

1.5 Porosity in Carbons

1.5.1 Principles of gas adsorption

Adsorption in the present context, i.e. gas/solid interface is the enrichment of one or more components in an interfacial layer[34]. The amount of gas adsorbed at equilibrium depends upon pressure, temperature and the chemical nature of the solid surface. However, if temperature and pressure are kept constant, the amount adsorbed will depend on the nature of the solid surfaces; for example, surface area, porosity and the chemical nature of solid surface.

There are two types of adsorption; namely, physical adsorption (physisorption) or van der Waal's adsorption, and chemical adsorption (chemisorption). The main distinguishing characteristics of the two kinds of adsorption are summarised below in Table 1.2.

Table 1.2

Distinction between physical adsorption and chemisorption

	Physical	Chemical
Heat of adsorption	20-40 kJ/mol	>80 kJ/mol
Rates of adsorption	At 273 K fast	At 273 K slow
Desorption	Easy	Difficult
Specificity	Non specific	Very specific
Coverage	Multilayer	Monolayer

1.5.2 Classification of pores

Active carbons and carbon molecular sieves (CMS) owe their high adsorption capacity to the existence of a micropore system, although a wide range of pores may occur in the material. The porosity of a solid is a measure of its volume accessible to the specific vapour under investigation and is usually classified according to the pore sizes. The pores vary in size from cracks of micrometer or macropore dimensions to those which are closed even to helium at room temperature. Table 1.3 gives the

International Union of Pure and Applied Chemists (IUPAC) classification of pores according to their effective width.

Table 1.3

IUPAC classification of Pores[34]

Micropores	width less than 2 nm
Mesopores	width between 2 nm and 50 nm
Macropores	width greater than 50 nm

These classification limits are somewhat arbitrary as the pore shape, the size of adsorbed molecule and nature of adsorbate-adsorbate interactions are critical in determining the adsorption characteristics. In micropores the walls are very close so that interaction is very high leading to enhanced adsorption at a given relative pressure. In mesopores, adsorption is by capillary condensation showing a hysteresis loop.

Figure 1.14 shows the different pore types found in the solids[35].

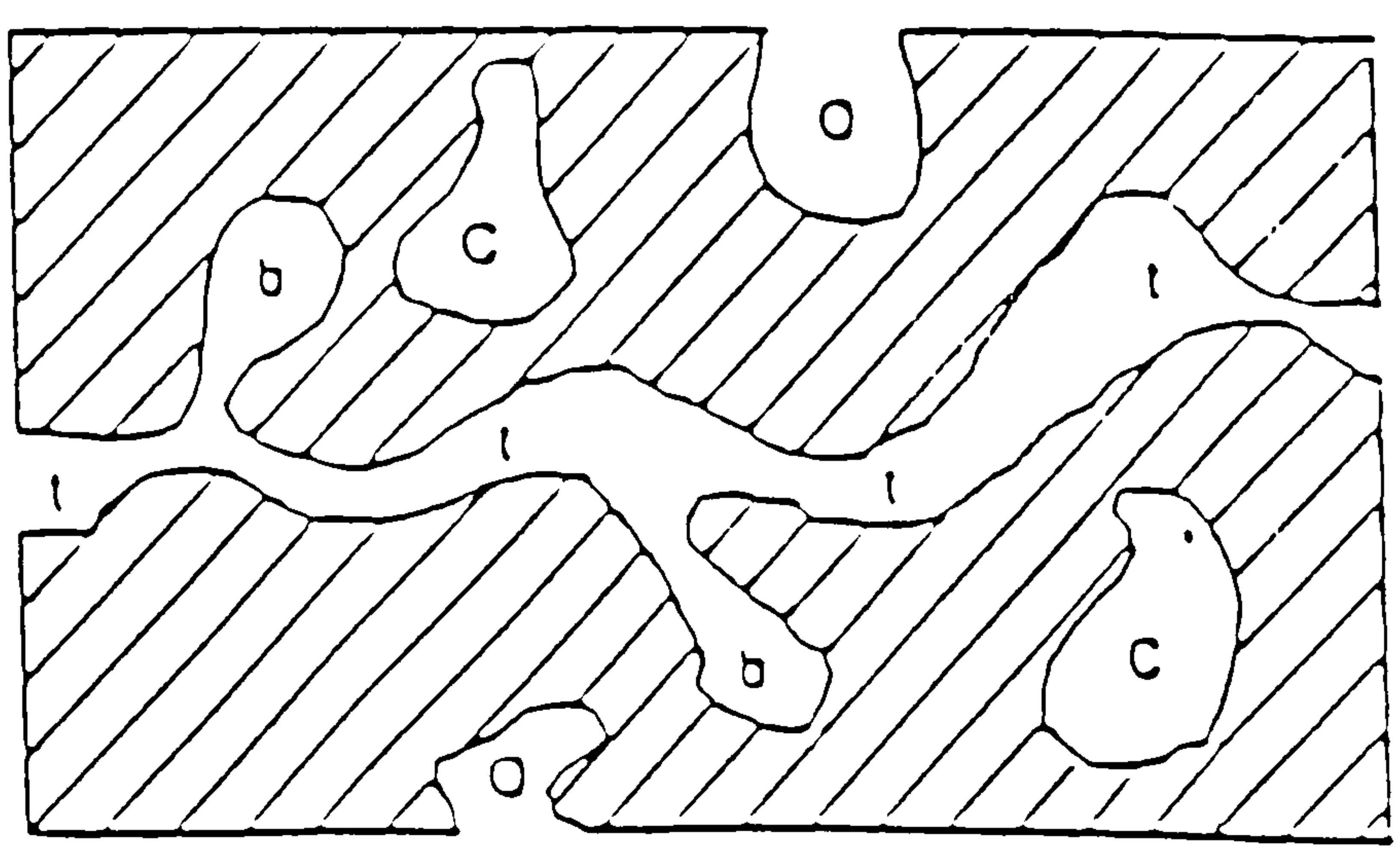

Different types of porosity in a porous solid.
O - open pores: C - closed pores: t - transport pores: b - blind pores.

Figure 1.14 Different types of pores[35]

Open pores denote pores which are connected to the external surface of solids and allow the passage of fluids. vapours into and out of the solid through these pores. ***Closed pores*** denote a void and are isolated from the external surface of a solid. Besides open and closed pores it is often useful to refer to the solid surface of solids as either ***internal*** or ***external*** surface. In most cases, the distinction is not clear; fissures and cracks which penetrate deeply into the interior contribute to internal surface area, whereas superficial cracks which are wider than deep make up the external surface. The external surface refers to open pores, but this is difficult to define as solid surfaces are rarely smooth on an atomic scale, whereas the internal surface surrounds the closed pores. ***Transport pores*** are pores which connect different parts of the external surface of the solid to the microporosity. ***Blind pores*** are connected to the transport pores.

1.5.3 Classification of adsorption isotherms

Physisorption measurements are widely used for the investigation of the structure of porous materials. The adsorption isotherms are studied in order to provide the following information: (1) estimation of surface area, (2) estimation of pore volumes in porosities present, (3) fundamentals of adsorption processes and (4) assessments of efficiency of industrial carbons employed in separation and purification techniques.

The extent of adsorption on a surface generally depends on the nature of the adsorbent and the adsorbate and is a function of adsorbate pressure *(p)* and temperature *(T)*. If '*n*' is the quantity of gas adsorbed, this is expressed as[36]:

$$n = f\,(p,T,gas,solid) \qquad (1.0)$$

For a particular gas-solid system at constant temperature equation (1.0) simplifies to:

$$n = f\,(p)_{T,gas,solid} \qquad (1.1)$$

If the gas is kept below its critical temperature and the pressure of the gas increases the gas will liquify. The pressure at which gas liquifies is the saturation vapour pressure.

If pressure is expressed in terms of relative vapour pressure, i.e. p/p_o (p_o is saturation vapour pressure of the adsorbate) then equation (1.1) becomes:

$$n = f(p/p_o)_{T,gas,solid} \qquad (1.2)$$

Thus, using relative pressure instead of absolute pressure, the adsorption of various adsorbates can be readily compared.

The relationship between the amount of substance adsorbed at any given relative pressure and at constant temperature can be represented graphically by means of an ***'adsorption isotherm'***(using equation (1.1) and (1.2)) as shown in Figure 1.15. In the adsorption of gases on solid surfaces six general types of isotherms have been observed.

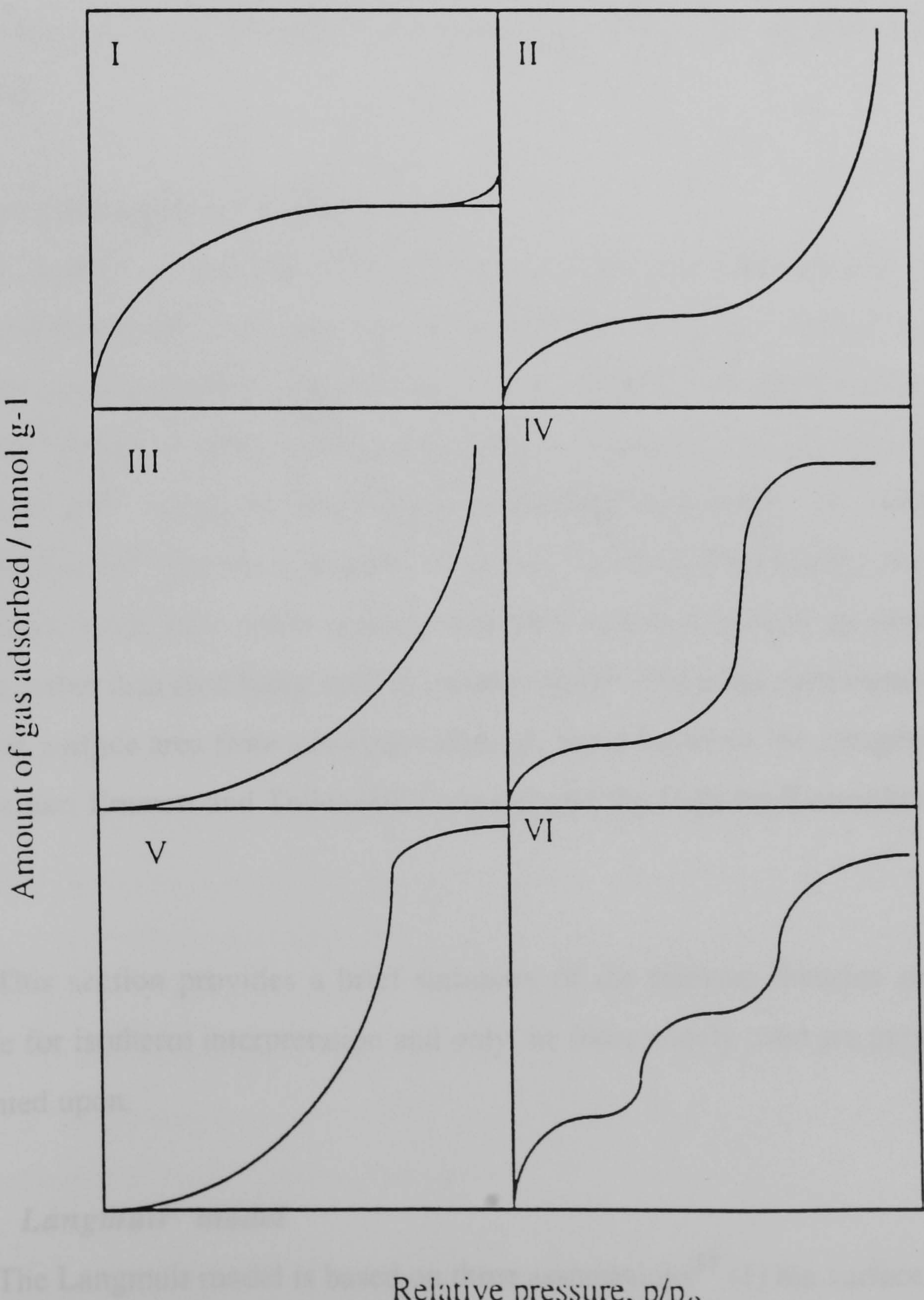

Figure 1.15 Showing different adsorption isotherms.

Type I isotherm is characteristic of the microporous carbons (i.e. active carbons and carbon molecular sieves) and gives a good indication of the approximate total microporous volume of the solid by directly reading the amount of vapour at the plateau of the isotherm. In contrast, Type II isotherms represent the adsorbate-adsorbent system with unrestricted monolayer-multilayer adsorption on a non-porous or macroporous adsorbent. The characteristic features of the Type IV isotherm are its hysteresis loop and limiting uptake at high p/p_0. These features are associated with capillary condensation occurring in mesopores. The remaining isotherms are less common: Type VI represents stepwise multilayer adsorption on a uniform non-porous surface, whereas Type III and V are associated with weak adsorbent-adsorbate interactions.

1.5.4 Determination of surface area

A number of attempts have been made to develop mathematical models to interpret isotherms obtained from porous and non-porous solids. In most cases these adsorption models ignore structural features of the adsorbent, except for distribution of adsorption energy or pore width. Information regarding surface area, pore size distribution and micropore volume etc. is incorporated within the isotherm and extracting this information is a matter of debate. Hence, all equations are based on assumptions made from these models and then matched against an experimental isotherm, rather than data being used to create a model. The adsorption theories used in evaluating surface area from adsorption data are those based on the Langmuir model, the Brunauer, Emmett and Teller (BET) model and the Dubinin-Radushkevich (DR) model.

This section provides a brief summary of the relevant theories and models available for isotherm interpretation and only the most widely used are presented and commented upon.

1.5.4.1 Langmuir model

The Langmuir model is based on three assumptions[37] (1) the surface of a solid is composed of a two-dimensional array of energetically homogeneous sites, (2) only one molecule can be adsorbed on a site and saturation of the surface is reached when a monolayer is completed and, (3) interaction does not occur by either repulsion or attraction between the adsorbed molecules. Using these assumptions, Langmuir[38] derived, by kinetic methods, an equation which is expressed as:

$$\frac{P}{V} = \frac{1}{V_m b} + \frac{P}{V_m} \qquad (1.3)$$

Where V is the amount of gas sorbed per gram of sorbent at equilibrium pressure P, V_m is the amount sorbed per gram of sorbent to complete a monolayer, b is the an adsorption coefficient specific to each sorbate sorbent system. If the experimental data satisfies the isotherm equation, a graph of P/V against P will give a straight line and V_m the saturation value is calculated from the slope. The specific surface area A is calculated using the equation:

$$A = V_m A_m L \qquad (1.4)$$

Where A_m is the average area occupied by a molecule of the adsorbate in the completed monolayer, L is the Avogadro constant, and V_m is expressed in moles of adsorbate per gram of sorbent.

It has been shown that disagreements occur in V_m values calculated from Langmuir equations plotted from different pressure ranges of the adsorption data[37]. Values of V_m calculated from isotherms obtained at the higher pressures are higher than those calculated from isotherms of lower pressure conditions. The disagreement in V_m values is a result of the first assumption in the Langmuir model which overlooks the fact that only few sorbents possess energetically homogeneous surfaces. At low pressures adsorption occurs only on more energetic sites which usually have high free energies of adsorption; however, at high pressures adsorption occurs at a wider range of energetic sites so that V_m has higher values.

1.5.4.2 The Brunauer-Emmett-Teller model (BET)

The BET method is still the most widely used model despite receiving considerable criticism. It was first proposed by Brunauer, Emmett and Teller[39]. BET is an extension of the kinetic model of adsorption process proposed by Langmuir to account for multilayer adsorption. It assumes that (1) the adsorbent surface is an array of energetically homogeneous sites, (2) no interaction occurs between adsorbed molecules, (3) each adsorbed molecule in the monolayer is an adsorption site for second layer molecules so that several layers are built up until bulk condensation occurs at higher relative pressure and (4) the energy of adsorption of second and all higher molecules is assumed to be equal to that of liquefaction and the total amount adsorbed is taken as the sum of the amounts adsorbed in all layers.

The BET equation is usually expressed in linear form:

$$\frac{p}{n(p_o-p)} = \frac{1}{N_mC} + \frac{C-1}{N_mC}\,\frac{p}{p_o} \tag{1.5}$$

Where n is the amount adsorbed at equilibrium pressure p, N_m is the monolayer capacity, p_o is the saturated vapour pressure and C is a dimensionless constant which is related to adsorption energy and is expressed as:

$$C = \exp\left(\frac{(q_1-q_2)}{RT}\right) \tag{1.6}$$

Where (q_1-q_2) is the net heat of adsorption and q_1 = heat of adsorption in the first adsorbed layer, q_2 = heat of adsorption in the second and subsequent layers, i.e. the molar heat of condensation. For adsorption data that obeys the BET equation, a graph of $p/n(p_o-p)$ against p/p_o will give a straight line with slope, $s = C-1/N_mC$ and intercept, $i = 1/N_mC$. Solution of these two simultaneous equations gives the values of N_m and C. The surface area is calculated using N_m, L and A_m, as shown previously for the Langmuir method.

In practice the value of C can be used to characterise the shape of the isotherm in the BET range. If the value of C is high, i.e. >100 then the intercept $1/N_mC$ becomes so small that it can be approximated to zero and under that condition the graph of $p/n(p_o-p)$ against p/p_o passes through the origin. Under this situation an approximate value of N_m can be obtained by using only one point in the range p/p_o = 0.2-0.3 and drawing the line from that point through the origin. This constitutes the so-called one-point method of surface area measurement.

Although the BET equation has succeeded in describing adsorption data for a large number of systems the deviation from the BET equation in the low relative pressure region p/p_o <0.05 and in the high relative pressure region p/p_o >0.35 must be recognised[37]. The deviation in the low relative pressure region is caused by the assumption of homogeneous surface which is not valid. The deviation in the higher relative pressure region is caused by the assumed absence of lateral interaction between adsorbed molecules, an assumption which is not valid especially in a multilayer adsorption system.

The BET method is probably the most widely accepted for determining the monolayer capacity. However, the BET model has been subjected to number of criticisms such as (1) an energetically homogeneous surface never exists, (2) adsorbate-adsorbent and adsorbent-adsorbent interactions are not taken into account, (3) enthalpy and entropy terms predicted by the model do not agree well with those measured experimentally[40,41,42] and, (4) purely localised adsorption is unlikely to occur above 77 K[43], since the adsorbate molecule has surface translational energy.

1.5.4.3 Empirical procedures

As previously stated that there is no current theory for adsorption that can provide an exact mathematical description of an experimental isotherm over a complete range of p/p_o. Two different procedures can be used to analyse the isotherm data. The first one is to apply a semi-empirical equation - the Frenkel-Halsey-Hill (FHH) equation. This particular mathematical form depends upon the range of the isotherm to be fitted and the nature of gas/solid interactions. The second procedure makes use of standard isotherms on selected non-porous reference materials.

*(I) **FHH equation***

The FHH equation is usually stated in the form [44]:

$$\ln\left(\frac{p}{p_o}\right) = \frac{k}{n^r} \tag{1.7}$$

where n is the multilayer coverage at relative pressure p/p_o and k and r are characteristic constants for a given gas-solid system. The exponent r is obtained from the plot of log log (p/p_o) against log n and is related to the decay of interaction energy with distance from the surface. For example it has been found that the value of $r = 2.70 \pm 0.03$ for nitrogen adsorption 77 K on a wide range of porous and non-porous oxides and carbons[45,46]. The effect of mesoporosity decreases the value of r, whereas microporosity tends to increase it.

(II) t-plot and α_s - plot method

A standard isotherm provides useful information regarding a number of points, such as (1) making allowance for the thickness 't' of the adsorbate film of the pore walls, in pore size calculations and (2) in detecting both the onset of capillary condensation and the presence of microporosity.

The t method and its extension provide a simple means for comparison of the shape of a given isotherm with that of a standard on a non-porous solid. The BET procedure enables construction of a t-curve (t against p/p_0) by measuring the isotherm on a non-porous sample of the substance, expressing it in reduced form of n/n_m (where n is the amount adsorbed at relative pressure p/p_0 and n_m is the monolayer capacity) against p/p_0, and then using the conversion $t = (n/n_m)\,\sigma$, where σ is the thickness of a single molecular layer. A number of studies conducted by several workers[47,48] showed that the isotherms of a variety of substances fell sufficiently close together ($\pm$ 5%) enabling the t-curve to be used in routine pore calculations.

In order to determine the onset of capillary condensation and the presence of microporosity, one may re-plot n against t. If the t-plot is a straight line passing through the origin (Figure 1.16 a), the isotherm under test must be identical to the standard isotherm; an upward swing at C in Figures 1.16 b and 1.16 d, denotes capillary condensation; and positive intercept as at D in Figures 1.16 c and 1.16 d, indicates the presence of micropores having a total volume equivalent to ED.

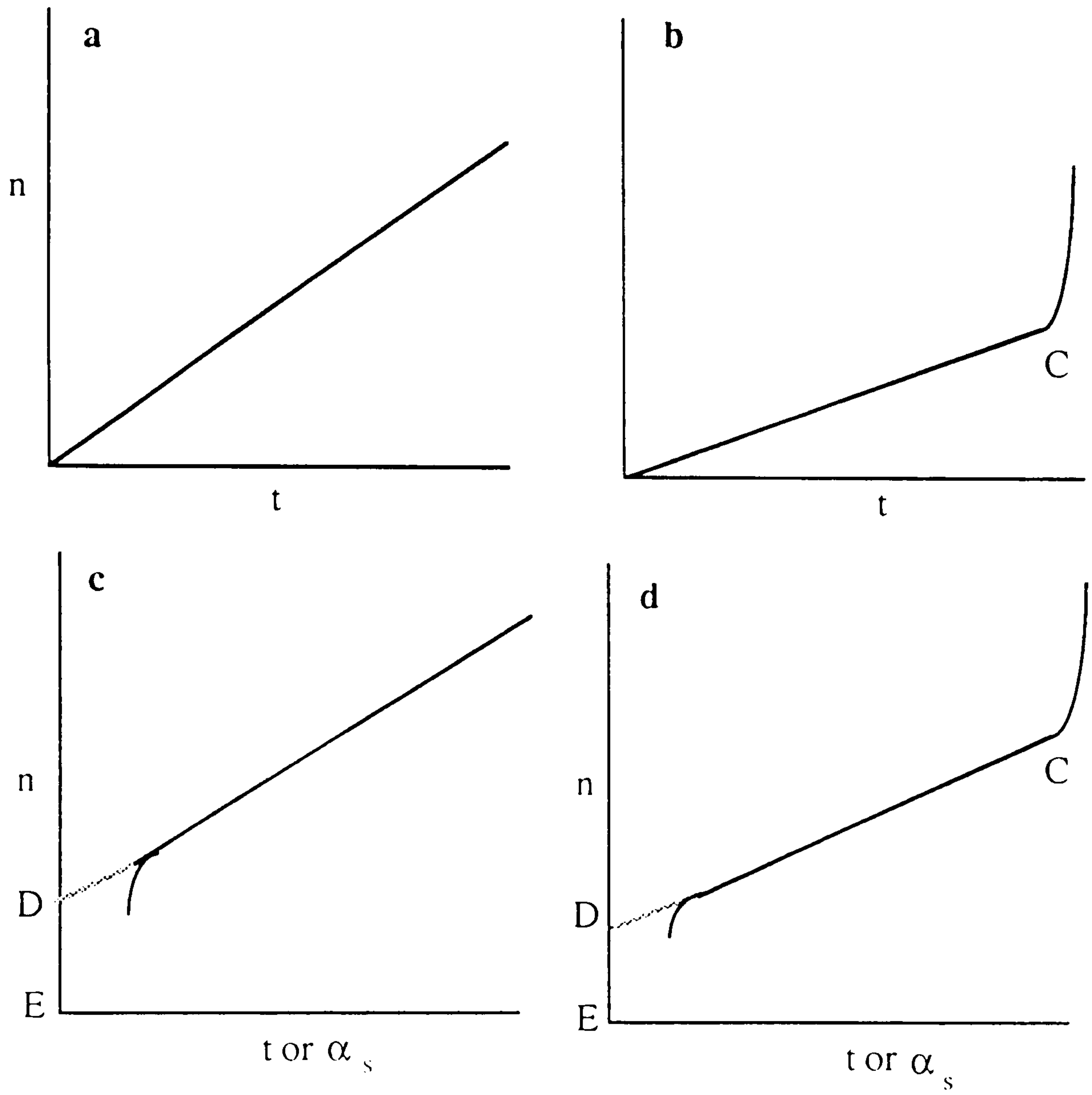

Figure 1.16 t (or α_s)plots[34]

However, the common t-curve can produce misleading results. The small differences between the reduced isotherm of different substances, which are immaterial in pore size calculation, can no longer be ignored. Hence, it becomes essential that the reference isotherm for the t-plot be measured on a non-porous sample as similar as possible in surface structure to the substance under test[34]. In the comparison of isotherms involvement of t and n_m gives rise to complications. Sing[49] proposed the use of α_s in the place of t, where $\alpha_s=n/n_{0.4}$ (where $n_{0.4}$ = adsorption at p/p_o= 0.4). A curve of α_s against p/p_o and an α_s-curve can be derived from the appropriate reference isotherm, and used to construct α_s-plots which can be used in the same way as t-plots.The α_s plots are quite useful for comparison of two isotherms; for example, in studying the compaction of a powder and the uncompacted powder can be used as a reference material. Since n_m is not involved, the α_s - plot may still be used if C is very small and the BET monolayer capacity is therefore unreliable. When the isotherm is of Type III, BET the t-plots are unsatisfactory.

1.5.5 Assessment of mesoporosity

This form of porosity is an intermediate between the micro and macro porosity. The pore diameters are in the range 2-50 nm and are much wider than the diameter of the adsorbate molecule. Capillary condensation occurs in the mesoporosity and gives rise to adsorption/desorption hysteresis at high relative pressures due to different mechanisms of filling and emptying of the pores.

1.5.5.1 Capillary condensation

The characteristic mechanism of adsorption in mesopores is capillary condensation which is illustrated by a Type IV isotherm. As the pores are much larger than the adsorbate molecule, at low relative pressure, layer by layer adsorption occurs. The adsorbed film acts as a surface upon which further adsorption can eventually occur resulting in capillary condensation. The low pressure region follows the same path as that of a Type II isotherm indicating a monolayer coverage, but at a certain point it starts to deviate and, as the relative pressure increases, enhancement of adsorption occurs giving rise to a multilayer formation and a further sorption occurs resulting in capillary condensation. As the pressure increases the multilayers increase until they combine in the narrowest cross-section of cylindrical or wedge-shaped pores and form a meniscus of condensed adsorbate, which is concave when the adsorbate condenses at a pressure lower than the saturated vapour pressure of the gaseous phase.

Capillary condensation occurs because the equilibrium vapour pressure, p, over a concave meniscus of an adsorbate which wets the surface, is less than the saturated vapour pressure, p_o, of the gaseous phase, i.e. even less than unity.

There are two forms of capillary condensation-reversible capillary condensation and capillary condensation with hysteresis. Capillary condensation cannot occur in the absence of a solid surface which serves to nucleate the process. Within a mesopore the adsorbed film acts as a nucleus upon which condensation can occur. The reversibility and non-reversibility of condensation hysteresis processes depend upon the shapes of the pores. Reversible capillary condensation is thought to occur in single pores which are closed-ended cylinders, wedge shaped or conical. However, capillary condensation giving rise to hysteresis is thought to occur in slit-shaped pores, open-ended cylindrical pores and pores with narrow necks and wide bodies. These are often referred to as ***'ink bottle'*** pores. Hysteresis may also take place through the presence of narrow channels connecting larger pores, which effectively reduces the pressure at which pores can be evacuated.

The BET method is still reliable for calculating the monolayer coverage, since capillary condensation occurs above the monolayer region of the isotherm, i.e., above $p/p_0 = 0.4$ provided there is no micropore filling in the lower region.

1.5.5.2 Computation of mesopore size

The mesopore size is usually calculated by using Kelvin equation in the form[34]:

$$\ln\left(\frac{p}{p_0}\right) = -\frac{2\gamma V_L}{RT}\,\frac{1}{r_m} \qquad (1.8)$$

Where p/p_0 is the relative pressure at temperature T, V_L is the molar volume of liquid adsorbate, R is the gas constant, r_m is the curvature of the hemispherical meniscus and γ is the surface tension.

In order to calculate the mesopore size from a physisorption isotherm it must be assumed that the (1) pores are rigid and of uniform shape, (2) the micropores are absent (or can be taken into account independently), (3) there are no pore blocking effects and (4) pore size distribution does not extend continuously into the macropore range.

1.5.5.3 Hysteresis

In the gas physisorption isotherm, condensation/evaporation usually gives rise to hysteresis in the multilayer region. Hysteresis is not always observed for mesoporous solids: for example, in tapered pores closed at the narrow end, adsorption initially produces a hemispherical meniscus which advances up the pore until the whole pore is filled. Desorption is the exact reverse of this process resulting in the absence of hysteresis. To this end four types of hysteresis loops have been defined as shown in Figure 1.17[34].

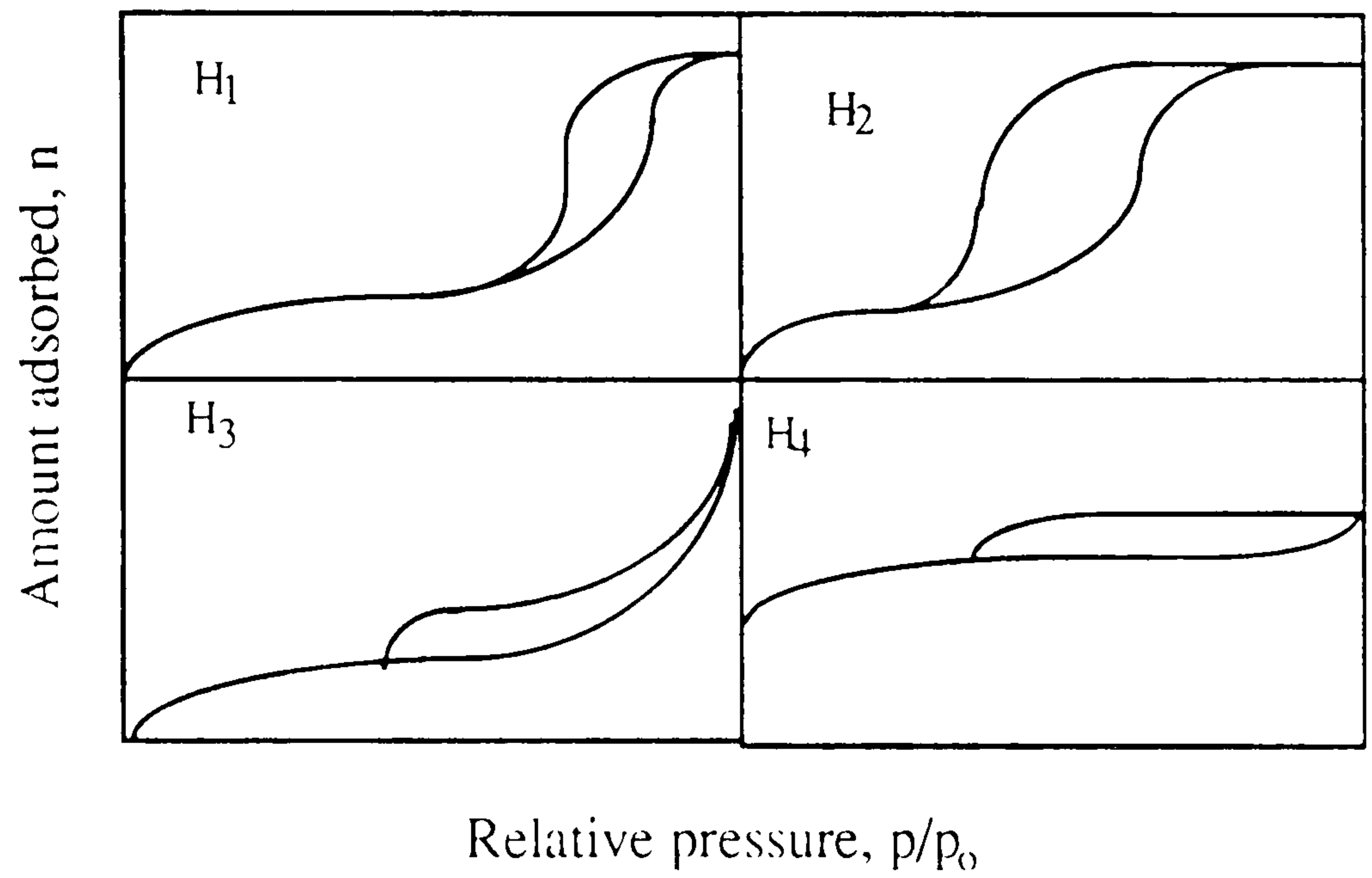

Figure 1.17 Classification of hysteresis loops[34]

Although adsorption isotherms can provide a good indication of the porous structure of a carbon, sometimes a mixed isotherm is obtained which is difficult to analyse due to the different types of pores present. In order to obtain more information it is useful to study the desorption isotherm which generally does not coincide with the adsorption isotherm over the entire pressure range. The hysteresis loop may be present over high or low relative pressure. Hysteresis loops have been found to exhibit a wide variety of shapes which are associated with a specific pore structure. Type H_1 and H_4 refer to two extremes types, where as type H_2 and H_3 may be regarded as intermediate between the two (i.e. H_1 and H_4). Type H_1 is often associated with porous materials known to consist of agglomerates or compacts of approximately spherical particles of uniform size and hence have a narrow distribution of pore size. Type H_2 loops arise from some corpuscular systems, in which the distribution of pore sizes and shape is not well defined. Type H_3 and H_4 are associated with adsorbents having slit-shaped pores. In the case of H_3 the slit shaped pores are derived from plate like particles. The Type I isotherm character, when associated with H_4, indicates the presence of microporosity[34].

1.5.6 Assessment of microporosity

1.5.6.1 Micropore filling

Micropore filling is a phenomenon that gives rise to the Type I adsorption isotherm (refer Figure 1.15). Micropores are filled with physisorbed molecules before capillary condensation begins. Hence, the process of micropore filling does not take capillary condensation into account, but the mechanism of pore filling is dependent on the nature of the adsorption system and the ratio of pore width (d_p) to molecular diameter (σ) i.e. d_p/σ rather than the absolute value of d_p. Pores of molecular dimensions (i.e. $d_p/\sigma = 1$-2) are filled preferentially at very low p/p_o, whilst the wider micropores ($d_p/\sigma = 2$-5) are filled by a cooperative process at higher p/p_o[50].

Enhanced adsorption occurs in narrow micropores due to overlap of the potentials from neighbouring walls only a few molecular diameters apart. The initial part of the isotherm is associated with micropore filling rather than surface coverage. Hence, it is inappropriate to use the BET method in order to evaluate the specific surface area of a microporous solid; however, the BET method can still be applied to find the apparent specific surface area.

Evaluation of microporosity depends upon the evaluation of micropore volume. In order to assess the micropore volume it is necessary to understand the phenomenon and different types of adsorption occurring in the micropores.

1.5.6.2 Theories of adsorption in micropores

The width of micropores are <2nm according to the IUPAC description. Furthermore, micropores are often subdivided into ultramicropores (<0.7 nm) which are distinguished by primary micropore filling and supermicropores (0.7-1.5 nm) which are distinguished by secondary micropore filling[36], although the terminology for the ultramicropores and supermicropores needs to be fully established[34]. However, there is evidence to suggest that adsorption within the micropore follows a different mechanism depending on the width of micropores.

In micropores the close proximity of the pore walls and the overlap of adsorption potentials results in enhanced adsorption at low relative pressure. This results in a pore filling mechanism for adsorption in micropores[51,52].

The mechanism of adsorption in supermicropores is attributed to cooperative effects. Ultramicropores are several molecular diameters smaller in width than supermicropores and enhancement of the adsorption potential in supermicropores is less than that in ultramicropores. The nature of secondary process in supermicropores can be explained by a simplified model of a slit as shown in Figure 1.18. Once the monolayer has been formed on walls, and if molecules (1) and (2) happen to condense opposite to one another, the probability that molecule (3) will condense increases. The increase in the residence time of molecules (1), (2) and (3) promote the condensation of molecule (4) and still further molecules, as shown in Figure 1.18. The critical parameter in the enhancement of the adsorption energy is not the pore size itself but the ratio of the size of pore to that of the adsorbate.

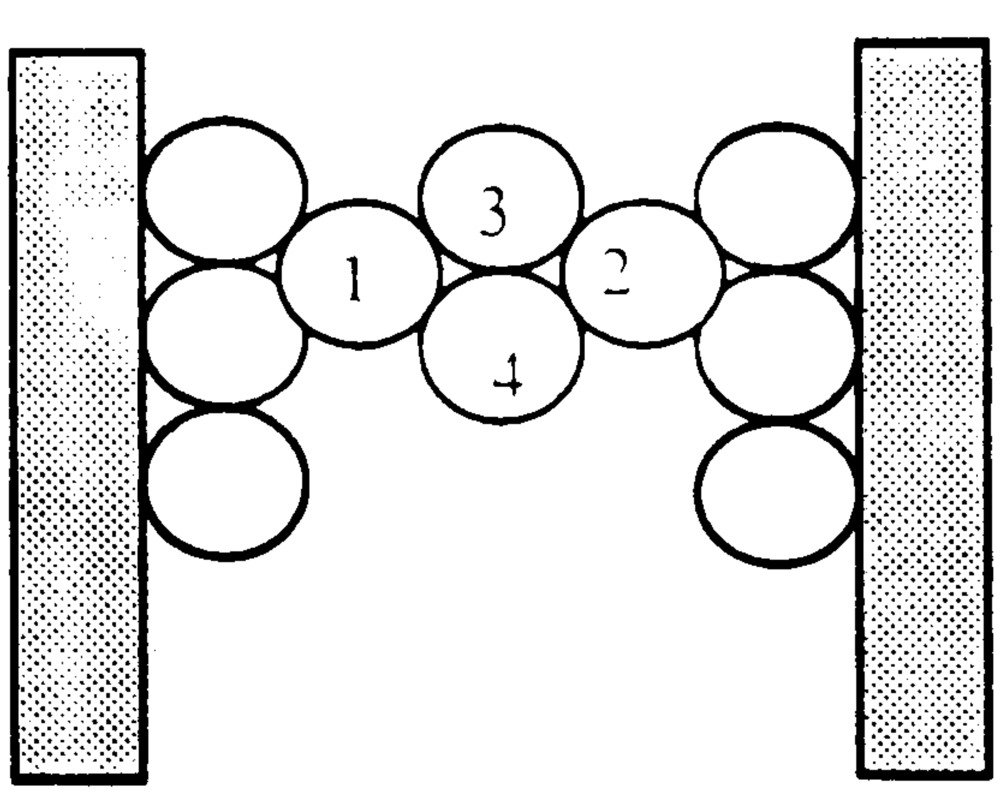

Figure 1.18 Model of cooperative adsorption in a slit shaped-pore[36]

In narrower pores (i.e. ultramicropores) the diffusion of adsorbate molecules through narrow constrictions into micropores occurs by an activated process. In such narrow pores, repulsive forces between the adsorbate molecule and pore wall come into play resulting in an energy barrier to diffuse through the pore. Hence, in order for an adsorbate molecule to be adsorbed in a pore beyond a microporous constriction, it must have sufficient kinetic energy to pass over the energy barrier. At high temperatures the rate becomes faster and reaches equilibrium faster and the measured uptake diminishes with rising temperature. The apparent activation energy can be given by the Arrhenius equation:

$$k = A\, e^{-E_a/RT} \qquad (1.9)$$

Where E_a = apparent activation energy, k is the measured rate of uptake at temperature T and A is the pre-exponential factor.

Equation 1.9 suggests a plot of ln k versus 1/T is a straight line of slope - E_a/R and intercept = A. A is referred to as the ***'pre-exponential factor'*** or ***'frequency factor'***.

Diffusion in micropores whose diameter is approximately that of the adsorbate molecule still has some ambiguities in the estimation of the order of magnitude of adsorption rate when adsorption is controlled by this type of diffusion. The study of CMS is important because they contain a variety of pores. The micropores in the CMS are considered to be slit shaped of around 0.5 nm opening between graphitized layer planes. Table 1.4 lists the work carried out on the diffusivity of gases into coal, zeolites and CMS materials; only those gases which have been used to study kinetics on CMS materials in this thesis have been taken into account.

Table 1.4

Activation energies of different gases on coal, carbon molecular sieves and zeolites.

Gas	Material	Activation energies ($kJ\ mol^{-1}$)	Reference
CO_2	Coal	3.36-16.38	53
CO_2	CMS	23.1	54
CO_2	PVDC	25.2-27.3	55
CO_2	Zeolite	42-58.8	56
CO_2	Zeolite 0.4 nm	20.58	57
CH_4	Coal	21.64-23.52	58
CH_4	Zeolite 0.4 nm	18.9	57
CH_4	Coal	10.5	59
CH_4	Zeolite 0.5 nm	18.48-22.68	60
CH_4	Zeolite 0.5 nm	20.16	61
O_2	Zeolite 0.4 nm	10.45	57
O_2	CMS	26.04	62
O_2	CMS	25.2	63
O_2	CMS	25.2	66
O_2	CMS	10.08	61
N_2	Zeolite 0.3 nm	12.6	64
N_2	Coal	10.5.-26.9	53
N_2	CMS	27.3	63
N_2	CMS	15.54	65
N_2	CMS	31.08	66
C_2H_4	CMS	20.2	61
C_2H_2	Active carbon	10.0-44.5	67

Molecular sieving is a process that occurs in micropores and limits the diffusion of adsorbate through the microporous network[68]. The adsorption of a molecule is influenced by the rate at which the molecule moves from one site to another. The rate of adsorption is also controlled by the temperature, size and the shape of the adsorbate molecule. Work conducted by Lamond *et al.*[69] on a series of microporous carbons showed that the amount of carbon dioxide adsorbed (at 195 K) was higher than nitrogen (at 77 K). This was attributed to the close proximities of walls in micropores leading to a region of high potential energy as compared to the surrounding external surface. In turn this increased energy enhances the interactions between the adsorbate molecule and the adsorbent, which may be further increased if walls contain a polar species. The degree of interaction once again is dependent upon the pore width in relation to that of the diameter of the adsorbate molecule.

1.5.6.3 Evaluation of micropore volume using Dubinin-Radushkevitch (D-R) equation

Various empirical and semi empirical procedures can be used to evaluate the micropore volume. In order to quantify the micropore volume it is usually assumed that the pores are filled by liquid adsorptive. However, this is a simplified version as the degree of molecular packing in pores depends upon the pore size and shape.

The micropore volume can be estimated by the Type I isotherm. The micropore volume can be obtained from the amount of adsorption represented by the plateau in the isotherm. If the microporosity is associated with significant external area then further adsorption occurs at higher relative pressure and no plateau is obtained.

Dubinin and coworkers proposed a theory for estimation of micropore volume based on the Polanyi adsorption theory. Physical adsorption of gases and vapours in micropores has been described by the D-R equation[70,71,72]. This utilises the mechanism of pore filling rather than the layer by layer technique used by BET method. The D-R equation is expressed as follows in order to determine micropore volume of the solid:

$$\log_{10} V = \log_{10} V_o - D \log^2_{10} (p/p_o) \qquad (1.10)$$

where V is the volume filled at relative pressure p/p_o, V_o is the total amount of adsorbate within microporous systems and D relates to the pore size distribution.

In a plot of $\log_{10}V$ against $\log^2_{10} (p/p_o)$, the gradient can be used to obtain V_o. However deviation from the predicted plot can occur depending on the extent of the micropore volume, pore size distribution and on the deviation from Gaussian distribution. Some common deviations from the D-R plot are shown in Figure 1.19 (b) and(c)[73]. However, McEnaney[35] recommends caution in interpreting deviations from the D-R equation since some are due to activated diffusion.

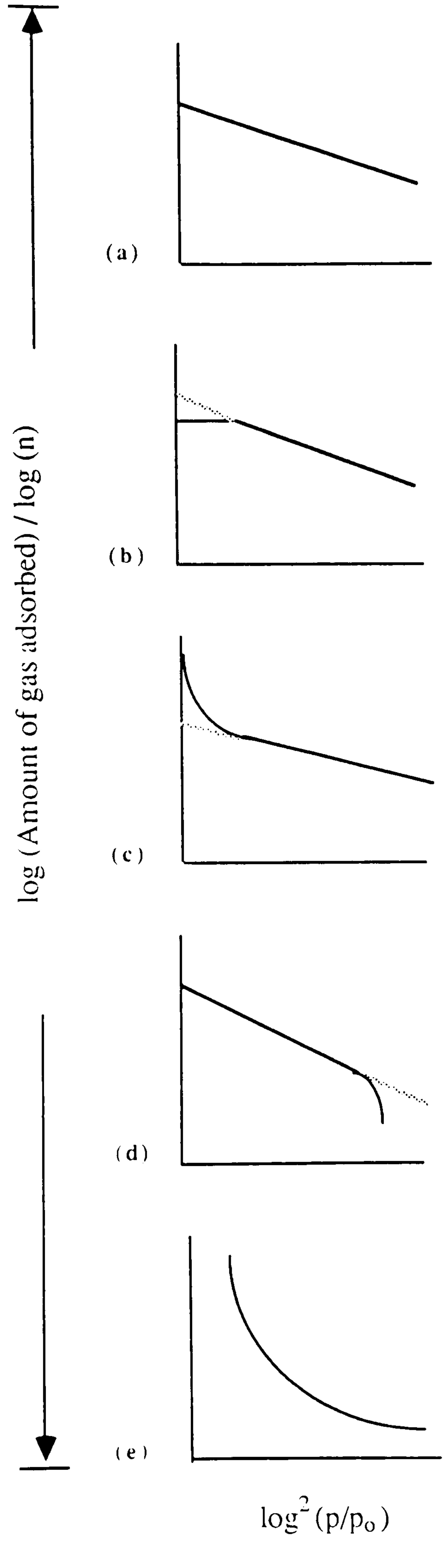

(a) Adsorption is a continuous process i.e. the ultramicropores are filled initially followed by adsorption in super-micropores.

(b) This type of D-R plot is typical of a microporous carbon. The cut-off corresponds to the plateau in the isotherm reached when monolayer coverage is reached in microporous carbons.

(c) The upwards swing in this D-R plot is believed to occur through the occurence of either: [1] supermicroporosity, or [2] adsorption in mesopores or, [3] multilayer adsorption on non-porous solids.

(d) This type of D-R plot is thought to occur due to the process of activated diffusion or molecular sieving, that is the adsorbate is excluded from the smallest micropores.

(e) This type of D-R curve occurs in microporous solids where the microporosity is either developing or closing.

········ predicted

——— actual

Figure 1.19 Common deviations from D-R curve[73]

The surface areas obtained on some adsorbents vary according to the gas used. Hence, it is not valid to quote absolute values of surface area but to make comparison of surface areas provided the same adsorbate has been used. Surface areas obtained using the Langmuir, the BET and DR plots give different values as these theories apply to different sections of the adsorption isotherm. For example, while the Langmuir and BET methods are applied to the relative pressure range of about 0.05-0.4 of the adsorption isotherm the D-R equation is applied to a much lower relative pressure region[74]. It is clear that surface area is valid only for purposes of comparison and for this purpose the same adsorbate must be used; also, some theory must be used for evaluation of the required parameter.

1.5.7 Diffusion in porous media

Diffusion in a pore system can be considered as a transport process by which molecules are transported from one part of the porous system to another part. This transport phenomenon also depends upon the ratio of pore diameter to that of the diffusing molecule and the sorbate concentration. Generally, carbon molecular sieves have a well defined bimodal pore size distribution which consist of microporous regions with a macroporous network. The diffusion mechanism begins with free diffusion, in which the average path length is large compared to that of the pore diameter. If the pore diameter becomes smaller free gas diffusion changes to capillary or Knudsen diffusion. This surface diffusion has an Arrhenius temperature dependence. When the pore diameter is approximately equal to the diameter of the gas molecule, activated diffusion occurs. This has a higher activation energy than the surface diffusion because of the stronger interaction forces between the gas molecules and the pore walls. Diffusion occurs in this region by activated process and is referred to as ***'configurational diffusion'*** or simply ***'micropore diffusion'***.

Quantitative measurements of rates at which a diffusion process occurs are generally expressed in terms of a diffusion coefficient. The rates of adsorption and desorption in porous adsorbents are generally controlled by transport within the pore network, rather than by the intrinsic kinetic sorption at the surface. As there may be bulk flow through the pores, it is convenient to consider interparticle transport as a diffusive process and to correlate kinetic data in terms of diffusivity, which can be defined in accordance with Fick's first equation which states that the rate of transfer of diffusing substance is proportional to the concentration gradient into the particle and is represented mathematically as:

$$F = -D\ \delta C/\delta x \qquad (1.11)$$

Where F is the rate of transfer per unit area of section, C is the concentration gradient of diffusing substance, x is the surface coordinate measured normal to the section and D is the diffusion coefficient.

The empirical diffusion equation for rate of diffusion of a gas into a spherical particle can be given as[75] (the defination of M_t and M_∞ is given below):

$$\frac{M_t}{M_\infty} = k\, t^n \qquad (1.12)$$

The diffusional exponent (n) can be evaluated from a plot of log (M_t/M_∞) against log t. When n = 0.5 then the diffusion mechanism is Fickian and if n = 1 then it is described as Case II. If n lies between 0.5 and 1 then the mechanism is said to be anomalous and is supercase II if n is greater than 1.

For most particle shapes, representation as an equivalent sphere is an acceptable approximation and the transport may therefore be described by Fick's law for dimensional diffusion into a sphere of radius r with D being the diffusivity, the equation can be written in spherical coordinates as:

$$\frac{\partial C}{\partial t} = D \left(\frac{\delta^2 C}{\delta\, r^2} + \frac{2\delta C}{r\delta r} \right) \qquad (1.13)$$

If diffusion is constant for a one dimensional radial diffusion in a sphere of radius 'r' with a constant gas diffusion coefficient, D, it can be given as:

$$\frac{\partial C}{\partial t} = D \left(\frac{\delta^2 C}{r^2} + \frac{2\delta C}{r\delta r} \right) \qquad (1.14)$$

The diffusion into a homogeneous spherical particle for isothermal diffusion assuming that the diffusion coefficient is constant is given by following equation:

$$\frac{M_t}{M_\infty} = 1 - \frac{6}{\pi^2} \sum_{n=1}^{\infty} \frac{1}{n^2} \exp\left(\frac{- D\, n^2 \pi^2 t}{r^2} \right) \qquad (1.15)$$

Where M_t is the gas uptake at time t, M_∞ is the gas uptake at equilibrium, D is the diffusion coefficient , r is the radius of the particle.

The solution for short times:

$$\frac{M_t}{M_\infty} = 6\left(\frac{Dt}{r^2}\right)^{1/2}\left(\pi^{-1/2} + 2\sum_{n=1}^{\infty} \text{iefrc}\ \frac{nr}{\sqrt{Dt}}\right) - \frac{3Dt}{r^2} \tag{1.16}$$

M_t/M_∞ is the fractional approach to equilibrium. Expansion of the series in (1.15) and neglecting the second and higher terms gives:

$$\frac{M_t}{M_\infty} = 1 - \frac{6}{\pi^2}\left(\exp\left(-\frac{D\pi^2 t}{r^2}\right)\right) \tag{1.17}$$

so that:

$$\frac{M_\infty - M_t}{M_\infty} = \frac{6}{\pi^2}\left(\exp\left(-\frac{D\pi^2 t}{r^2}\right)\right) \tag{1.18}$$

Expansion of the series of (1.16) and neglecting the second and higher terms gives:

$$\frac{M_t}{M_\infty} = \frac{6}{\pi^{1/2}}\ \frac{D^{1/2}\ t^{1/2}}{r} \tag{1.19}$$

Hence for long time behaviour a plot of $\ln((M_\infty - M_t)/M_\infty)$ against t will have a slope of $D\pi^2 / r^2$, and for short time behaviour a plot of M_t/M_∞ versus $t^{1/2}$ will have a slope of $(6D^{1/2})/\pi^{1/2}r$. A graph of $\ln(1-M_t/M_\infty)$ against time (t) for theoretical Fickian diffusion is shown in Figure 1.20. The graph is slightly curved at very low values of t due to the importance of higher terms at low t values. On the other hand, for uptake above 50% and the best least squares straight-line fit for the data, > 50% uptake gives a value of D/r^2 very close to the theoretical value. This is due to the rapid convergence of equation 1.15 the higher terms in the series expansion becoming insignificant.

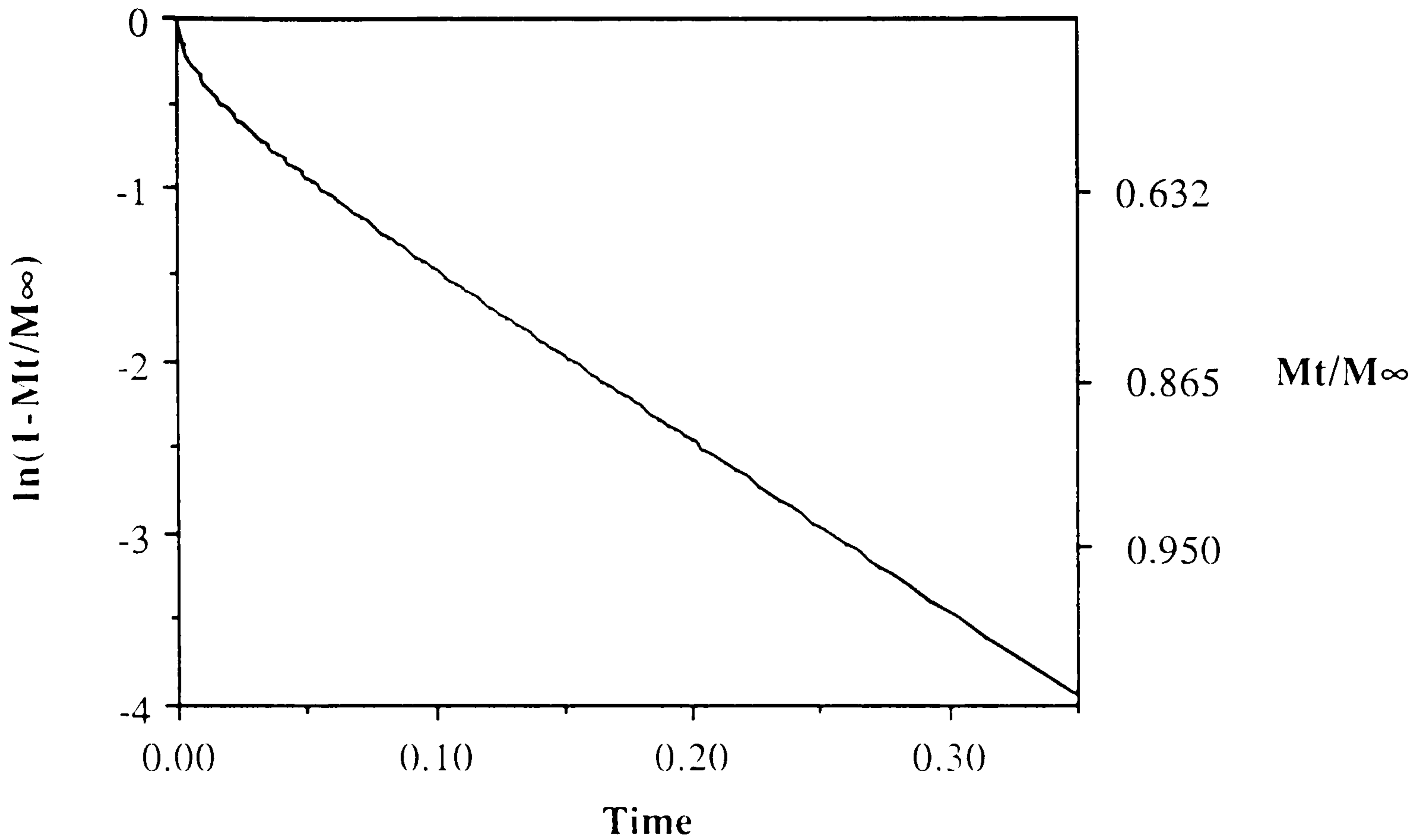

Figure 1.20 The variation of $\ln(1-M_t/M_\infty)$ with time for theoretical Fickian process.

Long time and short time diffusion behaviour are the two convenient ways of studying diffusion data and of checking both these solutions for consistency.

The classical idea of a carbon molecular sieve (CMS) is that it has pores with restrictions of a certain size. These restrictions are supposed to be of molecular dimensions equivalent to that of smaller molecules enabling them to diffuse in rapidly with respect to larger molecules[76]. Selective carbon molecular sieves can be prepared by two methods (1) careful control of the carbonisation conditions and (2) carbon deposition to introduce selectivity into a previously non-selective substrate. In the case of the former the selectivity is throughout the material since the carbon structure is reasonably homogeneous[77]. The mechanism of diffusion of gases in such CMS would tend to agree with the Fickian diffusion model where the molecule diffuses into the CMS pellet through the restrictions in the pore structure. In commercial CMS the selectivity is usually introduced by the deposition of carbon on pore mouths during the manufacturing process of CMS (refer to Chapter 2 Section 2.2.2 for details). In this case the carbon deposition is heterogeneous and particle size reduction leads to a loss of kinetic selectivity. The differences in gas diffusivities result in a molecular sieving action which is directly related to the size and kinetic dimensions of the adsorbate. LaCava *et al.*[78] have proposed a rate model based on a different view of the structure of CMS. This model is based on a conceptual model of sieving action of CMS proposed earlier by Nandi and Walker[79]. According to this model the carbon crystallites are loosely cross-linked with other crystallites to form an aperture cavity structure. The aperture is considered to be slit-shaped which serves as an entrance to the cavity. This model has also been used by Rao *et al.*[80] who suggested that the sieving action is produced by the interaction of van der Waals potential forces in the slit of the molecules. Smirnova and coworkers[81] calculated the shape of interaction potential between two model graphite layers and an argon atom. For some values of distance between the graphite layers, the calculations showed that the highest energy barrier occurred at the slit entrance. LaCava *et al.*[78] concluded that the rate uptake of gases by non-Fickian CMS can be described by an activated Langmuir rate model. In this model the CMS is considered to have a slit-shaped pore mouth where the slit-molecule interaction potential controls the rate of entrance of molecules into the cavity. The slit potential was found to be characteristic for each molecular species. The slit potential was found to be greater for nitrogen as compared to oxygen. Hence, the nitrogen molecule was adsorbed more slowly in comparison to the oxygen molecule. A $\ln(1-M_t/M_\infty)$ versus time graphs for this model is a straight line. Hence there are similarities with the corresponding graph for the Fickian diffusion model at high levels of uptake. However, the graph for Fickian diffusion is non-linear in the initial phase up to 50% gas uptake. Fickian behaviour is observed for CMS gas uptake kinetics where the material was prepared by controlling the carbonisation conditions thereby producing a material where the pore size distribution is homogeneous.

References

(1) Kroto H.W., Allaf A.W. and Balm S.P., *Chem. Rev.*, **91**, 1213 (1991).

(2) Kasatochkin V.I., Korshak V.V., Kudryavtsev Yu.P., Sladkov A.M. and Stenenberg I.E., *Carbon*, **11**, 70, (1973).

(3) Nightingale R.E, 'Structure' in *Nuclear Graphite*, Academic Press, N.Y. p. 87, (1962).

(4) Debye P. and Scherrer P., *Physik. Z.*, **18**, 291 (1917).

(5) Hull A.W., *Phys. Rev.*, **20**, 113 (1922).

(6) Bernal J.D., *Proc. Royal Soc.*, **A106**, 749 (1924).

(7) Lipton H. and Stokes A.R., *Proc. Roy. Soc.*, **A181**, 101 (1942).

(8) Kochanovska A., *Czech. J. Phys.*, **3**, 193 (1953).

(9) Amelinckx S., Delavignette P. and Heerschap M., in *Chemistry and Physics of Carbon*, Ed. Walker P.L.Jr., Marcel Dekker, N.Y., **1**, 1 (1965).

(10) Riley H.L., *Quart. Revs.*, **1**, 59 (1947).

(11) Franklin R.E., *Proc. Roy. Soc.*, **A209**, 196 (1951).

(12) Biscoe J. and Warren B.E., *J. Appl. Phys*, **13**, 364 (1942).

(13) Marchand A., 'Physico-chemical and structural characterisation of carbons' in *Carbon and Coal Gasification - Science and Technology*, Eds. Figueiredo J.L. Moulijn J.A. and Martinus Nijhoff, Dordrecht, p. 93, (1986).

(14) Mering J. and Marie J., *J. Chim. Phy.*, **57**, 803 (1960).

(15) Pinnick H.T., *J. Chem. Phy.*, **20**, 756 (1952).

(16) Roosky H.P., *Elect. Times*, **102**, 19 (1942).

(17) Bacon G.E., *Acta Cryst.*, **3**, 137 (1950).

(18) Franklin R.E., *Acta Cryst.*, **4**, 253 (1951).

(19) Smith T.D., *J. Chem. Soc.*, **1**, 923 (1952).

(20) Kipling J.J., Sherwood J.N., Shooter P.V. and Thompson N.R., *Carbon*, **1**, 315 (1964).

(21) Brooks J.D. and Taylor G.H., in *Chemistry and Physics of Carbon*, Ed. Walker P.L.Jr., Marcel Dekker, N.Y., **4**, 243 (1968).

(22) Marsh H., *Proc. 4th London Int. Carbon and Graphite Conf.*, S.C.I., London 2 (1976).

(23) Lewis R.T., *Ext. Abs., 12th Biennial Conf. on Carbon.* A.C.S., Pittsburgh, U.S.A., 215 (1975).

(24) Zimmer J.E. and White J.L., *Disclination structure in carbonaceous mesophase and graphite,* Aerospace report (1976).

(25) Kovac C.A. and Lewis I.C., *Ext. Abs. 13th Biennial Conf. on Carbon. American Carbon Society,* 199 (1977).

(26) Huttinger K.J., *Ext. Abs. Carbon'72,* Arbeitskreis Kohlenstaff der Deutschen Keramischen Gesselschaft E.V. Ansburg, 5 (1972).

(27) Smisek M. and Cerny S., *Active Carbon,* Elsevier, Amsterdam (1970).

(28) Capelle Vooys F. de, *Active Carbon,* Norit N.V., Amsterdam, (1983).

(29) Mrozowski S., *Carbon,* **20**, 303 (1982).

(30) Marsh H. and Menendez R., 'Mechanism of formation of isotropic and anisotropic carbons', in *'Introduction to Carbon Science'*, Ed. Marsh H., Butterworths, London p. 37, (1989).

(31) Oberlin A., *Carbon,* **22**, 521 (1984).

(32) Johnson C.A., Patrick J.W. and Thomas K.M., *Fuel,* **65**, 1284 (1986).

(33) Forrest R.A. and Marsh H., *Carbon,* **15**, 348 (1977).

(34) Sing K.S.W., Everett D.H., Haul R.A.W., Moscou L., Pierotti R.A., Rouquerol J. and Simemieniewska T., (IUPAC), *J. Pure Appl. Chem.,* **57**(4), 603 (1985).

(35) McEnaney B. and Mays T.J., 'Porosity in carbons and graphites' in *'Introduction to Carbon Science'*, Ed. Marsh, H., Butterworths, London p. 153 (1989).

(36) Gregg S.J. and Sing K.S.W., *Adsorption Surface Area and Porosity,* 2nd Edition, Academic press, p. 244, (1991).

(37) Sutherland J.W., in *Porous Carbon Solids*, Ed. Bond R.L., Academic press, London, p. 1, (1967).

(38) Langmuir I., *J. Amer. Chem. Soc.,* **40**, 1361 (1918).

(39) Brunauer S., Emmett P.H. and Teller E., *J. Amer. Chem. Soc.,* **60**, 309 (1938).

(40) Davis R.T. and DeWitt T.W., *J. Amer. Chem. Soc.,* **70**, 1135 (1948).

(41) Kingston G.L, Beebe R.A., Polley M.H. and Smith W.R., *J. Amer. Soc.,* **72**, 1775 (1950).

(42) Kingston G.L. and Aston J.G., *J. Amer. Chem. Soc.,* **73**, 1929 (1951).

(43) Hill T.L., *J. Chem. Phys.,* **14**, 263 (1946).

(44) Pierce C., *J. Phy. Chem.,* **63**, 1076 (1959).

(45) Carrott P.J.M., McLeod A.I. and Sing K.S.W., in *Adsorption at Gas-Solid and Liquid-Solid Interface*, Eds. Rouqerol J. and Sing K.S.W., Elsevier, Amsterdam, p. 403, (1982).

(46) Baker F.S. and Sing K.S.W., *J. Coll. Inft. Sc.*, **55**, 605 (1976).

(47) Shull C.G., *J. Am. Chem. Soc.*, **70**, 1405 (1948).

(48) Pierce C., *J. Phy. Chem.*, **72**, 3673 (1968).

(49) Sing K.W.S., *Surface Area Determination* (Proc. Int. Symp. 1969), Butterworths, p. 25, London (1970).

(50) Atkinson D., Carrott P.J.M., Griller Y., Rouqerol J. and Sing K.S.W., in *Fundamentals of Adsorption*, Ed. Liapis A.I., Engineering Foundation, N.Y., p. 89, (1987).

(51) Dubinin M.M., Erachko T.I., Kadlec O., Ulin V.I., Voloshchuk A.M. and Zolotarev P.P., *Carbon*, **13**, 193 (1975).

(52) Dubinin M.M., *Carbon*, **19**, 321 (1981).

(53) Nandi S.P. and Walker P.L.Jr., *Fuel*, **43**, 385 (1964).

(54) Walker P.L.Jr. and Shelef M., *Carbon*, **5**, 7 (1967).

(55) Lamond T.G. and Marsh H., *Carbon*, **1**, 293 (1963).

(56) Kingston G.L. and Macleod A.C., *Trans. Faraday Soc.*, **55**, 1799 (1959).

(57) Haq N. and Ruthven D.M., *J. Coll. Intf. Sc.*, **112(1)**, 164 (1986).

(58) Anderson R.B.and Hofer L.J.E., *Fuel*, **44**, 303 (1965).

(59) Sevensterr P.G., *Fuel*, **38**, 403 (1959).

(60) Nandi S.P. and Walker P.L. Jr., *Fuel*, **49**, 309 (1970).

(61) Chihara K,.Suzuki M and Kawazoe K., *J. Coll. Intf. Sc.*, **64(3)**, 584 (1978).

(62) Ruthven D.M., *Chem. Engng. Sc.*, **47(17/18)**, 4305 (1992).

(63) Ruthven D.M., Raghavan N.S. and Hassan M.M., *Chem. Engng. Sc.*, **41(5)**, 1325 (1986).

(64) Nelson E.T. and Walker P.L.Jr., *J. Appl. Chem.*, 11 Sept., 358 (1961).

(65) Kawazoe K., Suzuki M. and Chihara K., *J. Chem. Engng. Japan,* **7**, 151 (1974).

(66) Chihara K. and Suzuki M., *Carbon*, **17**, 339 (1979).

(67) Ghosh A.K. and Agnew J.B., *Chem. Eng. Commun.*, **40**, 169 (1986).

(68) Walker P.L.Jr., Austin L.G. and Nandi S.P., *Chemistry and Physics of carbon,* Ed. Walker P.L. Jr., Marcel Dekker, N.Y., **2**, 257 (1966).

(69) Lamond T.G. and Marsh H, *Carbon*, **1**, 281 (1964).

(70) Dubinin M.M., *Carbon,* **27**, 457 (1989).

(71) Marsh H. and Rand B., *J. Coll. Intf. Sci.*, **33**, 101 (1970).

(72) Carrott P.J.M., Carrott R.M.M.L. and Roberts, R.A., *Coll. and Surfaces*, **58**, 385 (1991).

(73) Marsh H., *Carbon*, **25**, 49 (1987).

(74) Freeman E.M., Siemieniewska T., Marsh H. and Rand. B., *Carbon*, **8**, 7 (1970).

(75) Crank J., *The Mathematics of Diffusion*. 2nd Edition, Oxford University press, p. 90, (1975).

(76) Juntgen H., Knoblauch K. and Schroter H.J., *Berichte der Bunsen-Gesellschaft fur Physikalische Chemie*, **79**, 826 (1975).

(77) Chagger H.K., Ndaji F., Sykes M.L., Thomas K.M., Submitted to *Carbon* yet to be published.

(78) LaCava A.I., Koss V.A. and Wickens D., *Gas Separation and Purification*, **3(4)**, 180 (1989).

(79) Nandi S.P. and Walker P.L.Jr., *Separation Science*, **11**, 441 (1976).

(80) Rao M.B., Jenkins R.R. and Steele W.A., *Langmuir*, **1**, 137 (1985).

(81) Smirnova L.F., Bakaev V.A. and Dubinin M.M., *Carbon*, **25**, 599 (1987).

Chapter 2

Activated carbons and carbon molecular sieves

This chapter reviews active carbons and carbon molecular sieves (CMS), their synthesis, structure, properties and various applications. CMS are a special type of activated carbons. In order to have a better understanding of CMS materials it is important to understand the various aspects of the synthesis and properties of activated carbons. These are discussed in the following section.

2.1 Activated Carbons

Carbon in different forms plays an important role in the fields of industry and science. Active carbons are synthesised from naturally occurring carbonaceous materials like coal, oil, peat, coconut shell and wood by pyrolysis (carbonisation) and activation processes. After the removal of volatile components by heating in an inert atmosphere to typically 873-1173 K a highly carbonaceous material - ***'char'*** is obtained. Generally the char structure obtained is porous, and a suitable activation process is used to increase the available porosity. Hence the term ***'activated carbon'*** is used which in its broadest sense includes a wide range of microporous carbon-based materials prepared from a wide range of materials which have been activated to give a high degree of porosity and extended interparticular surface area[1].

The pore structure is the most important property of an activated carbon and its adsorption capacity is determined by primarily its microporous structure. A high micropore volume indicates that the carbon can adsorb large amounts of gases or vapours. The structure and porosity of carbon, which develops during activation, depends initially upon the nature of the precursor to carbon. However, any pretreatment which the precursor undergoes prior to carbonisation or variations in the carbonisation conditions can change the porous structure and hence, the adsorptive properties of the carbon. Methods of controlling pore development of active carbons provide a means of preparing adsorbents suited to a wide range of applications. Some applications of different carbons are given in Table 2.1

Table 2.1

Different characteristics and applications of some active carbons[1,2]

Applications	Characteristics
Air purification	Removal of slight odours from inhabited spaces for example-hospitals, offices and removal of toxic gases from industrial exhaust.
Respirators	Sorption of toxic vapours like chloropicrin and cyanogen chloride may occur via physisorption and chemisorption (for impregnation carbons).
Nuclear plant gas hold up	Delayed bed of xenon, krypton and gases in nuclear reactors.
Beverages	The removal of (negligible) slight odours like aldehyde in raw distillate also accelerates maturing, and used for the regeneration of old wines and enhancing the flavour by removal of phenol and colouring matter.
Medicine	Carbon is an antidote to food and chemical poisoning and is also used in the treatment of gastritis and enteritis.
Gold recovery	Adsorption of gold from cyanide leach liquors.
Waste water treatment	The removal of heavy metals, for example, cadmium; halomethanes such as chloroform; and pesticides for example-DDT, dieldrin, aldrin etc.

2.1.1 Structure of activated carbons

The majority of non-graphitizable carbons originate from non-fusing coals, for example anthracite or low rank coals and plant material such as wood, nut-shells etc. which are used to produce activated carbons industrially. In coking coals the development of a thermoplastic phase produces orientation effects which lead to anisotropic graphitizable carbons. It is the polymeric cellulose or lignin within these naturally occurring materials which when pyrolysed, yields microporous carbon. During carbonisation hydrogen and oxygen are released gradually, leaving behind the basic skeleton of the polymer which forms cross-linkages thereby preventing fusing. The pore size distribution of an active carbon depends on the nature of the precursor and both the carbonisation and activation experimental conditions. Figure 2.1 shows typical pore size distributions of an active carbon and a carbon molecular sieve.

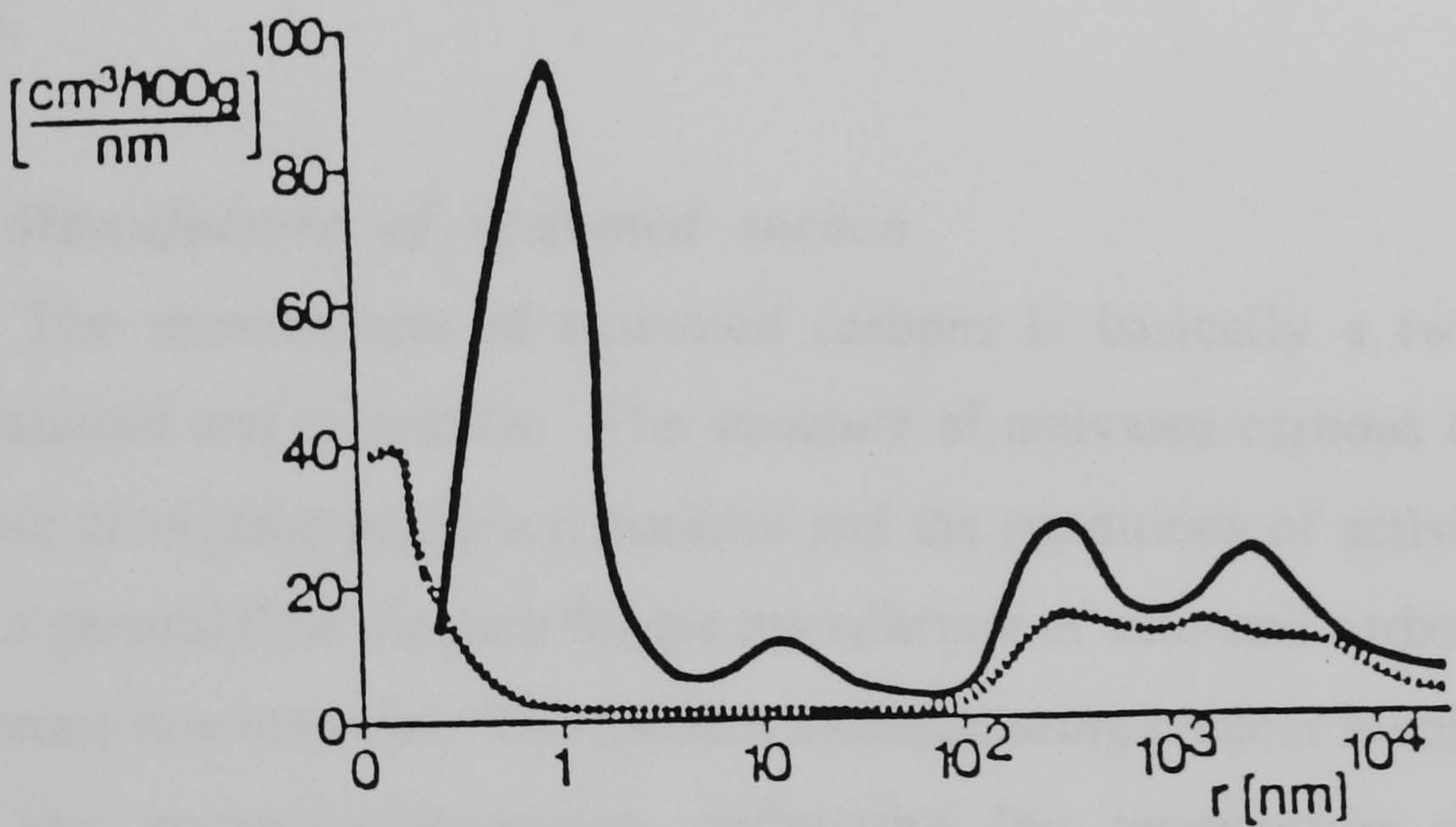

Figure 2.1 Typical pore size distribution for a carbon molecular sieve (.......) and an activated carbon (———)[3]

High resolution transmission electron microscopy has confirmed the general picture of the structure of porous carbons. The graphene layers are disorganised[4] with regions resembling crumpled paper, with gaps of varying molecular dimensions between them i.e. the micropores are as shown in the schematic diagram in Figure 2.2.

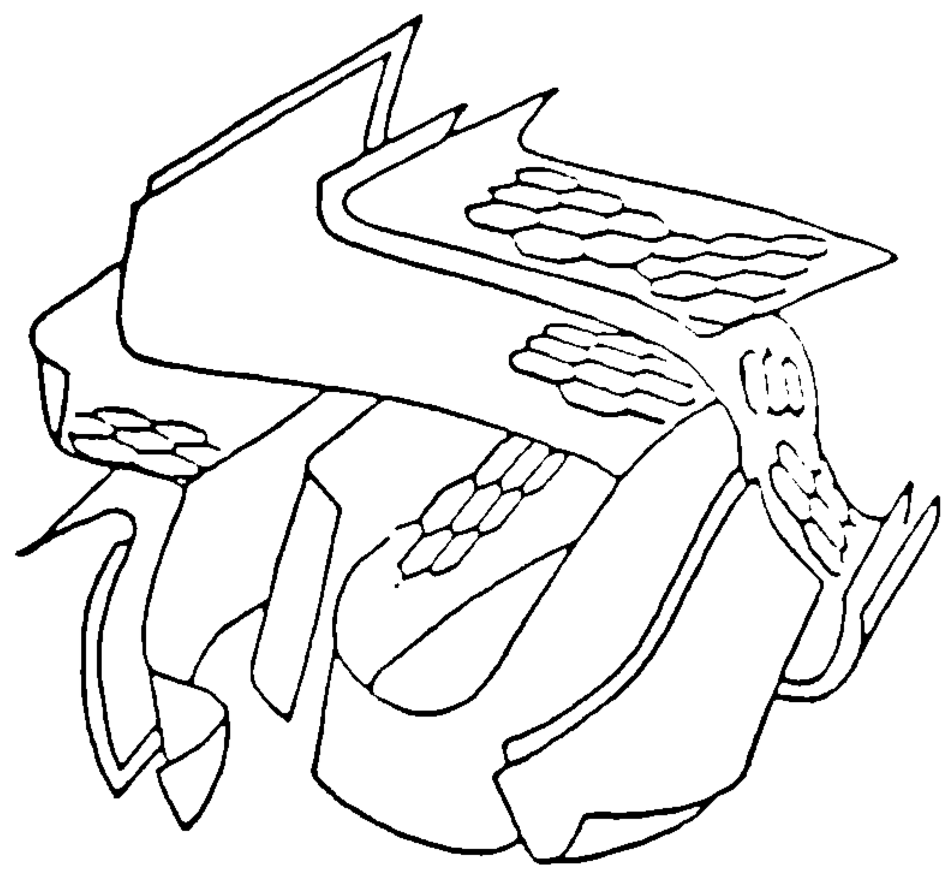

Figure 2.2 Schematic representation of microstructure of active carbons[4]

The char porosity is not always accessible to gases such as helium. It is termed closed porosity. The pores are often filled or blocked by disorganised carbons resulting from the decomposition of tars etc. released in the carbonisation process. The way to make this porosity available is by slow activation or partial gasification of the carbon.

2.1.2 Manufacture of activated carbon

The manufacture of activated carbons is basically a two step process - carbonisation and activation. The structure of activated carbons depends upon the structure of organic precursor material and the conditions of activation. Figure 2.3 shows a general flow diagram for the manufacture of activated carbon starting from an appropriate raw material. The modern manufacturing process involves the following steps: raw material preparation, pelletizing, low temperature carbonisation and activation. The conditions are carefully controlled to achieve the desired pore structure and mechanical strength.

Starting with the initial porous structure present in the carbonaceous raw material, closed pores are made accessible and pores are widened by the so-called *'activation process'*. The activation process may be divided into two types-(1) physical and (2) chemical. After the initial treatment of carbonisation to eliminate the bulk of the volatile matter, the heat treated carbons are then subjected to partial gasification in steam or carbon dioxide or mixtures thereof at temperatures of 1073-1273 K to develop the porosity and surface area. The activation process is usually

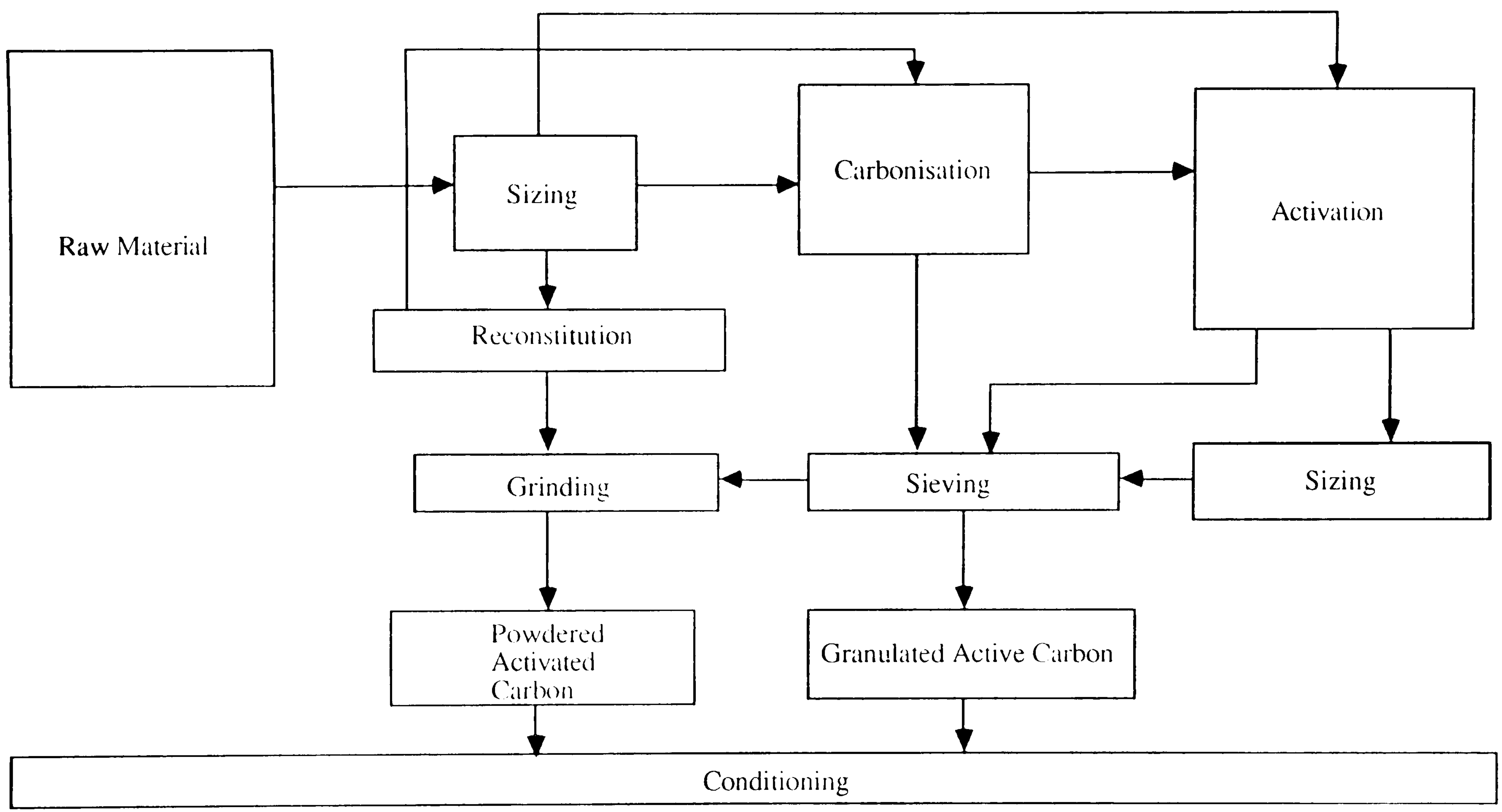

Figure 2.3 Flow diagram of manufacture of active carbons.[1]

carried out in fixed beds or rotating drums but in recent years fluidised beds have also been used. The activated carbons created by this process are used primarily for gas and vapour adsorption processes. The chemical activation process is carried out simultaneously with carbonisation by using phosphoric acid, zinc chloride or sulphuric acid in order to degrade and dehydrate cellulosic materials and to prevent shrinkage during carbonisation. All these processes result in production of activated carbons which depending on the precursor material are suitable for a variety of special applications. A highly microporous activated carbon with a suitable pore size distribution can be further modified by pore blocking techniques to synthesise a carbon molecular sieve (CMS).

2.1.2.1 Raw materials

The structure of a resulting carbon product (char) is a function of the organic precursor. Different types of materials used include vegetable by-products (olive stones, almond shells or coconut shells), fossil fuel (coal) etc. Some of the precursor materials are listed in Table 2.2 together with the corresponding amount of activated carbon production.

Table 2.2

Consumption of different precursor materials[1]

Wood	1.3 M tons/year
Coal	0.1 M tons/year
Lignite	0.05 M tons/year
Coconut shell	0.035 M tons/year
Peat	0.035 M tons/year
Others	0.01 M tons/year

The criteria for selecting the raw materials depends upon several factors some of which are listed below.

(1) It should have a high carbon content and low in inorganic matter in order to make the process economical in terms of reactivity.

(2) Low cost.

(3) High density also plays an important role as it contributes to the structural

strength of the carbon so that it can withstand size degradation during use. Low density woods produce carbons with large pore volumes. Coconut, coal and high density wood have high volatile content and they produce microporous carbons used for both vapour and solution phase applications.

2.1.2.2 Carbonisation

Carbonisation is a process whereby the carbonaceous material is subjected to thermal decomposition in an inert atmosphere and is converted to a carbon rich mass. This process is generally carried out in a continuous flow of an inert gas. The products of this process are either coke or char and tars and gases such as carbon dioxide, water etc. Char can be distinguished from coke on the basis that it does not pass through a thermoplastic state during carbonisation and is isotropic when viewed through an optical microscope. As a result the char maintains its precursor shape although shrinkage and loss in strength are generally observed.

In addition to the nature and physical properties of the precursor, the important parameters that determine the quantity and yield of products are the heating rate, heat treatment temperature, carbonisation pressure and the soak time at final heat treatment temperature. Low heating rate during pyrolysis tends to result in lower devolatilisation and higher char yield, increased secondary reactions and better stabilisation of the polymeric decomposition products. The basic microporosity is formed around 773 K although some of the pores are blocked by pyrolysis products which can be made accessible upon further heat treatment to higher temperatures[5]. However, the development of the porous structure is a function of temperature.

Wood materials are dried at temperatures up to 443 K. The partial degradation begins at around this temperature leading to evolution of carbon dioxide, carbon-monoxide and methanol. When the temperature reaches 543-553 K exothermic decomposition occurs leading to evolution of methanol and tarry substances. The primary devolatilization in the carbonisation is almost complete at around 873 K. The rate of pyrolysis is significantly influenced by the moisture content and temperature of carbonisation.

During the carbonisation of coal two processes play an important role in determining the porosity in the char. The first stage is the softening period during which the macromolecular coal structure begins to decompose. After the softening period and passing through the major devolatilization stage etc. the char begins to shrink and harden. The shrinkage of char may result in the development of porosity in the char, but excessive shrinkage can result in reduction in pore volume, which can be later developed during the activation stages. In the case of low rank coal the heating rate applied should be slow so that gases can escape through the pores in the granules without collapse or deformation. In the case of sub-bituminous coals and bituminious coals low heating rate can promote shrinkage which can lead to a drastic reduction in the pore volume, so it is advantageous to by-pass the slow carbonisation step and to activate the chars immediately to enlarge the pores before shrinkage occurs.

2.1.2.3 Activation

The aim of activation is to enhance the volume of the existing pores created during carbonisation and to create some new porosity by opening closed porosity. Although the mechanism of the activation process is not completely understood, it can be visualised as an interaction between the activation agent and the carbon active sites. The precise procedures for the activation depend on the carbon precursor and on the require characteristics of the carbonaceous material. Nevertheless activation of carbonised materials falls into two categories - (1) Physical activation and (2) Chemical activation

2.1.2.3.1 Physical activation

Partial gasification is generally known as ***'physical activation'*** . The activating agents most often used are steam, carbon dioxide, air or combustion products at temperatures between 1073-1373 K. The activating agent gasifies the more reactive portions of the carbon skeleton. The products of the activation processes are carbon monoxide and carbon dioxide. The extent of burnoff (gasification) depends on the carbon properties e.g. reactivity, particle size etc. and the conditions under which the activating agent reacts with carbon e.g. temperature, gas composition etc. This can be said to occur in two steps:

(1) Gasification of carbon active sites, (for example-edge atoms {zig-zag sites, dangling carbons, arm chair sites}, heteroatoms etc.) in particular, disorganised

carbon which, ideally should not exceed 10% weight loss. This results in opening of the blocked pores.

(2) Production of active sites and wider pores as the carbon of the graphene layer system starts gasifying.

The carbon atoms which form the carbonised structure differ in reactivity and affinity towards the activation agent. During the activation of the carbonised intermediate product the disorganised carbon is gasified, and the closed porosity becomes accessible leading to the development of the porous structure. The gasification of carbon proceeds at different rates on different parts of the exposed surface enabling the enlargement of pores and formation of new pores. Thus, the removal of disorganised carbon and non-uniform gasification leads to the formation of new pores and subsequent development of the porous structure. In the later stages the effect is more pronounced with the widening of existing pores, and the complete burn-out of walls between adjacent micropores leading to the production of transitional and macropores, with the loss of microporosity. Kalback *et al.*[6] observed that a major part of the early pore development occurred by preferential gasification of single aromatic sheets which constitute active carbon structure. The pores developed in this way reached a maximum number and then cease to form probably because the exposed aromatic sheets were exhausted. This is followed by gasification of the wall of the layer planes, resulting in formation of larger pores, which is the first step towards development of porosity. In some cases further activation is required in order to have access to the closed porosity within the porous material. This can be done by activating with gases like carbon-dioxide, water and oxygen etc. or by heat treatment methods and chemical activation. According to Dubinin[7] when the burnoff is less than fifty percent a microporous active carbon is obtained; when the gasification level exceeds seventy five percent a macroporous product is obtained and when the burnoff range is between fifty and seventy five percent the product contains both micropores and mesopores. These must be regarded as approximations.

Activation with carbon dioxide promotes external oxidation and development of large pores compared to activation with steam. The relative amount of the internal and external oxidation depends upon how well developed the pores are in the carbonised material. Gasification of the material with steam and carbon dioxide occurs by following endothermic reactions over a wide temperature range[8]:

$$C + H_2O \text{ ----> } CO + H_2 \qquad \Delta H=+118.5 \text{ kJmol}^{-1} \qquad (2.1)$$

$$C + CO_2 \text{ ----> } 2CO \qquad \Delta H=+159 \text{ kJmol}^{-1} \qquad (2.2)$$

The reaction of steam with carbon is accompanied by water-gas formation reaction, which is catalysed by the carbon surface as:

$$CO + H_2O \text{ ----> } CO_2 + H_2 \qquad \Delta H=-42.3 \text{ kJmol}^{-1} \qquad (2.3)$$

Since the reaction of carbon with steam and carbon dioxide are both endothermic, the activation process leads itself to accurate control of conditions in the kiln. External heat is required to drive reactions (2.1) and (2.2) and maintain the temperature.

The rate of reaction with steam is retarded by the product hydrogen which is strongly adsorbed on the active centres i.e. chemisorbed and reduces the rate of activation by formation of C-H sites. Activation with carbon dioxide is also retarded by hydrogen and carbon monoxide. Gasification reactions (2.1) and (2.2) show a strong product inhibition. Differences between the reaction with carbon dioxide and water involve the following:

Differences in carbon activation using carbon dioxide compared with water can be ascribed to:

(1) the slower diffusion of carbon dioxide into the porous system of the carbon[9],

(2) the restricted accessibility of carbon dioxide to micropores[10],

(3) a significantly slower reaction rate for reaction of carbon dioxide with the carbon[11].

Reaction (2.1) is favoured by elevated temperature and reduced pressure and in the absence of a catalyst occurs slowly at temperature below 1200 K. The uncatalysed reaction is generally somewhat faster than the C-CO_2 (2.2) reaction under the same conditions. In a practical system the distribution of products will depend upon the occurrence of secondary processes such as the water gas shift reaction i.e. (2.3) and reaction (2.1). Under practical conditions, with temperatures higher than 1100 K, the water gas shift reaction is at equilibrium and this means that both reactions (2.1) and (2.2) are important, despite the fact that in most cases super heated steam is the primary activation agent.

Rand and Marsh[12] observed that the presence of carbon monoxide helps in making the gasification rate more uniform. These workers used mixtures of carbon dioxide and carbon monoxide for gasification of polyfurfuryl alcohol carbon, carbonised at 1123 K, and observed that the addition of carbon monoxide in the gas stream resulted in the development of more uniform microporous structure as well as in decreasing the rate of gasification. In the case of an iron catalysed reaction, the development of microporosity was also better when the mixture of carbon dioxide and carbon monoxide was used. The rate of gasification was retarded only when the iron catalyst was rendered inactive[1]. In actual industrial processes, the activating agent used is generally flue gas to which a certain amount of steam is added so that a combined activation with steam and carbon dioxide can occur. In the case of activation with oxygen, the rate of reaction with carbon is more than 100 times faster than with steam or carbon dioxide[8].

$$C + O_2 \text{ ----> } CO_2 \qquad \Delta H = -393.5 \text{ kJmol}^{-1} \qquad (2.4)$$

$$2C + O_2 \text{ ----> } 2CO \qquad \Delta H = -221.0 \text{ kJmol}^{-1} \qquad (2.5)$$

Both reactions (2.4) and (2.5) are exothermic and the reaction is difficult to control. Since there is always some local heating, the product obtained is not always uniform. As a result of the exothermic reaction the gasification is not restricted to pores but also occurs on the surface of the grains, causing excessive weight loss, hence the method is rarely used commercially.

Marsh and Rand[13] observed that the activation of polyfurfuryl alcohol (PFA) with carbon dioxide resulted in the opening of inaccessible porosity and widening of existing pores. Tomkow *et al.*[14] studied activation of brown coals in carbon dioxide, steam and oxygen. Activation with water resulted in widening of all sized pores at a burnoff of 70%. Although the total adsorption volume increased from 0.6 to 0.83 cm^3/g there was not a significant increase in the surface area. Activation with carbon dioxide resulted in more uniform porosity, but the carbon produced by carbon dioxide activation had lower total pore volume (0.49 cm^3/g) than that obtained by steam activation. Activation with oxygen at a very low burnoff less than 1% resulted in activation of non-porous carbon. The micropore volume increased from 0.002 to 0.2 cm^3/g. There was only a slight increase of 0.23 to 0.27 cm^3/g in the micropore volume with increasing burn-off from 8 to 25%. On increasing the burn-off to 70% there was a slight decrease in the pore volume. This indicated that different distributions of porosity were produced. Although activation with all three gases resulted in microporous carbons, the highest was with oxygen. A higher degree of mesoporosity was observed with steam activation rather than with carbon dioxide or oxygen. At higher burnoff levels the effect was more pronounced. The activation of carbonised wood char as a function of weight loss[1]. Initially the adsorption capacity of the activated carbon increased as the weight loss increased. Subsequently the porous potential of carbon reached a maximum and then decreased. This implies that in the initial stage, the opening of closed microporosity occurs but there is a finite limit to the amount of closed porosity. Consequently as the burnoff increases the average pore diameter increases.

McEnaney and Dovaston[15] prepared a series of carbons from cellulose triacetate by heat treatment in temperature ranges 1230-2275 K and activated to 30% burn-off. The porosity development was measured by mercury density and nitrogen adsorption. Activation at low temperatures resulted in development of mesopores and macropores. The heat treatment temperatures (1500-1700 K) resulted in annealing of the structure with a loss of porosity.

The main factors influencing the gasification of carbon with a gas during the activation process are:

(1) the diffusion of reactive gases to active sites in the porous structure,

(2) the gasification experimental conditions, pressure, temperature, particle size, flow rate, gas concentration etc.,

Carbon structural characteristics

(3) the accessible surface area which is measured by TSA,

(4) the variation in active sites

(a) zig-zag, arm chair

(b) heteroatoms

(c) inorganic

(5) diffusion limitations due to porous structure, particle size and reaction temperature.

However, no direct proportionality can be found between reactivity and BET surface area due to the inability to define the structure precisely and the complex nature of the reaction.

In the case of the measurements of surface area in microporous solids, there are problems sometimes because of activated diffusion effects and volume filling/capillary condensation effects. Hence, carbon dioxide at 273 K has been used for adsorption studies in order to determine a reasonable approximation for the microporous surface area. In this case the low (p/p_0) at pressures up to atmospheric virtually eliminates condensation effects and because of the comparatively high temperature and there are no activated diffusion effects.

2.1.2.3.2 Chemical activation

Chemical activation is generally carried out on lignocellulose based precursor materials. The starting material is impregnated with chemical agents usually by mixing and kneading. The chemical impregnated material is carbonised to temperatures in the range (673-1073 K) depending on the precursor and generally washed on cooling to produce the final active carbon. The activating agent is later recycled. The basic function of the chemical incorporated is to react with the products resulting from the thermal decomposition of the precursor and to reduce the evolution of the volatile matter, thus inhibiting shrinkage of the particle and enhancing the yield of carbon. The most widely used activating agents are phosphoric acid, zinc chloride, sulphuric acid, potassium sulphide, potassium thiocyanate and hydroxides and carbonates of alkali metals. Chlorides of calcium, magnesium and ferric oxide have also been suggested[16].

The chemically activated carbons obtained in powdered form possess high capacity and are generally used for the adsorption of larger molecules (for example - decolourisation). Kadlec[17] observed that the pores obtained by physical and chemical activation were different. In the case of chemical activation, pores were bottle shaped, compared to cone shaped in physical activation. This was attributed to the development of bottle shaped pores during the course of activation around temperatures of 573 K when the carbon mass is undergoing major structural changes. The gases evolved during thermal decomposition create hollows in the structural matter and escape through it. In contrast, in the steam activation of wood there is a water vapour concentration gradient in the particle. The oxidation occurs in the vicinity of the pore entrance rather than in the pore centre, thus leading to conical shaped pores with wide pore entrance.

Weunerberg and O'Grandy[18] obtained active carbons of high surface area from coal, petroleum coke and their mixtures impregnated with hydrated sodium hydroxide. The process involved calcination between 573-673 K and further heating to 1073 K. The resultant product upon washing was found to be highly microporous and had a cage like structure. The magnitude of surface areas ranged from 3000-4000 $m^2\ g^{-1}$ for coke to 1800-3000 $m^2\ g^{-1}$ for coal derived carbons. Schafer[19] synthesised active carbons from brown coal which was first heated with hydrochloric acid to remove cations and converted into potassium coal by addition of potassium hydroxide. This was pelletized and pyrolysed in stream of nitrogen to a temperature of 1173 K. The carbon obtained was later leached with hot water and the surface area obtained by this method was of the order of 1100-1500 $m^2\ g^{-1}$. Ehrburger and co-workers[20] found that upon pyrolysis of coals with alkalis like sodium hydroxide and potassium hydroxide the microporosity decreased upon small additions of alkali (up to 10% by weight) but increased appreciably with the addition of large amounts of alkali. Micropore yield was higher in the case of potassium hydroxide. Kwok and Miller[21] prepared active carbons from petroleum coke by treating with polyphosphoric acid. The phosphoric acid-treated coke was treated with steam between 973-1173 K. The surface area obtained was about 700 $m^2\ g^{-1}$ for these carbons.

2.2 Carbon Molecular Sieves

For many years the separation of air into oxygen and nitrogen was carried out by liquefication/distillation. In recent years alternative processes, namely pressure swing adsorption (PSA) and membrane separation have been developed. These are used on a large scale and are economic for all but the largest capacities. Table 2.3 lists some commercial processes, most of which utilise PSA.

Table 2.3

Representative commercial gas adsorption separation[22]

Separation	Adsorbent
I Gas bulk separations.	
Normal paraffins/iso-paraffins,aromatics	Zeolite
N_2 from O_2	CMS
O_2 from N_2	CMS
$CO, CH_4, CO_2, N_2, Ar, NH_3/H_2$	Zeolites, Active carbons
Acetone/Vent streams	Active carbons
C_2H_4/Vent streams	Active carbons
II Gas purification.	
H_2O/olefin-containing cracked gas, natural gas, air, synthesis gas etc.	Silica, alumina, Zeolite
CO_2, C_2H_4, natural gas	Zeolites
Organics/Vent streams	Active carbon, others
Odours/air	Active carbon
NO_x/N_2	Zeolite
NO_x/SO_2	CMS
SO_2/Vent streams	Zeolite
Hg/Chlor-alkali cell gas effluent	Zeolite
Sulphur compounds/natural gas, hydrogen liquified petroleum gas (LPG)	Active carbon

The discussion presented in this section involves the structure and properties of the CMS and the principles of the PSA process for air separation using CMS.

Carbon molecular sieves (CMS) represent one member of the family of activated carbons, which fall into the category of non-graphitizing carbons (for details refer to Section 1.3.2 of Chapter One). Carbon adsorbents having the molecular sieving properties have been studied extensively since Emmett[23] discovered the molecular sieving characteristics in Saran carbon in 1942. In 1969[24] a 0.5 nm type of CMS was developed[25]. Subsequently a nitrogen generating air separation plant was developed by Bergbau Forschung Co.[26].

For the production of oxygen and nitrogen from air, it is more economical to use PSA than cryogenic means for production rates below 30 metric tons per day. Figure 2.4 shows the comparison between the cost of production of nitrogen from cryogenic and PSA processes. PSA is more economic compared with gas separation using a cryogenic process, which is labour intensive and demands a higher energy consumption. Thus, developments in CMS result in lower-cost nitrogen production.

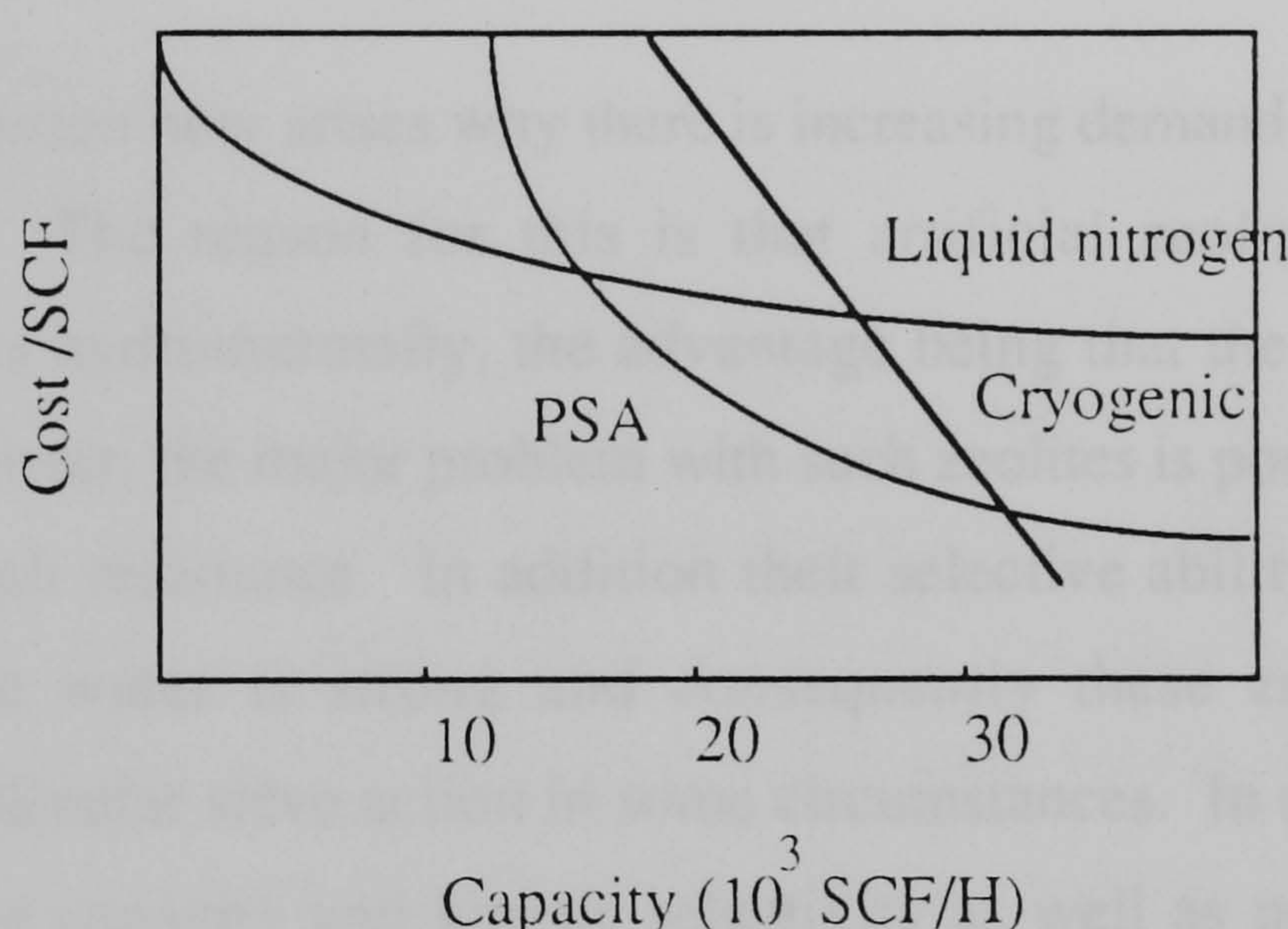

Figure 2.4 Cost comparison of nitrogen: PSA using 0.5 nm zeolite and cryogenic process[27]

In 1990 US statistics[28] indicated that there had been an increase in production of commercial chemicals. Nitrogen is the second largest chemical (57 billion pounds) and oxygen fourth largest (39 billion pounds). At present only 2-5% of, the latter is produced using PSA and hollow membrane fibres. The attraction, besides purity levels, of using solid sorbents at customer sites is the fact that it avoids transportation of gases and liquids by trucks. Figure 2.5 shows various applications of nitrogen obtained from PSA[29]. Oxygen obtained from PSA is used to enrich air in combustion and waste incineration, steel production and in the removal of chlorine in pulp and paper industry etc.

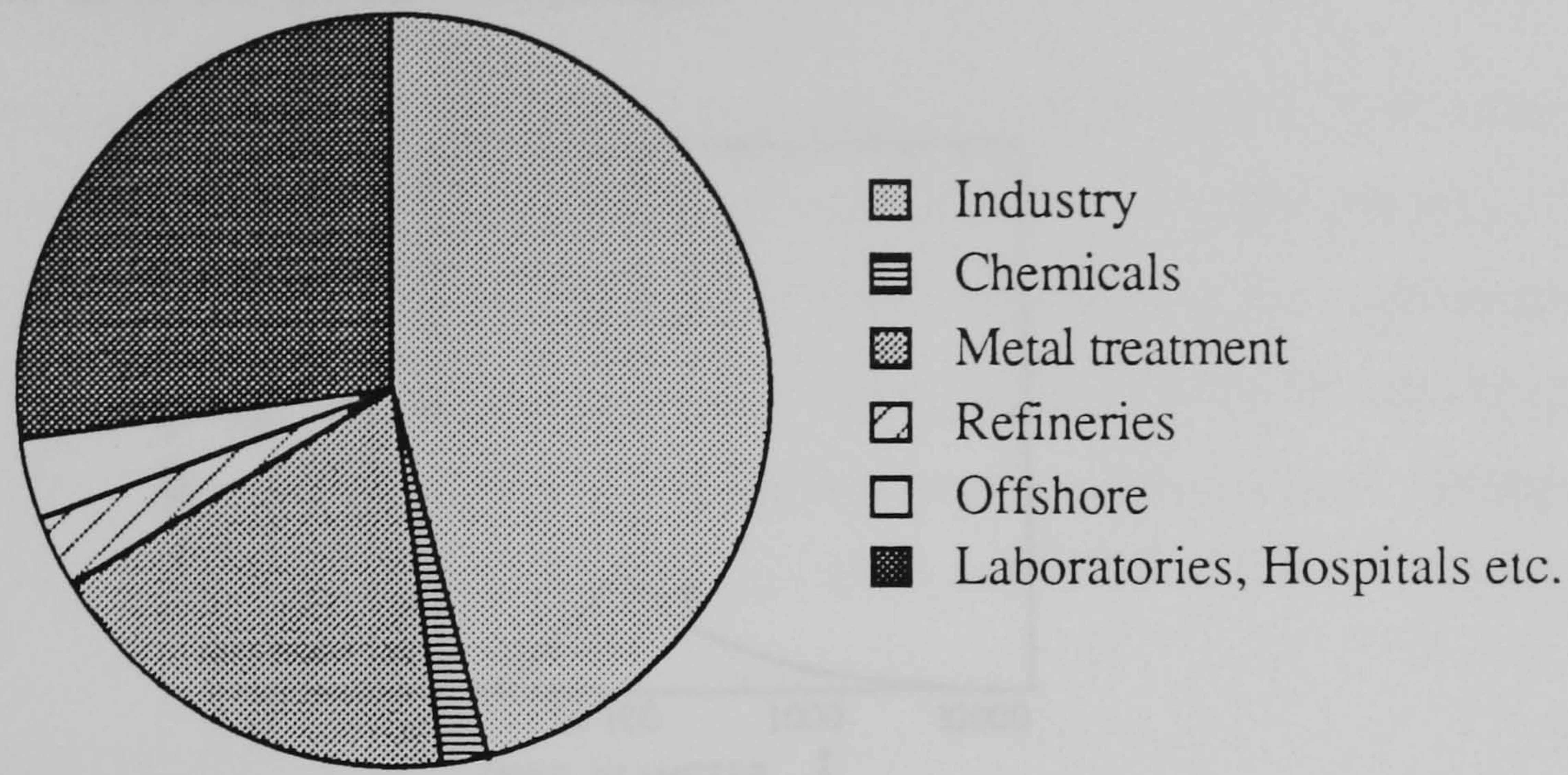

Figure 2.5 Application of nitrogen obtained from PSA.

The question now arises why there is increasing demand of using CMS material over zeolites? The reason for this is that artificial zeolites are prepared from aluminosilicates hydrothermally, the advantage being that the size can be controlled precisely. However, the major problem with such zeolites is poor thermal stability, and poor acid - alkali resistance. In addition their selective ability with respect to polar substances like water is strong and consequently these zeolites do not have a satisfactory molecular sieve action in some circumstances. In comparison, CMS have good adsorptive capacity and kinetic selectivity as well as possessing well defined microporous system they are also stable materials which can operate successfully for many years.

2.2.1 Pore size distribution of CMS

As stated previously CMS are activated carbons. CMS utilised in industrial gas separation processes in general have a bimodal pore size distribution. The porous structure generally comprises of transport porosity responsible for diffusion of the adsorbate into the CMS and the microporosity for the gas adsorption capacity of the material. Figure 2.6 shows the pore size distribution of various carbons used in separation process. However, kinetic separation is possible only with carbon molecular sieves because of its pore size distribution. For example in the separation of oxygen and nitrogen from air the separation is due to the result of a slight difference in the kinetic diameters of the two gases, which results in a high rate of diffusion for oxygen into the CMS compared with nitrogen.

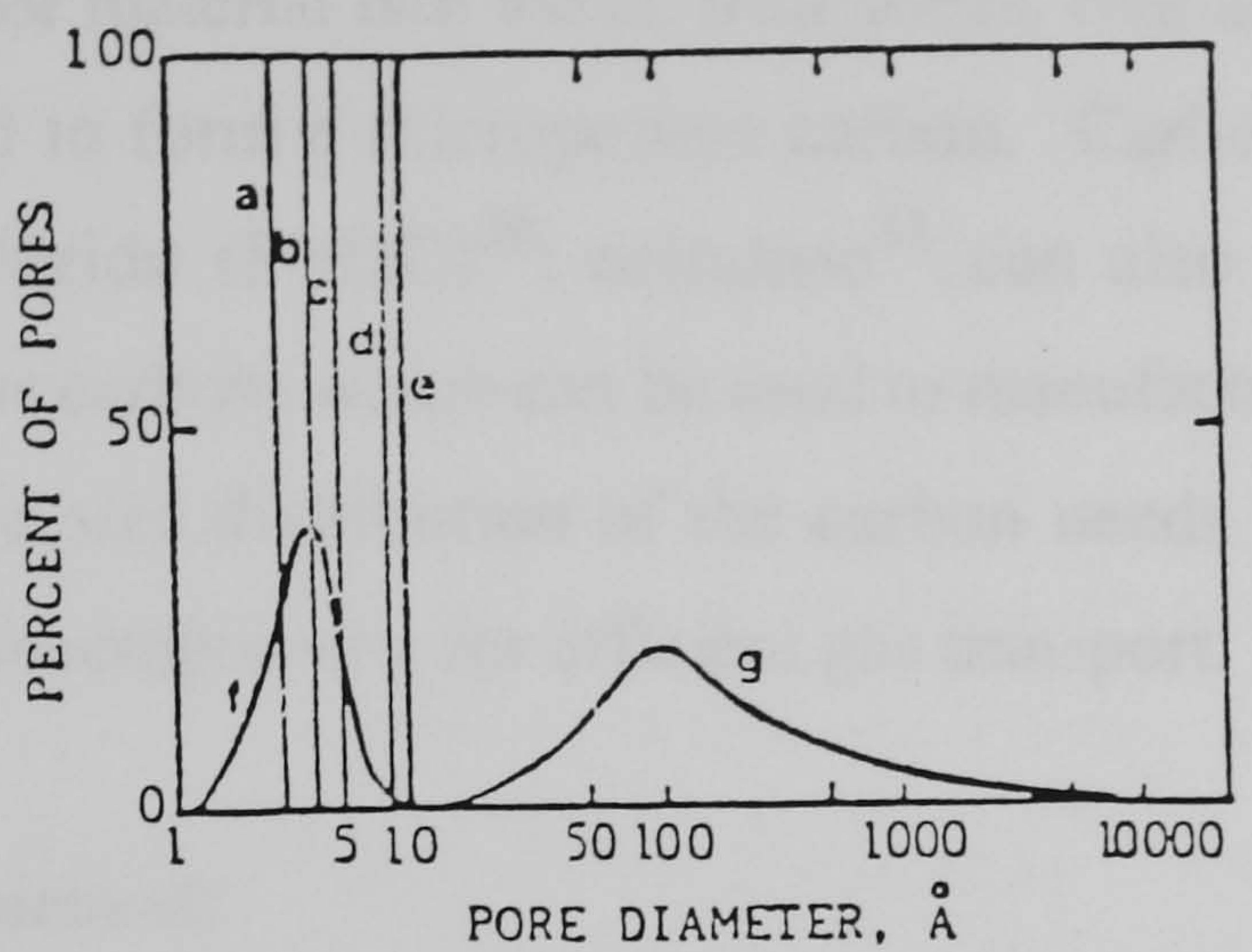

Figure 2.6 Micropore distribution of (a) zeolite type 0.3 nm (b) 0.4 nm (c) 0.5 nm (d) 10 X (e) 13 X (f) CMS and (g) activated carbon[27]

2.2.2 *Manufacture of CMS*

Within the last decade CMS have been used commercially in proprietary processes. The average pore size distribution of the adsorbent must be below 0.4 nm to effect oxygen separation from nitrogen. The average pore diameter can be adjusted by liquid impregnation and vapour deposition techniques. In order to be effective for air separation by pressure swing adsorption (PSA) the adsorbent must exhibit a high adsorption, a high rate of gas throughput and selectivity for appropriate gases. It is known that CMS having micropores of the order of ~ 0.4 nm can be used successfully for this purpose. There are several methods used for the production of CMS's the manufacture details are outlined briefly below:

(I) Synthesis of a microporous carbon with a suitable pore size distribution

(i) *Thermal treatment*

(ii) *Gas activation*

(II) Introduction of selectivity

(a) *Coating*

(b) *Vapour deposition*

(I) Synthesis of a microporous carbon with a suitable pore size distribution

(i) Thermal treatment

The precursor material like wood, fruit shells, coal and synthetic resins etc. are initially carbonized to form a microporous carbon. Carbonisation of polymers like polyvinylidene chloride (PVDC)[30]; cellulose[31]. can also lead to the production of suitable microporous carbons which can be used to manufacture CMS materials by pore blocking. The pore size distribution of the carbon needs to have a high micropore volume with some macroporosity for efficient gas transport.

(ii) Gas activation methods

Gas activation method using carbon dioxide or steam are generally employed in order to activate porous carbons to increase their adsorption capacities. Figure 2.7 shows the process used by Bergbau Forschung Co. for the production of carbon molecular sieves[25]. Care must be taken not to widen the micropore size distribution greatly since it is critical that the pores are not too large. The ease with which kinetic selectivity can be introduced is critically dependent on the pore size distribution of the microporous carbon substrate.

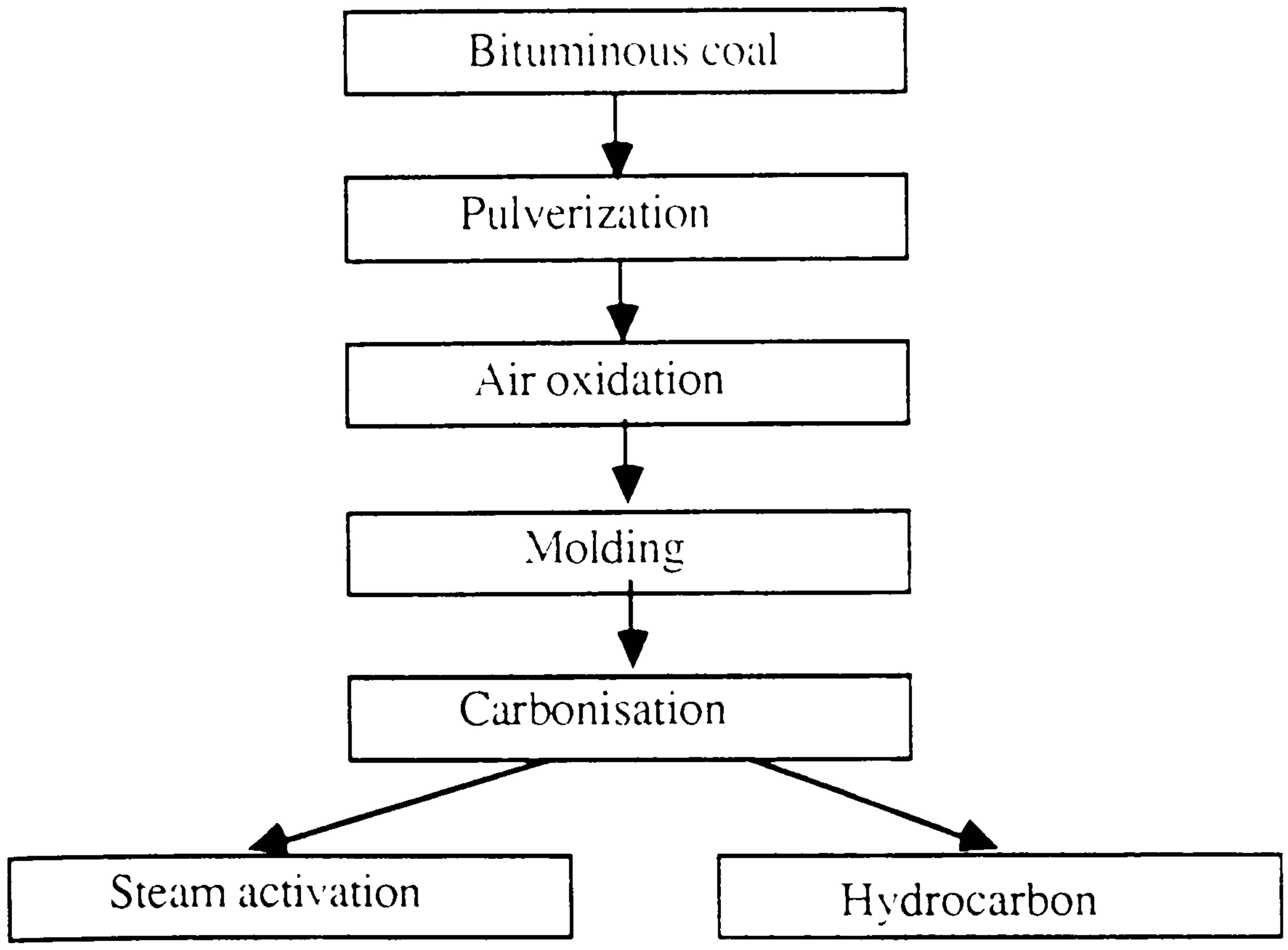

Figure 2.7 Process for production of CMS of Bergbau Forschung Co[26]

(II) Introduction of selectivity

(a) Coating method

Porous carbons like those used in the thermal treatment method are impregnated with resins or tars. This is done in order to reduce the pore diameter by coating the pore walls e.g. impregnation of active carbons with caking agents like furfuryl alcohols[32].

(b) Vapour deposition method

Porous carbon materials are heat treated at a temperature range of 673-1173 K and allowed to come in contact with gas containing selected hydrocarbons like ethylbenzene[33], methane[34], benzene[35], propylene[36], isobutylene[37] etc. so that the decomposition of the vapour deposits carbon on the walls of the micropores thereby reducing the pore diameter.

Recent commercial synthetic methods usually consist of between three to five steps depending on the starting materials. CMS here have been produced from precursors such as coal, coconut shell and polymers. Usually the starting material is subjected to some sort of pretreatment procedure followed by carbonisation and activation treatment. Table 2.4 gives a summary of the synthetic routes to commercial materials.

Table 2.4

Synthetic routes to commercial CMS materials.

Patent	Material	Pretreatment	Carbonization	Activation	Pore blocking	Other	Result
EP146909[38]	Activated carbons				C_3H_6 adsorbed, outgassed and cracked 573-773 K	H_2 treatment 373-473 K for stabilization.	Increased selectivity and H_2O stability
EP119925[39]	Coconut char Coal tar pitch starch water	Pelletized	N_2, 1073 K 15 min		Impregnated <2% polyethylene glycol		$k'O_2/k'N_2 = 43.3$ $O_2 < 4$ cc/cc of carbon
EP102902[40]	Coconut char		N_2, 1255 K 30 min			Continuous flow furnace	$k'O_2/k'N_2 = 6.68$ $O_2 = 5.22$ cc/cc of carbon
US4810266[41]	Crosslinked polymer	Shaped	N_2, 1173 K @ 110 K/h soak 1.5 h	Steam 1123 K 1h		Sprayed diethanol amine	For CO_2 removal

$k'O_2/k'N_2$ = selectivity ratio of oxygen diffusivity/nitrogen diffusivity into CMS.
k' = rate of diffusivity of oxygen or nitrogen.

Table 2.4 continued

Patent	Material	Pretreatment	Carbonization	Activation	Pore blocking	Other	Result
EP282053[42]	Thermosetting phenol resin	pelletized with resin, polyvinyl alcohol,starch	N_2, 1023 K @ 60 K/h soak 1hr				$k'O_2/k'N_2 = 4.3$
US4820681[43]	Crosslinked polymer	Pelletized	N_2, 1173 @ 110 K/h soak 1.5 h				Pore volume = 0.4 - 0.8 cc/g
JP62176908[44]	Coconut shell powder plus binders	Pelletized with coal tar and water	To 973 K in 40 min then to 1173 K		5 parts creosote mixed at 673 K for 20 min in N_2	N_2, 973 K in 20 min	$k'O_2/k'N_2 = 35$ $O_2 = 7$ cc/g
JP62059510[45]	Melamine resin phenolic resin polyvinyl alcohol		N_2, 943 K				Porosity 87% Surface area = 524 m^2/g
JP61191510[46]	Coal		N_2, 1123 K 30 min	CO_2, 1123 K 4 h	5% Coal tar in C_6H_6	N_2, 1173 K	99.9% N_2 obtained
JP61068312[47]	Coal	O_2, 5-18 % 573-773 K. Mixed 2-20% coal tar pitch and coal oil. Extruded.	973-1273 K inert atmosphere				N_2 enrichment in air

$k'O_2/k'N_2$ = selectivity ratio of oxygen diffusivity/nitrogen diffusivity into CMS.
k' = rate of diffusivity of oxygen or nitrogen.

Table 2.4 continued

Patent	Material	Pretreatment	Carbonization	Activation	Pore blocking	Other	Result
JP59230637[48]	Lignite	823 K 2hr				Powdered mixed starch extruded dried and heated 433 K N_2 4h	Adsorbed CO_2 but not C_2H_6
JP63201008[49]	Phenolic resins	Powder and liquid extruded and dried at 353 K 24 h	N_2, 1123 K				O recovery 16.6 mg/g
DE3618426[50]	Semicoke		N_2, 1133 K	N_2+35% H_2O 1133 K 15 min	N_2+8% benzene 1073 K 4 min	Vibratory furnace	desorbed 48.3% O_2
DD252550[51]	Brown coal	Pressed and pelletized	0.9K/min to 623 K then 2.9K/min to 1273 K			ground to 1-2mm	

2.2.3 *Pressure swing adsorption (PSA): Principle and process*

Air separation using CMS and PSA is a kinetic separation process resulting from different diffusivities of oxygen over nitrogen in to the CMS, and is not due to equilibrium selectivity. Since the invention of the Skarstrom cycle[52] in 1960, PSA has emerged as a major technology in the gas separation process. The history of PSA commercialisation is given in Table 2.5.

Table 2.5

PSA Commercial development highlights[53]

1960	Skarstron cycle and Guerin-Domine cycle.
1960	Drying of air and other gases.
1961	n-Paraffin.
1966	Hydrogen purification.
1970	Oxygen production from air.
1976	Nitrogen production from air using CMS.
1977	Nitrogen(and oxygen) from air by "Vacuum - swing adsorption" using zeolites.
1977	"Polybed" systems for large scale hydrogen production.
1980	Single bed PSA for medical oxygen.
1983	Nitrogen from air by zeolite PSA.

CMS are generally bimodal in pore size distribution, comprising macropores (needed for gas transport) and high micropore volume for capacity. They are kinetically selective and, in contrast to zeolites[54], sorb oxygen over nitrogen. Zeolites are equilibrium selective sorbents which sorb nitrogen from air, thus, the dimensions of the gases to be separated play an important role. CMS can be compared to that of a mechanical sieve in which small molecules *'pass'* through the mesh at a fast rate, intermediate size molecules pass through slowly and, the larger remain behind. This is represented schematically in Figure 2.8.

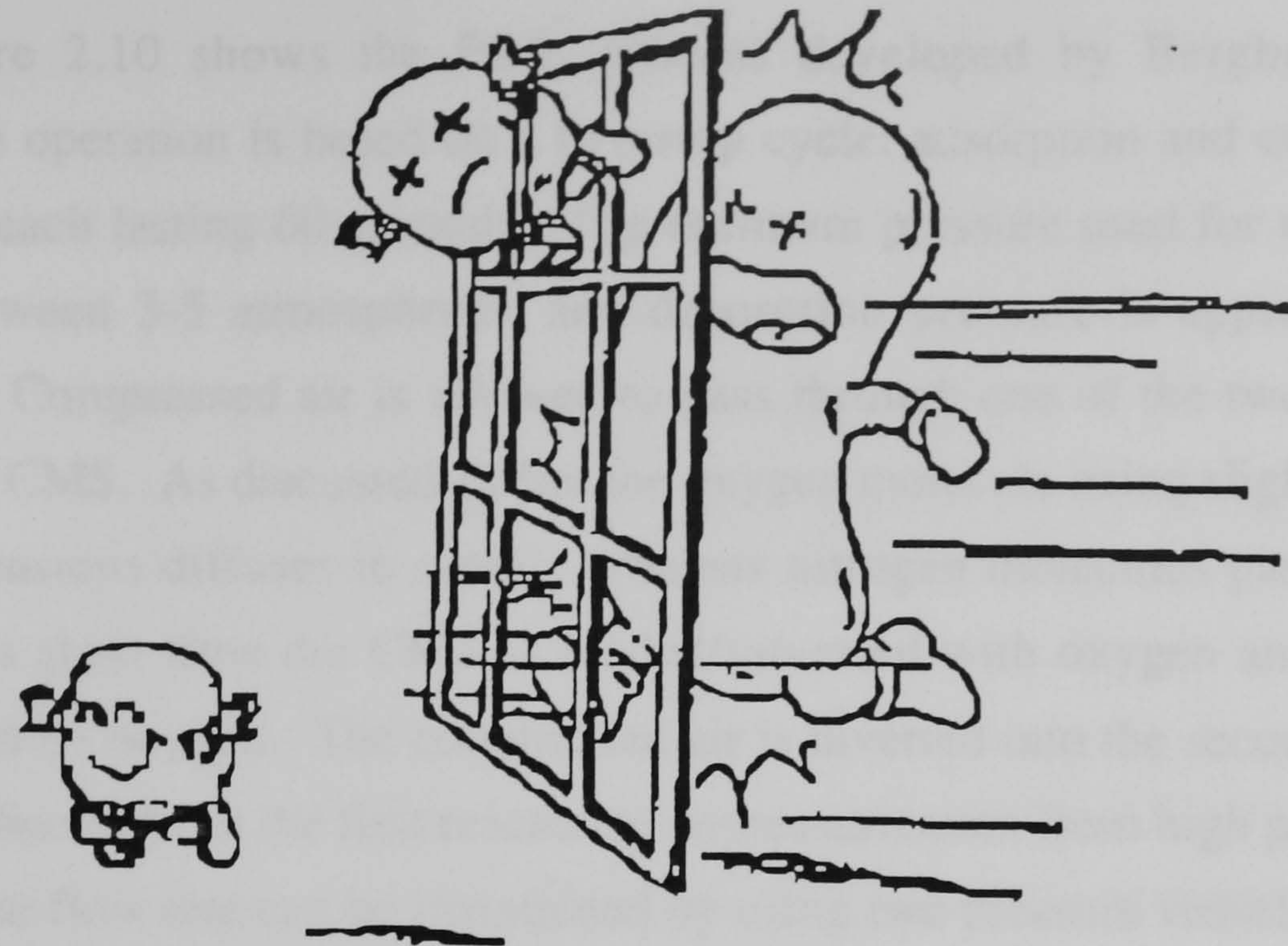

Figure 2.8. Molecular sieving.

In the case of oxygen and nitrogen, oxygen diffuses more rapidly into CMS than nitrogen which is a slightly larger molecule. In order to effect separation the adsorbent must have pore openings of about the molecular diameter of the larger gas in the mixture (nitrogen in air). This allows a rapid adsorption of the smaller component, resulting in high kinetic selectivity as shown in Figure 2.9[55]. Work carried out by Knoblauch show diffusion constants (D/r^2) of $1.7 \times 10^{-4}\ s^{-1}$ for oxygen and $7.0 \times 10^{-6}\ s^{-1}$ for nitrogen, where r is the micro particle radius and D is micropore diffusivity[56].

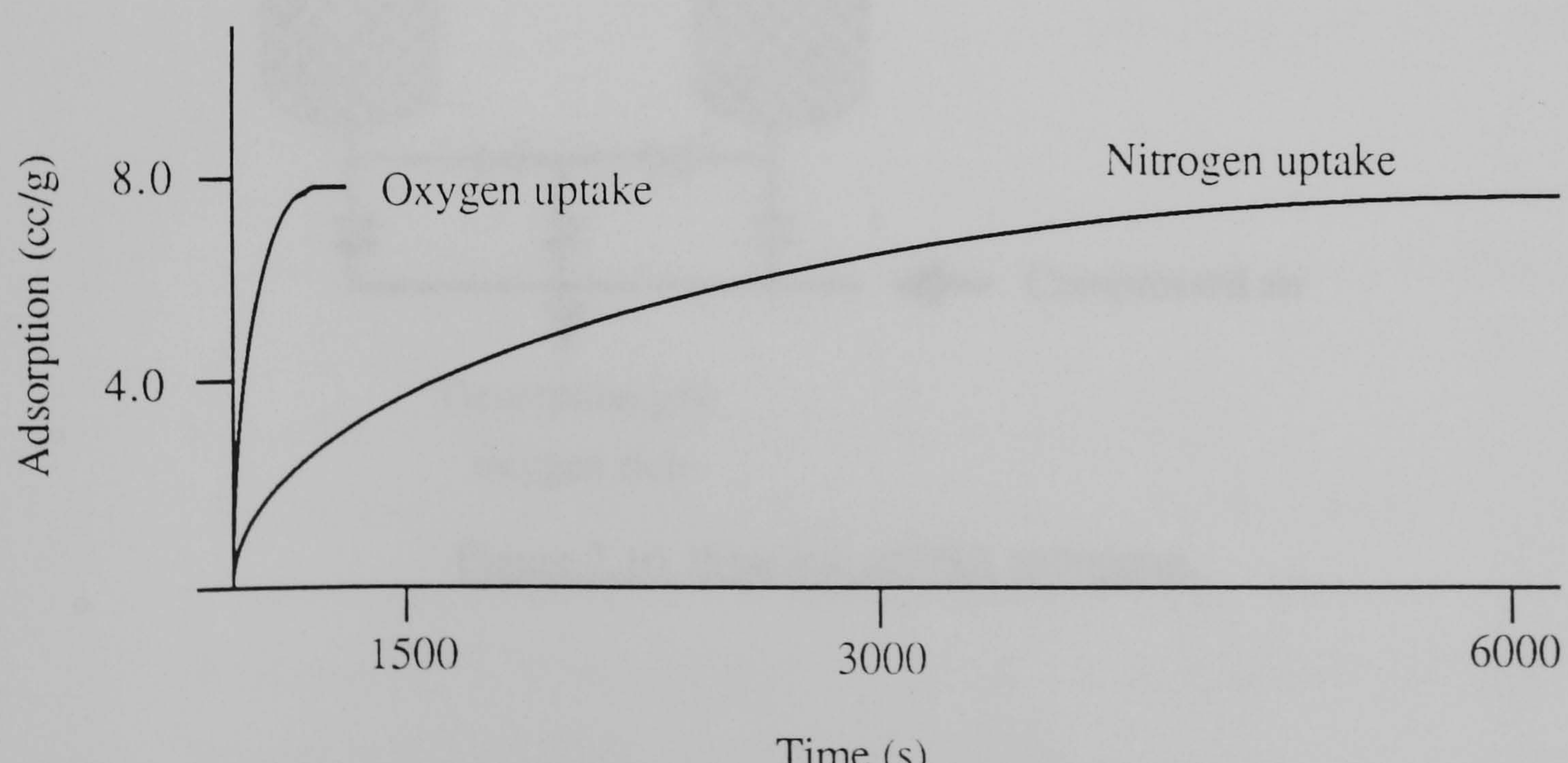

Figure 2.9 Graph showing oxygen and nitrogen uptake on CMS material at 275 K[55]

Figure 2.10 shows the PSA, process developed by Bergbau-Forschung GmbH. The operation is based on a two-step cycle: adsorption and counter current evacuation, each lasting 60 seconds. The optimum pressure used for the adsorption cycle is between 3-5 atmospheres, and desorption pressure is approximately 0.1 atmosphere. Compressed air is allowed to pass through one of the two reactor beds packed with CMS. As discussed earlier the oxygen molecule being slightly smaller in kinetic dimensions diffuses in rapidly whereas nitrogen molecules pass through the bed. After a short time the CMS is loaded/saturated with oxygen and thus cannot absorb any more oxygen. The compressed air is diverted into the second reactor and oxygen is released from the first reactor by depressurization from high pressure to low pressure. The flow rate can be maintained by using two pressure vessels alternatively so that a continuous supply of nitrogen is produced.

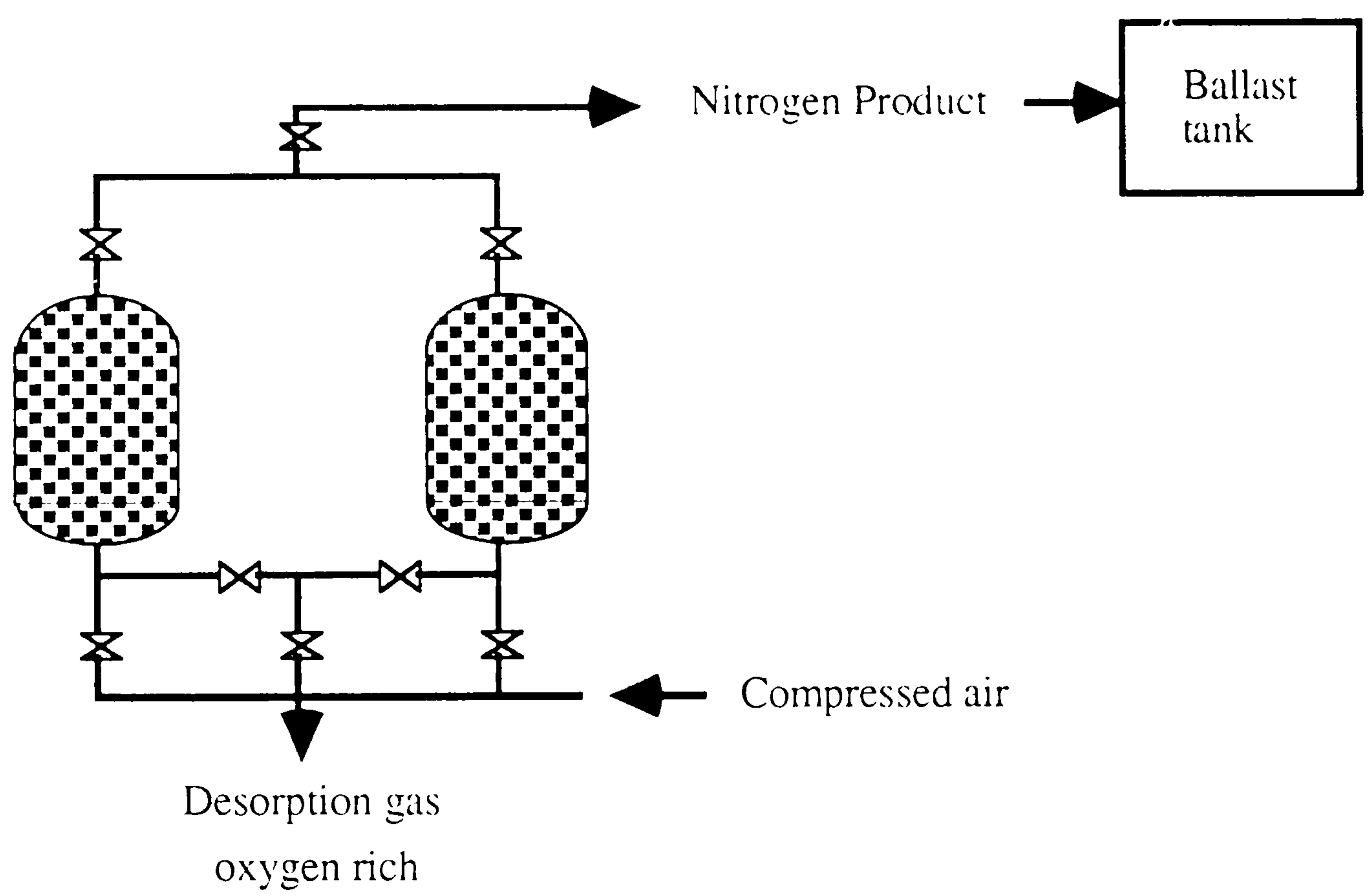

Figure 2.10 Principle of PSA technique.

References

(1) Bansal R.C., Donnet J.B. and Stoeckli H.F., *Active carbon,* Marcel Deckker Inc., N.Y., U.S.A. (1988).

(2) Nishino H., *Kagaku to Kogyo*, **59**(5), 161 (1985).

(3) Dubinin M.M., *Chemistry and Physics of Carbon,* Ed. Walker P.L.Jr., Marcel Deckker, N.Y., **2**, 51 (1966).

(4) Stoeckli H.F., *Carbon,* **28,** 1 (1990).

(5) Dubinin M.M., *Progress in Surface and Membrane Science*, **9**, Eds. Cadenhead D.A., Danielle J.F. and Rosenberg M.D., Academic Press, N.Y. p. 1, (1975).

(6) Kalback W.M., Brown L.F. and West R.E., *Carbon*, **8**, 117 (1970).

(7) Dubinin M.M. and Zaverina E.D., *Dokl Akad Nauk S.S.S.R.*, **65**, 295 (1949).

(8) Rodriguez R.F., *NATO ASI Series No.* **192**, *Fundamental Issues in Control of Carbon Gasification Reactivity*, Eds. Lahaye J. and Ehrburger P., Kulwer Academic, p. 533, (1991).

(9) Jungten H., *Carbon*, **6**, 297 (1968).

(10) Thrower P.A., Bognet J.C. and Matthew G.K., *Carbon*, **20**, 457 (1982).

(11) Walker P.L.Jr., Rusinko F.Jr. and Austin L.G., *Adv. Catal.*, **11**, 133 (1959).

(12) Rand B. and Marsh H., *Carbon*, **9**, 79 (1971).

(13) Marsh H. and Rand B., *Carbon*, **9**, 47 (1971).

(14) Tomkow K., Siemieniewska T., Czechowski F. and Jankowska A., *Fuel*, **56**, 121 (1977).

(15) McEnaney B. and Dovaston N., *Carbon*, **13**, 515 (1975).

(16) Dubinin M.M. and Stoeckli H.F., *J. Coll. Intf. Sc.*, **75**, 34 (1980).

(17) Kadlec O., Varhanikova A. and Zukal A., *Carbon*, **8**, 321 (1970).

(18) Weunnerberg, A.N. and O'Grady, T.M., *U.S. Patent 4,082,694* (1973).

(19) Schafer H.N.S., *U.S. Patent 4,039,473* (1977).

(20) Ehrburger P., Addoun A., Addoun F. and Donnet J.B., Proceedings of *Fundamentals of Catalytic Coal and Carbon Gasification: Int. Symp. Papers (FUCAT COGAS) 5/7 May 1986*, p. 279, Rolduc, The Netherlands.

(21) Kwok J. and Miller A., *U.S. Patent 3,767,592* (1973).

(22) Keller G.E. II, *ACS Symp. Series No.* **233** (Washington DC:Am. Chem. Soc.), 145 (1983).

(23) Emmett P.H., *Chem. Rev.,* **43**, 69 (1948).

(24) Lamond T.G., Metcalfe J.E. III and Walker P.L. Jr., *Carbon,* **3**, 59 (1965).

(25) Eguchi Y., Nishino H., Itoga K. and Sawada T., *Nippon Kagakkai Dai 22 Nenki*, No. 12326 (1969).

(26) Juntgen H., Knoblauch K. and Harder K., *Fuel*, **60**, 817 (1981).

(27) Yang R.T., *Gas Separation by Adsorption Processes*, Butterworths Publishers, Boston, p. 5 (1987).

(28) Shelly S., *Chem. Eng.*, June p. 30 (1991).

(29) Schroter H.J. and Juntgen H., *NATO ASI Series No.* **158**, *Adsorption Science and Technology*, Eds. Rodrigues A., LeVan M.D. and Tondeur D., Kulwer Acedemic, Vimerio, Portugal, p. 269 (1988).

(30) Darcey J.R. and Thomas D.G., *Trans. Faraday Soc.*, **50**, 740 (1954).

(31) Lamond T.G., Metcalf J.E. III and Walker P.L. Jr., *Fuel*, **42**, 233 (1963.)

(32) Walker P.L. Jr., Lamond T.G. Jr., Metcalfe J.E. III, 2nd *Conf. Ind. Carbon Graphite, Soc. Chem. Ind.*, London, p. 7 (1966).

(33) Chihara K. and Suzuki M., *Carbon*, **17**, 339 (1979).

(34) Vnukov S.P., Polyakov N.S., Dubinin M.M., Fedoseev D.V. and Nickolaev K.M., *Bull. Ace. Sci. U.S.S.R. Div. Chem. Sci.*, **32**, 293 (1986).

(35) Moore S.V. and Trimm L.C., *Carbon*, **15**, 177 (1977).

(36) Verma S.K. and Walker P.L. Jr., *Carbon*, **30**, 837 (1992).

(37) Cabrera A.L., Zehner J.E., Coe C.G., Gaffney T.R., Farris T.S. and Armor J.N., *Carbon*, **31**, 969 (1993).

(38) Verma S.K. and Walker P.L. Jr., *E.P. Patent 146909* (1985).

(39) Sutt R.F. Jr., *E.P. Patent 119925* (1984).

(40) Sutt R.F. Jr., *E.P. Patent 102902* (1984).

(41) Zinnen H.A., Oroskar A.R. and Chang C.H., *U.S. Patent 4810266* (1989).

(42) Marumo C., Hayata E. and Shiomi N., *E.P. Patent 282053* (1988).

(43) Chang C.H. and Seminara G J., *U.S. Patent 4820681* (1989).

(44) Takao O., *J.P. Patent 62176908* (1987).

(45) Marumo C., *J.P. Patent 62059510* (1987).

(46) Kashiwase M., *J.P. Patent 61191510* (1986).

(47) Ida S., Matsuoka M. and Matsufuji Y., *J.P. Patent 61068312* (1986).

(48) Kanai Y., *J.P. 59230637* (1984).

(49) Marumo C., Hayata E. and Shiomi N., *J.P. Patent 63201008* (1988).

(50) Knoblauch K., Tarnow F. and Heimbach H., *D.E. Patent 3618426* (1987).

(51) Heschel W., Mueller G., Fischer E., Klose E. and Naundorf W., *D.D. Patent 252550* (1987).

(52) Skarstrom C.W., *U.S. Patent 2944627* (1960).

(53) Cassidy R.T. and Holmes E.S., *AIChE Symp. Series*, **80** (NO.233), 68 (1984).

(54) Chao C.C., *U.S. Patent 4859217* (1989).

(55) Chagger H.K., Sykes M.L. and Thomas K.M., unpublished work.

(56) Knoblauch K., *Chem. Eng.*, **87**, Nov. 6 (1978).

Chapter 3

Objectives

3.1 Overall Objectives

(a) To assess flow microcalorimetry (FMC) as a technique for characterizing the molecular sieving ability of carbon molecular sieves and activated carbons and to compare and contrast the results with those of gravimetric uptake studies.

(b) To measure the adsorption capacity, kinetic selectivity and activation energy of adsorption and desorption for carbon molecular sieves using probe molecules of different size and shape.

(c) To investigate the possibilities of preparing from a wide range of starting materials active carbons of suitable pore structure and density as precursors for the preparation of carbon molecular sieves by carbon deposition.

3.2 Specific Objectives

3.2.1 Flow microcalorimetry (FMC)

(1) To compare the adsorption of oxygen and nitrogen on CMS materials in terms of equilibrium capacities, kinetics and selectivity using both gravimetric and FMC techniques.

(2) To develop a kinetic model for the analysis of FMC data for adsorption of gases on CMS materials.

3.2.2 Kinetics and selectivity of commercial CMS material

To measure the adsorption and desorption kinetics, selectivities, activation energies and frequency factors for the following gases: argon, oxygen, nitrogen, carbon dioxide, nitrous oxide, ethyne and ethene on CMS A3. These data can be used to develop models for the adsorption/desorption kinetics and the selectivity process.

3.2.3 Development and characterization of active carbons from different precursor materials.

3.2.3.1 Synthesis of microporous carbons

a) To synthesise microporous carbons by varying the carbonization pressure to control the development of the pore size distribution.

b) To manufacture carbons from a wide range of precursor materials by varying the carbonization conditions to control the development of the pore size distribution.

3.2.3.2 Characterisation of carbons obtained

To characterise of active carbon precursor and commercial carbon molecular sieve materials by the following techniques.

(1) Surface area measurements

(2) Gravimetric capacities and kinetics

(3) Helium density

(4) Molecular probe analysis

(5) Differential thermal analysis (DTG)

(6) Thermogravimetric analysis (TGA)

3.2.3.3 Introduction of selectivity

To introduce selectivity in high capacity carbons either by carbon vapour deposition or by impregnation with pitch.

Chapter 4

Experimental

4.1 Materials

4.1.1 Commercial CMS materials and activated carbons

A total of six commercial CMS materials were used. CMS A and CMS B were coconut based coded 7691-58-55 and 7461-77-72 and were supplied by Air Products and Chemicals Inc. Four coal based CMS samples EP 1 - EP 4 manufactured by DMT, Germany were obtained by NCRL. Activated carbons like those supplied by Sutcliffe Speakman Co. and Chemviron Carbon were also obtained by NCRL. Besides this a wide range of precursor materials (listed) below were chosen for the preparation of active carbons.

4.1.2 Carbon precursors

Precursor material	*Supplier*	*% Purity*
(1) Acenaphthylene	Aldrich, U.K.	85
(2) Acridine	Aldrich, U.K.	99
(3) Carbazole	Aldrich, U.K.	99
(4) Cellulose triacetate	Aldrich, U.K.	99.99
(5) Coconut shell	Air products, U.S.A.	-
(6) Dibenzofuran	Aldrich, U.K.	98
(7) Dihydroxy-napthalene	Aldrich, U.K.	97
(8) Novolak	Hoechst Resins, Resinous Chemical, U.K.	
(9) Polyether-etherketone (PEEK)	ICI Advanced materials, U.K.	

(10)	Polyether sulphone (PES)	ICI Advanced materials, U.K.
(11)	Pitch	(Rutgerswerke AG, 4620 Castrop-Rauxel).
(12)	Polyvinylidene chloride (PVDC)	ICI Advanced materials, U.K.('viclan' 542)
(13)	Polyvinylidene fluoride (PVDF)	Aldrich, U.K.
(14)	In house PFA carbons	
(15)	Beech	Supplied by Robert Duncan Ltd., U.K.
(16)	Teak	Supplied by Robert Duncan Ltd., U.K

4.1.3 Gases

	Gas	*Supplier*	*Grade*	
(1)	Argon	B.O.C., U.K.	N4.9	99%
(2)	Butane	B.O.C., U.K.	N1.85	98.50%
(3)	Carbon dioxide	B.O.C., U.K.	N3.5	99.95%
(4)	Ethyne	B.O.C., U.K.	N5.0	99.99%
(5)	Ethene	B.O.C., U.K.	N3.0	99.90%
(6)	Methane	B.O.C., U.K.	N4.5	99.99%
(7)	Nitrogen	B.O.C., U.K.	N4.8	99.99%
(8)	Nitrous oxide	B.O.C., U.K.	N4.7	99.99%
(9)	Oxygen	B.O.C., U.K.	N2.6(Zero)	99.60%

4.1.4 Liquids

	Liquid	*Supplier*	*% Purity*
(1)	Chloroform	Aldrich, U.K.	99.8%
(2)	Carbon tetrachloride	Aldrich, U.K.	99.9%
(3)	1,3 Dichloromethane	Aldrich, U.K.	99.0%
(4)	2 Methyl butane	Aldrich, U.K.	99.0%

4.2 Experimental techniques

4.2.1 Carbonisation

(1) Atmospheric pressure carbonisation

Carbon precursor materials were carbonised at atmospheric pressure under argon in a silica boat located in a horizontal tube furnace which was controlled by a Eurotherm temperature programme controller. A heating rate of either 1 K min^{-1} or 50 K min^{-1} was used in the carbonisations. The carbon was held at the final heat treatment temperature for a 1 hour soak time and the furnace allowed to cool after this period. The materials were carbonised with final heat treatment temperatures in the range 873 K to 1173 K.

(2) Vacuum carbonisation

Vacuum carbonisation studies were carried out in an Inconel vacuum carbonisation horizontal apparatus placed inside a tube furnace which was controlled by a Eurotherm temperature programme controller. The carbonaceous material was placed in a silica boat. The vacuum carbonisation apparatus was connected to a vacuum pump via a moisture trap. The vessel was pumped out for 20 minutes and samples carbonised to HTT's of 873-1173 K for individual samples at heating rates of either 1 K min^{-1} or 50 K min^{-1}. The carbon was held at the final heat treatment temperature for a soak time of 1 hour. The vacuum was maintained overnight until the vessel and sample had cooled down to room temperature.

(3) Elevated pressure carbonisation

A wide range of carbonisation pressures was used to investigate the relationship between carbonisation conditions and the porous structure of the resulting carbon. The samples were carbonised at constant pressures in the range of 6.6 - 12.24 MPa in a helium atmosphere at heating rates of either 1 K min^{-1} or 50 K min^{-1}. The final heat treatment was 873 K and the soak time was 1 hour.

The elevated pressure carbonisation apparatus contained a finite volume of gas which, along with volatile matter release, gave rise to a pressure change during heating. The initial pressure at 293 K was noted, as well as the final pressure at 873 K. In order to combine these into one figure an 'Effective Carbonisation Pressure' (ECP) was calculated on the basis that the volatile matter was released at 723 K, an arbitrary temperature between the temperature range of 293 K to 873 K. To calculate effective carbonisation pressure at 723 K, the difference in pressure between 293 K and 873 K was taken and multiplied by 430/580 and added to the initial pressure.

$$(ECP) = P_i + (430/580) \times (P_f - P_i)$$

where: P_i = Initial pressure at 293 K

P_f = Final pressure at 873 K

A schematic diagram of this apparatus can be seen in Figure 4.1 below.

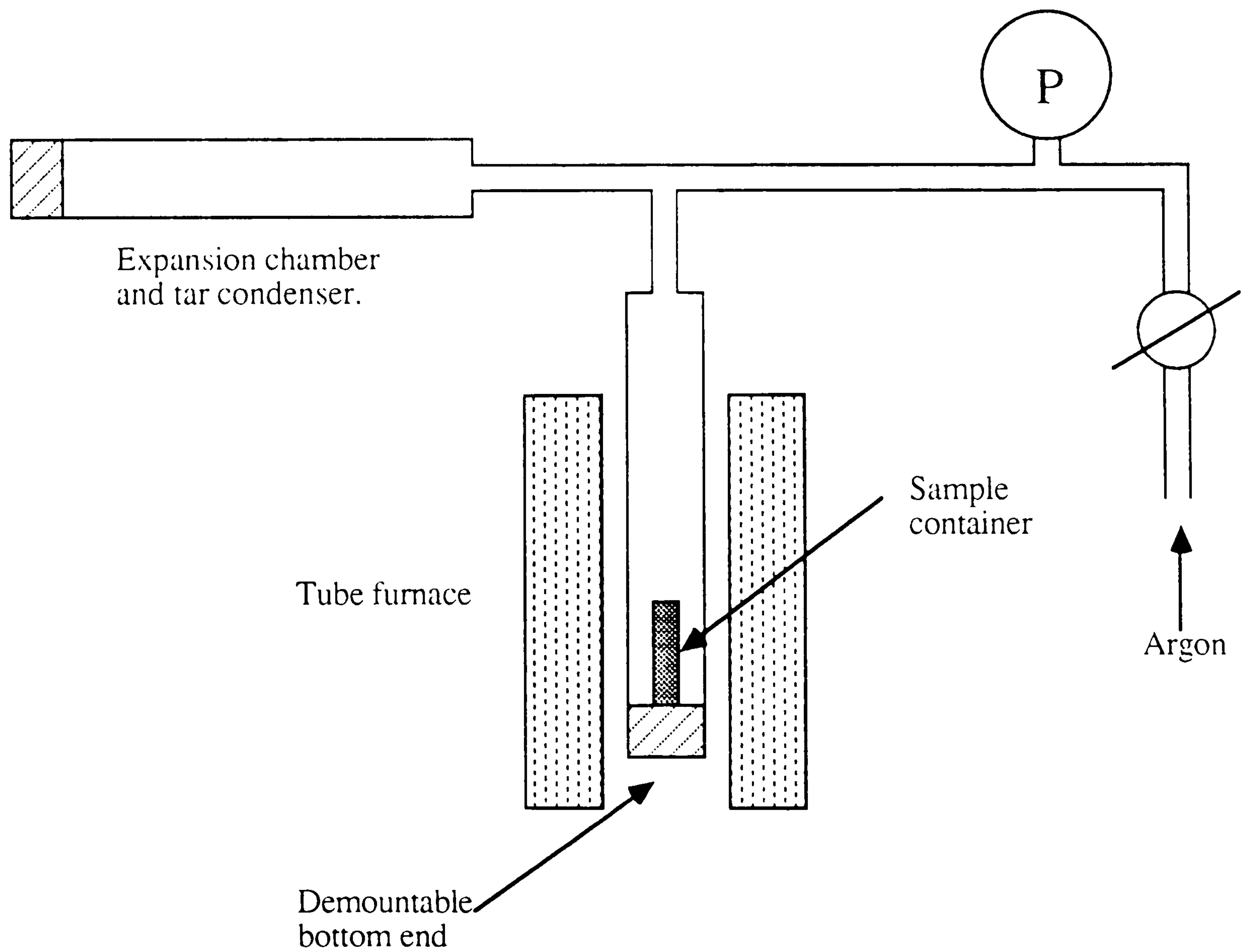

Figure 4.1 Elevated pressure carbonisation apparatus.

4.2.2 Gravimetric adsorption/desorption measurements

4.2.2.1 Apparatus and procedure

A CI vacuum microbalance was connected to a Robal balance controller through an RS232 interface to an IBM PC which was used to measure the rate of uptake of gases in a flowing system as well as the equilibrium capacity of each sample for all gases. The reaction tube with a diameter of 2.5 cm (shown in Figure 4.2) was chosen in order to cut down the dead volume. A perforated bucket was used for the study of commercial CMS materials. The bucket was placed near the sinter in order to reduce flushing out time, ensure that the gas flow was distributed evenly and minimise fluctuations in flow rate changes during gas change over. The reaction tube was also enclosed within a thermostatically controlled water jacket. The system was positioned within a heating mantle to facilitate outgassing at 383 K to remove any moisture and gases adsorbed on the CMS material.

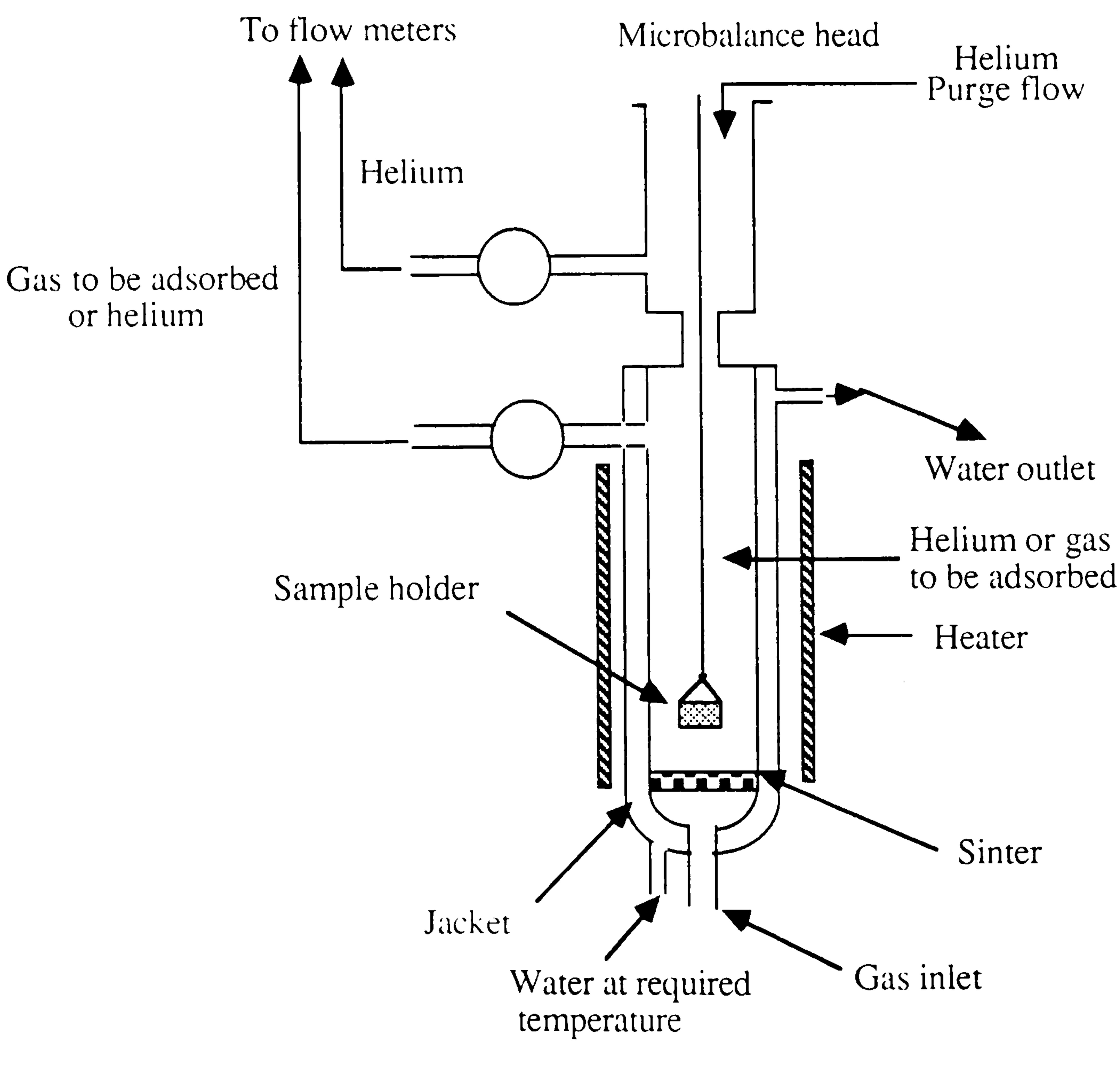

Figure 4.2 Reaction tube for activation energy determination.

The procedure for measurement of gas capacity and kinetics of uptake consisted of following stages:

1. After zeroing the balance the setting was made to give a 2 mg full scale deflection on the chart recorder. Approximately 150 mg of the sample was placed in the bucket.

2. The water jacket was drained and the sample tube and heating mantel were placed in position with the vacuum joint being regreased.

3. The sample was outgassed at 383 K under $<10^{-3}$ torr vacuum for 1 hour or until the weight stabilised after degassing.

4. A purge flow of 100 cm^3min^{-1} of helium was placed through the balance head along with a pre-adjusted flow of helium (100 cm^3min^{-1}) which was introduced through the bottom of the sample tube. After 20 min the jacket was filled with water at the required temperature (275-333 K) and flowed through the jacket enclosing the sample tube. This was then left for 1 hour in order to obtain a steady baseline.

5. The helium was replaced with oxygen, nitrogen or other gas (argon, carbon dioxide, ethyne, ethene or nitrous oxide), with pre-adjusted flow rates of 100 cm^3min^{-1}. The weight uptake with time was monitored and the data stored via an R232 link, on an IBM microcomputer. Measurements of weight were recorded every second until equilibrium was achieved. The gas uptakes were calculated after correction for buoyancy effects.

6. Desorption studies were carried out using the reverse procedure to that used for adsorption. After the sample had reached equilibrium for either oxygen, nitrogen or other gases at a flow rate of 100 cm^3min^{-1}, the gas was switched back to helium at the same flow rate. The gas desorption was followed gravimetrically in the same manner as the adsorption. Corrections for changes in buoyancy were also required in order to measure weight loss during desorption.

The initial uptake readings are difficult to measure accurately, as the response of the microbalance to the rapid change in density when the gas is changed from helium to the gas to be adsorbed, produces an instrument response factor which needs to be taken into account. However, the gas uptake can be estimated from the extrapolation of the uptake curve to time = 0. Also the initial period of uptake was ignored because the experiment needs a finite time to flush out the helium around the sample bucket. Usually the initial 20 s of gas uptake was ignored. In this analysis equilibrium uptake is more important since it is W_{eq} - W that is plotted, which can be measured more accurately. A typical profile of mass uptake for adsorption of a gas on a carbon adsorbent is illustrated in Figure 4.3.

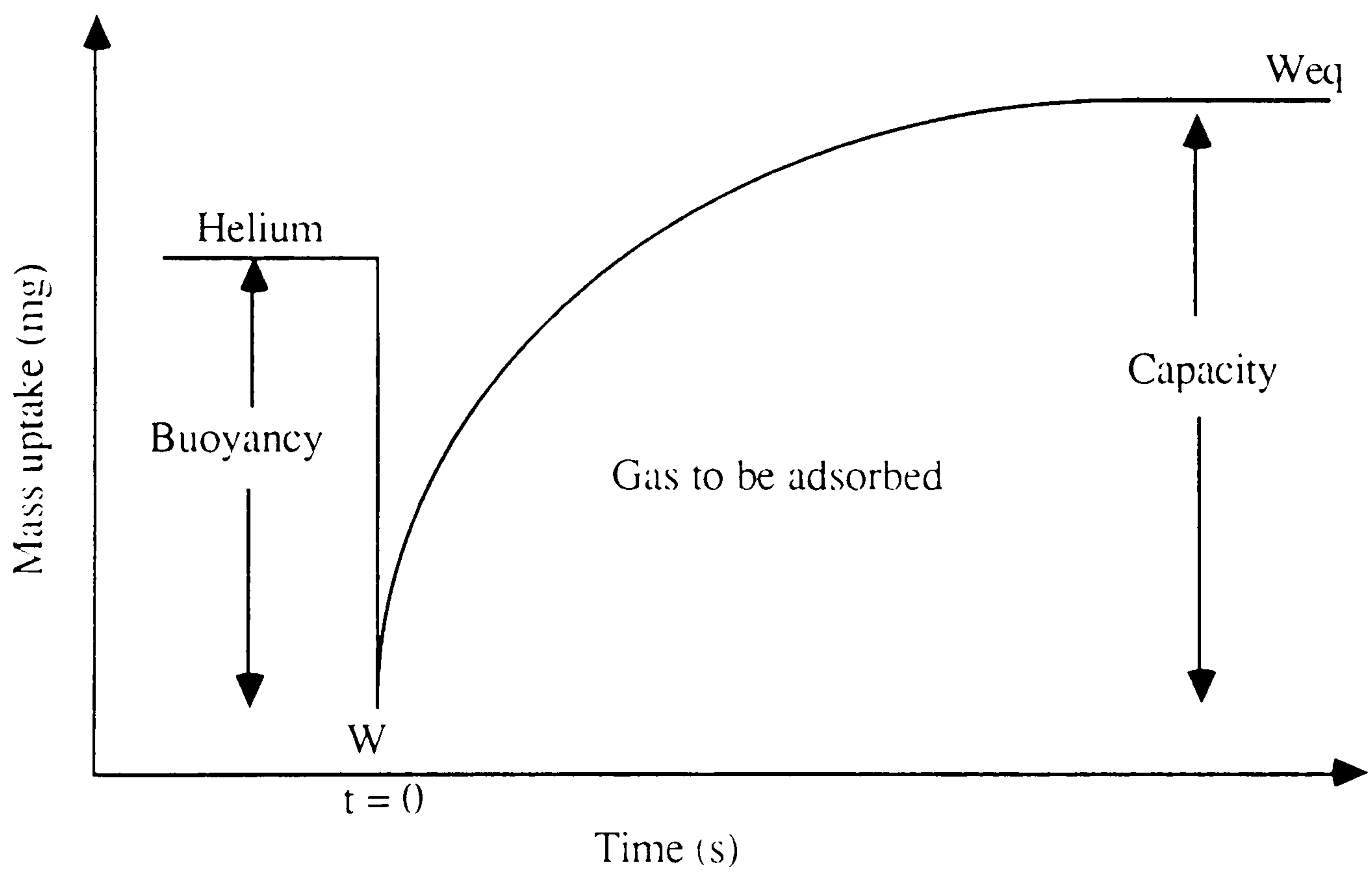

Figure 4.3 A typical uptake profile of gas adsorbed on a carbon adsorbent.

4.2.2.2 Capacity calculations

Capacity can be defined as the volume or mass of gas adsorbed by the given volume or mass of CMS or active carbon. The difference in densities of the various gases give rise to buoyancy effects can be corrected by determining mass changes experienced by the bucket and hangdown with various amounts of powdered silica when changing from helium to oxygen, nitrogen or other gases as appropriate. In the case of a perforated bucket the buoyancy corrections were determined using glass beads. The graphs of buoyancy correction for a given mass of sample for various gases against molar mass of the respective gas are shown in Figures 4.4 to 4.8.

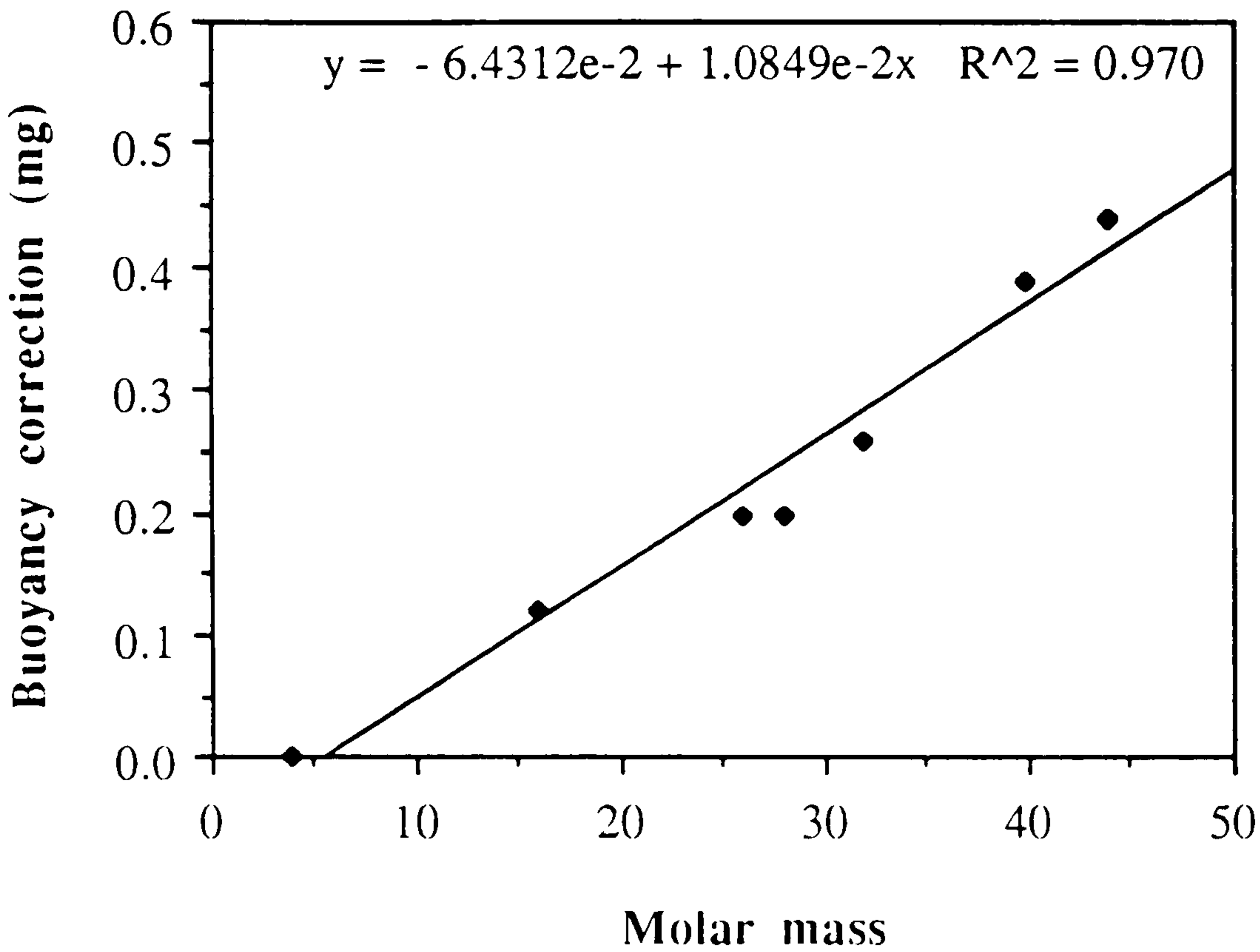

Figure 4.4 A graph of buoyancy correction versus molar mass of various gases:mass of bucket (0.49g).

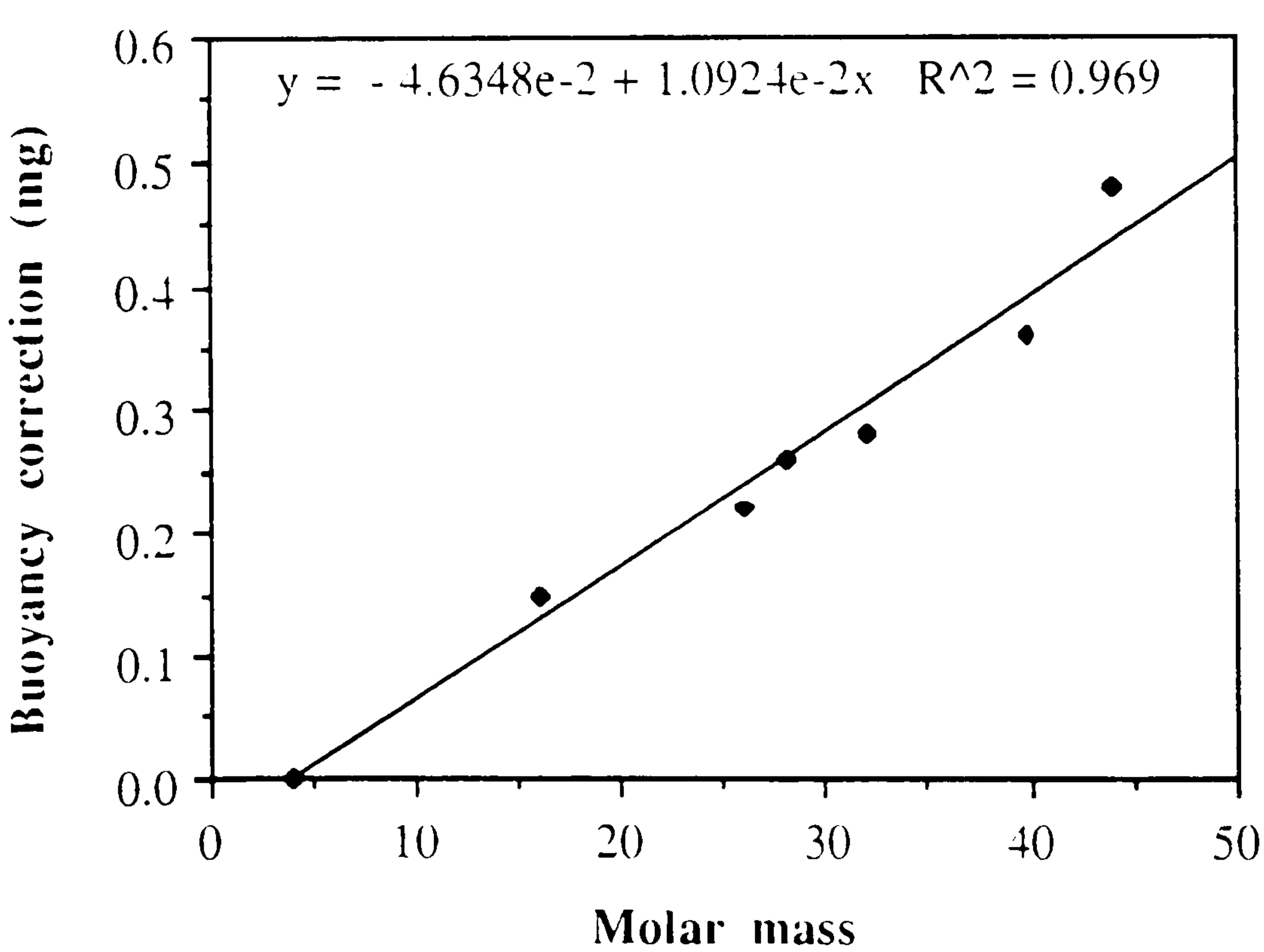

Figure 4.5 A graph of buoyancy correction versus molar mass of various gases: mass of bucket (0.49g) + 0.36 mg of glass beads.

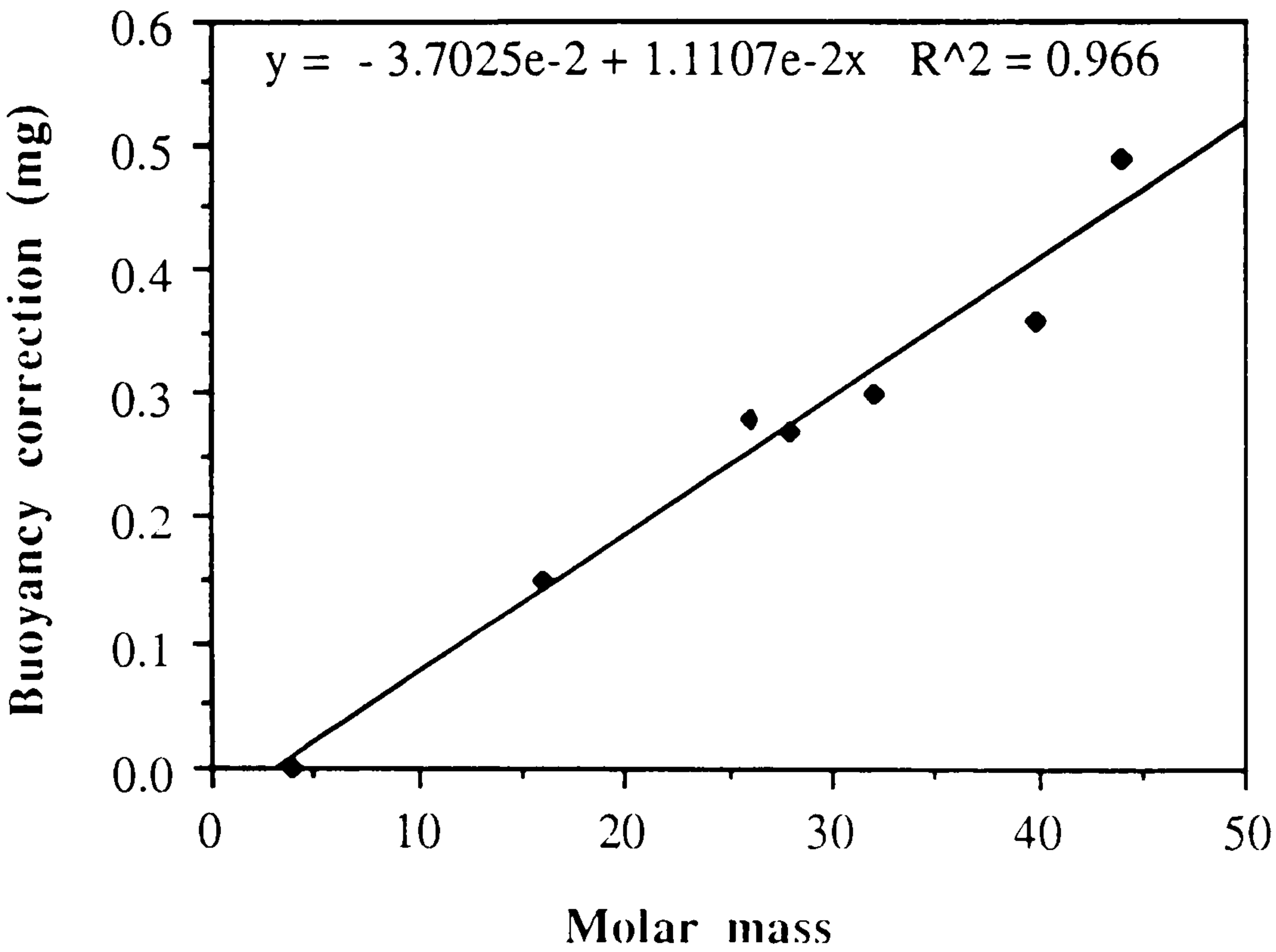

Figure 4.6 A graph of buoyancy correction versus molar mass of various gases: mass of bucket (0.49g) + 108 mg of glass beads

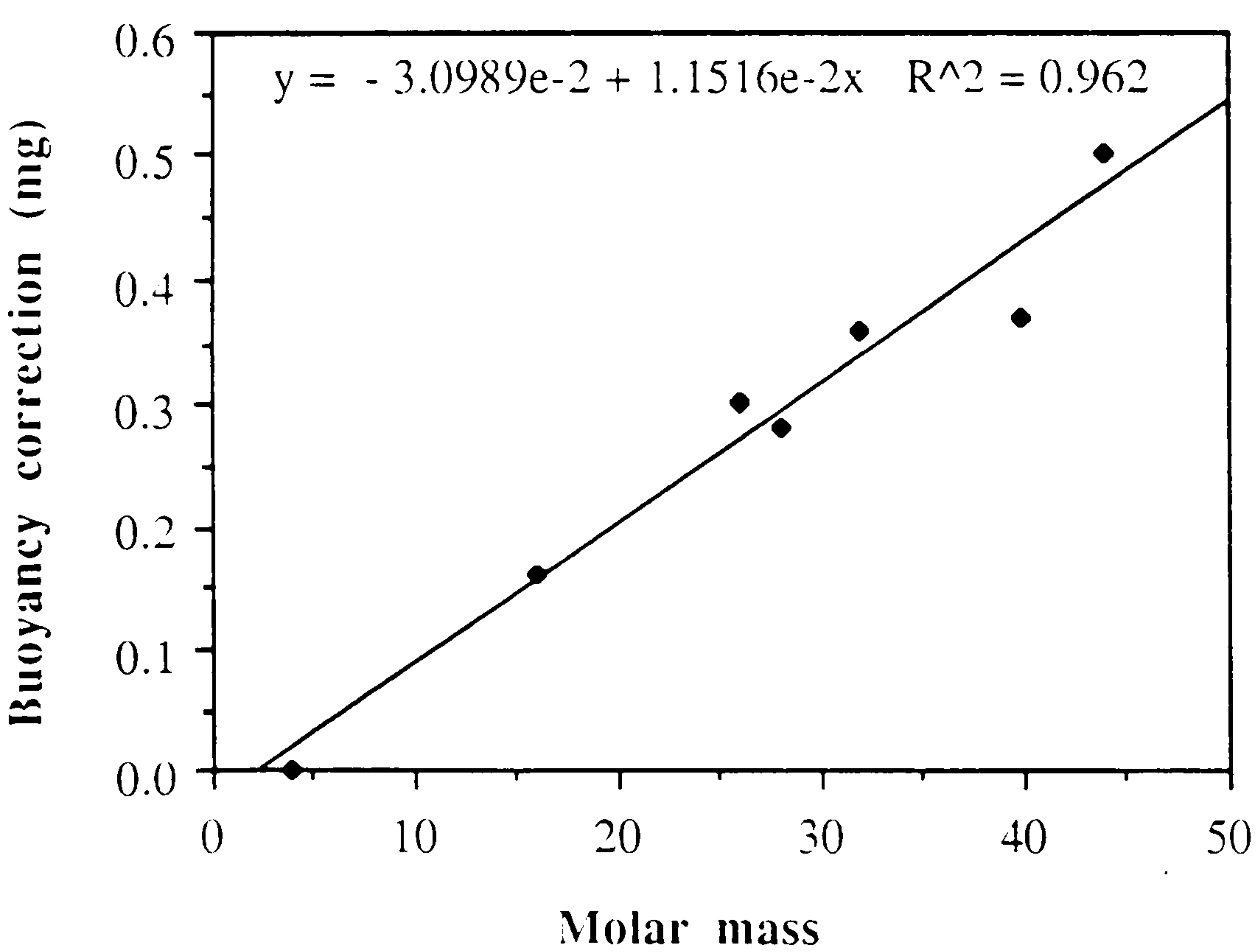

Figure 4.7 A graph of buoyancy correction versus molar mass of various gases: mass of bucket (0.49g) + 144 mg of glass beads

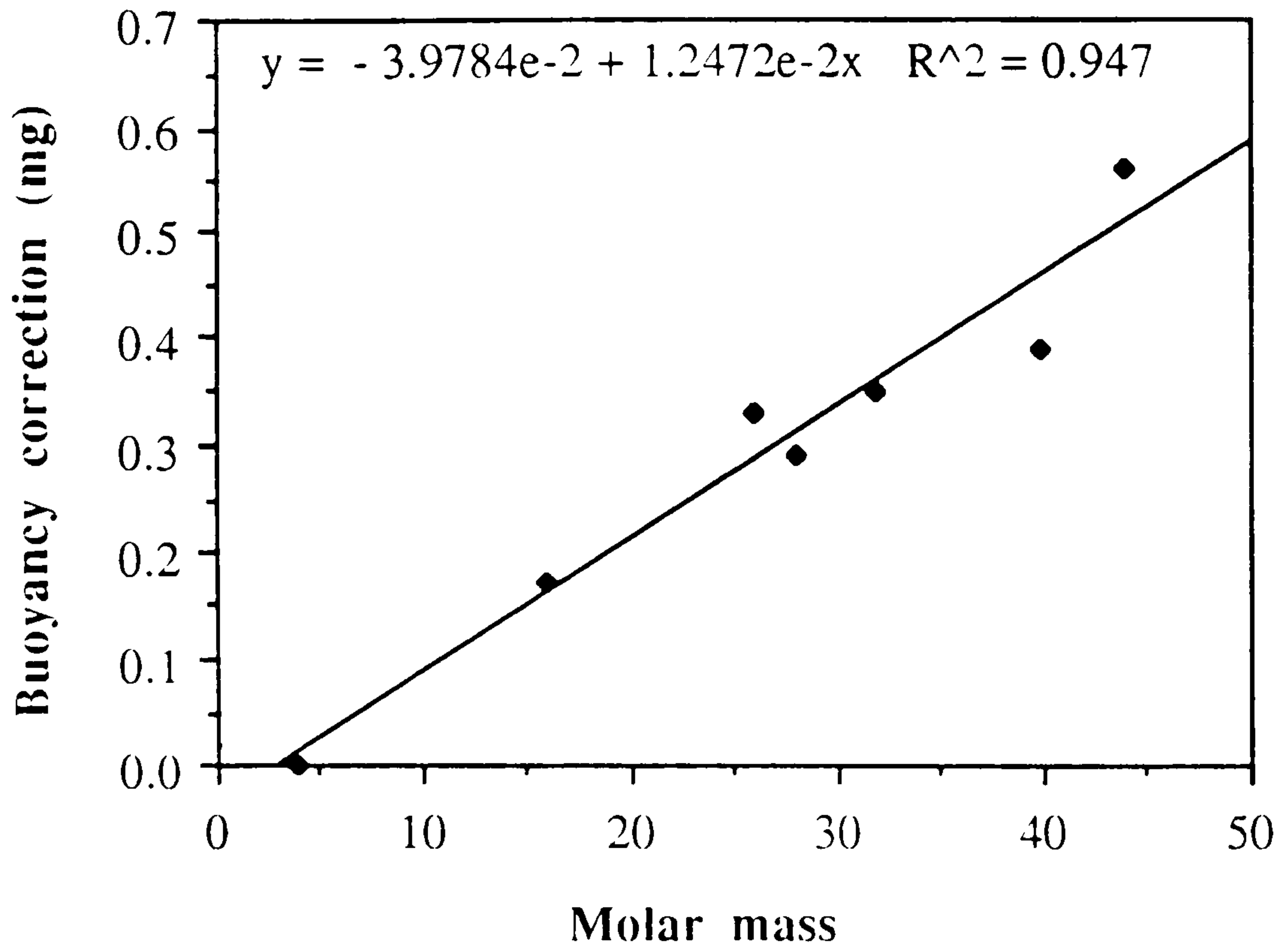

Figure 4.8 A graph of buoyancy correction versus molar mass of various gases: mass of bucket (0.49g) + 180 mg of glass beads.

The buoyancy correction depends on the density of the material used. Therefore a comparison was made between the corrections for graphite and the non-porous glass beads. A comparison is shown in Figures 4.9. There is a small difference in the masses of graphite and glass beads used but this was not significant as far as the comparison is concerned. It is apparent that the correction for graphite is slightly higher (~ 0.05mg or 10%) than the correction for glass beads. The difference is within the experimental error for the gas uptake and is mainly due to the lower density (2.25gcm^{-3}) for the graphite compared with the glass beads (2.85 gcm^{-3}). In addition, small amounts of gas adsorption may occur in the graphite. Therfore the buoyancy corrections used were those determined with the non-porous glass beads.

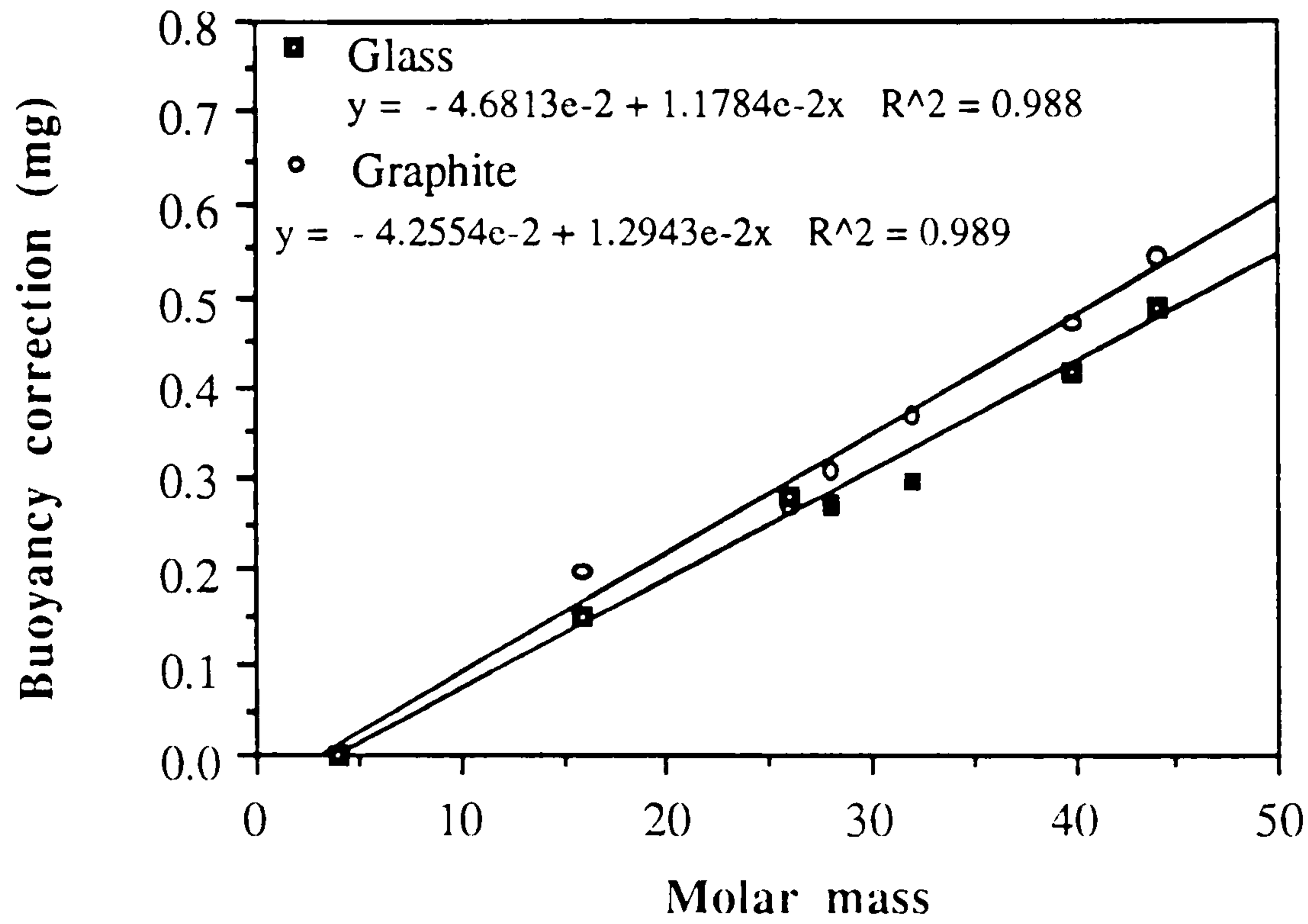

Figure 4.9 Graphs of buoyancy correction versus molar mass of various gases: mass of bucket (0.49g) + of glass beads(108 mg) and graphite (113 mg).

Figure 4.10 shows buoyancy corrections used when changing from various gases as a function mass of sample (glass beads).

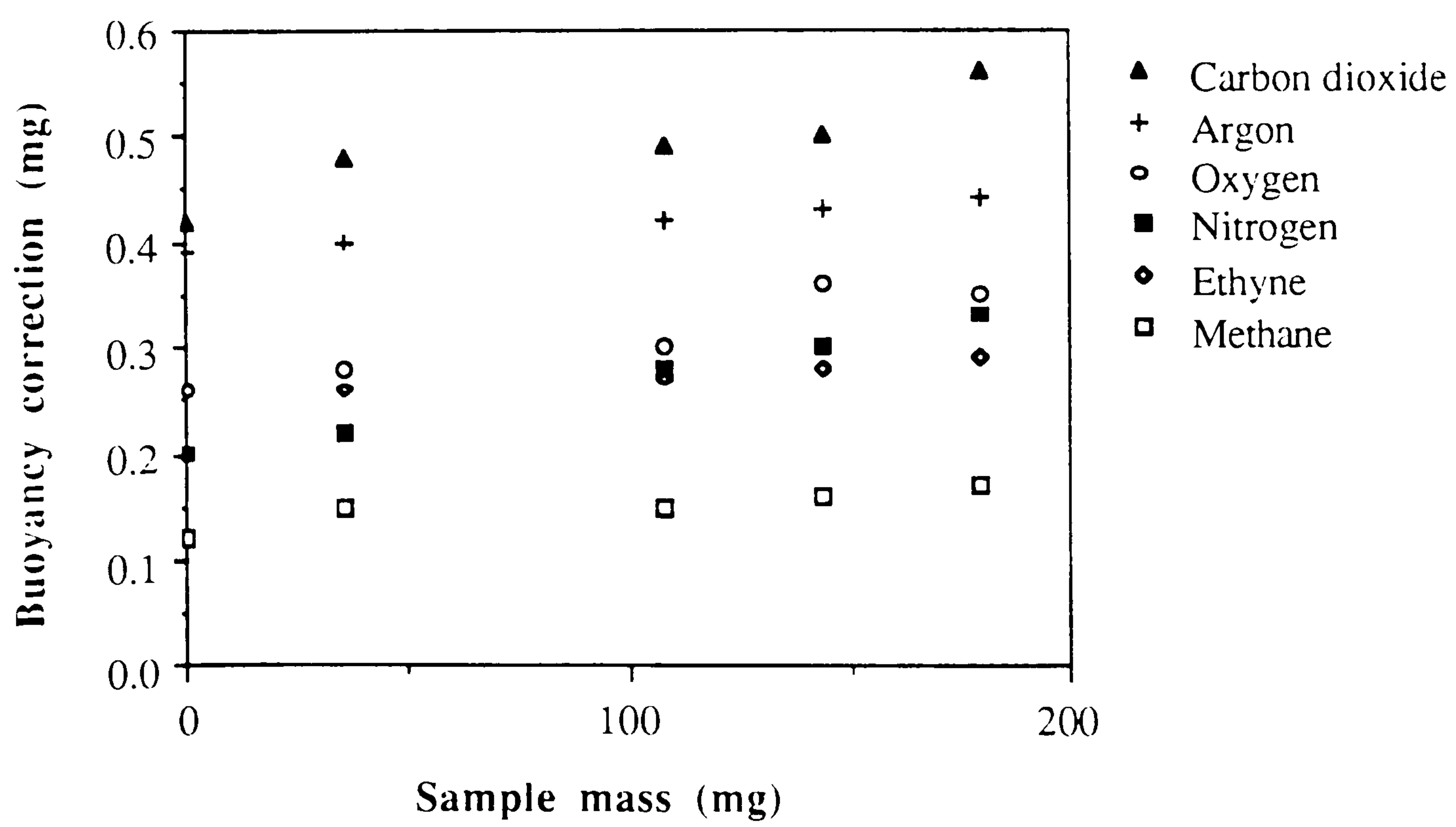

Figure 4.10 Showing the buoyancy correction factor for glass beads for the various gases studied.

Hence, the adsorption capacities can be determined in two ways. Firstly a buoyancy correction relative to helium can be added to the difference between initial mass in helium and the mass after adsorption of the particular gas being studied. In order to calculate the gas capacity of each carbon sample its mass in helium was subtracted from its mass in the particular gas after the equilibrium uptake had been achieved; the buoyancy correction was then added to this to give the mass of gas adsorbed. This figure was then converted to g g^{-1} of sample. The equilibrium capacity was determined at STP by multiplying mmol g^{-1} by 22.4 as shown in the equation below:

In summary this can be expressed as:

$$\text{Capacity (cc g}^{-1}\text{) (At STP)} = \frac{(MG - MH + B)}{\text{Mass of carbon}} \times \frac{1000}{MW} \times 22.4 \qquad (4.1)$$

where:
- MG = Equilibrium mass in gas.
- MH = Equilibrium mass of sample in helium.
- B = Buoyancy correction.
- MW = Relative molar mass of the gas.

The buoyancy corrections over the range of temperatures studied were calculated using the ideal gas equation and the buoyancy corrections obtained at 293 K. The gas uptake was determined as explained in section 4.2.2.1, but the change over of gas from helium to the adsorptive gas gives rise to a very rapid mass change due to buoyancy difference and also a fast uptake of gas on the clean surface of the sample. The progression of adsorption to equilibrium implies the diffusion of gas into the porous network. Hence, in order to determine the gas adsorption kinetics the values obtained by extrapolation of gas uptake to time t = 0 were used.

4.2.2.3 Kinetic measurements

The rate was also determined from gravimetric gas uptake as a pseudo-first order rate constant, k for the gas uptake at atmospheric pressure. The derivation of the rate constant is based on a simplied version of Langmuir kinetics, where θ is considered to be fraction of surface that is covered; $1-\theta$ is the fraction remaining.

$$- dW/dt = k \text{ (fraction of carbon active sites available) (Concentration of gas)}^n \qquad (4.2)$$

where the fraction of carbon active sites = $(1-W/W_{eq}) = 1 - \phi$ (4.3)

W = Weight uptake at time t

W_{eq} = weight uptake at equilibrium $(t = \infty)$

The concentration of gas can be considered constant at atmospheric pressure in a flowing system and thus can be taken into the rate constant. Hence:

$$- dW/dt = k'(W_{eq}-W) \qquad (4.4)$$

Integrating: $\log_e (W_{eq}-W) = - k't + C$ (4.5)

When $t = 0$; $C = \ln W_{eq}$; substituting the value of C in equation 4.5

$$\log_e (1-W/W_{eq}) = - k't \qquad (4.6)$$

Rearranging equation 4.7

$$\log_e (1-W/W_{eq}) = - k't$$

The graph obtained of this obtained $\log_e (1-W/W_{eq})$ versus time 't' was a straight line of gradient k'. A graph was plotted as above and a gradient calculated from the resulting straight line. The above description is a simplified description related to Langmuir's rate model which gives the equation below

$$dW/dt = C k_d (k C (1-\sigma) -\sigma) = C (k_a C (1-\sigma) - k_d) \qquad (4.7)$$

where $\varnothing$ = fractional surface coverage by species (W/Weq)

k_d = Langmuir desorption rate constant

k_a = Langmuir adsorption rate constant

k = Langmuir equilibrium constant

C = concentration of gas phase species

The kinetic selectivity for the CMS can be defined as ratio of rate constant of oxygen/rate constant of nitrogen = $k'O_2/k'N_2$. A high selectivity ratio means that the sieve readily discriminates between gases on basis of molecular diameter, size and shape.

However there are assumptions in the Langmuir example zero activation energy for adsorption and for desorption, the activation energy is equal to the heat of adsorption. The adsorption into CMS was found to be an activated process which indicates that the above model is not strictly valid although the results were consistent with the model in same respect.

The gravimetric uptake analysis was carried out for all commercial samples. An example of results obtained for adsorption of argon for CMS A3 can be seen in Figure 5.2 Chapter 5. The gradient in this case can be seen to be 4.15 x 10^{-4} s^{-1}. The possible errors for the Arrhenius plots were determined using linear regression.

The desorption kinetics were fitted to an equation involving two exponential terms. This equation was of the form:

$$\frac{M_t}{M_\infty} = A_1\, e^{-E_1 T} + A_2\, e^{-E_2 T} \qquad (4.7)$$

This was carried out using the computer programme 'Origin' supplied by MicroCal.

4.2.3 Flow microcalorimetry (FMC)

4.2.3.1 Description of apparatus

FMC was used to investigate the heats of adsorption at gas solid interfaces with high sensitivity. The samples were examined using Microscal series 3-V microflow calorimeter. A schematic diagram of electronics is shown in Figure 4.11 and sample cell is illustrated in Figure 4.12.

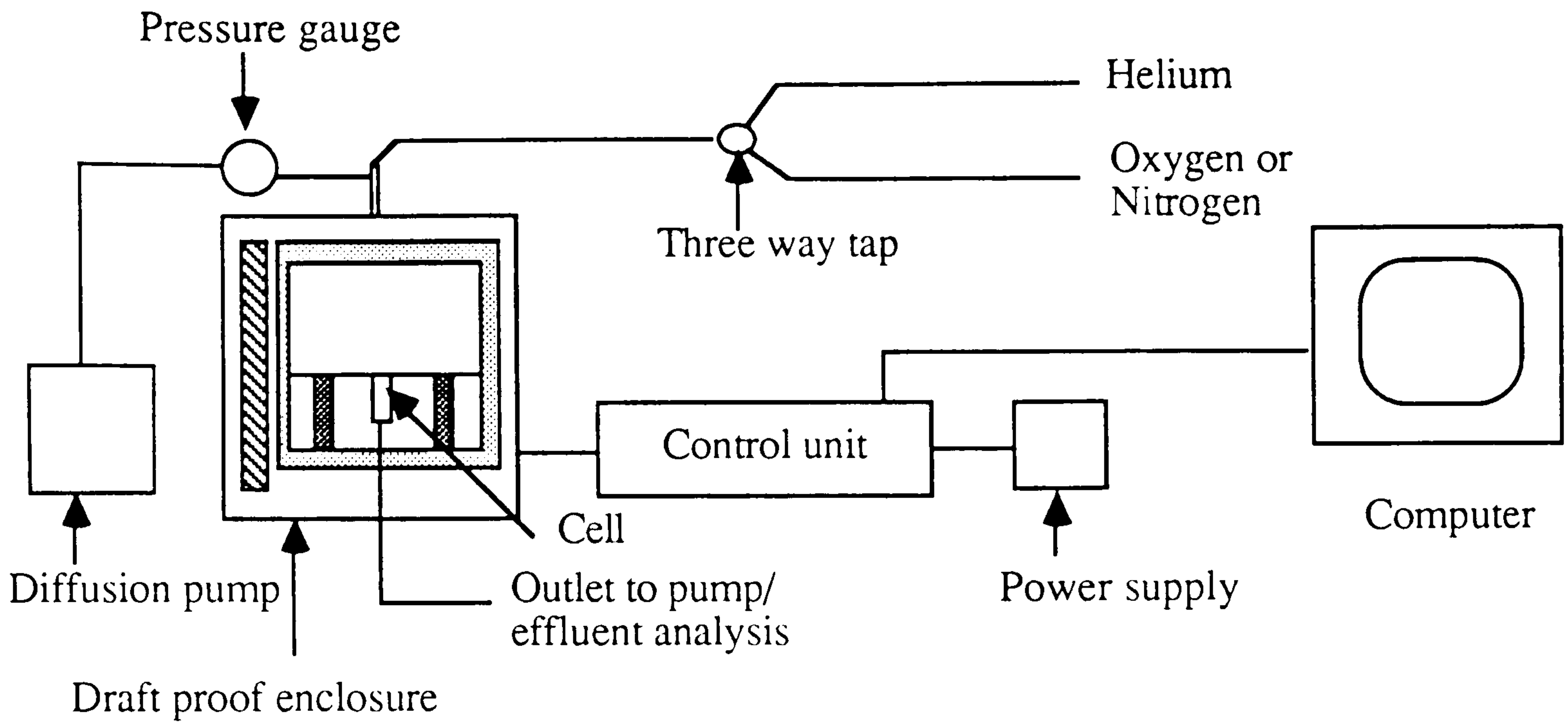

Figure 4.11 A schematic diagram of the Flow Microcalorimeter (FMC).

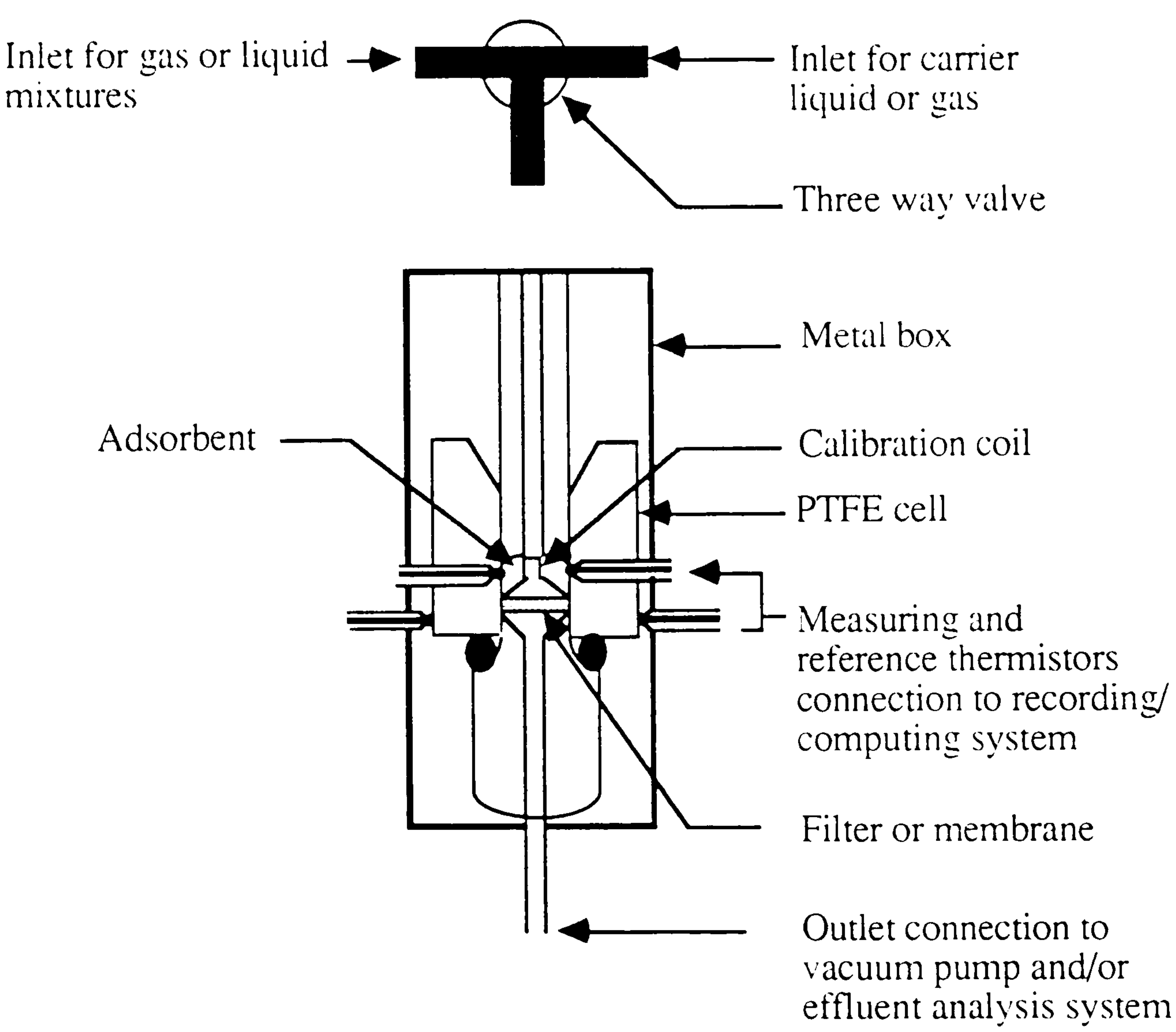

Figure 4.12 Sample cell of FMC

The FMC is housed in a draft proof enclosure and is connected to a control unit which houses the amplifier and electronic accessories and controls. A stabilised power supply can be used as a heating block. The FMC cell is connected to vacuum pump which enables evacuation of the sample cell. The temperature detection can be of 10^{-5}K magnitude; the cell has a maximum sensitivity of 4 μJ and a resolution time range of 1 to 999 seconds.

4.2.3.2 Procedure

Firstly a known mass of ground sample (approximately 100 mg) was placed into the sample cell surrounding the calibration coil. The recommended particle size for this analysis is that retained by a 72 mesh sieve and that which can pass through a 25 mesh sieve (i.e. 600 - 212 μm). The sample cell was evacuated until no heat exchange occurred i.e. endothermic or exothermic.

A flow of dry helium was passed over the sample within the calorimeter at a flow rate of either 1 or 14 cm^3min^{-1}. Following a steady baseline with helium, nitrogen or oxygen was introduced at the same flow rate. The heat of adsorption and desorption were recorded as a trace on a flat-bed recorder by following the temperature as a function of time. The output from the calorimeter was stored in the Calmon unit until data could be retrieved by the computer and peaks could be marked and peak areas integrated. Once no further heat change was observed the gas supply was switched back to helium and an endothermic desorption peak obtained. The peak area obtained for adsorption or desorption is proportional to the total heat evolution as established by electrical calibration. This is assessed by passing a known pulse of electrical energy through the coil situated in the calorimeter cell.

4.2.3.3 Calculation of heat of adsorption

The heats of adsorption of oxygen or nitrogen on a clean carbon surface were measured as a heat output thermogram. The total peak area was related to the amount of gas adsorbed, the shape of the peak being related to the kinetics of gas adsorption. The peak areas were calibrated by the introduction of a peak of known heat output per gram of sample. In all cases the adsorption cycle was repeated until successive peak areas were reproducible to within 50 mJg^{-1}. The two peak areas were then averaged and figures quoted to the nearest mJg^{-1}.

4.2.3.4 Calculation of the kinetic parameters

In the case of CMS materials oxygen is adsorbed at high rates giving sharp peaks, whereas nitrogen is adsorbed more slowly giving elongated heat evolution peaks. The FMC values that arose from the variation in measured peak areas were used for the calculation of rate. The data for the peak height, i.e. the heat given out at any particular time, can be taken from the microcalorimeter and used to calculate the uptake kinetics and selectivity of the carbon. Experiments were conducted to obtain peaks for both nitrogen and oxygen on commercial CMS materials and activated carbon.

Considering the adsorption to be a pseudo first order process then the rate of heat output should be equal to a rate constant multiplied by the reagent concentrations. Assuming the concentration of gas to be constant the following equation is obtained:

$$-\frac{dA}{dt} = k'' \text{[carbon active sites available]} \qquad (4.8)$$

where A is the peak area which in the case of the FMC thermogram corresponds to the heat output and k" is the rate constant.

As in the case of gravimetric gas uptake, the concentration of active sites available can be taken as one minus the fractional surface coverage. In the case of the FMC heat output thermogram the fractional surface coverage can be taken as the total cumulative heat output (peak area) to time (t) divided by the total heat output at equilibrium; thus the concentration of active sites available is given by:

$$\text{[carbon adsorption sites]} = (A_{eq} - A) \qquad (4.9)$$

where: A = the total peak area to time (t)

A_{eq} = the equilibrium peak area.

Considering the kinetics in a similar way to that for the gravimetric uptake case:

Firstly: $$\frac{dA}{dt} = - k'' (A_{eq} - A) \tag{4.10}$$

Rearranging: $$\frac{1}{(A_{eq} - A)}\frac{dA}{} = - k''dt \tag{4.11}$$

Integrating: $$\ln(1 - A/A_{eq}) = - k''t + c \tag{4.12}$$

Thus a graph of $\ln(1 - A/A_{eq})$ against time should be a straight line of gradient k". The gradient of this linear portion has been taken as FMC rate constant for the oxygen and nitrogen and the ratio of the two taken as FMC selectivity factor for molecular sieving ability.

The drawbacks of this technique are the limiting gas flow supply to the FMC sample cell and heat loss characteristics which gave rise to differences in the calibration peak areas at different flow rates. The $\ln(1-A/A_{eq})$ graph shows deviation at the beginning where the FMC peak was still increasing due to flushing out of the reactant gas and the end part of the peak which consisted of sample cooling rather than heat evolution.

4.2.4 Surface area measurement

Total surface area measurements have been obtained using a McBain spring apparatus. The sample was placed in an aluminium bucket and suspended by a pyrex hook from a silica spring, as shown in Figure 4.13. The system was connected to an oil diffusion pump and a rotary pump. The samples were outgassed for about 4 hours at 383 K. The adsorptive carbon dioxide was introduced into the system with the sample immersed in ice (273 K). The time taken for the system to reach equilibrium was established by monitoring weight increases of the carbon sample after admission of each volume of gas. The pressure readings were increased stepwise and weight uptake

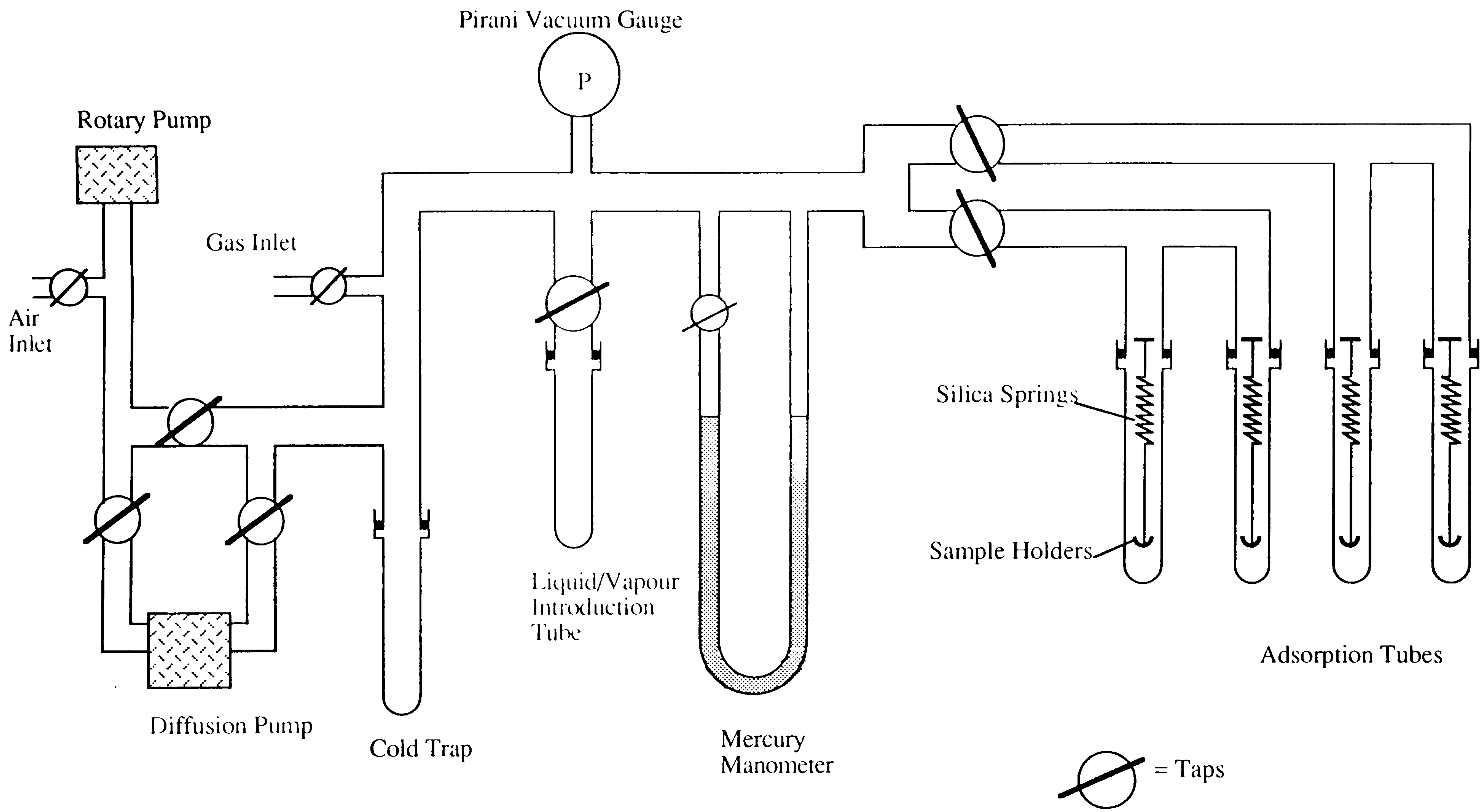

Figure 4.13 McBain spring balance.

measured until the pressure reached about 1 atmosphere (0.1 MPa). The extension of the pre-calibrated spring was measured using a cathetometer and the amount of gas adsorbed on the surface was calculated. The adsorption isotherm was used to estimate the surface areas using a value of 2×10^{-19} m^2 for the area of carbon dioxide molecule. The isotherm was plotted for gas adsorbed against p/p_o (where p_o is saturation vapour pressure of carbon dioxide, 26144 torr (3.49 MPa)). From the adsorption isotherm it was possible to derive a value for the monolayer capacity of the solid. The monolayer capacity can be defined as the amount of adsorbate which can be accommodated in a completely filled single molecular layer (monolayer) on the surface of a unit mass of solid. The surface area was obtained from the following equation:

$$S_a = N_m \times a_m \times L \tag{4.13}$$

where:

	S_a	=	Surface area /m^2 g^{-1}
	N_m	=	Monolayer capacity / mmol g^{-1}
	a_m	=	Cross-sectional area of molecule
			for $CO_2 = 2 \times 10^{-19}$ m^2
	L	=	Avogadro's number (6.022×10^{23})

From the D-R plot equation as given below the number of gas molecules adsorbed and gradient D were obtained:

$$\log_{10} V = \log_{10} V_o - D \log^2{}_{10}(p/p_o) \tag{4.14}$$

where V is the amount adsorbed at relative pressure p/p_o, V_o is the total amount of adsorbate within the micropore system and D is related to pore size distribution. From the plot of $\log_{10} V$ against $\log^2{}_{10}(p/p_o)$ the gradient D, of the plot and intercept V_o can be found.

Carbon dioxide isotherm was also measured and plotted at 0°C (273 K) for commercial sample CMS A3 using a Micromeretics digisorb 2600 high speed surface area analyser after degassing the sample for two hours at 393 K. The adsorption isotherms were plotted using the amount adsorbed mmol g^{-1} against p/p_o where p_o is the saturation vapour pressure of carbon dioxide as given before.

4.2.5 Density measurements

The helium densities for commercial and laboratory samples were evaluated using Micrometerics helium densitometer-AccuPyc 1330. Conventionally helium densities of carbons have been determined at room temperature. The principle is based on expanding the volume of helium occupied in a one container into a second container of known volume which also contains the sample as shown in Figure 4.14.

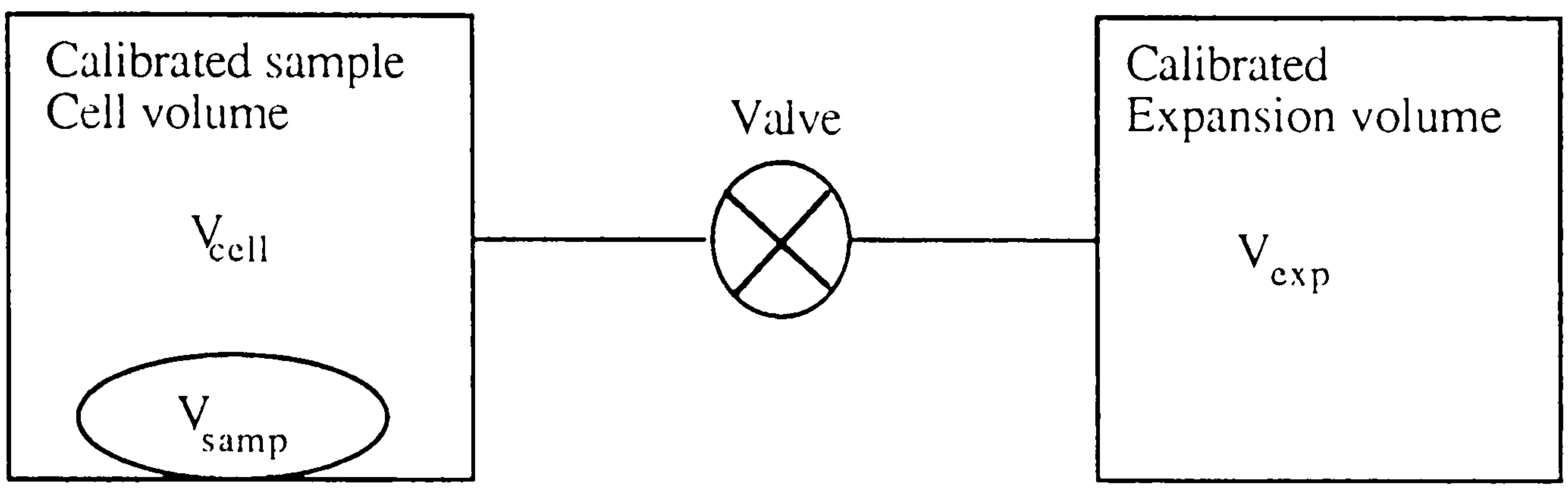

Figure 4.14 Simplified block diagram of AccoPyc 1330 helium densitometer.

The measured volume of gas at known pressure and temperature was expanded to the evacuated sample container and the pressure and temperature of gas in both were then measured. The sample of known weight was placed in the cell and subjected to a series of helium purges and density output obtained. The accuracy of the instrument lies within the range of 0.03%. The AccuPyc 1330 pycnometer is a gas displacement pycnometer, which measures the volume of the solid. The working equation of the pycnometer is as follows:

$$V_{samp} = V_{cell} - (V_{exp}/[p_1/p_2 \; -1]) \qquad (4.15)$$

where:

V_{samp} = Volume.of sample

V_{Cell} = Calibrated sample cell volume.

V_{exp} = Calibrated expansion volume.

p_1 = Elevated pressure - ambient pressure.

p_2 = Intermediate pressure - ambient pressure.

This technique enables us to find the V_{samp} of the known mass and hence to calculate the helium density (by relation $\rho = M/V$, M =mass of sample, V= volume of sample) of the sample. The helium density was measured in order to assess the closed porosity of the carbons.

4.2.6 Thermogravimetric analysis

(1) Proximate analysis

Proximate analysis provides a measure of relative volatile and non-volatile compounds, water and non-combustible material by destructive thermal distillation. The moisture content, volatile matter, ash and fixed carbon content of the carbon material were determined by this method. This was measured on a Stanton Redcroft Thermogravimetric STA 780. The method used was an equivalent to BS standard 1016 part 5D. The procedure involved placing the sample in a bucket and flushing with nitrogen at 378 K to determine the weight loss on drying. Then it was heated to 1173 K at a heating rate of 99 min^{-1} K and held for 3 minutes to remove the volatile matter. The sample was cooled to 1073 K and the gas switched to air so that the sample gasified in air. The moisture, volatile matter and ash content were obtained. The volatile matter content of carbon was equivalent to weight loss on heating the sample in a covered crucible to 1173 K. The percentage of moisture, volatile matter and ash can be determined as follows:

Moisture % = ({Initial weight - Weight at 378 K}/Initial weight) x 100 + 0.16 (4.16)

Volatile matter % = ({Initial weight - Weight at 1173 K}/Initial weight) x 100 + 0.14 (4.17)

Ash % = (Weight at 1073 K in air/Initial weight) x 100 + 0.18 (4.18)

Small corrections were added for 'buoyancy effects' due to the upward flowing gas. This phenomenon was previously studied using inert materials to determine buoyancy correction factors. These results are designated 'as received'. The data may also be displayed on a 'dry basis' or 'dry ash-free basis'.

'dry basis' = ('as received' percentage x 100)/(100 - % moisture received) (4.19)

'dry ash free basis' = ('as received' percentage x 100)/(100 - % moisture as received - % ash as received) (4.20)

(2) Differential thermogravimetric analysis (DTG analysis)

DTG analysis was carried out using a Stanton Redcroft Thermogravimetric analyser STA-781. The technique involves the use of thermogravimetric analysis where the weight change can be followed as a function of temperature. The samples were subjected to pyrolysis at a heating rate of 5 K min^{-1} to a maximum temperature of 1073 K under nitrogen (flow rate 50 $cm^3 min^{-1}$). The weight loss profile was used to assess decomposition temperatures of various precursor materials like polymers and resins; for example PVDC, PEEK, PES, Novolak and PVDC with 25% polynuclear aromatics under atmospheric conditions in order to assess their decomposition temperature ranges so that suitability for blending could be assessed.

4.2.7 Probe molecule adsorption rig

The pore size distribution of carbons synthesised was determined using molecular probes of different sizes. The apparatus used for these studies is shown in Figure 4.15. The technique followed the Air Products and Chemicals, Inc. analytical technique CRSD-A-023-89. In summary this consisted of the following steps:

1. The spring extensions for the empty aluminium foil buckets were measured.

2. Each sample was weighed into lightweight aluminium foil buckets before being suspended from the silica springs within the adsorption apparatus.

3. The initial spring extensions were measured before outgassing the samples under vacuum at 383 K for a period of four hours, after which the outgassed spring extensions were measured.

4. The organic liquid was placed in a vapour tube, attached to the rig and subjected to continuous freeze/evacuate/thaw cycles to remove noncondensible vapours.

5. The samples were thermostated at the required temperature of 301 K

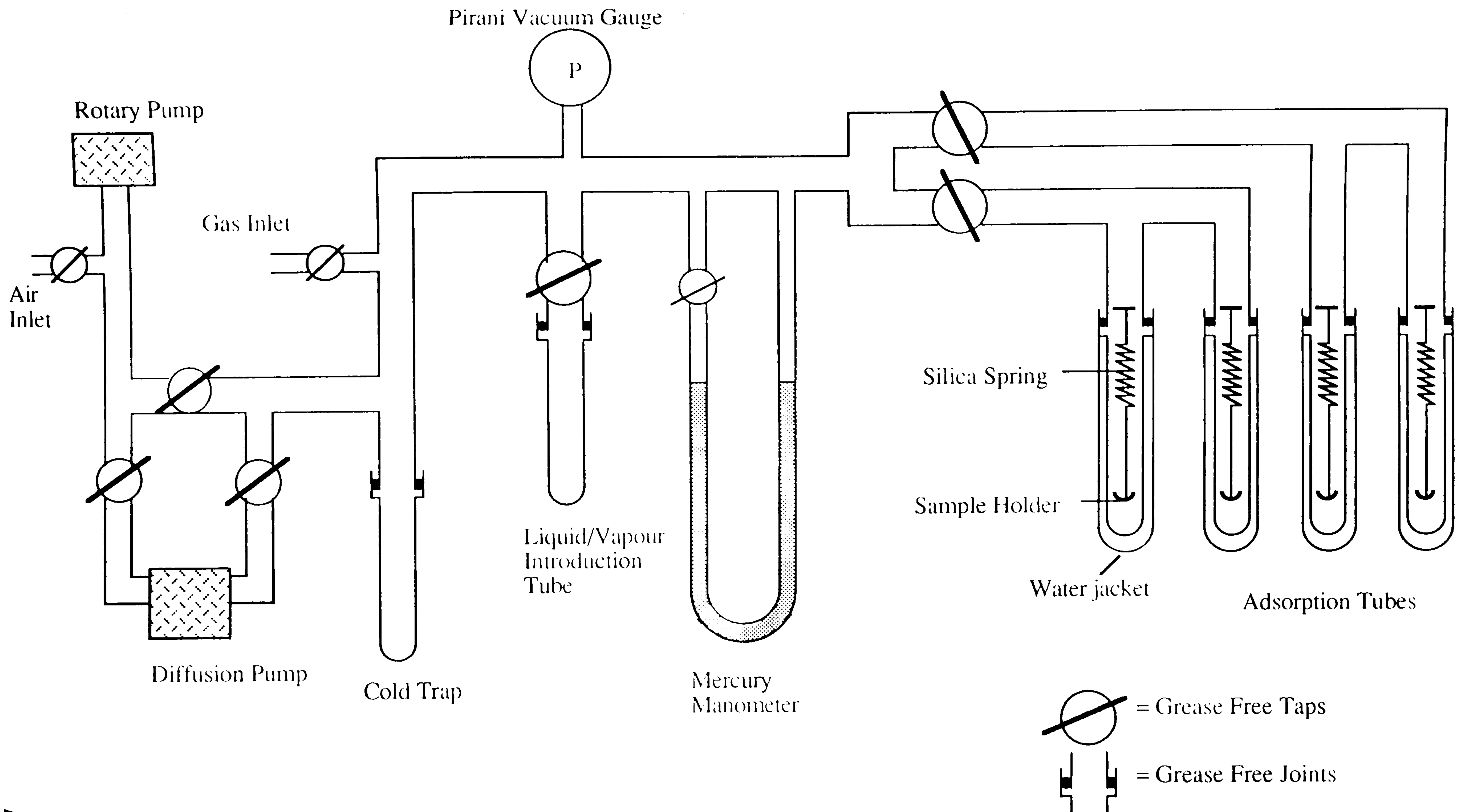

Figure 4.15 Grease-Free adsorption rig for probe molecule studies.

for all vapours other than butane, for which a temperature of 273 K was used before admission of the vapour to the required pressure, as shown in Table 4.1.

6. After a period of 24 hours the new spring extensions were taken indicating the extent of the adsorption.

7. The process was repeated for each of the vapours/gases shown in Table 4.1.

Table 4.1

Probe molecule adsorption vapours.

Chemical	Partial Pressure ($p/p_0 = 0.5$) at 301 K	Pore size (nm)
Methylene chloride	221	0.40
Butane*	380	0.43
Chloroform	100	0.46
Isopentane	360	0.49
Carbon Tetrachloride	60	0.60
(Water at 273 K)	(16)	(0.32)

* refers to 273 K

The deionised water adsorption was not studied in this series of experiments. It was decided that the carbons would be needed for further study and that water adsorption would be to some extent irreversible, and hence undesirable. The calculations are summarised as follows:

The aluminium foil buckets used weighed approximately 200 mg and for the buoyancy correction calculations their volume was taken to be 0.2 cm^3. The volume of the sample was taken to be the mass of sample (usually 200 mg) multiplied by a constant density of 1g cm^{-3}.

1. Uncorrected dry weight. = Extension due to outgassed sample / spring factor.

2. Buoyancy correction for dry weight. =

$$dw = \frac{MV}{RT} P \qquad (4.21)$$

where: M = Relative molar mass of gas (N_2 = 28).
V = Volume of load (bucket and sample - see above).
R = Gas constant (0.082), dm^{-3} atm K^{-1} mol.$^{-1}$
T = Temperature in kelvin.
P = Pressure in atmospheres.

3. Corrected dry weight. = Uncorrected dry weight (1) + buoyancy correction(2).

4. Weight adsorbed. = (Outgassed extension - final extension) / spring factor.

5. Buoyancy correction for adsorption. =

$$dw = \frac{MV}{RT(1000)} P \qquad (4.22)$$

where: M = Relative molar mass of vapour.
V = Volume of load (see above).
P = Final pressure in system/atmospheres.
R = 0.082 dm^{-3} atm K^{-1} mol^{-1}.
T = adsorption temperature/K.

6. Corrected weight adsorbed. = Weight adsorbed (4) + buoyancy correction (5)

7. Amount adsorbed. = Corrected weight adsorbed (6) - corrected dry weight.

9. Moles adsorbed/mmol. = Amount adsorbed x 1000/(molar mass of vapour)

An Excel spreadsheet was constructed incorporating all the above calculations and was used to calculate the adsorption of each vapour.

Chapter 5

Results

5.1 A Comparison of Flow Microcalorimetry and Gravimetric Methods for Studying CMS Materials

5.1.1 Capacity and selectivity of commercial materials

The capacity and selectivity were determined for six commercial CMS materials and two activated carbons using the gravimetric uptake technique as described in Section 4.2.2 and the Flow microcalorimetry (FMC) as described in Section 4.2.3.

Straight line graphs of $\ln(1\text{-}W/W_{eq})$ versus time were obtained from gravimetric uptake rate data for each sample for oxygen and nitrogen. The analogous rate data from the FMC for all samples were also calculated and both are shown in Table 5.1.

Table 5.1

Gas adsorption rate constants for CMS and activated carbons. (s^{-1} x 10^{-3})

	Gravimetric		FMC		FMC	
Flow rate	(100 cm^3min^{-1})		(3 cm^3min^{-1})		(14 cm^3min^{-1})	
Sample	N_2	O_2	N_2	O_2	N_2	O_2
CMS A	2.17	12.5	2.15	14.1	1.68	16.8
CMS B	0.89	15.7	1.46	21.1	1.19	18.4
EP 1	2.90	34.0	1.32	17.2	2.01	16.1
EP 2	1.72	24.5	2.76	17.1	1.39	15.2
EP 3	1.72	37.6	1.77	17.0	1.20	24.5
EP 4	1.71	7.76	2.14	21.3	1.10	14.1
Chemviron	76.6	54.7	3.49	35.3	2.51	24.0
Sutcliffe	162	156	3.21	37.6	2.09	29.9

An example of the rate graph of $\ln(1\text{-}W/W_{eq})$ versus time (t) for gravimetric uptake of nitrogen on CMS B is shown in Figure 5.1 and a corresponding example of the rate graph obtained from FMC is shown in Figure 5.2. The ratio of rates of adsorption of oxygen and nitrogen gives a selectivity factor for each carbon as assessed by each technique.

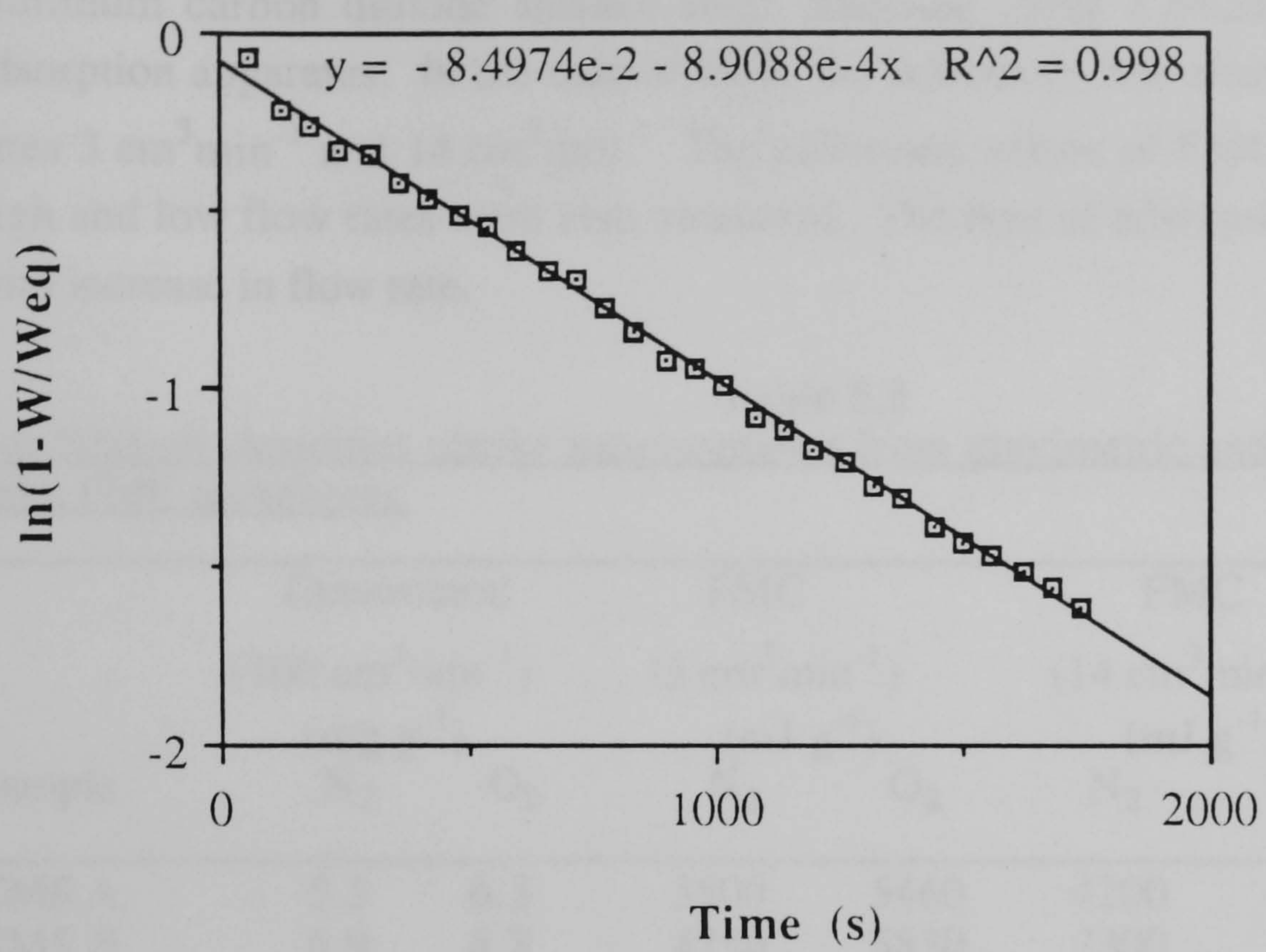

Figure 5.1 A graph of $\ln(1\text{-}W/W_{eq})$ versus time for adsorption of nitrogen on CMS B using gravimetric technique.

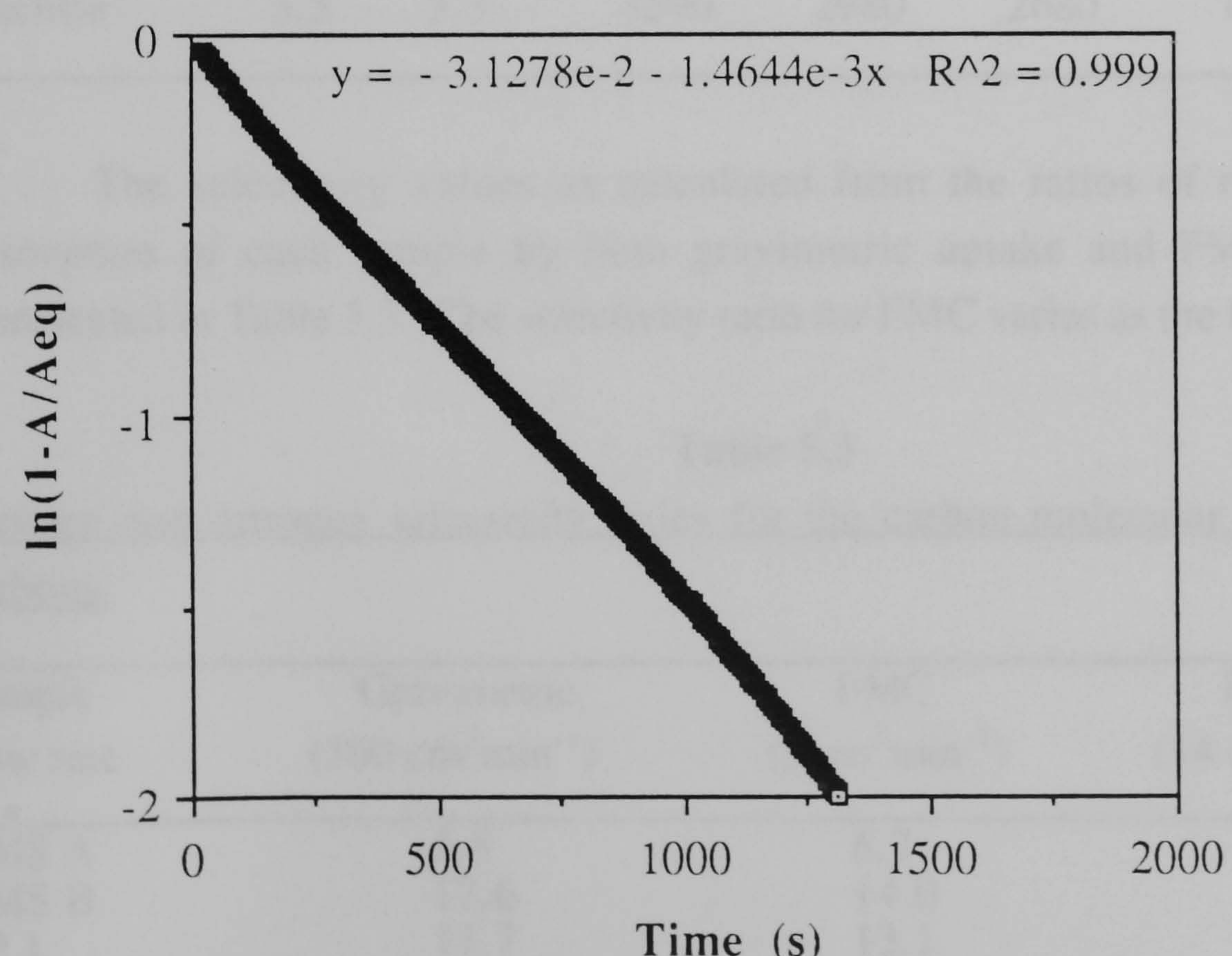

Figure 5.2 A graph of $\ln(1\text{-}A/Aeq)$ versus time for adsorption of nitrogen on CMS B using FMC (at flow of 3 cc/min).

Table 5.2 shows the equilibrium capacity values for oxygen and nitrogen obtained by using gravimetric uptake and FMC for each sample. It also shows the minimum carbon dioxide surface areas obtained using a McBain spring balance adsorption apparatus. In the case of FMC the selectivity was determined at two flow rates 3 cm^3min^{-1} and 14 cm^3min^{-1} The calibrated values of FMC peak areas at both high and low flow rates were also measured. The heat of adsorption show a decrease with increase in flow rate.

Table 5.2

Equilibrium capacities uptake measurements from gravimetric and heats of adsorption from FMC techniques.

Sample	Gravimetric ($100\ cm^3min^{-1}$) ($mg\ g^{-1}$) N_2	O_2	FMC ($3\ cm^3min^{-1}$) ($mJ\ g^{-1}$) N_2	O_2	FMC ($14\ cm^3min^{-1}$) ($mJ\ g^{-1}$) N_2	O_2	CO_2, 273K surface areas (m^2g^{-1})
CMS A	5.5	6.3	3500	5460	4200	7620	250
CMS B	6.9	8.8	4750	5830	2300	6570	355
EP 1	5.6	7.0	4020	3480	3270	5640	265
EP 2	5.3	5.9	3600	6470	2040	3790	341
EP 3	6.3	6.5	4200	5850	1900	5070	295
EP 4	6.0	7.6	4400	6680	1870	5970	315
Chemviron	8.8	9.8	6400	5890	6300	5220	355
Sutcliffe	5.5	5.3	3590	2980	2680	1970	250

The selectivity values as calculated from the ratios of rate constants for adsorption of each sample by both gravimetric uptake and FMC technique are represented in Table 5.3. The selectivity ratio for FMC varies as the flow rate changes.

Table 5.3

Oxygen and nitrogen selectivity ratios for the carbon molecular sieves and active carbons.

Sample flow rate	Gravimetric ($100\ cm^3min^{-1}$)	FMC ($3\ cm^3min^{-1}$)	FMC ($14\ cm^3min^{-1}$)
CMS A	5.8	6.7	10.0
CMS B	17.6	14.0	15.0
EP 1	11.7	13.1	8.0
EP 2	14.2	6.1	10.7
EP 3	21.9	9.4	20.0
EP 4	4.5	10.0	12.7
Chemviron	0.7	1.0	1.0
Sutcliffe	1.0	1.2	1.4

Table 5.4 shows the FMC peak areas and adsorption rates for nitrogen at different flow rates for Sutcliffe Speakman active carbon.

Table 5.4

Adsorption rates and peak areas obtained for various flow rates using FMC.

Flow rate (100 % = 14 cm^3min^{-1})	Calculated Adsorption rate constants (s^{-1})	Measured peak area (mJ g^{-1})
100%	6.7×10^{-2}	2620
90%	5.6×10^{-2}	2749
80%	5.4×10^{-2}	2824
70%	4.6×10^{-2}	3056
60%	3.8×10^{-2}	3304
50%	4.4×10^{-2}	3179
40%	4.6×10^{-2}	3111
30%	5.2×10^{-2}	2883

The results clearly show that the adsorption rate determined by the FMC and the measured peak areas are strongly dependant on the flow rate. This indicates that both the adsorption rates and capacities vary with flow rate. This is due to heat and mass transfer effects and the corrections are complex.

5.2 Adsorption/Desorption Kinetics and Gas Uptake Capacity for CMS A3.

5.2.1 Assessment of adsorption capacity

The adsorption capacities of the carbons for the various gases studied can be determined by two methods. Firstly a buoyancy correction relative to helium can be determined and this can be added to the difference between the initial mass in helium and the mass after adsorption of the particular gas being studied. In practice, it is difficult to measure an absolute buoyancy correction relative to vacuum with the system used because of the two flowing systems for the balance head and the sample container. The buoyancy corrections (BC) for various gases are related to their molar mass and have been shown earlier (Figures 4.4 to 4.9). A graph of buoyancy correction versus mass of sample for various gases is given in Figure 4.10. The accuracy of BC can be checked by extrapolation of the effect of mass of sample to BC = 0 should give the mass of the bucket and hangdown. A graph of BC relative to helium against molar mass should pass through zero at mass four since there will be zero BC in helium. The main problem with this method is that for adsorption of gases such as argon, nitrogen and oxygen the BC is large as compared to the difference in the masses in helium and the gas studied. The alternative approach is to extrapolate the gas uptake curve in the time region $t > 20$ s to $t = 0$. The gas uptake curve in the time range $t = 0 - 20$ s is subject to errors due to (1) the mechanical response of the balance to a rapid change in density and (2) gas flushing out effects during the change over of gases. Comparison of the results of both techniques shows that there is a systematic discrepancy with capacities calculated from the BC method being systematically higher. This can be explained as follows. After the carbon has been degassed and flushed out with helium, the surface is initially free of adsorbed species. When the adsorption kinetic experiment is carried out, the change over of gas from helium to the adsorptive gives rise to very rapid uptake of gas on the easily accessible clean external surface which rapidly reaches equilibrium. The kinetics that are measured represent the diffusion of gas into the porous system. Therefore, the capacities quoted in this thesis refer to the maximum capacity as determined from the BC method. The gas adsorption kinetics refer to the diffusion into the porous structure and the uptake value obtained by extrapolation of the gas uptake to time t = 0 was used since this is more appropriate in this case.

5.2.2 Probe molecule kinetic studies

Adsorption and desorption of a range of gases were studied on a commercial carbon molecular sieve CMS A3 over a temperature range of 275-333 K. These gases were selected on the basis of their molecular shape and dimensions. The 'probe molecules' chosen were spherical, linear or planar in shape. For some of the gases the time required for total desorption was very long. For these gases desorption studies were, therefore only carried out to >90% capacity and the equilibrium adsorption values for individual gas were taken in order to determine the kinetics for desorption. The results for each of the gases used are discussed in the following section and are presented numerically in Table 5.5 (page 142).

5.2.2.1 Argon adsorption/desorption

A typical gas uptake profile for carbon CMS A3 is shown in Figure 5.3. It is apparent that the adsorption kinetics are relatively slow. A graph of ln(1-W/Weq) against time, where W is mass uptake at time t and Weq is the total mass uptake at equilibrium, is shown in Figure 5.4. It is evident that the graph is a straight line demonstrating that the kinetics follow a first order kinetic rate law. The corresponding desorption graph is shown in Figure 5.5. It is apparent that the desorption follows a similar rate law but is significantly slower. This is true for all measurements carried out in the temperature range 275-333 K used in this study. The kinetic rate constants and adsorption capacities are given in Table 5.5. The adsorption capacities are markedly dependant on temperature. The experiments were carried out in the temperature range 275-333 K, which was above the critical temperature (150.8 K) of argon. The data for both adsorption and desorption capacities shows good agreement over the complete temperature range. As expected the adsorption capacities decrease with increasing temperature as showing in Figure 5.6. The activation energy graphs for adsorption and desorption of argon are shown in Figures 5.7 and 5.8. It is apparent that the activation energy for adsorption of argon (39.1 $kJmol^{-1}$) is high. The activation energy for desorption (45.4 $kJmol^{-1}$) is slightly higher. In comparison, there is a change in the pre-exponential factor from 2592 s^{-1} for adsorption to 25084 s^{-1} for desorption.

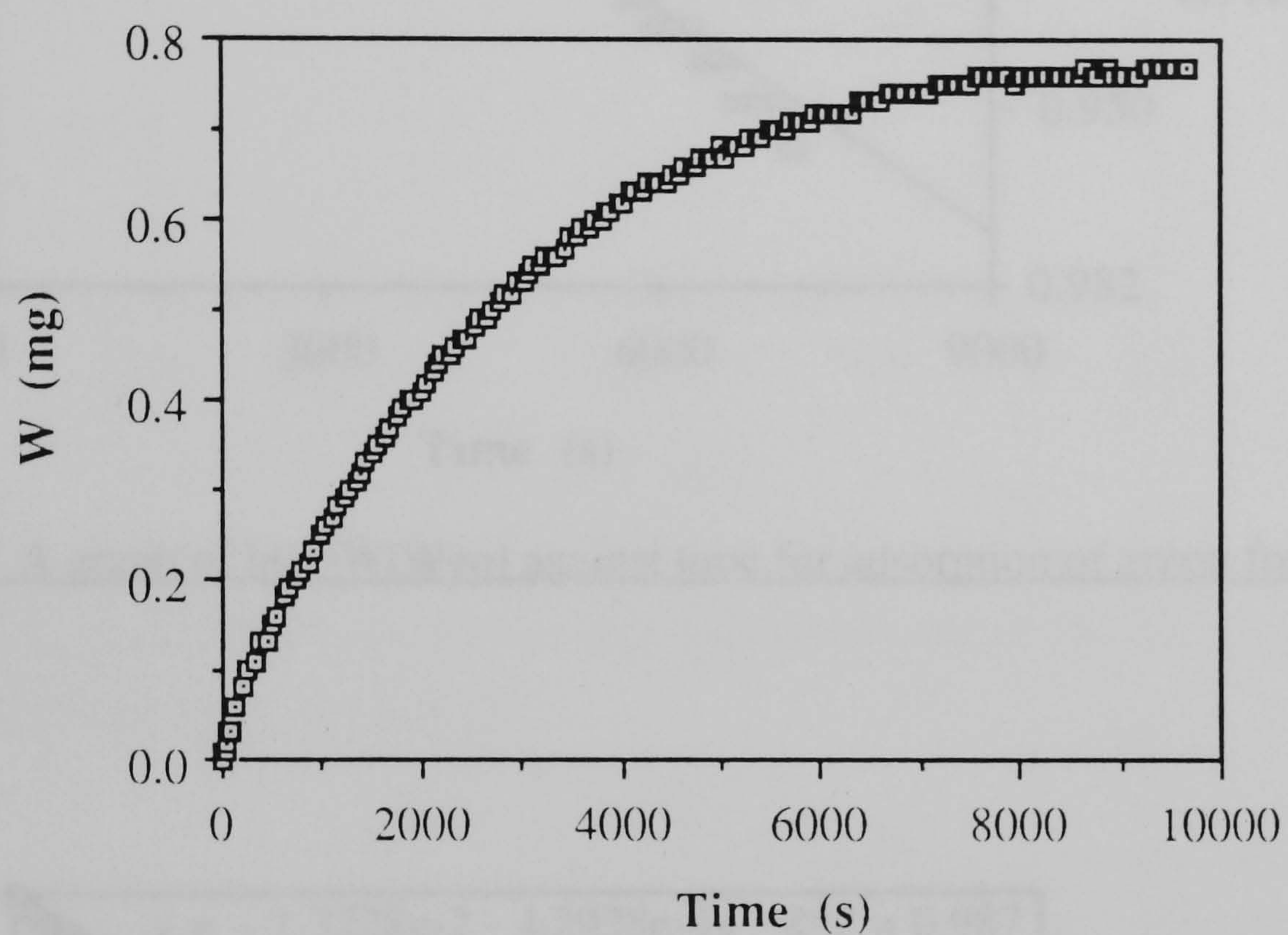

Figure 5.3 A typical profile of W against time for adsorption of argon for CMS A3 at 303 K.

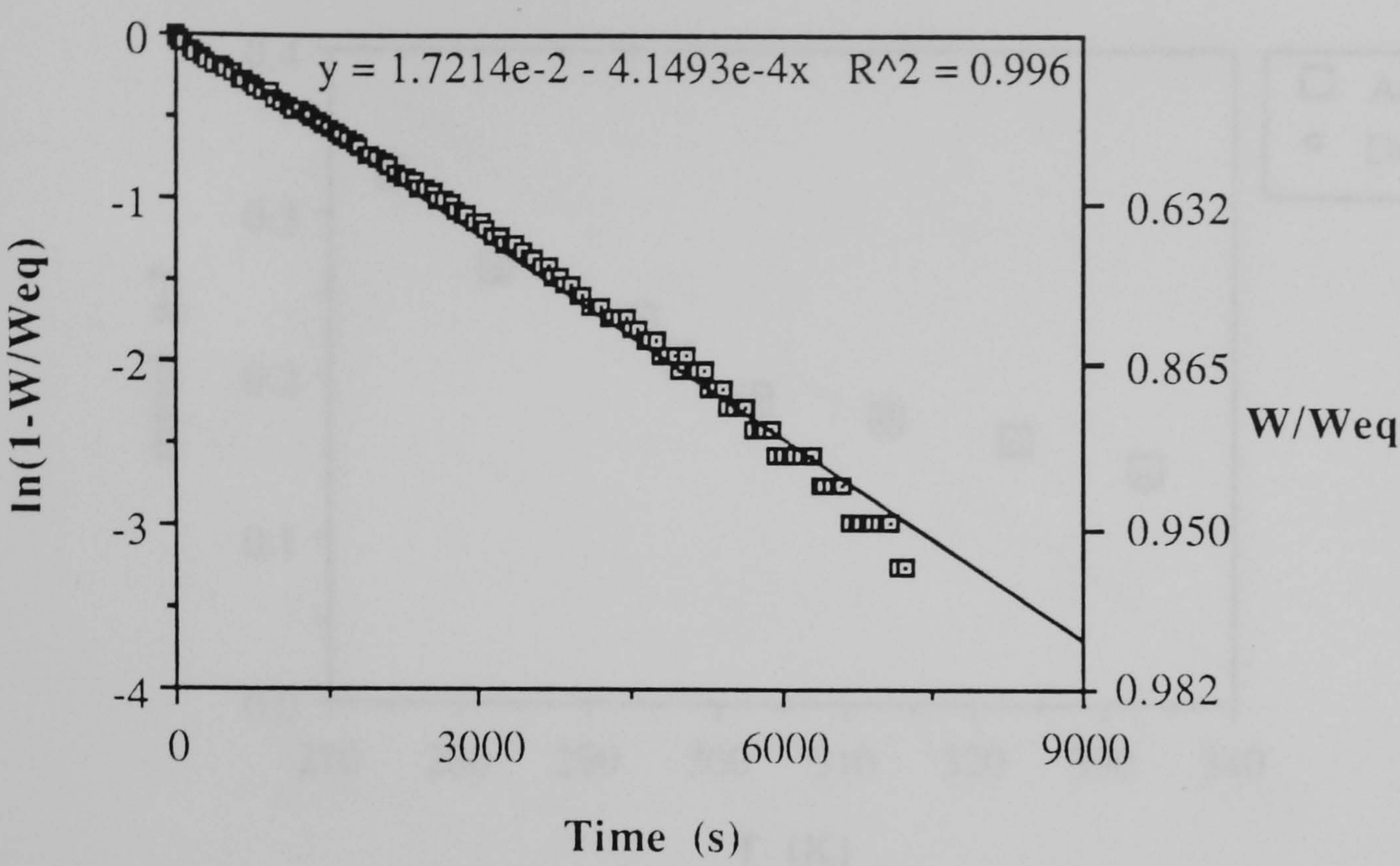

Figure 5.4 A graph of ln(1-W/Weq) against time for adsorption of argon for CMS A3 at 303 K.

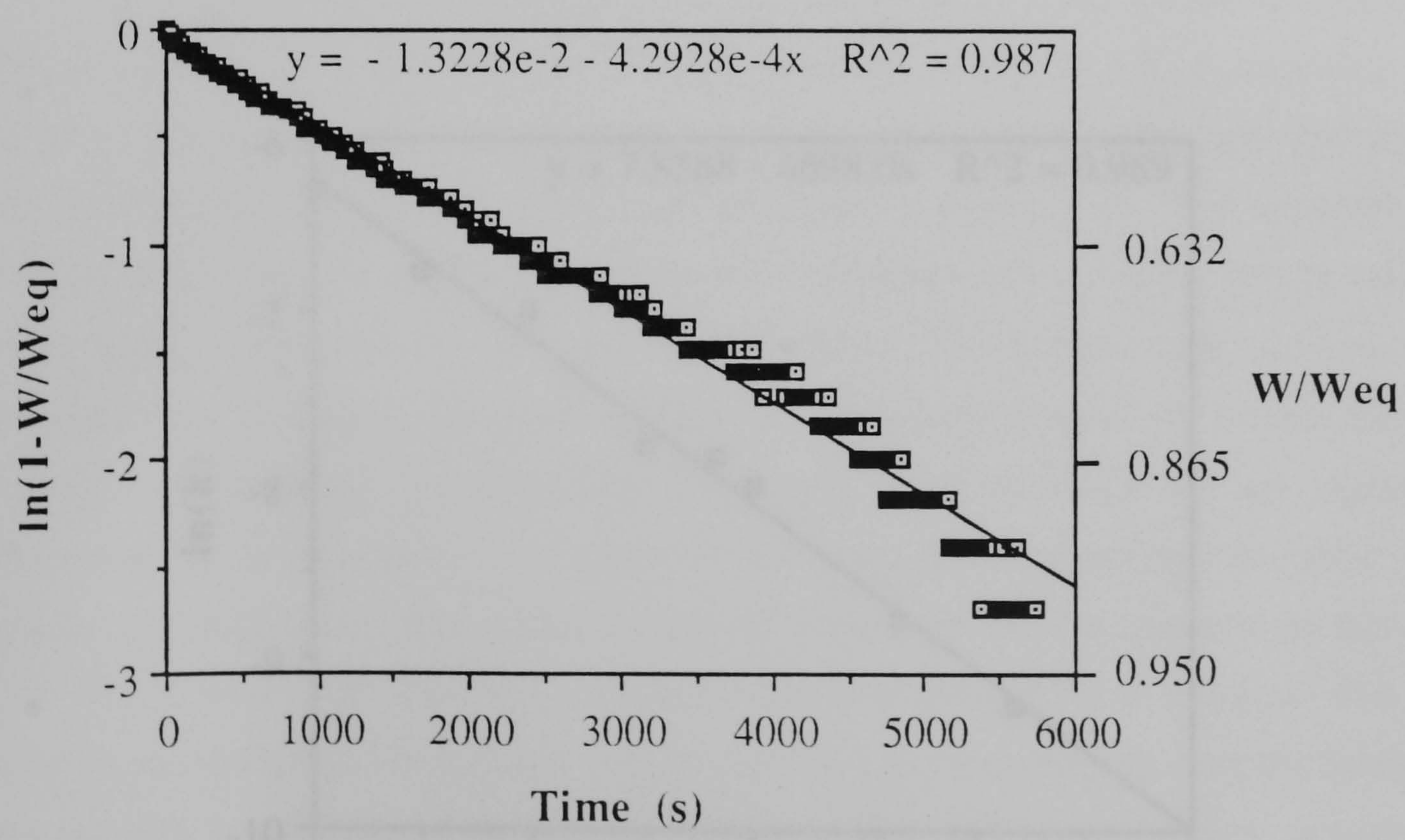

Figure 5.5 A graph of ln(1-W/Weq) against time for desorption of argon for CMS A3 at 303 K.

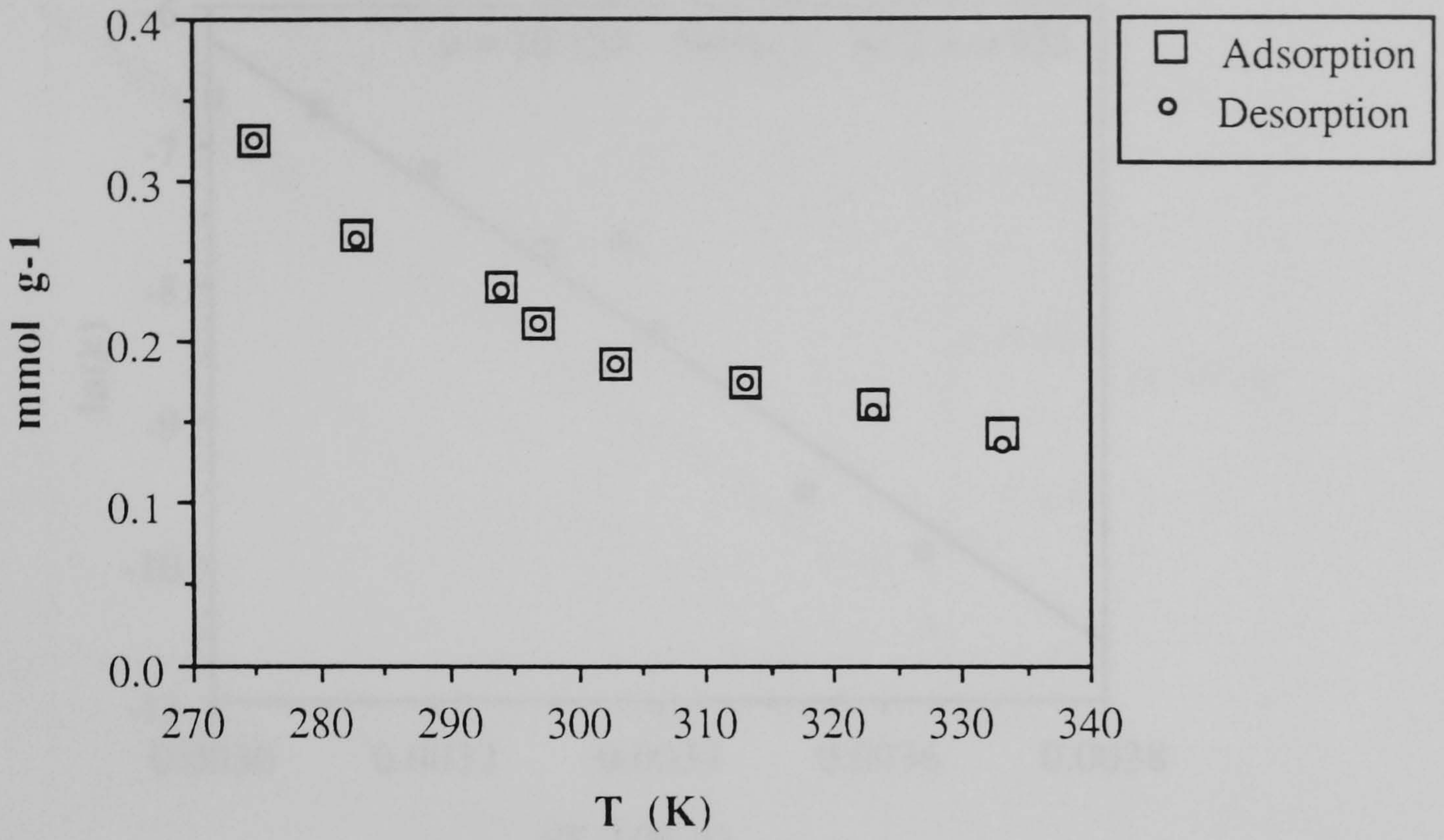

Figure 5.6 A graph of adsorption and desorption capacities of argon against increasing temperature for CMS A3.

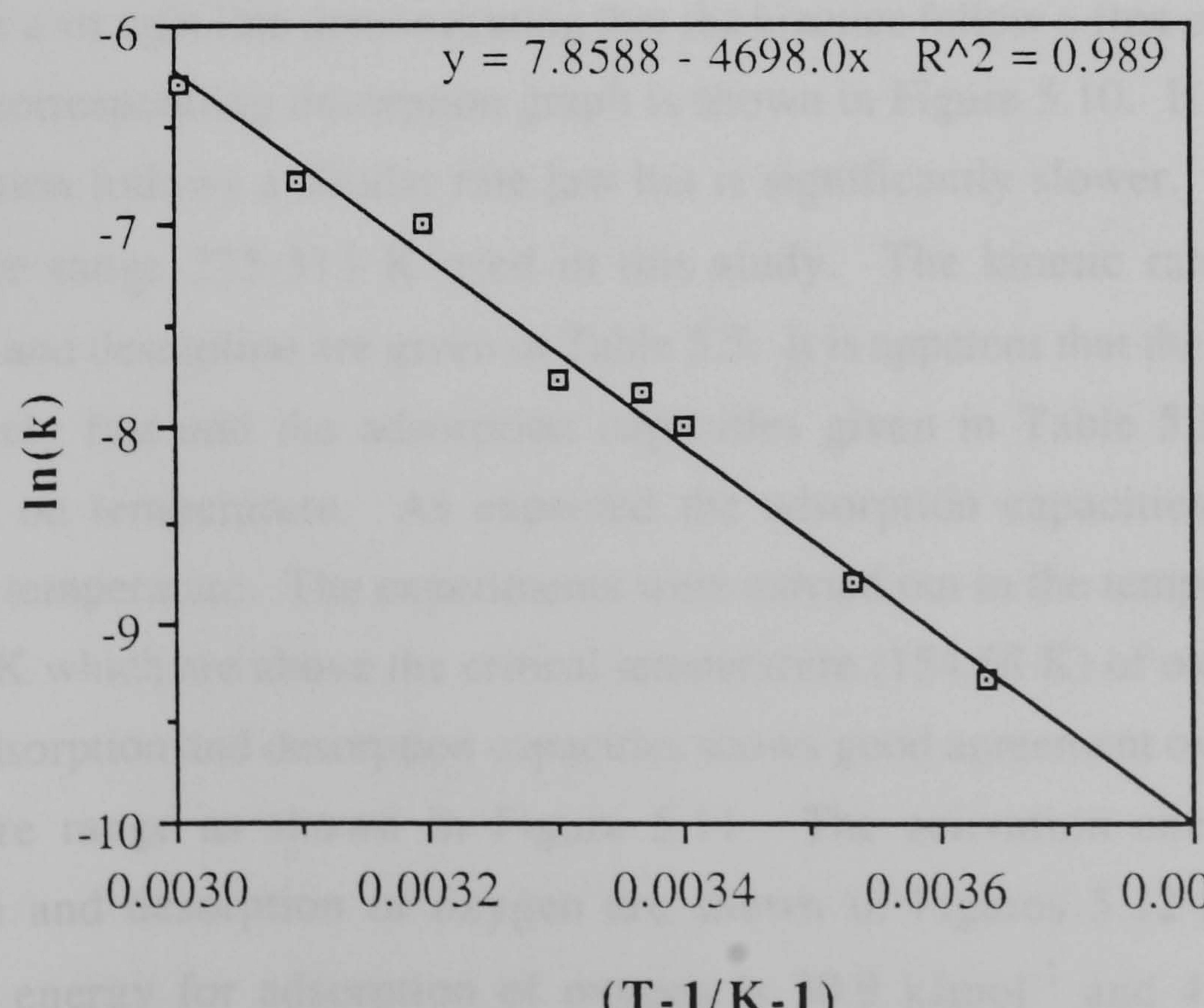

Figure 5.7 Arrhenius graph for adsorption of argon on CMS A3.

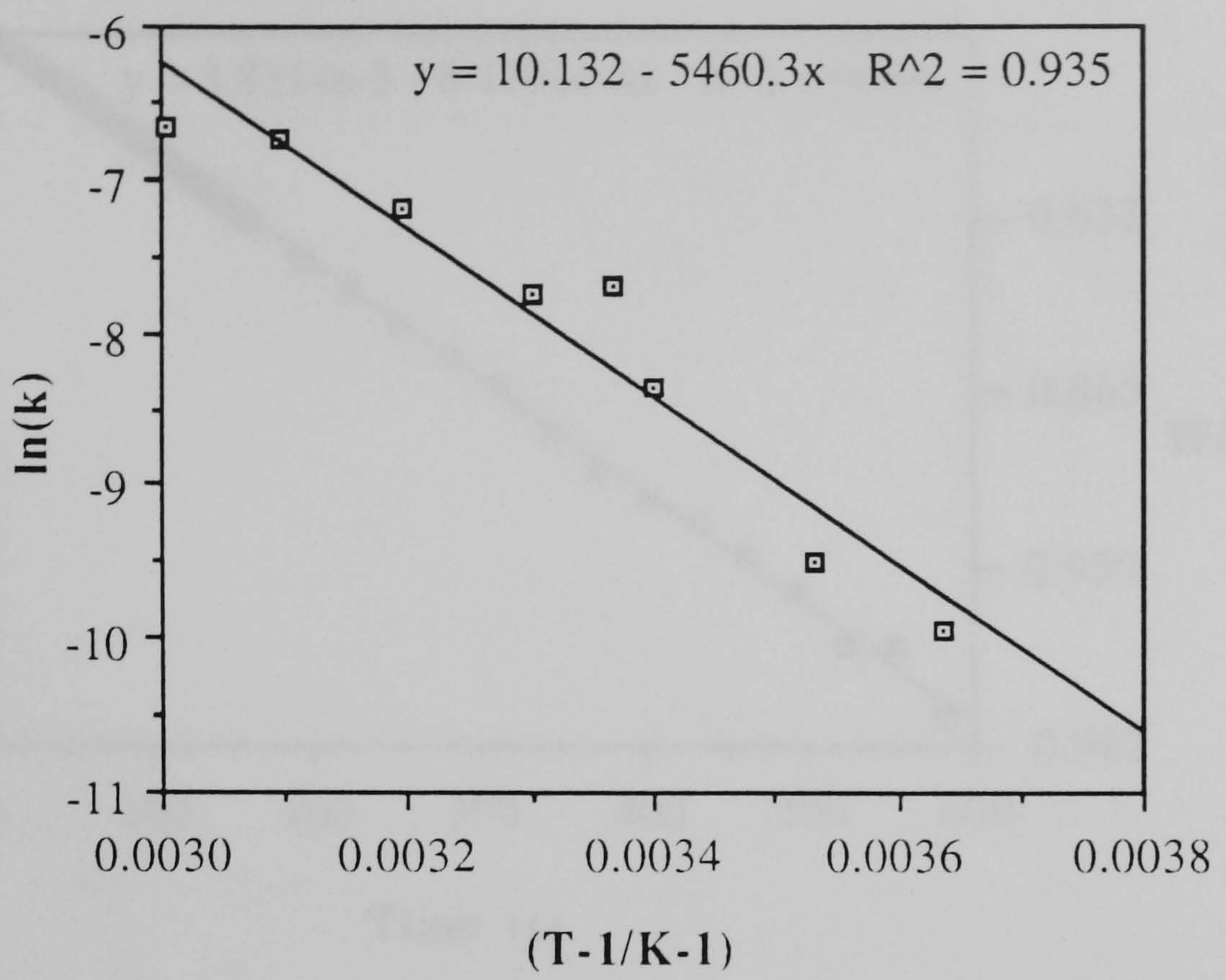

Figure 5.8 Arrhenius graph for desorption of argon on CMS A3.

5.2.2.2 Oxygen adsorption/desorption

A graph of ln(1-W/Weq) against time, where W is mass uptake at time t and Weq is the total mass uptake at equilibrium, is shown in Figure 5.9. It is evident that the graph is a straight line demonstrating that the kinetics follow a first order kinetic rate law. The corresponding desorption graph is shown in Figure 5.10. It is apparent that the desorption follows a similar rate law but is significantly slower. This is true for temperature range 275-313 K used in this study. The kinetic rate constants for adsorption and desorption are given in Table 5.5. It is apparent that the overall kinetics are relatively fast and the adsorption capacities given in Table 5.5 are markedly dependant on temperature. As expected the adsorption capacities decrease with increasing temperature. The experiments were carried out in the temperature range of 275 - 313 K which are above the critical temperarure (154.58 K) of oxygen. The data for both adsorption and desorption capacities shows good agreement over the complete temperature range as shown in Figure 5.11. The activation energy graphs for adsorption and desorption of oxygen are shown in Figures 5.12 and 5.13. The activation energy for adsorption of oxygen is 30.9 kJmol^{-1} and 43.2 kJmol^{-1} for desorption. In comparison there is a change in the pre-exponential factor from 3905 s^{-1} for adsorption to 369535 s^{-1} for desorption.

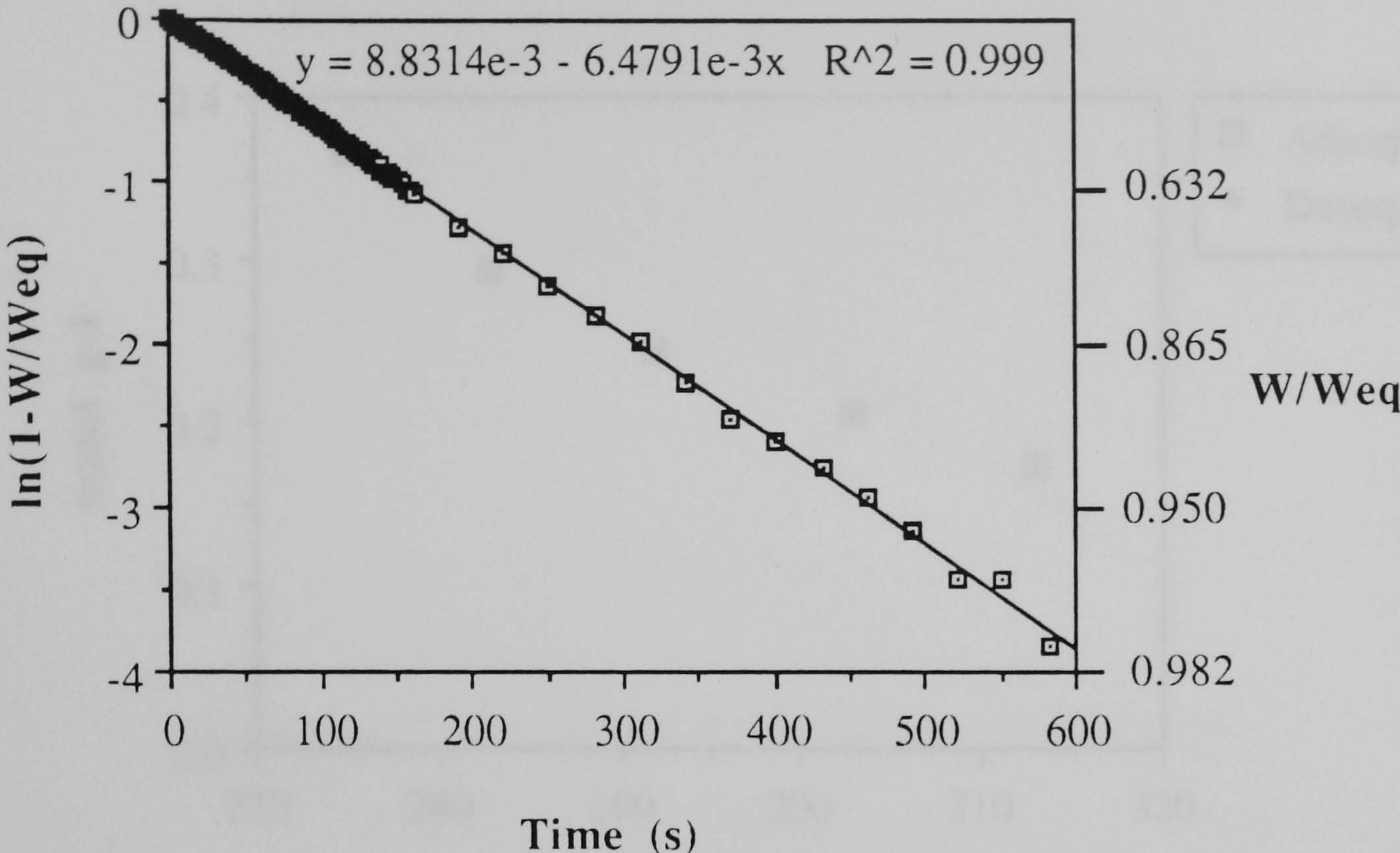

Figure 5.9 The variation of ln(1-W/Weq) against time for adsorption of oxygen for CMS A3 at 283 K.

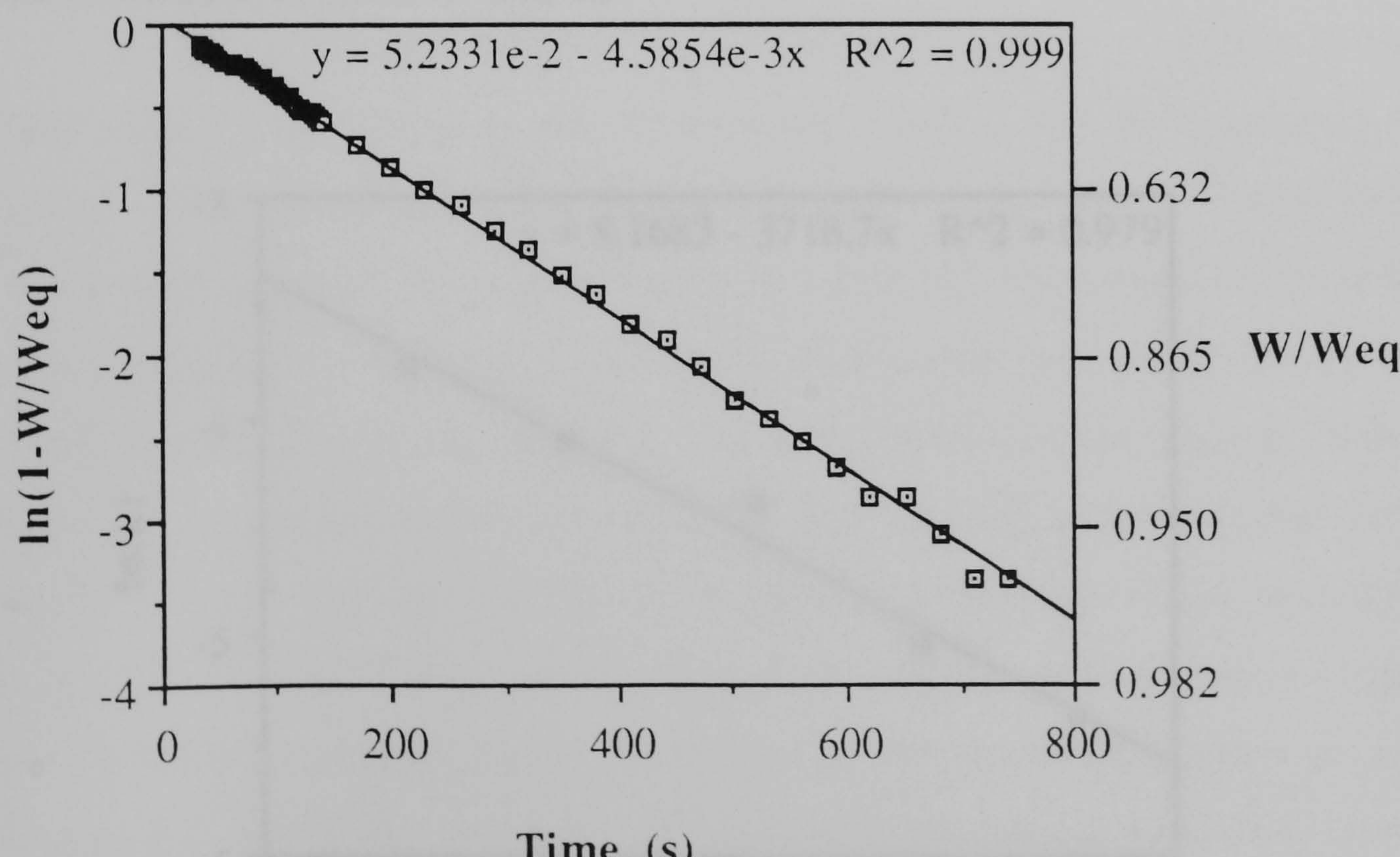

Figure 5.10 The variation of ln(1-W/Weq) against time for desorption of oxygen for CMS A3 at 283 K.

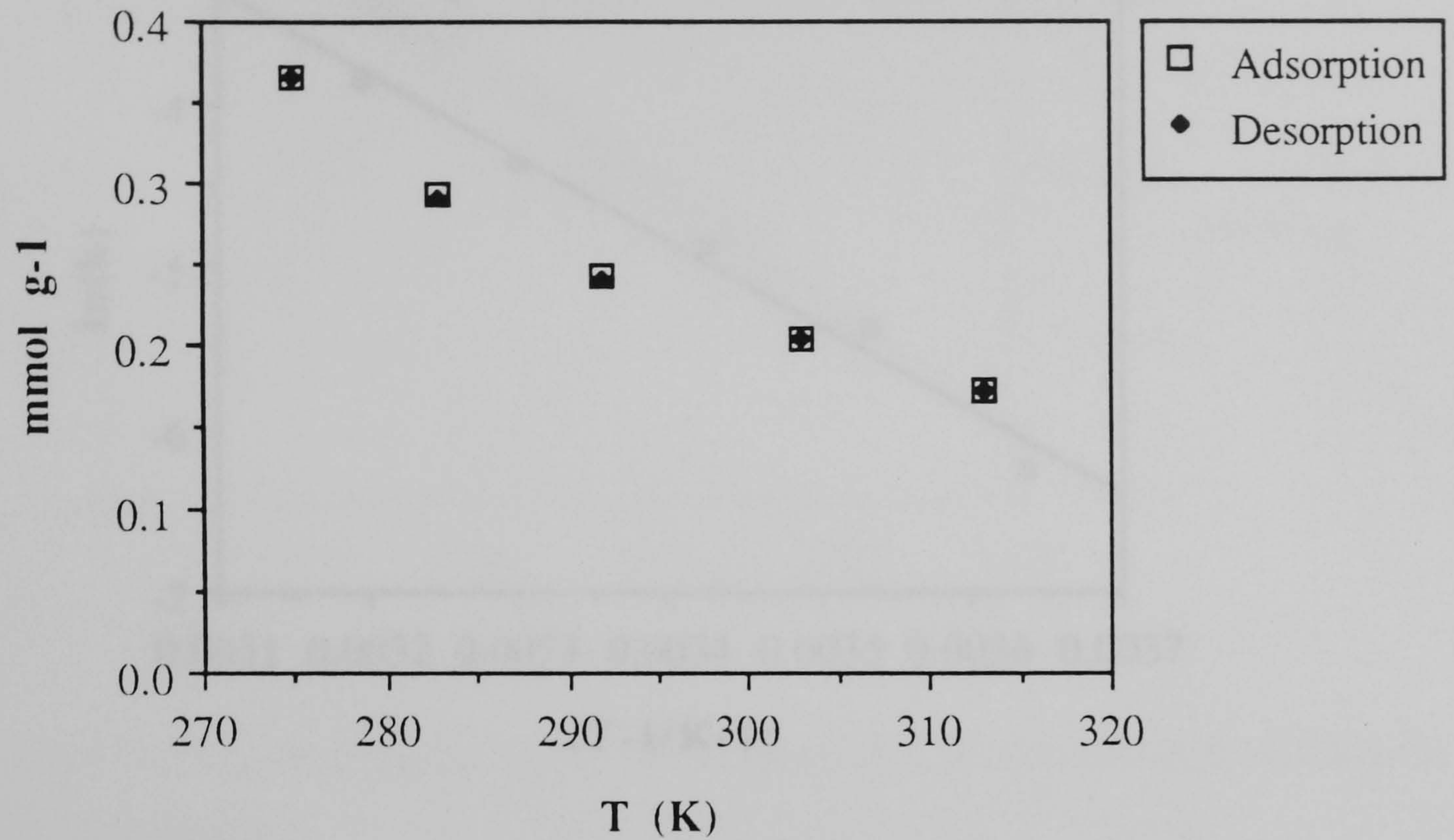

Figure 5.11 A graph of adsorption and desorption capacities of oxygen against increasing temperature for CMS A3.

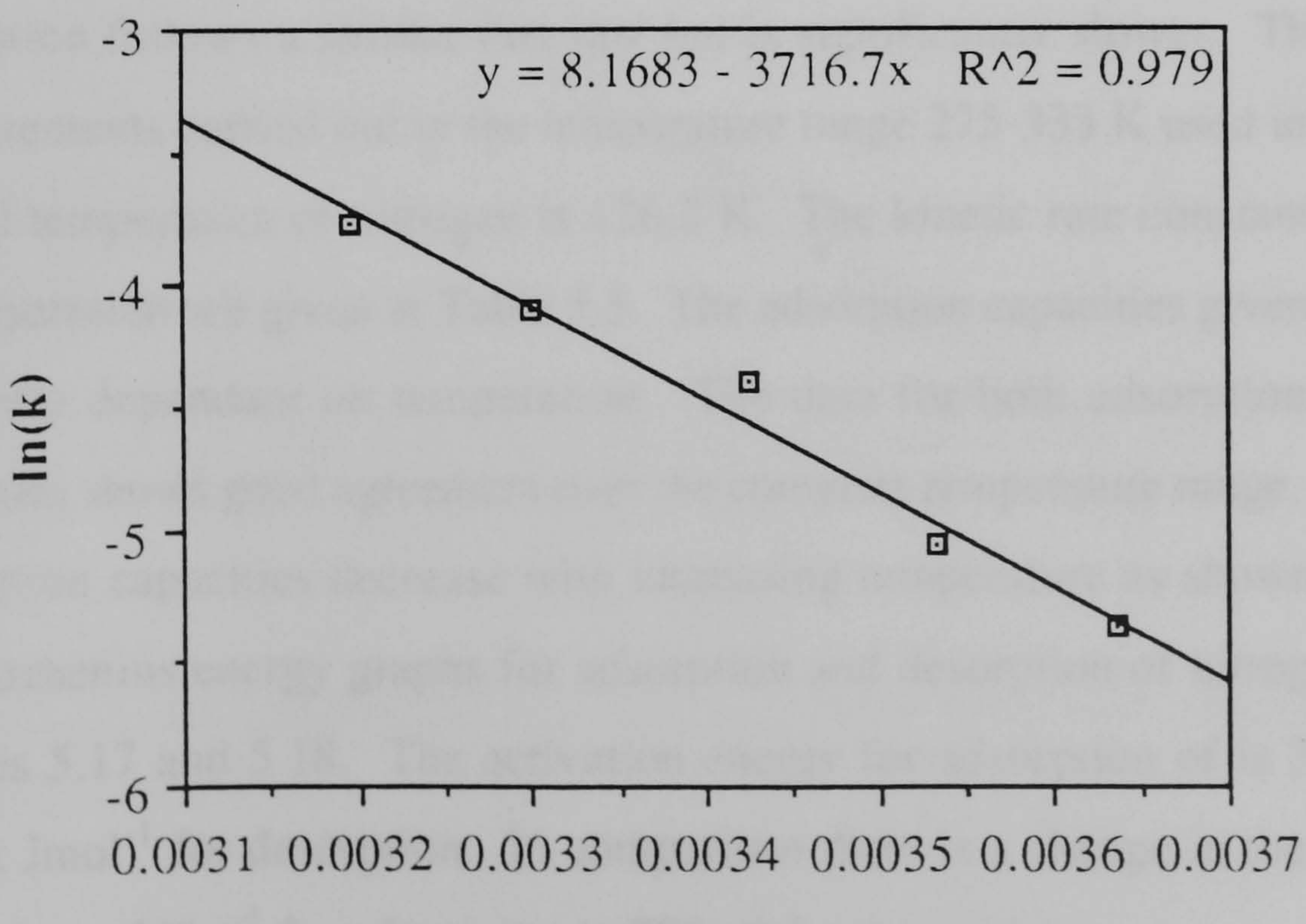

Figure 5.12 Arrhenius graph for adsorption of oxygen on CMS A3.

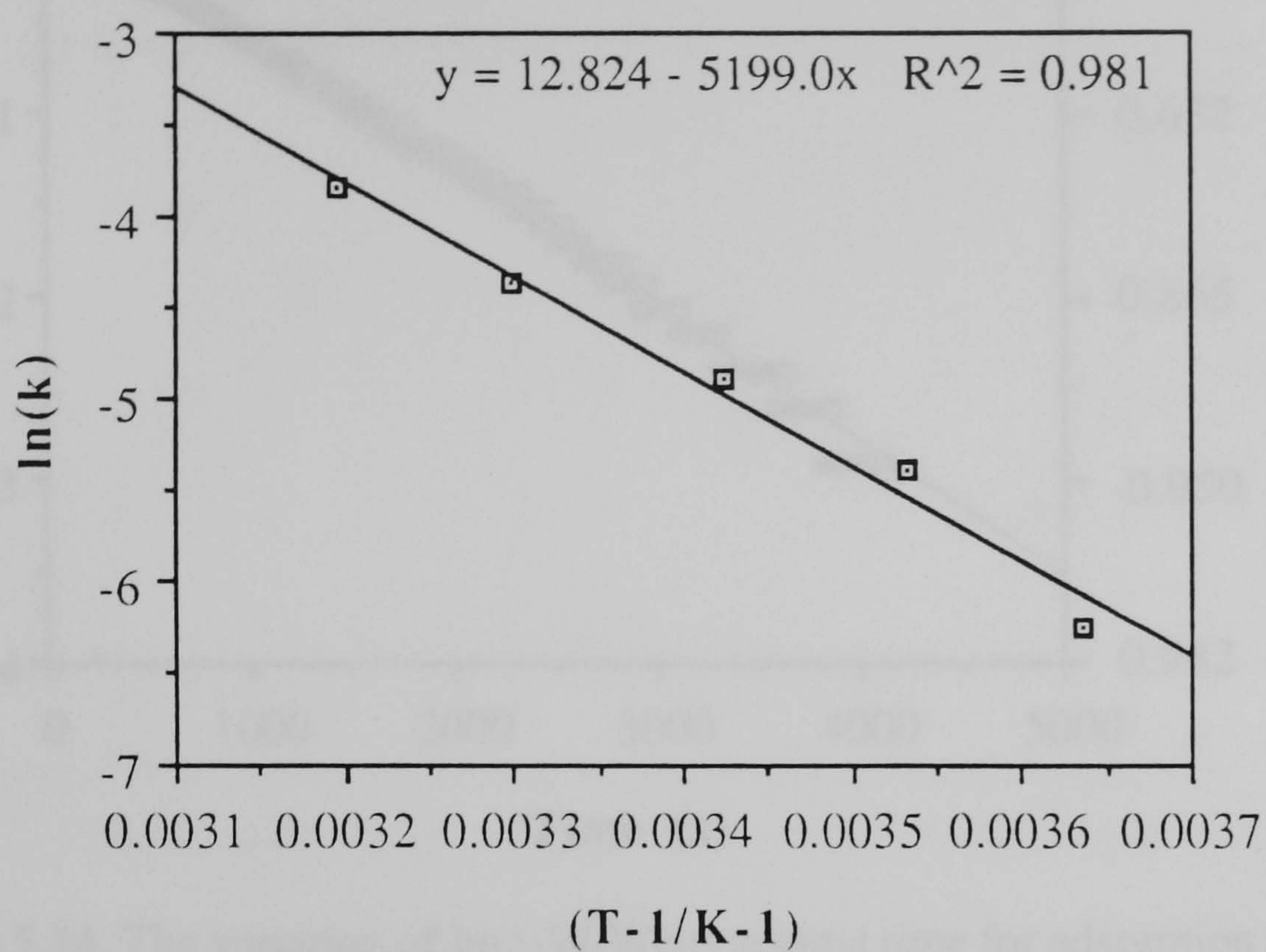

Figure 5.13 Arrhenius graph for desorption of oxygen on CMS A3.

5.2.2.3 Nitrogen adsorption/desorption

A graph of ln(1-W/Weq) against time, is shown in Figure 5.14. The corresponding desorption graph is shown in Figure 5.15. It is apparent that the desorption follows a similar rate law but is significantly slower. This is true for all measurements carried out in the temperature range 275-333 K used in this study. The critical temperature of nitrogen is 126.2 K. The kinetic rate constants for adsorption and desorption are given in Table 5.5. The adsorption capacities given in Table 5.5 are markedly dependant on temperature. The data for both adsorption and desorption capacities shows good agreement over the complete temperature range. As expected the adsorption capacities decrease with increasing temperature as shown in Figure 5.16. The Arrhenius energy graphs for adsorption and desorption of nitrogen are shown in Figures 5.17 and 5.18. The activation energy for adsorption of is 34.6 $kJmol^{-1}$ and 36.3 k $Jmol^{-1}$ for desorption. In comparison there is a change in the pre-exponential factor from 646 s^{-1} for adsorption to 796 s^{-1} for desorption.

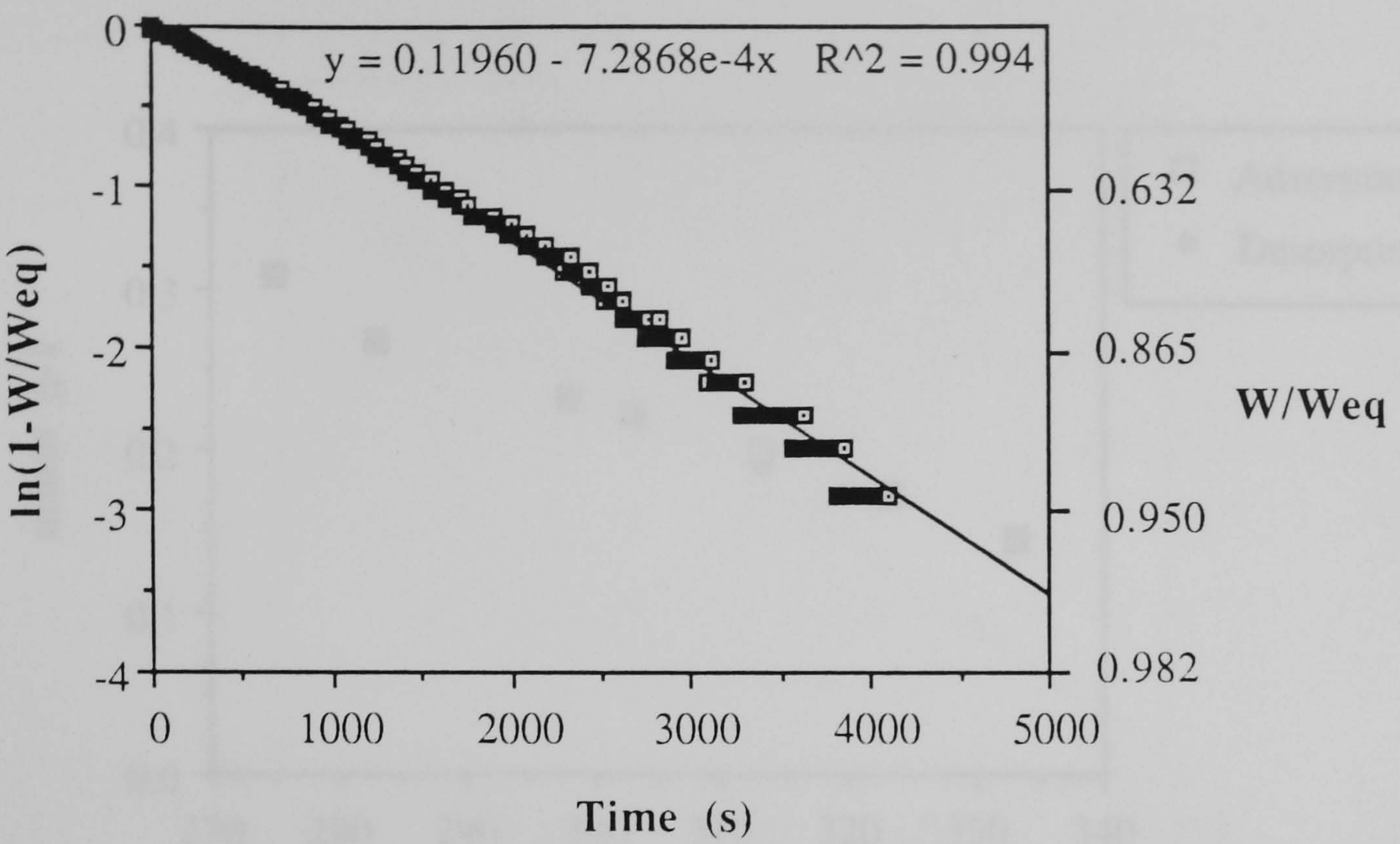

Figure 5.14 The variation of ln(1-W/Weq) against time for adsorption of nitrogen for CMS A3 at 303 K.

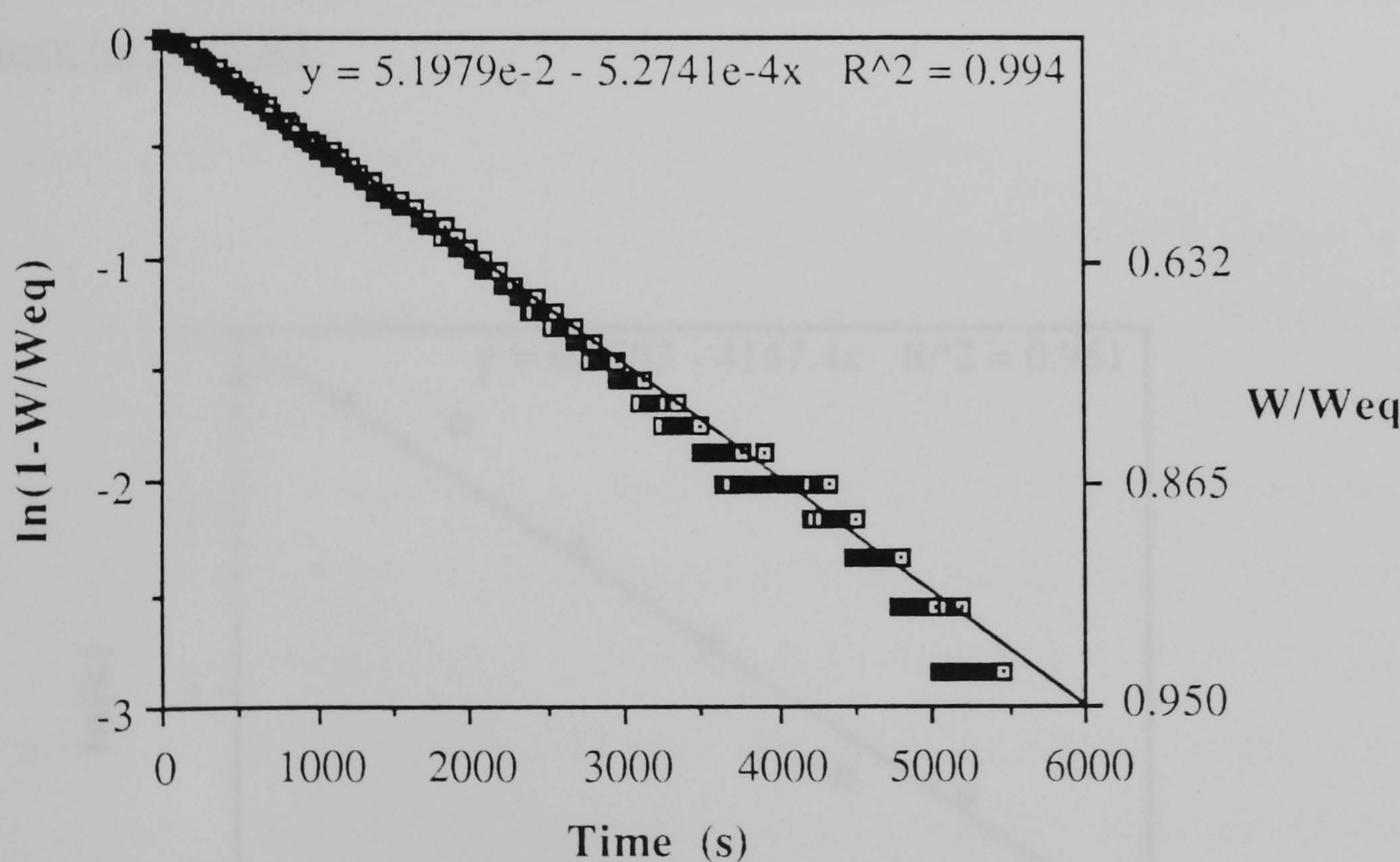

Figure 5.15 The variation of ln(1-W/Weq) against time for desorption of nitrogen for CMS A3 at 303 K.

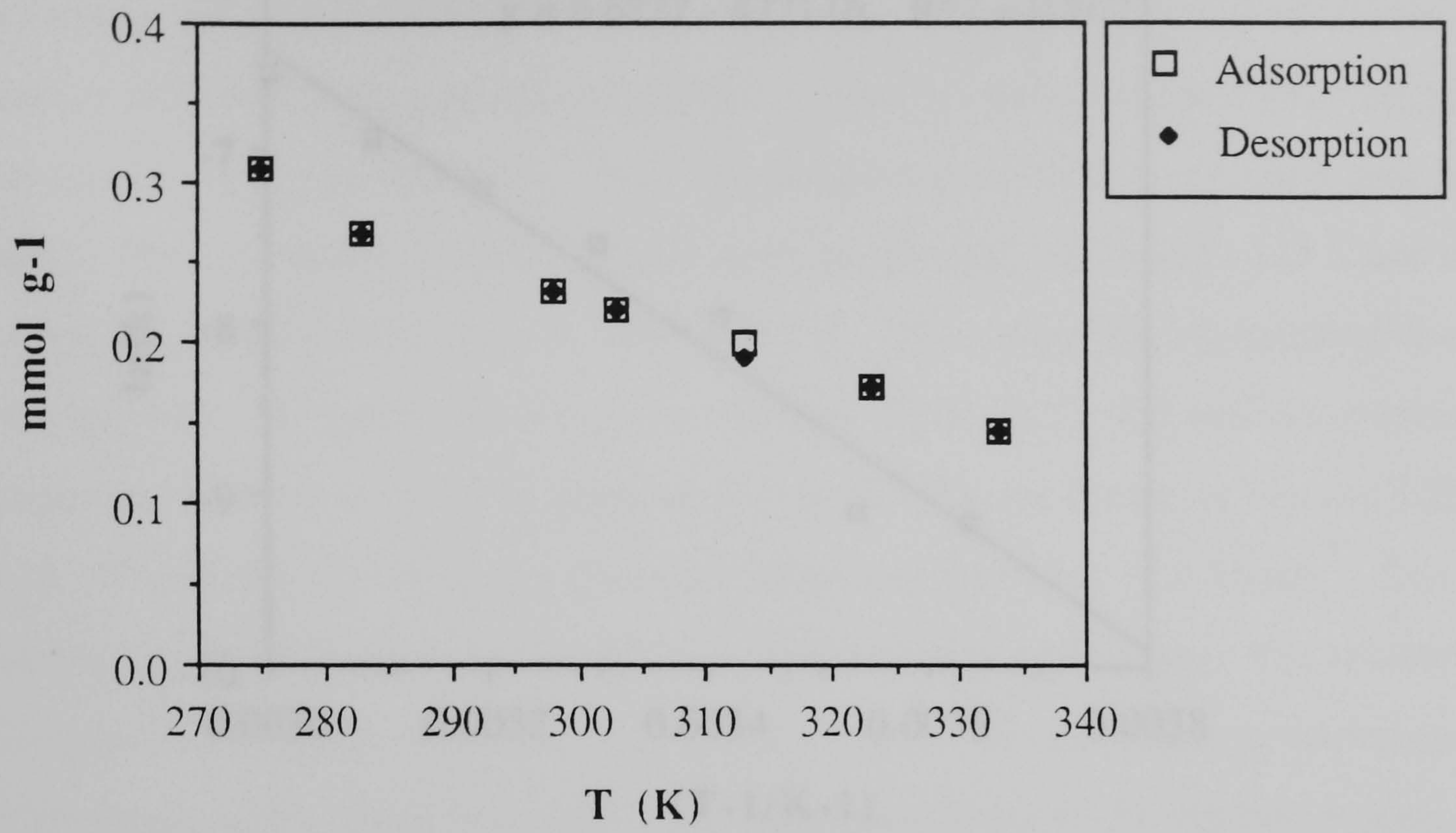

Figure 5.16 A graph of adsorption and desorption capacities of nitrogen against increasing temperature for CMS A3.

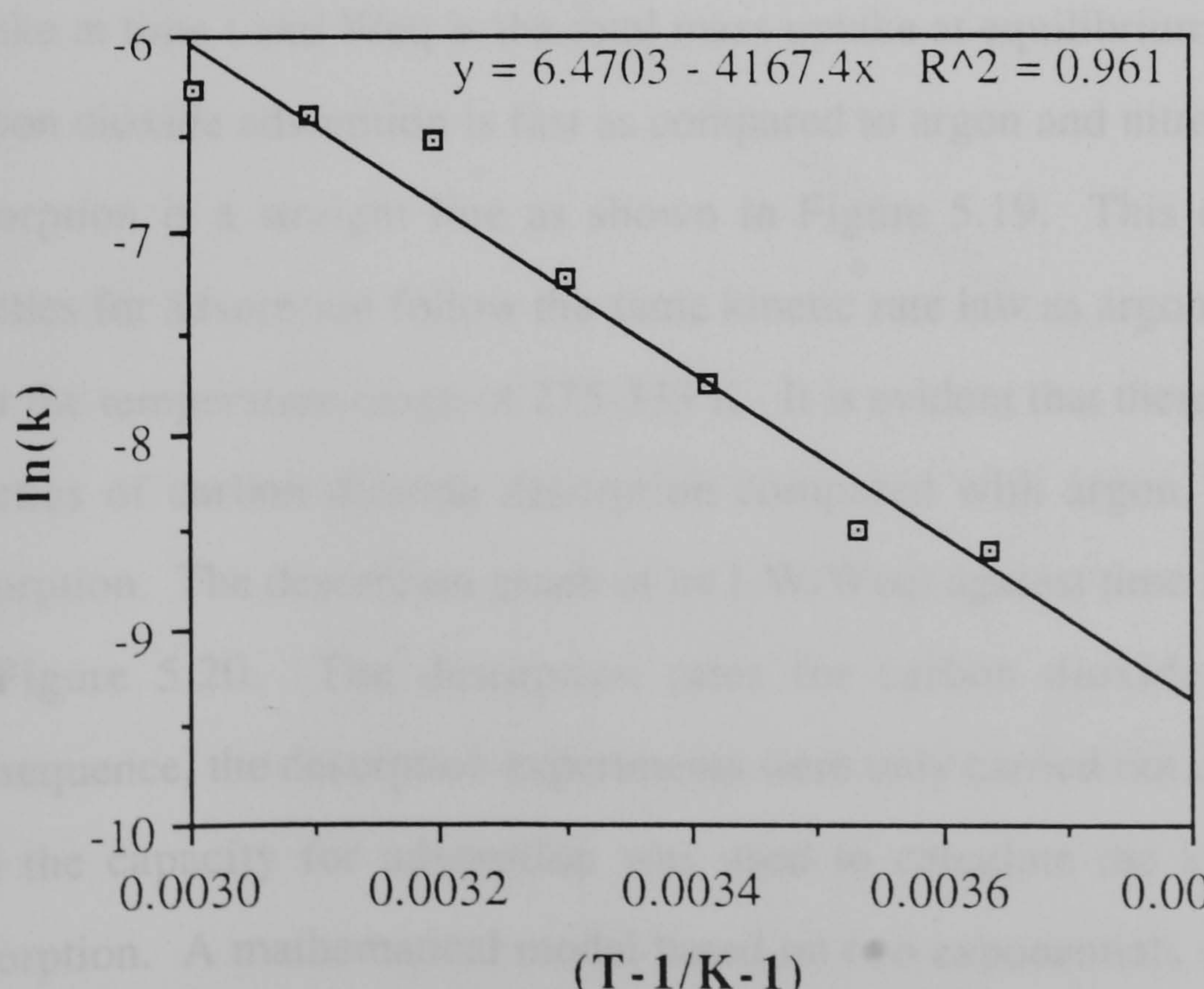

Figure 5.17 Arrhenius graph for adsorption of nitrogen on CMS A3.

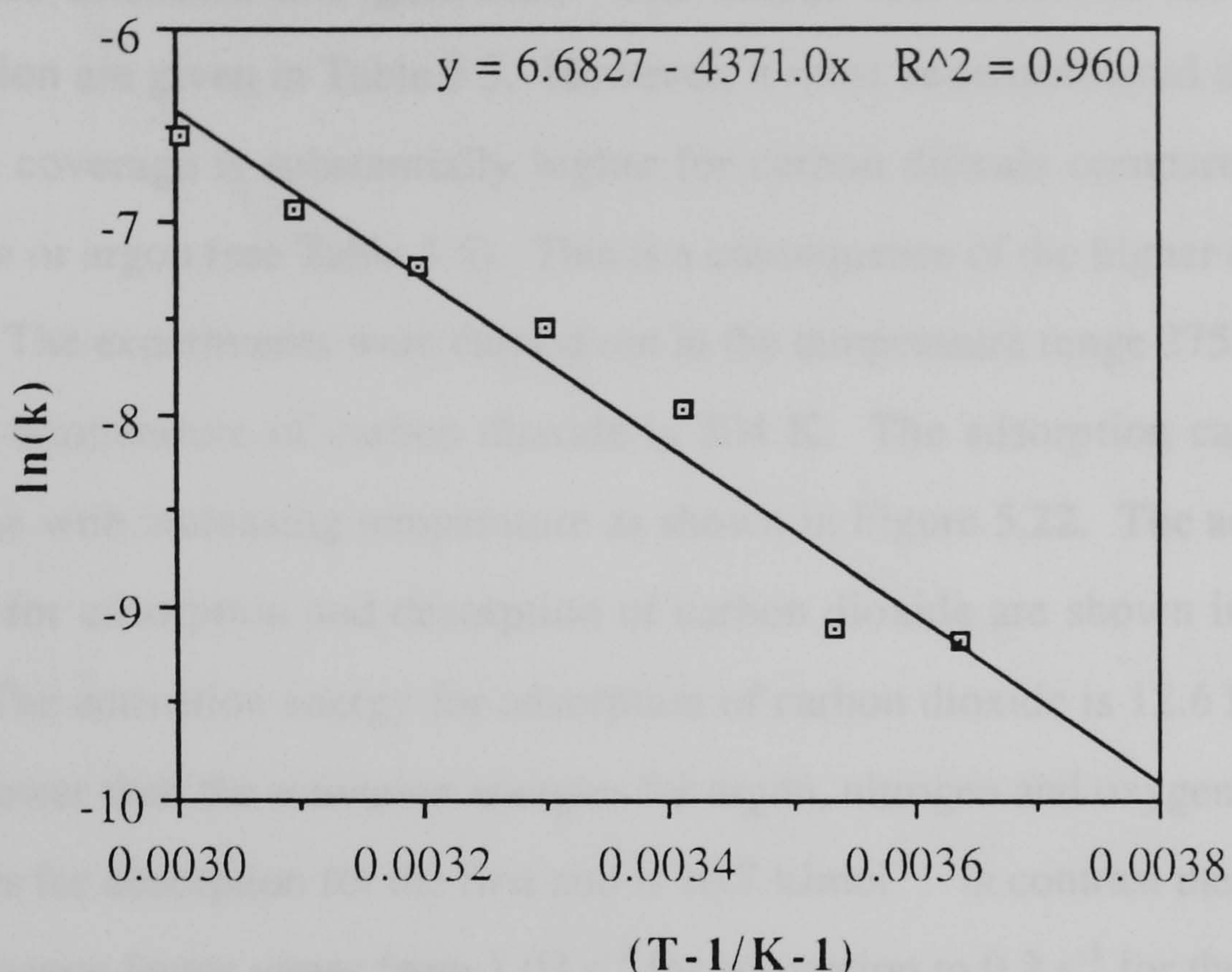

Figure 5.18 Arrhenius graph for desorption of nitrogen on CMS A3.

5.2.2.4 Carbon dioxide adsorption/desorption

Figure 5.19 shows a graph of ln(1-W/Weq) against time, where W is mass uptake at time t and Weq is the total mass uptake at equilibrium. The overall rate for carbon dioxide adsorption is fast as compared to argon and nitrogen and the graph for adsorption is a straight line as shown in Figure 5.19. This demonstrates that the kinetics for adsorption follow the same kinetic rate law as argon, oxygen and nitrogen over the temperature range of 275-333 K. It is evident that there are differences in the kinetics of carbon dioxide desorption compared with argon, oxygen and nitrogen desorption. The desorption graph of ln(1-W/Weq) against time is non-linear as shown in Figure 5.20. The desorption rates for carbon dioxide are slow, and as a consequence, the desorption experiments were only carried out until > 90% desorption and the capacity for adsorption was used to calculate the kinetic parameters for desorption. A mathematical model based on two exponentials of the form W/Weq = $A_1 e^{-k_1T} + A_2 e^{-k_2T}$ was fitted to the experimental data of fractional mass loss against time, where W is the mass desorbed at time t and Weq is the total mass desorbed at equilibrium, in order to obtain rate constants for fast k_1 and slow k_2 desorption processes as shown in Figure 5.21. The kinetic rate constants for adsorption and desorption are given in Table 5.5. However, it must be remembered that the extent of surface coverage is substantially higher for carbon dioxide compared with oxygen, nitrogen or argon (see Table 5.5). This is a consequence of the higher relative pressure (p/p_o). The experiments were carried out in the temperature range 275 - 333 K and the critical temperature of carbon dioxide is 304 K. The adsorption capacities show a decrease with increasing temperature as shown in Figure 5.22. The activation energy graphs for adsorption and desorption of carbon dioxide are shown in Figures 5.23 - 5.24. The activation energy for adsorption of carbon dioxide is 12.6 $kJmol^{-1}$. This is much lower than the activation energies for argon, nitrogen and oxygen. The activation energies for desorption for the first and is 10.7 $kJmol^{-1}$. In contrast the pre-exponential or frequency factor varies from 1.03 s^{-1} for adsorption to 0.2 s^{-1} for the first process of desorption.

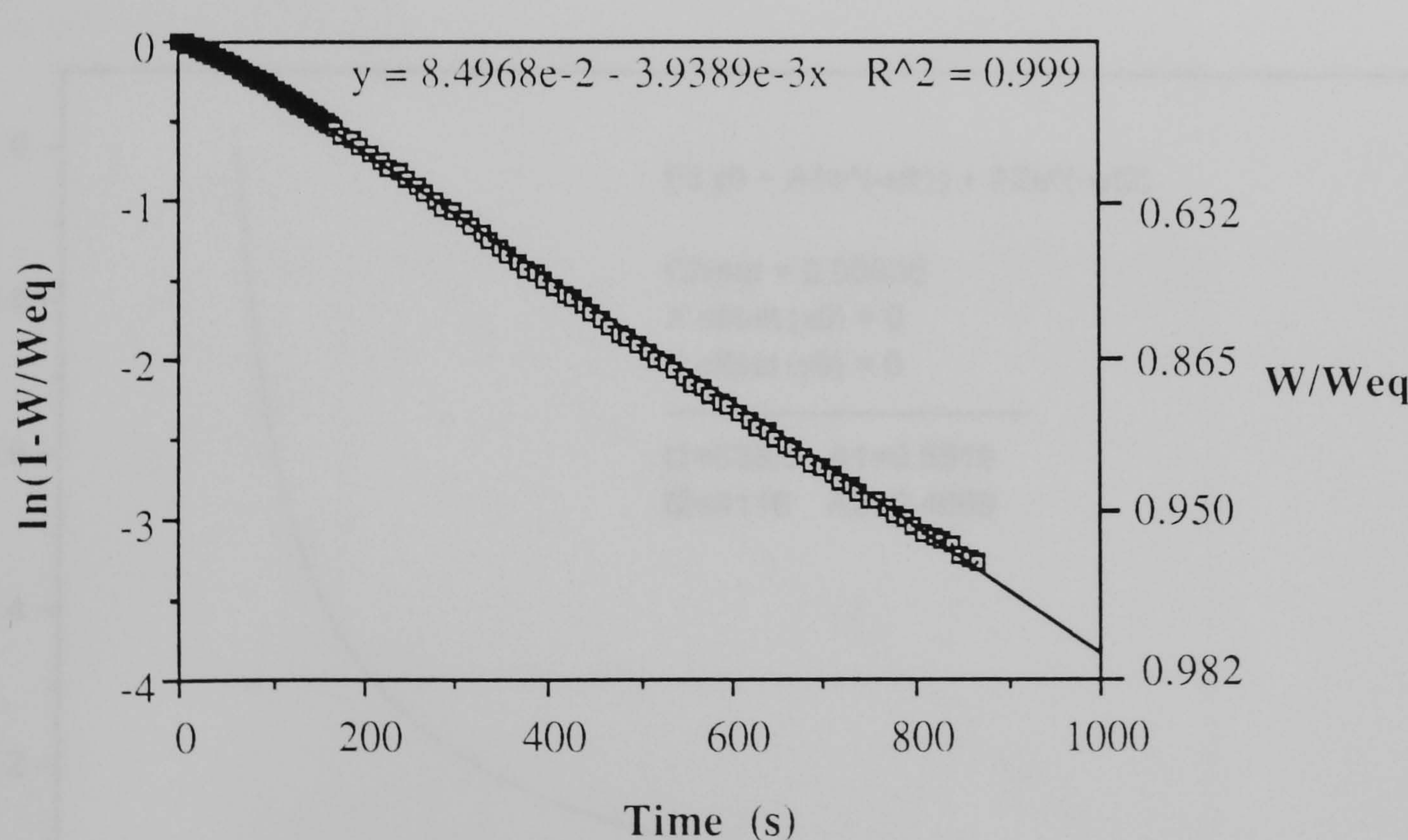

Figure 5.19 A graph of ln(1-W/Weq) against time for adsorption of carbon dioxide for CMS A3 at 275 K.

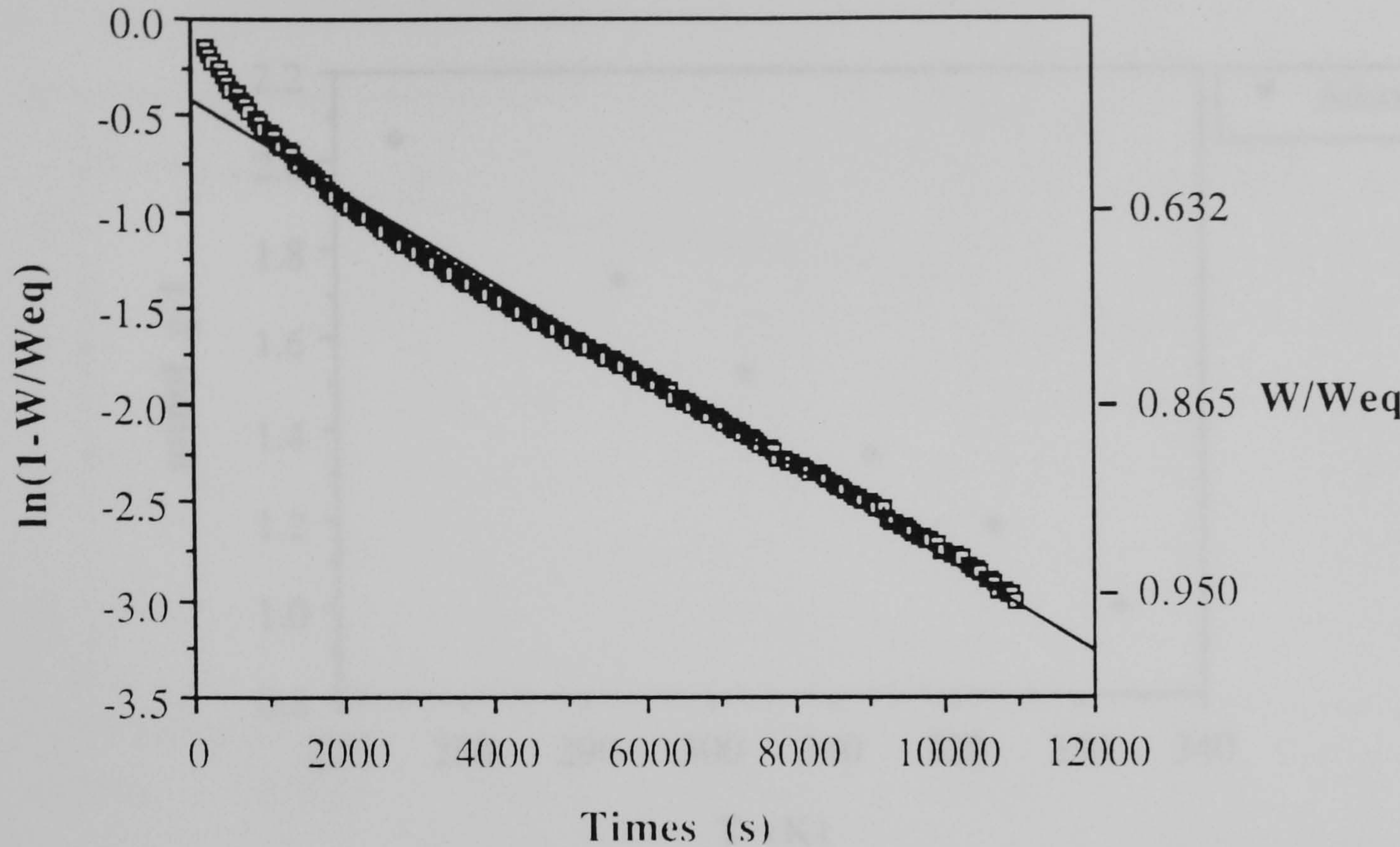

Figure 5.20 A graph of ln(1-W/Weq) against time for desorption of carbon dioxide for CMS A3 at 275 K.

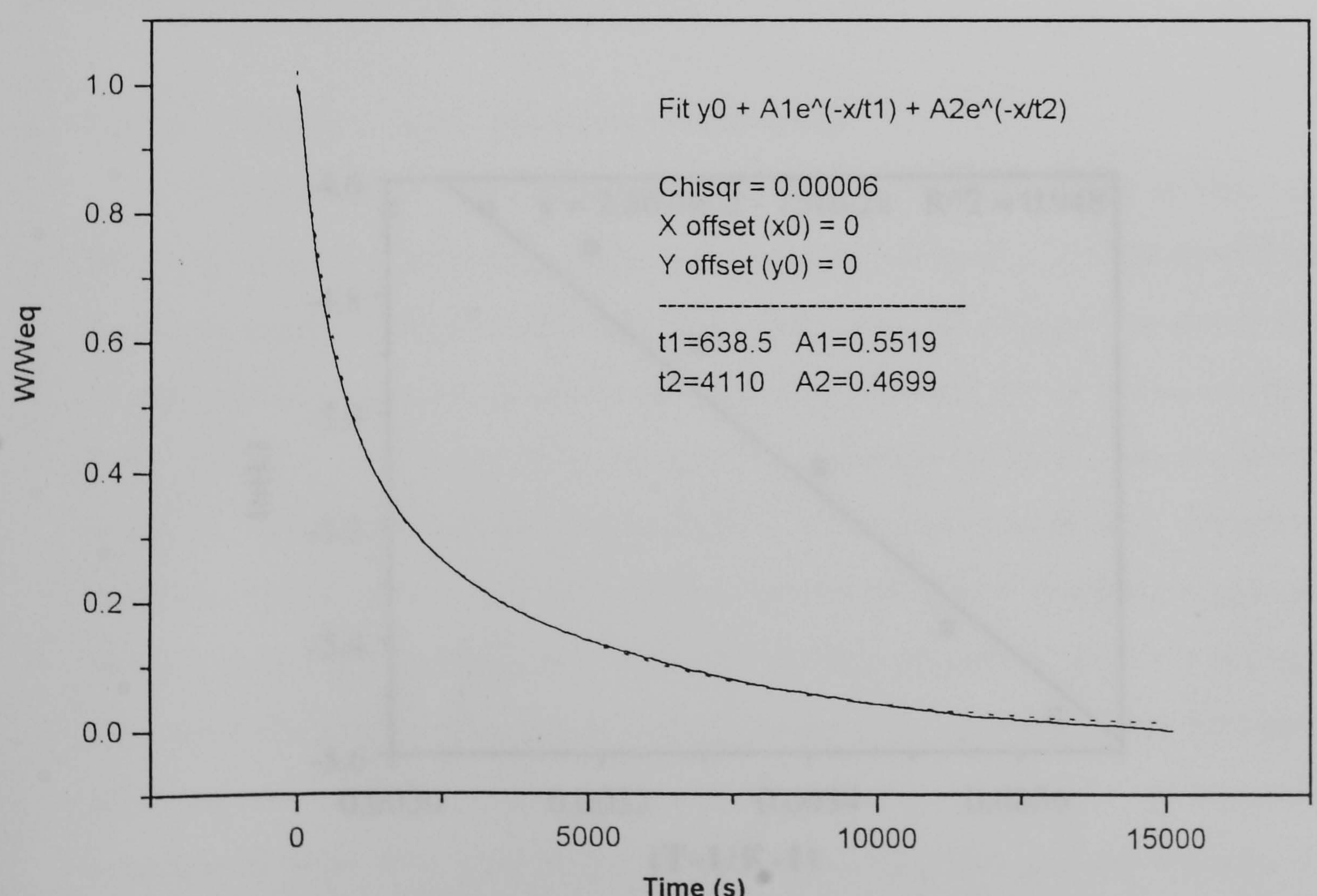

Figure 5.21 A graph of W/Weq against time for desorption of carbon dioxide for CMS A3 at 275 K.

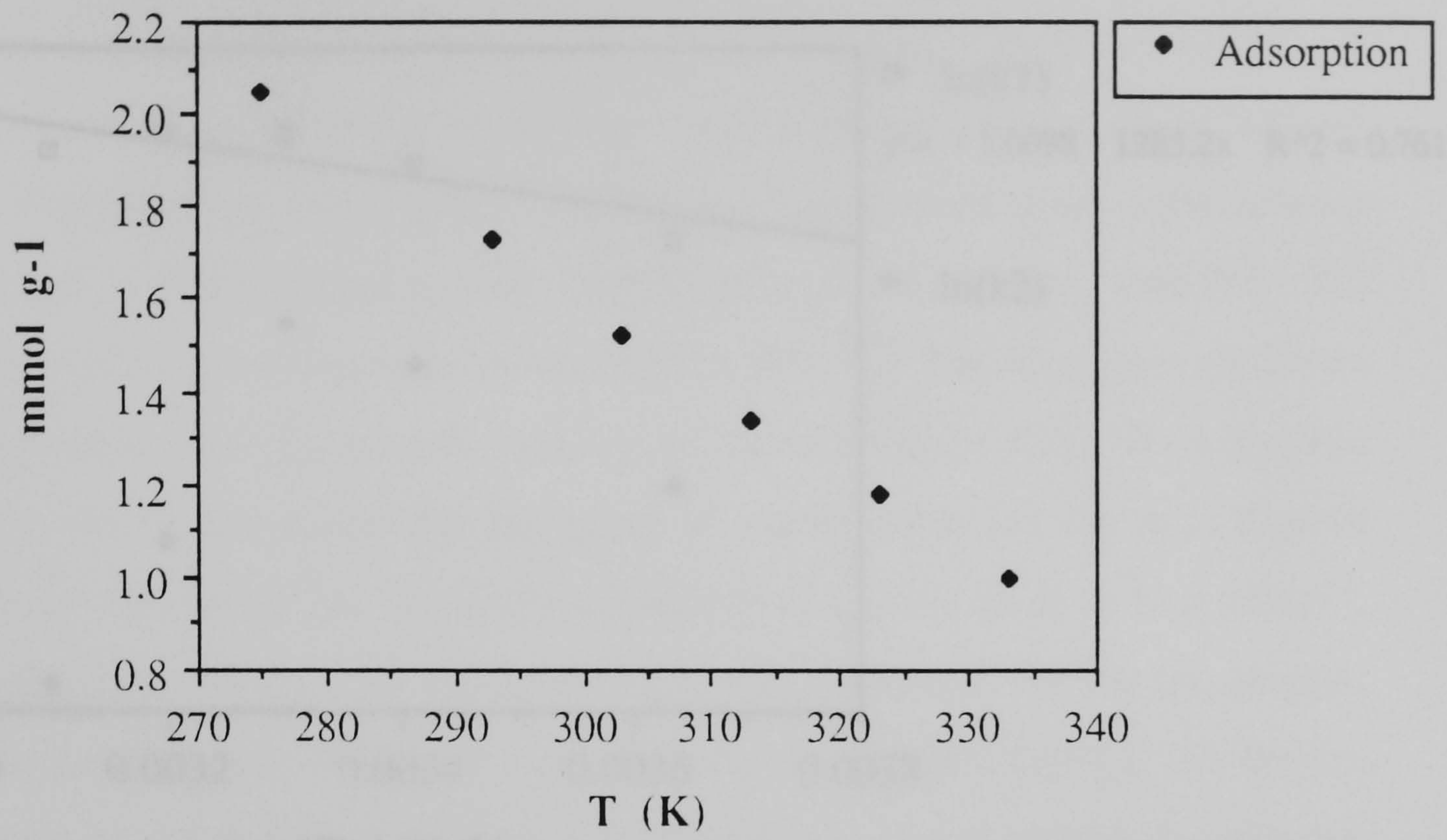

Figure 5.22 A graph of adsorption capacities of carbon dioxide against increasing temperature for CMS A3.

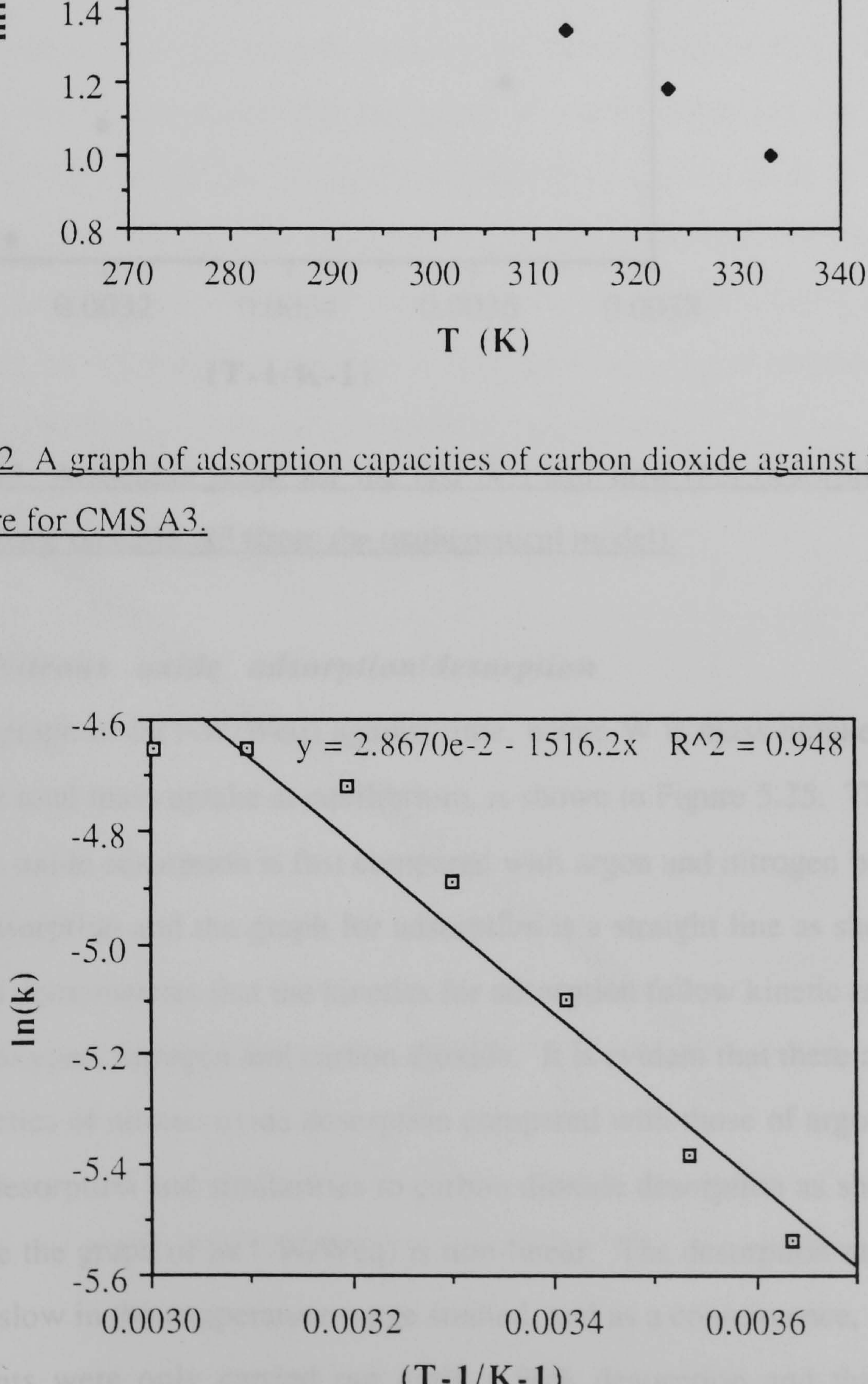

Figure 5.23 Arrhenius graph for adsorption of carbon dioxide on CMS A3.

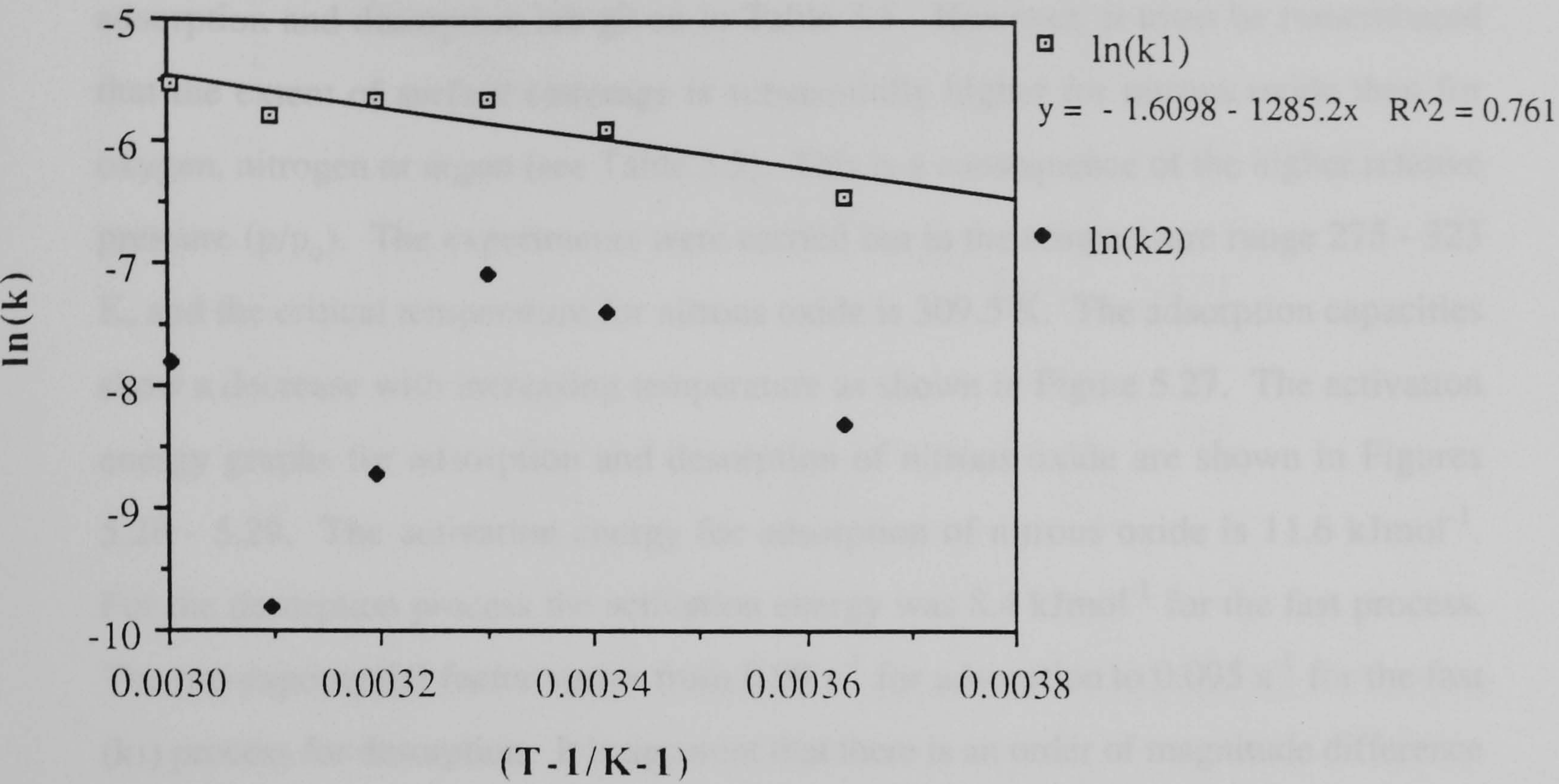

Figure 5.24 Arrhenius graph for the fast (k_1) and slow (k_2) desorption processes of carbon dioxide on CMS A3 (from the mathematical model).

5.2.2.5 Nitrous oxide adsorption/desorption

A graph of ln(1-W/Weq) against time, where W is mass uptake at time t and Weq is the total mass uptake at equilibrium, is shown in Figure 5.25. The overall rate for nitrous oxide adsorption is fast compared with argon and nitrogen but slower than oxygen adsorption and the graph for adsorption is a straight line as shown in Figure 5.25. This demonstrates that the kinetics for adsorption follow kinetic rate law similar to argon, oxygen, nitrogen and carbon dioxide. It is evident that there are differences in the kinetics of nitrous oxide desorption compared with those of argon, oxygen and nitrogen desorption and similarities to carbon dioxide desorption as shown in Figure 5.26, since the graph of ln(1-W/Weq) is non-linear. The desorption rates for nitrous oxide are slow in the temperature range studied, and as a consequence, the desorption experiments were only carried out until > 90% desorption and the capacity for adsorption used to calculate the kinetic parameters for desorption. A mathematical model based on two exponentials was fitted to a graph of fractional mass loss against time in order to obtain rate constants for the fast (k1) and slow (k2) desorption processes as carried out previously for carbon dioxide. The kinetic rate constants for adsorption and desorption are given in Table 5.5. However, it must be remembered that the extent of surface coverage is substantially higher for nitrous oxide than for oxygen, nitrogen or argon (see Table 5.5). This is a consequence of the higher relative pressure (p/p_o). The experiments were carried out in the temperature range 275 - 323 K, and the critical temperature for nitrous oxide is 309.5 K. The adsorption capacities show a decrease with increasing temperature as shown in Figure 5.27. The activation energy graphs for adsorption and desorption of nitrous oxide are shown in Figures 5.28 - 5.29. The activation energy for adsorption of nitrous oxide is 11.6 $kJmol^{-1}$. For the desorption process the activation energy was 8.4 $kJmol^{-1}$ for the fast process. The pre-exponential factor varies from 0.99 s^{-1} for adsorption to 0.095 s^{-1} for the fast (k1) process for desorption. It is apparent that there is an order of magnitude difference in the pre-exponential factors for adsorption and desorption.

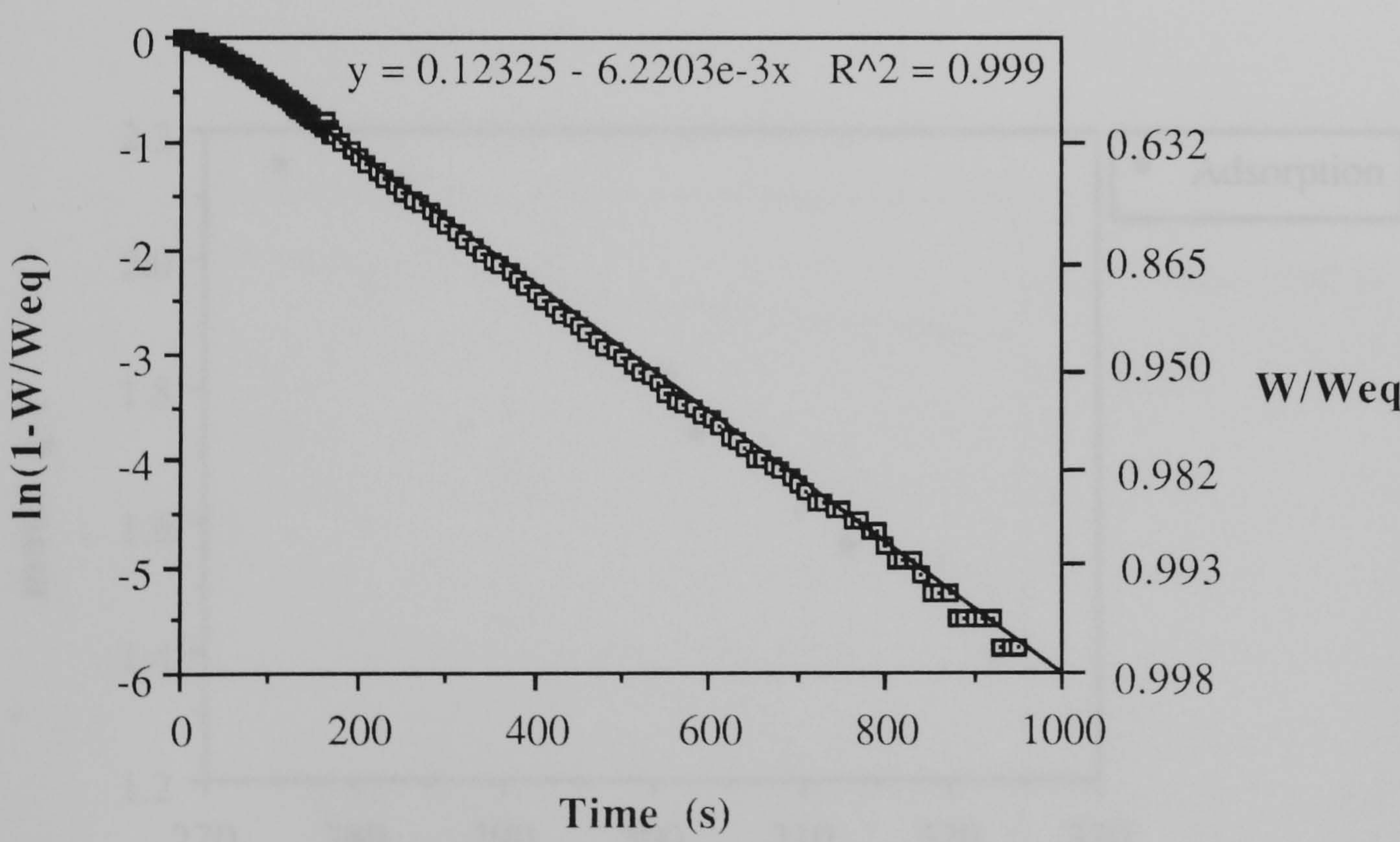

Figure 5.25 A graph of ln(1-W/Weq) for adsorption of nitrous oxide for CMS A3 at 275 K.

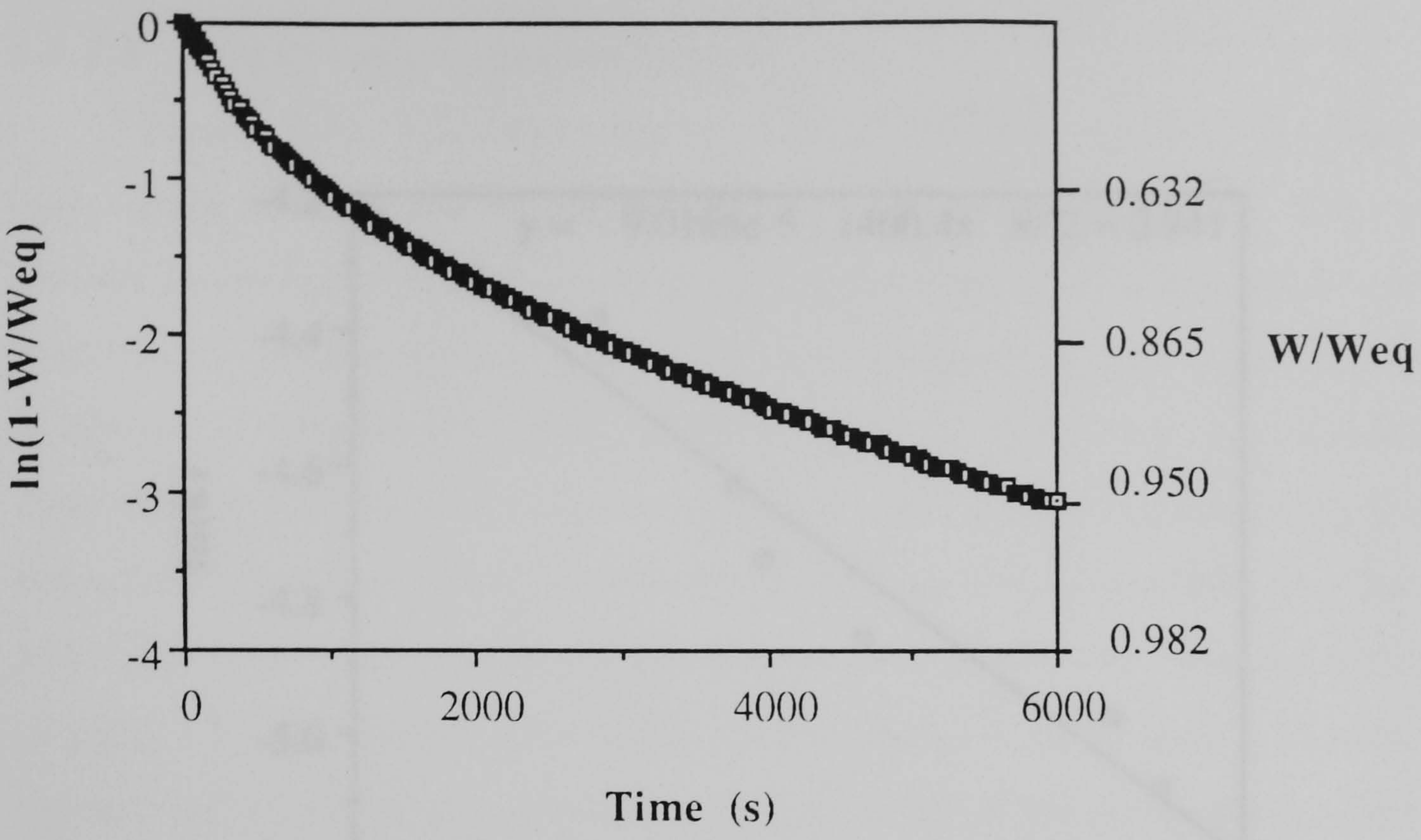

Figure 5.26 A graph of ln(1-W/Weq) for desorption of nitrous oxide for CMS A3 at 275 K.

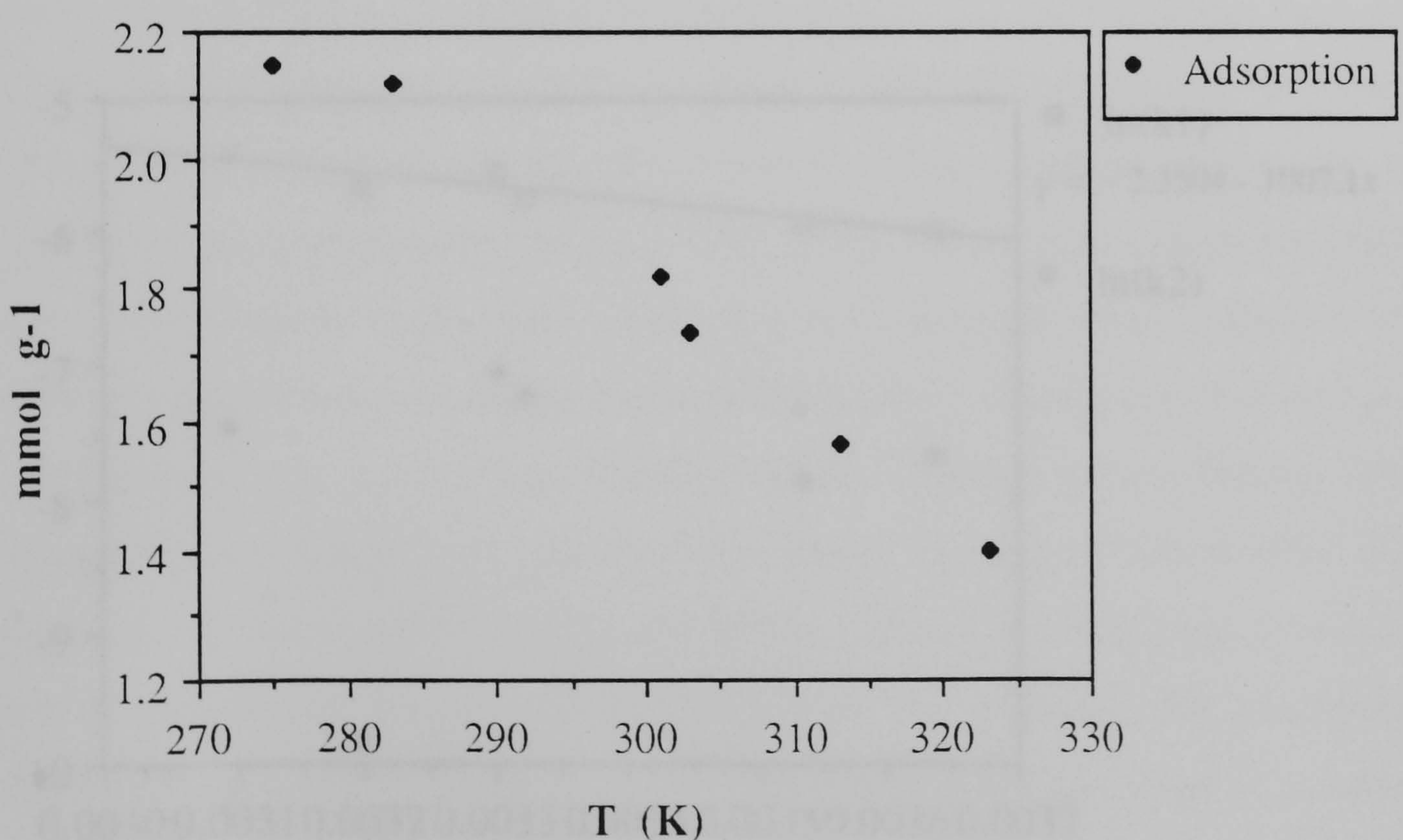

Figure 5.27 A graph of adsorption capacities of nitrous oxide against increasing temperature for CMS A3.

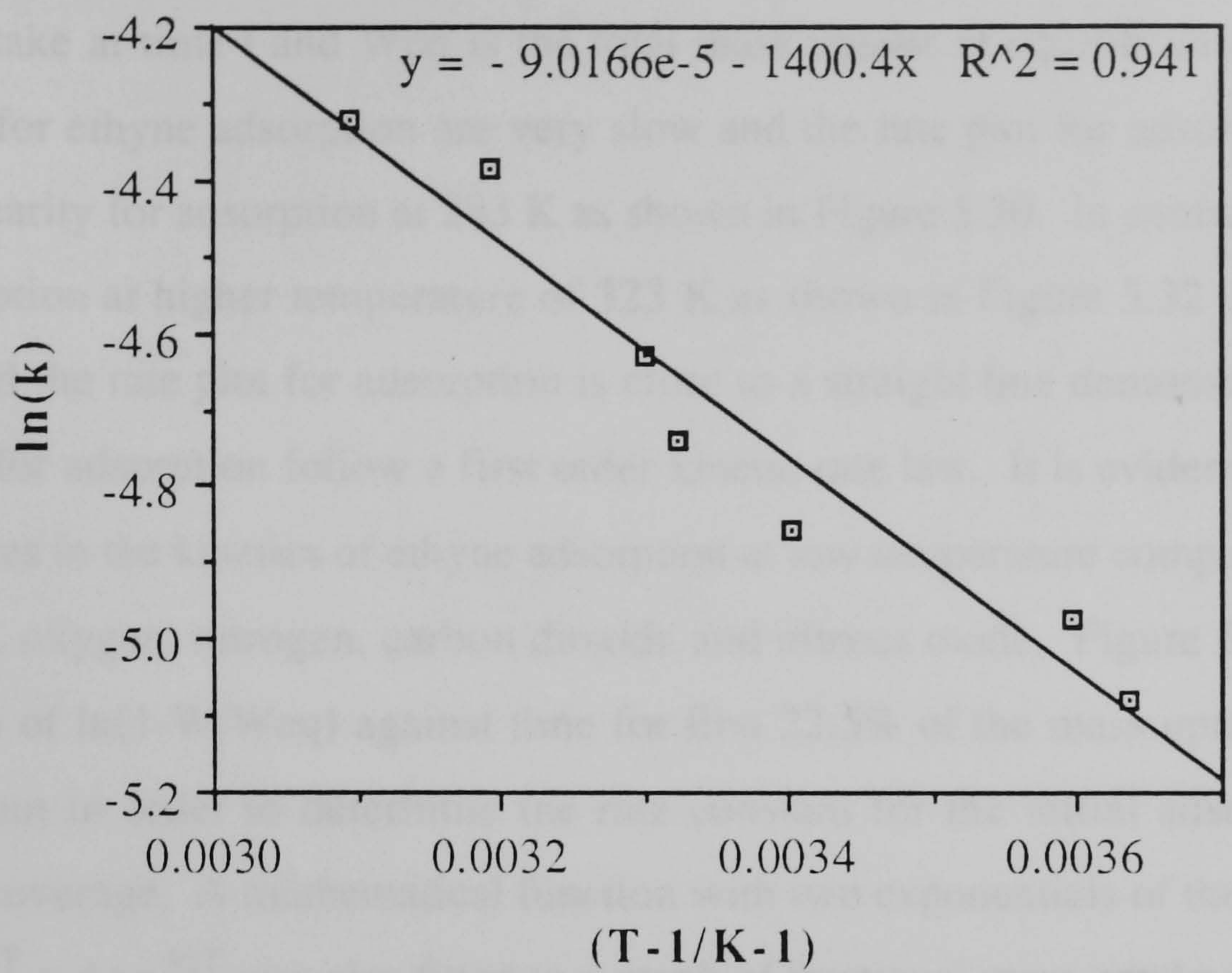

Figure 5.28 Arrhenius graph for adsorption of nitrous oxide on CMS A3.

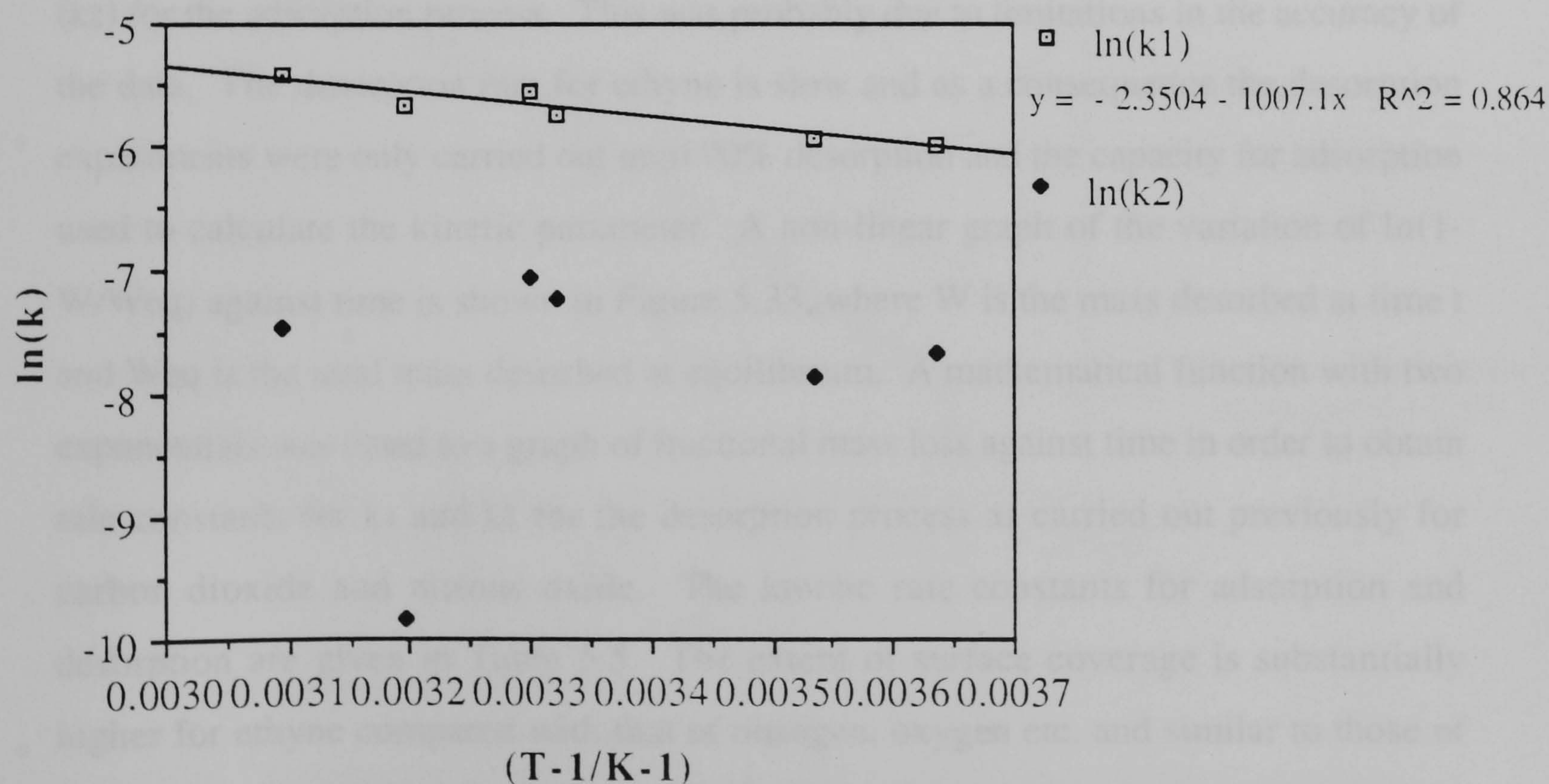

Figure 5.29 Arrhenius graph for the fast (k_1) and slow (k_2) desorption processes of nitrous oxide on CMS A3 (from the mathematical model).

5.2.2.6 *Ethyne adsorption/desorption*

Figures 5.30 - 5.32 show a variation of ln(1-W/Weq) against time, where W is mass uptake at time t and Weq is the total mass uptake at equilibrium. The overall kinetics for ethyne adsorption are very slow and the rate plot for adsorption deviates from linearity for adsorption at 283 K as shown in Figure 5.30. In contrast the kinetics of adsorption at higher temperature of 323 K as shown in Figure 5.32 is significantly faster and the rate plot for adsorption is close to a straight line demonstrating that the kinetics for adsorption follow a first order kinetic rate law. It is evident that there are differences in the kinetics of ethyne adsorption at low temperature compared with those of argon, oxygen, nitrogen, carbon dioxide and nitrous oxide. Figure 5.31 shows the variation of ln(1-W/Weq) against time for first 22.5% of the mass uptake. This was carried out in order to determine the rate constant for the initial adsorption at low surface coverage. A mathematical function with two exponentials of the form W/Weq = $A_1 e^{-k_1T} + A_2 e^{-k_2T}$ was also fitted to a graph of fractional mass uptake against time in order to obtain rate constants for the fast (k_1) and slow (k_2) for the adsorption process. The rate constant (k_1) for the fast adsorption process showed an increase as the temperature increased. In contrast, no trend was observed for the slower rate constant (k_2) for the adsorption process. This was probably due to limitations in the accuracy of the data. The desorption rate for ethyne is slow and as a consequence the desorption experiments were only carried out until 90% desorption and the capacity for adsorption used to calculate the kinetic parameter. A non-linear graph of the variation of ln(1-W/Weq) against time is shown in Figure 5.33, where W is the mass desorbed at time t and Weq is the total mass desorbed at equilibrium. A mathematical function with two exponentials was fitted to a graph of fractional mass loss against time in order to obtain rate constants for k_1 and k_2 for the desorption process as carried out previously for carbon dioxide and nitrous oxide. The kinetic rate constants for adsorption and desorption are given in Table 5.5. The extent of surface coverage is substantially higher for ethyne compared with that of nitrogen, oxygen etc. and similar to those of carbon dioxide and nitrous oxide (see Table 5.5). This is a consequence of the higher relative pressure (p/p_o). The experiments were conducted in the temperature range of 283 - 323 K and the critical temperature for ethyne is 308.5 K. The capacities tend to show a decrease with increasing temperature as shown in Figure 5.34. The activation energy plots for adsorption for the initial rate is shown in Figure 5.35 and Figure 5.36 shows the activation energy plot for the fast adsorption (k_1) process, Figure 5.37 shows activation energy plots for desorption. The activation energy for adsorption of ethyne for the initial 22.5% mass uptake was 24.5 $kJmol^{-1}$. The activation energy for the k_1 process from the mathematical model was 30.4 $kJmol^{-1}$. The activation energies for desorption for k_1 and k_2 were 31.0 $kJmol^{-1}$ and 36.1 $kJmol^{-1}$ respectively. In contrast, the pre-exponential factor varies from 2.33 s^{-1} for adsorption for the initial stage to 27.46 s^{-1} for fast process k_1 for adsorption from the mathematical model based on two exponentials. In comparison, the pre-exponential factor for the desorption process varies from 41.06 s^{-1} to 38.63 s^{-1} for the fast and slow desorption processes respectively.

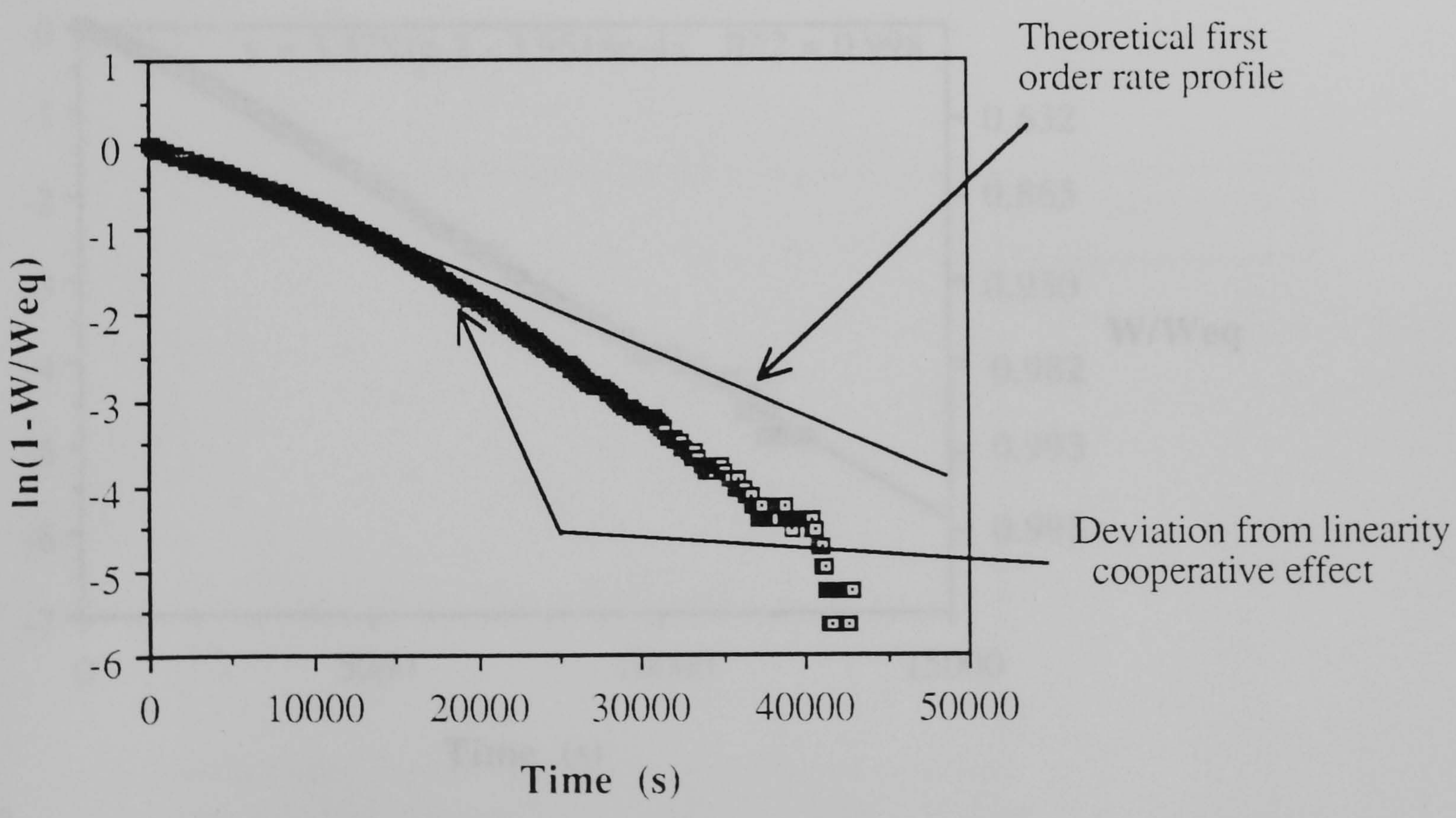

Figure 5.30 The variation of ln(1-W/Weq) against time for the adsorption of ethyne for CMS A3 at 283 K.

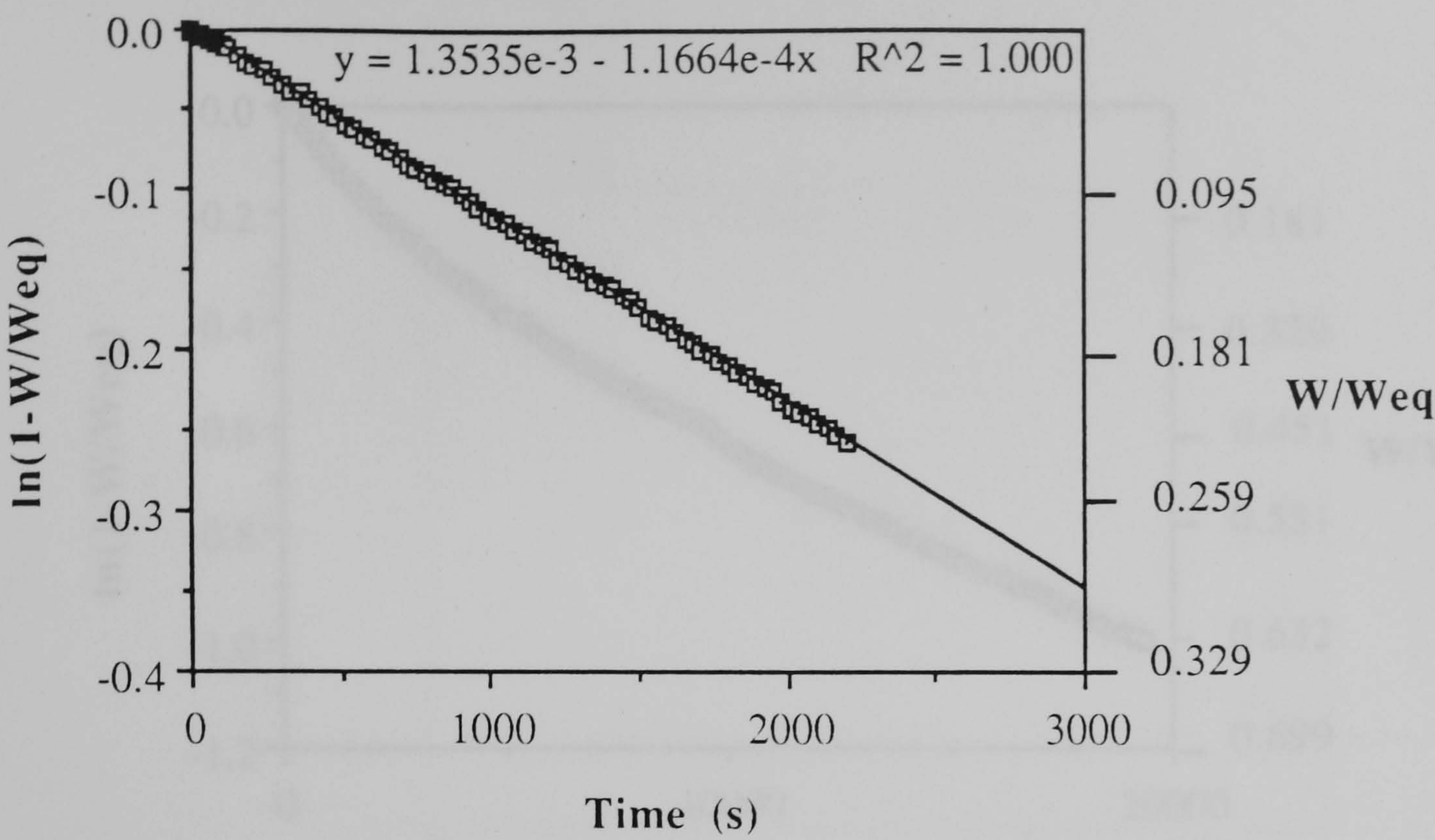

Figure 5.31 A graph of ln(1-W/Weq) against time for the initial rate of adsorption of ethyne for CMS A3 at 301 K.

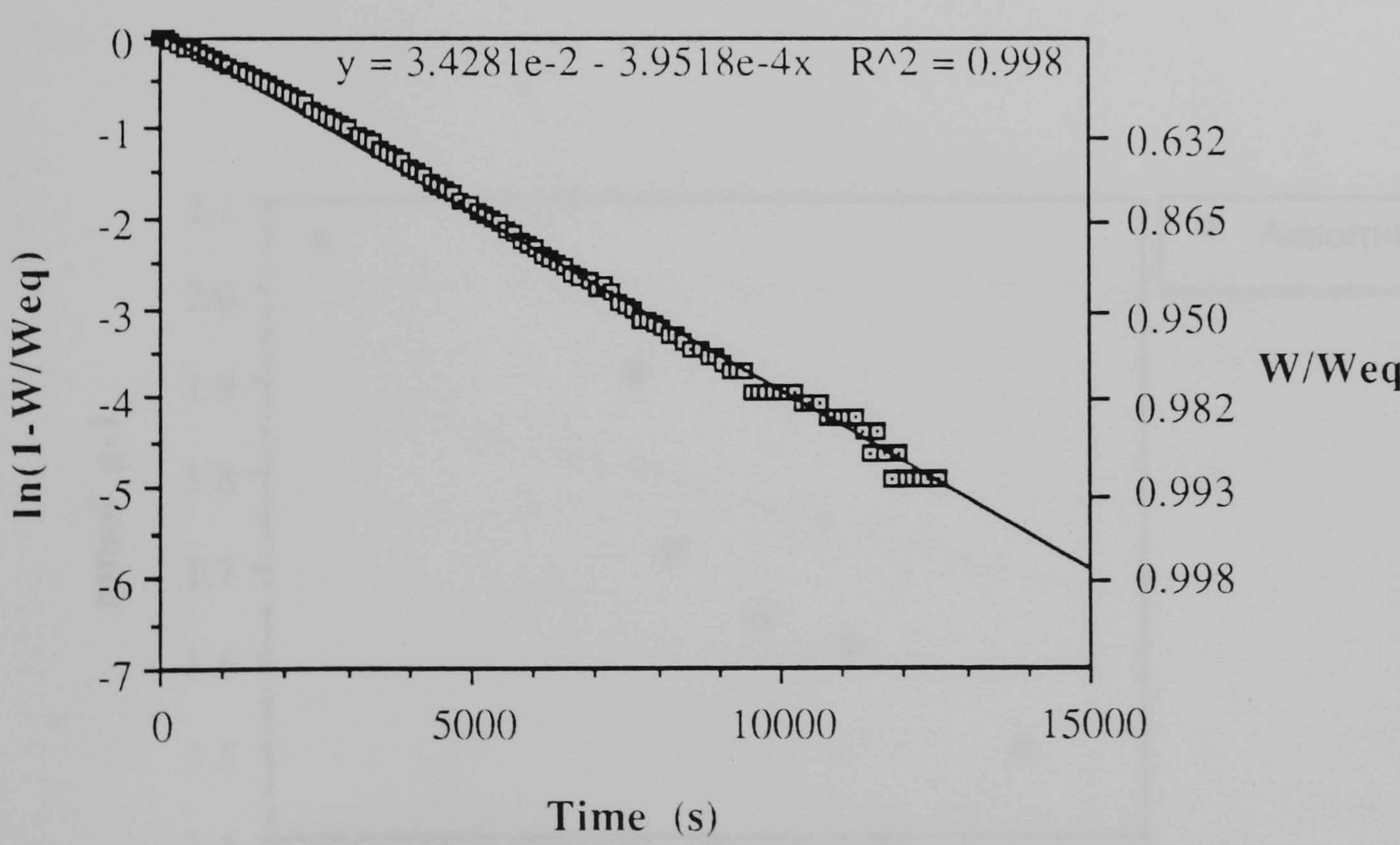

Figure 5.32 A graph of ln(1-W/Weq) against time for adsorption of ethyne for CMS A3 at 323 K.

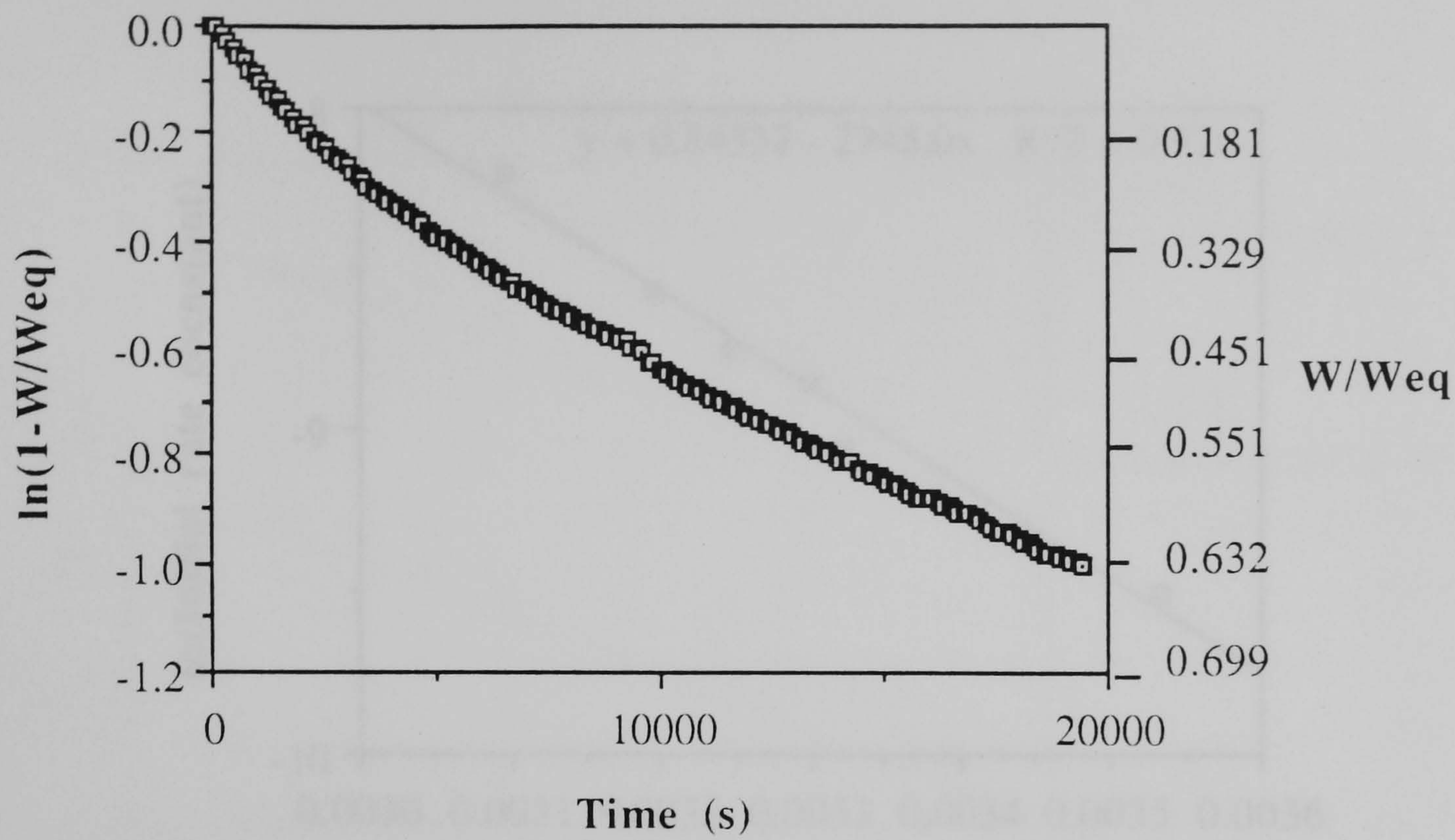

Figure 5.33 A graph of ln(1-W/Weq) for the desorption of ethyne for CMS A3 at 303 K for 63.9% data.

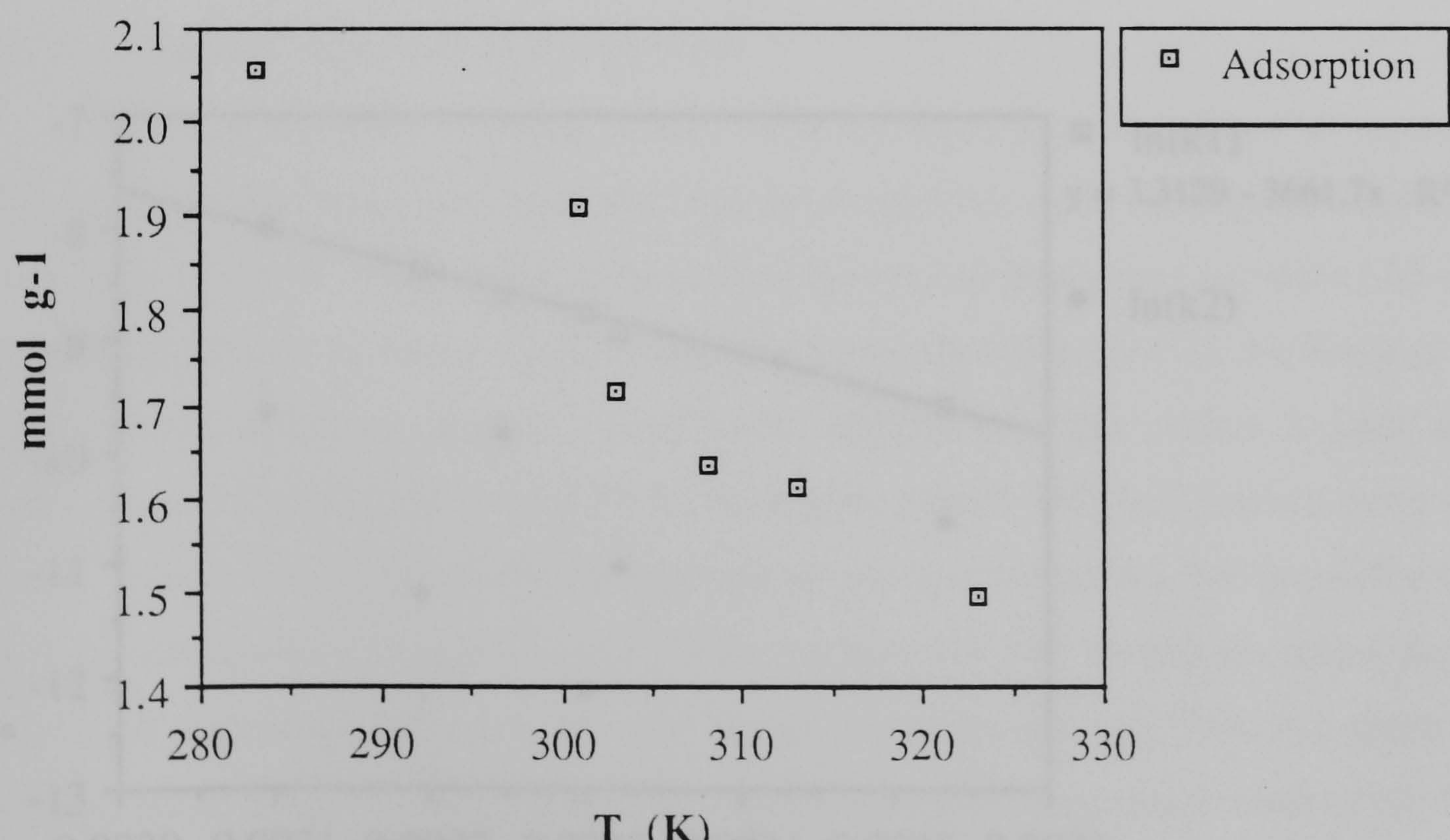

Figure 5.34 A graph of adsorption capacities of ethyne against increasing temperature for CMS A3.

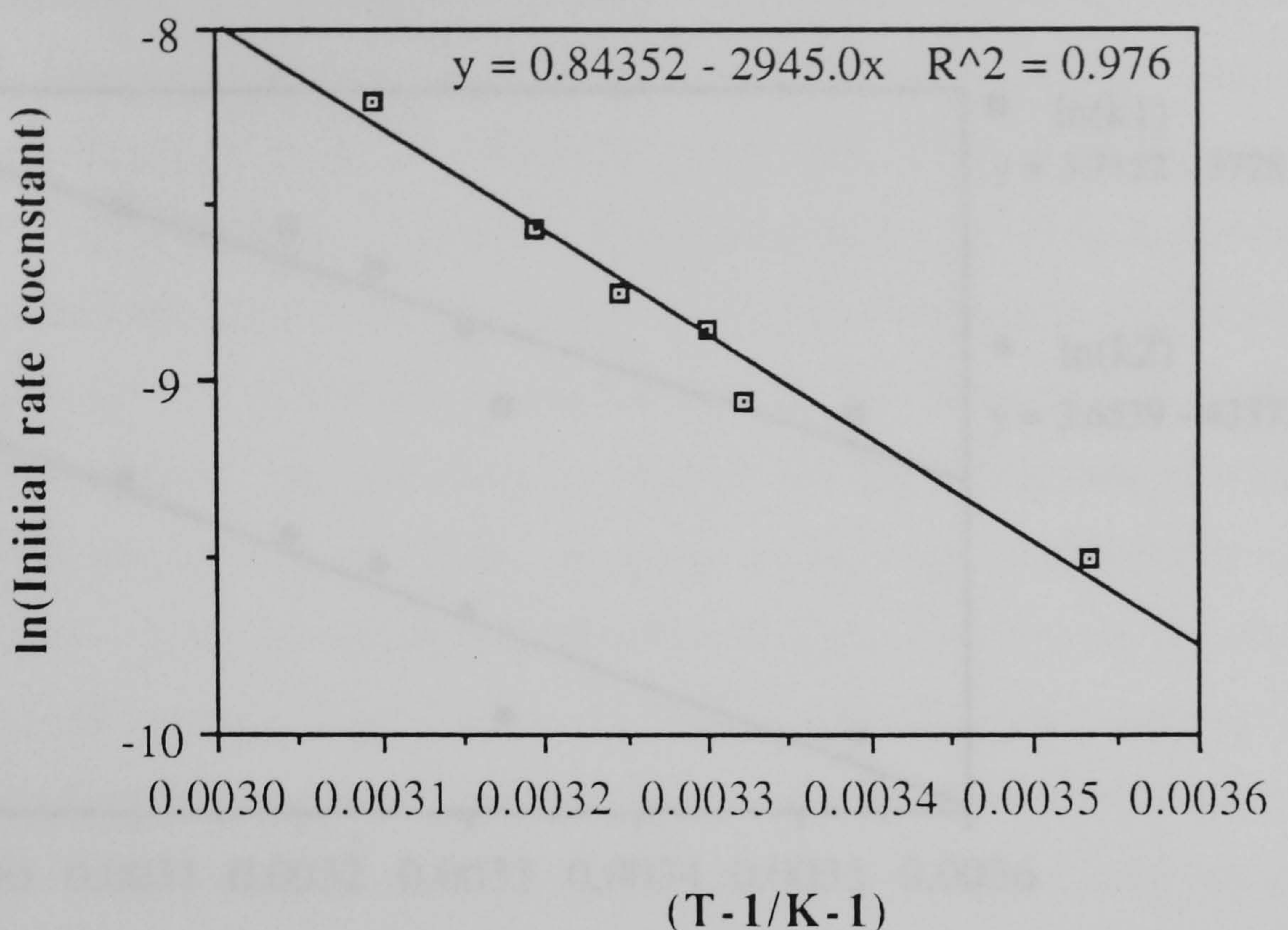

Figure 5.35 Arrhenius graph for adsorption of ethyne on CMS A3 (initial uptake 0.225 < W/Weq.

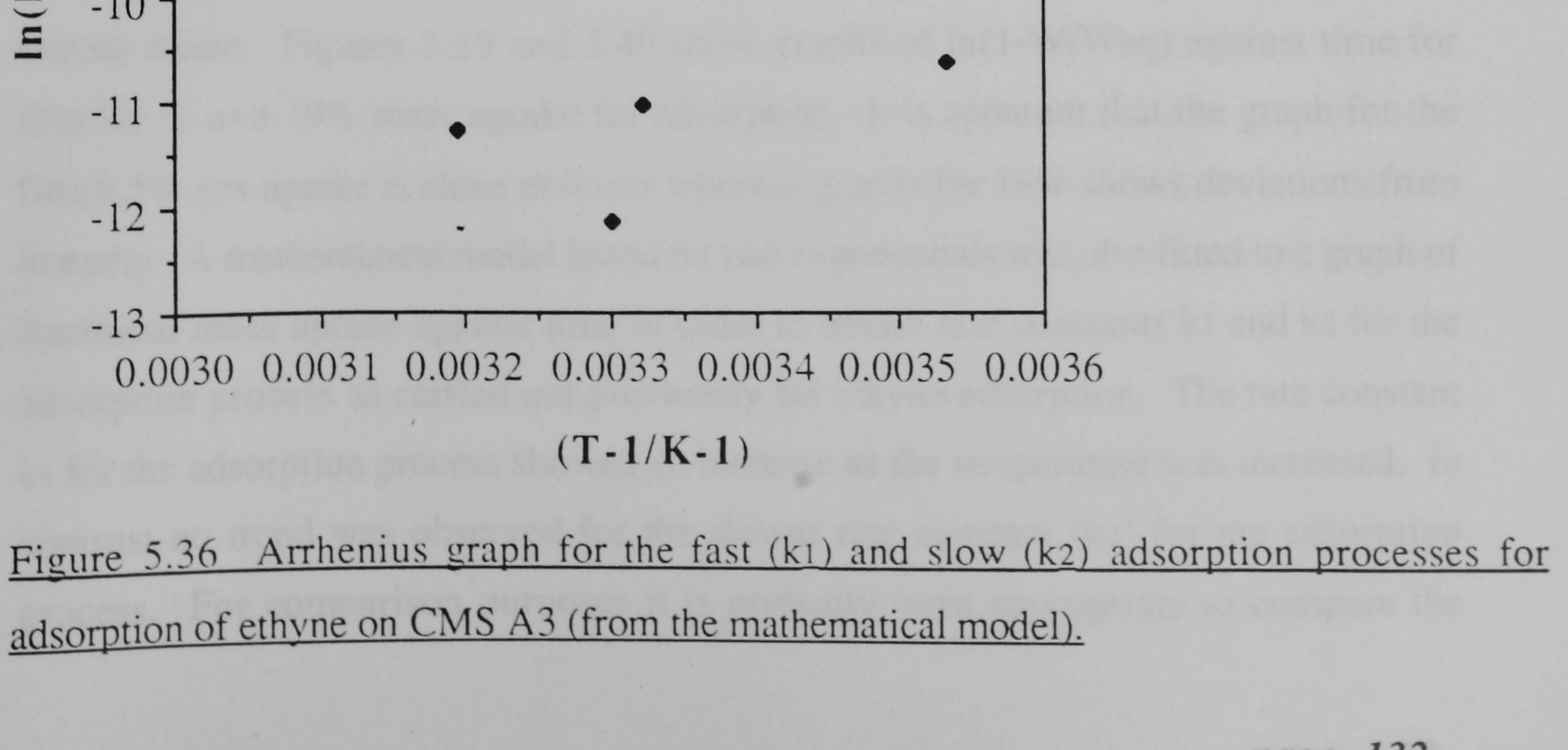

Figure 5.36 Arrhenius graph for the fast (k_1) and slow (k_2) adsorption processes for adsorption of ethyne on CMS A3 (from the mathematical model).

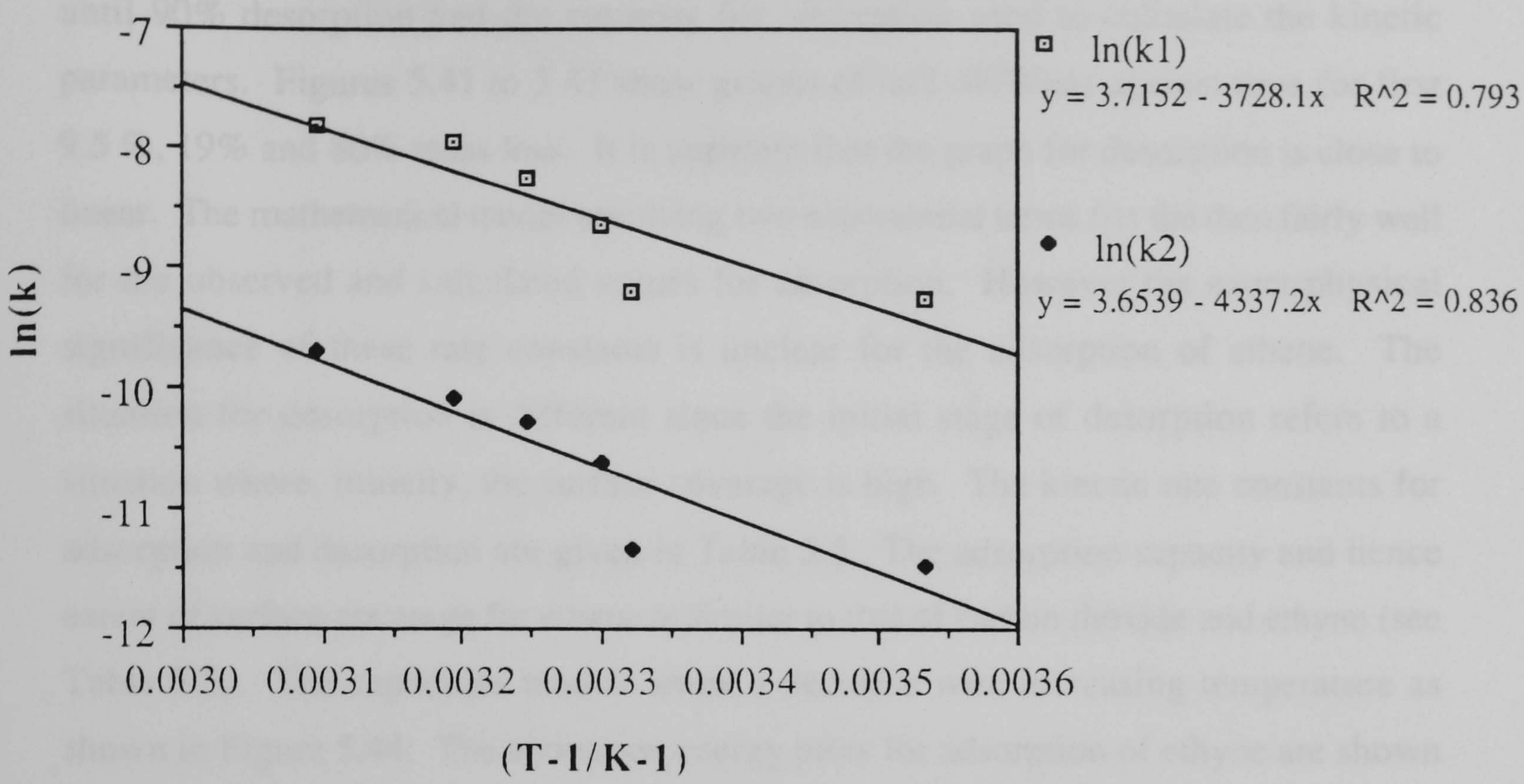

Figure 5.37 Arrhenius graph for fast (k_1) and slow (k_2) desorption processes for ethyne on CMS A3 (from the mathematicl model).

5.2.2.7 Ethene adsorption/desorption

Figure 5.38 shows a graph of ln(1-W/Weq) against time, where W is mass uptake at time t and Weq is the total mass uptake at equilibrium for adsorption of ethene on CMS A3 at 293 K. The overall kinetics for ethene adsorption are very slow and the graph deviates from linearity. It is evident that there are differences in the kinetics of ethene adsorption as compared to that of argon, oxygen, nitrogen, carbon dioxide and nitrous oxide. Figures 5.39 and 5.40 show graphs of ln(1-W/Weq) against time for first 9.5 % and 19% mass uptake for adsorption. It is apparent that the graph for the first 9.5% gas uptake is close to linear whereas graphs for 19% shows deviations from linearity. A mathematical model based on two exponentials was also fitted to a graph of fractional mass uptake against time in order to obtain rate constants k_1 and k_2 for the adsorption process as carried out previously for ethyne adsorption. The rate constant k_1 for the adsorption process showed an increase as the temperature was increased. In contrast no trend was observed for the slower rate constant (k_2) for the adsorption process. For comparison purposes it is probably most appropriate to compare the initial uptake rate constants since these refer to the low surface coverage region. Above this surface coverage there is a marked deviation from linearity. The desorption rate for ethyne is slow and as a consequence the desorption experiments were only carried out until 90% desorption and the capacity for adsorption used to calculate the kinetic parameters. Figures 5.41 to 5.43 show graphs of ln(1-W/Weq) against time for first 9.5 %, 19% and 80% mass loss. It is apparent that the graph for desorption is close to linear. The mathematical model involving two exponential terms fits the data fairly well for the observed and calculated values for adsorption. However the exact physical significance of these rate constants is unclear for the adsorption of ethene. The situation for desorption is different since the initial stage of desorption refers to a situation where, initially, the surface coverage is high. The kinetic rate constants for adsorption and desorption are given in Table 5.5. The adsorption capacity and hence extent of surface coverage for ethene is similar to that of carbon dioxide and ethyne (see Table 5.5). The capacities tend to show a decrease with increasing temperature as shown in Figure 5.44. The activation energy plots for adsorption of ethyne are shown in Figures 5.45 - 5.47. The activation energy graphs for desorption obtained using rate constants calculated for various parts of the data aand by two methods are shown in Figures 5.48 and 5.50. The activation energy for adsorption of ethene for 9.5% mass uptake was 39.6 $kJmol^{-1}$. In comparison, the activation energy for 19% mass uptake was 35.5 $kJmol^{-1}$. The corresponding pre-exponential factors are 115.58 s^{-1} for first 9.5% mass uptake and 25.12 s^{-1} for 19% mass uptake. The activation energy for adsorption for the fast process (obtained by fitting the mathematical model containing two exponentials to the graph of fractional uptake) was 36.1 $kJmol^{-1}$ and has a pre-exponential factor of 33.20 s^{-1}. It is apparent that the activation energies are very similar. The activation energies for desorption were 38.4 $kJmol^{-1}$, 30.9 $kJmol^{-1}$ and 30.6 $kJmol^{-1}$ for 9.5%, 19% and 80% mass loss respectively. In contrast, the pre-exponential factor for 9.5%, 19% and 80% mass loss for desorption process were 124.5 s^{-1}, 5.92 s^{-1} and 2.41 s^{-1} respectively. It is evident that the activation energies calculated for the various parts of the data are similar. However, the pre-exponential factors differ but the errors in the extrapolation to give lnA are relatively high.

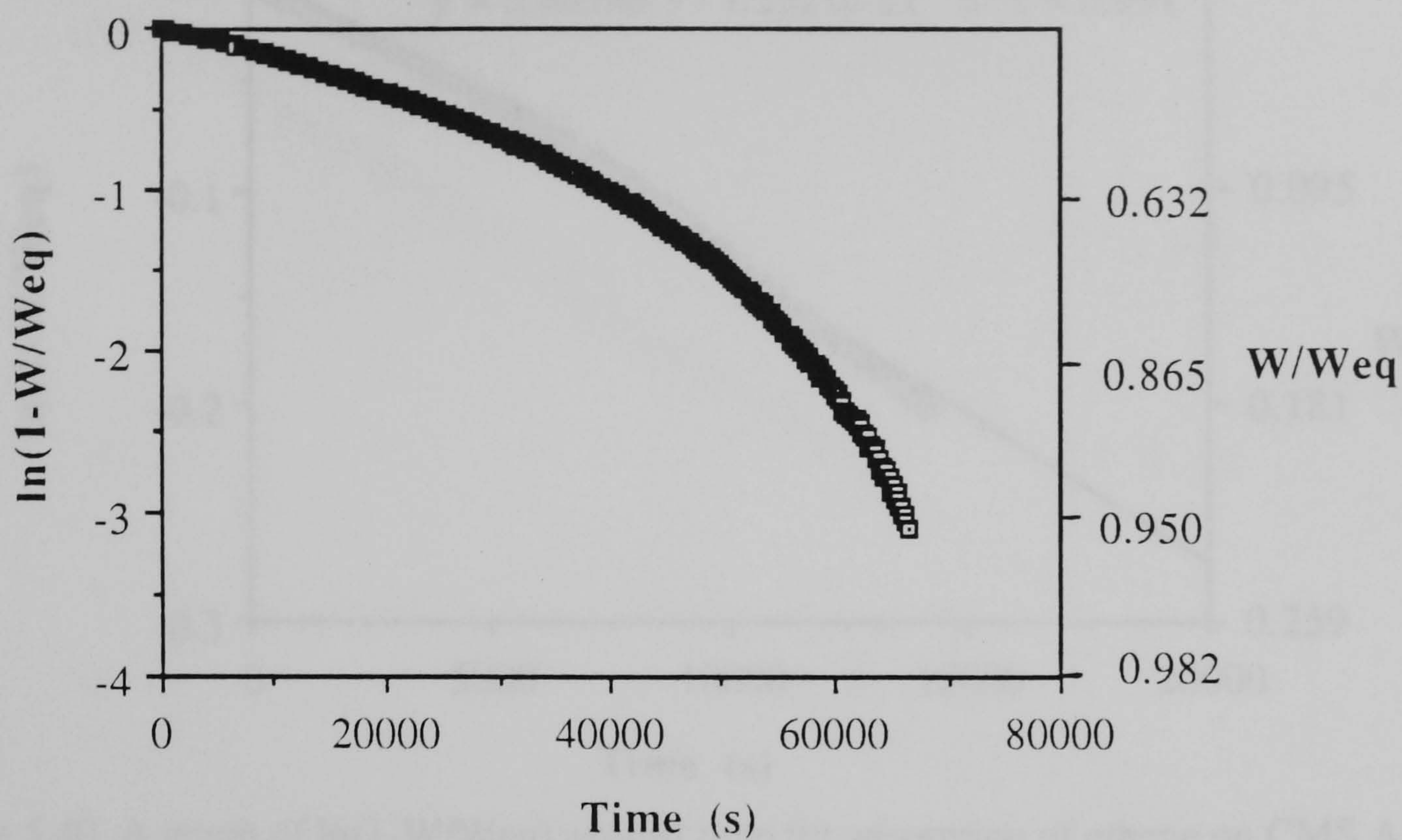

Figure 5.38 A graph of ln(1-W/Weq) against time for adsorption of ethene on CMS A3 at 293 K.

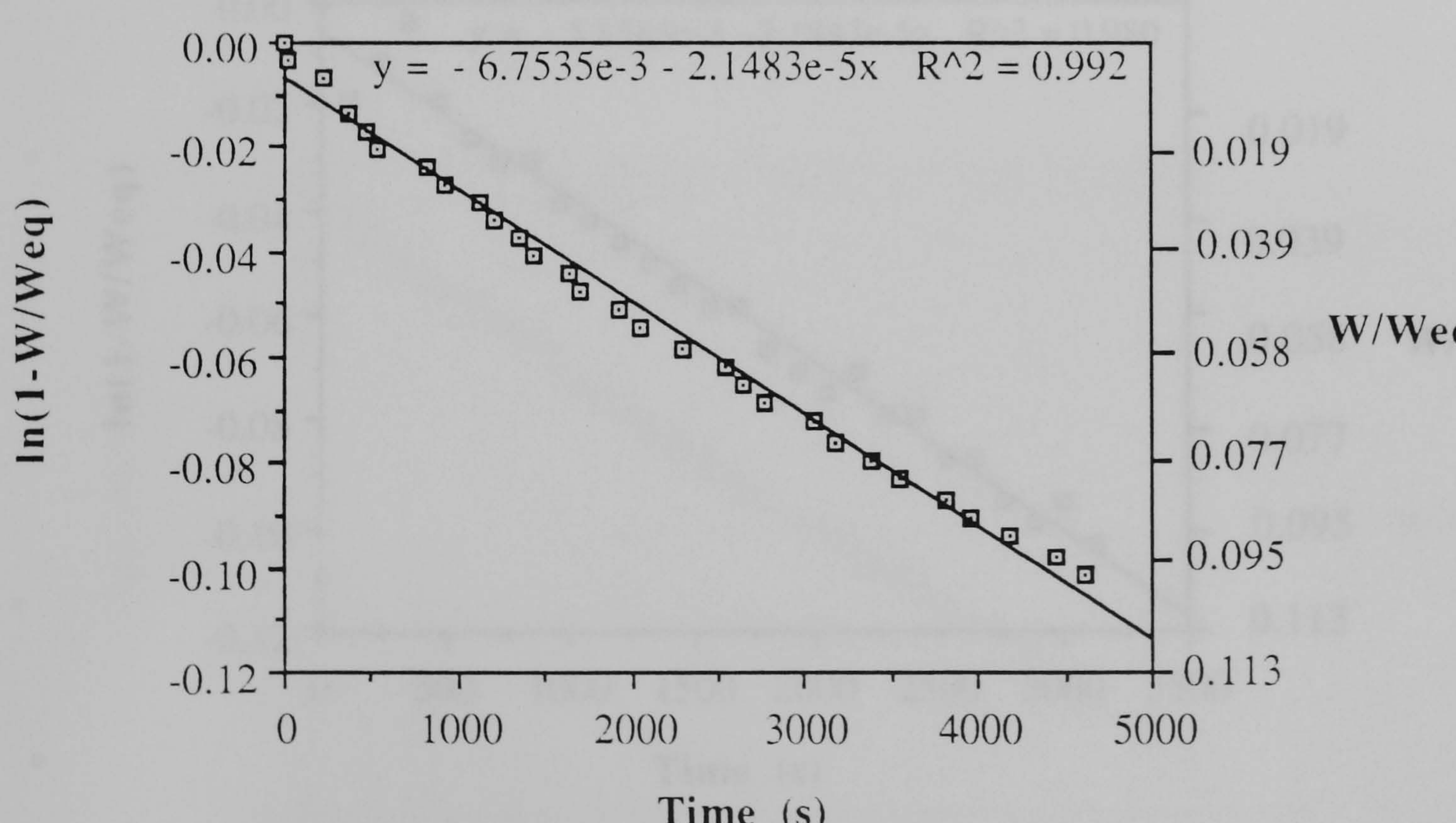

Figure 5.39 A graph of ln(1-W/Weq) against time for adsorption of ethene on CMS A3 at 293 K for first 9.5%.

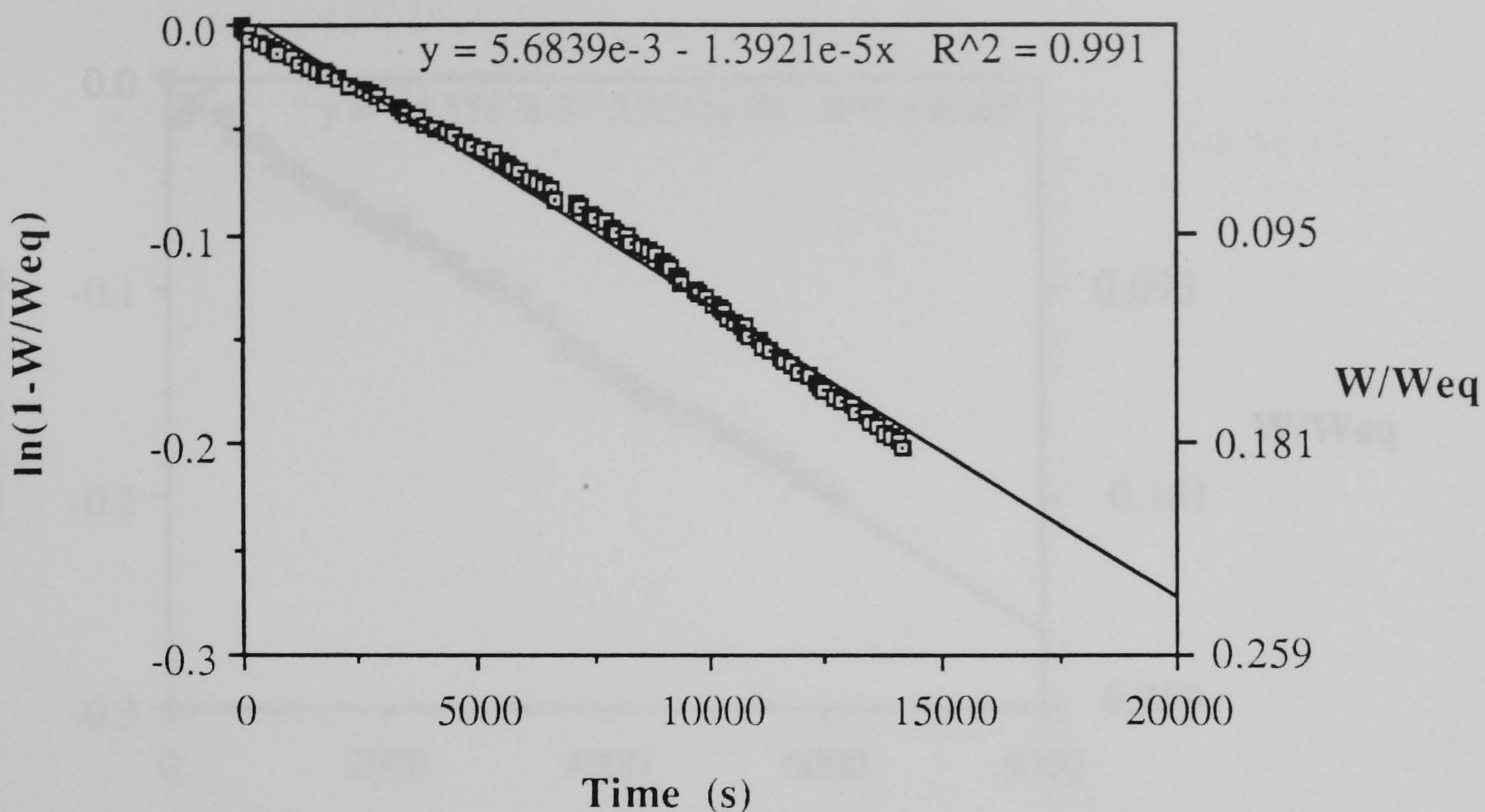

Figure 5.40 A graph of ln(1-W/Weq) against time for adsorption of ethene on CMS A3 at 293 K for first 19%.

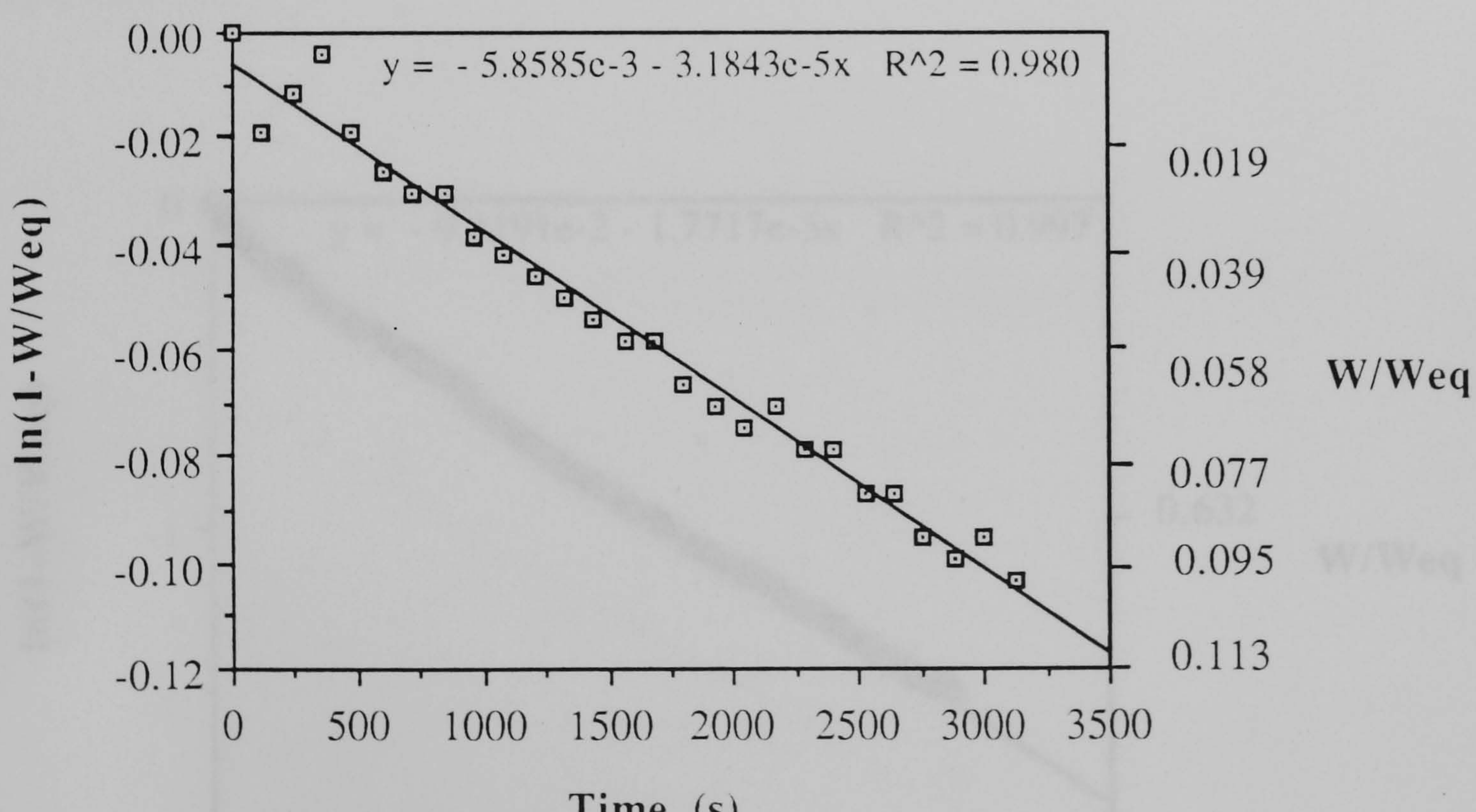

Figure 5.41 A graph of ln(1-W/Weq) against time for desorption of ethene on CMS A3 at 313 K for first 9.5%.

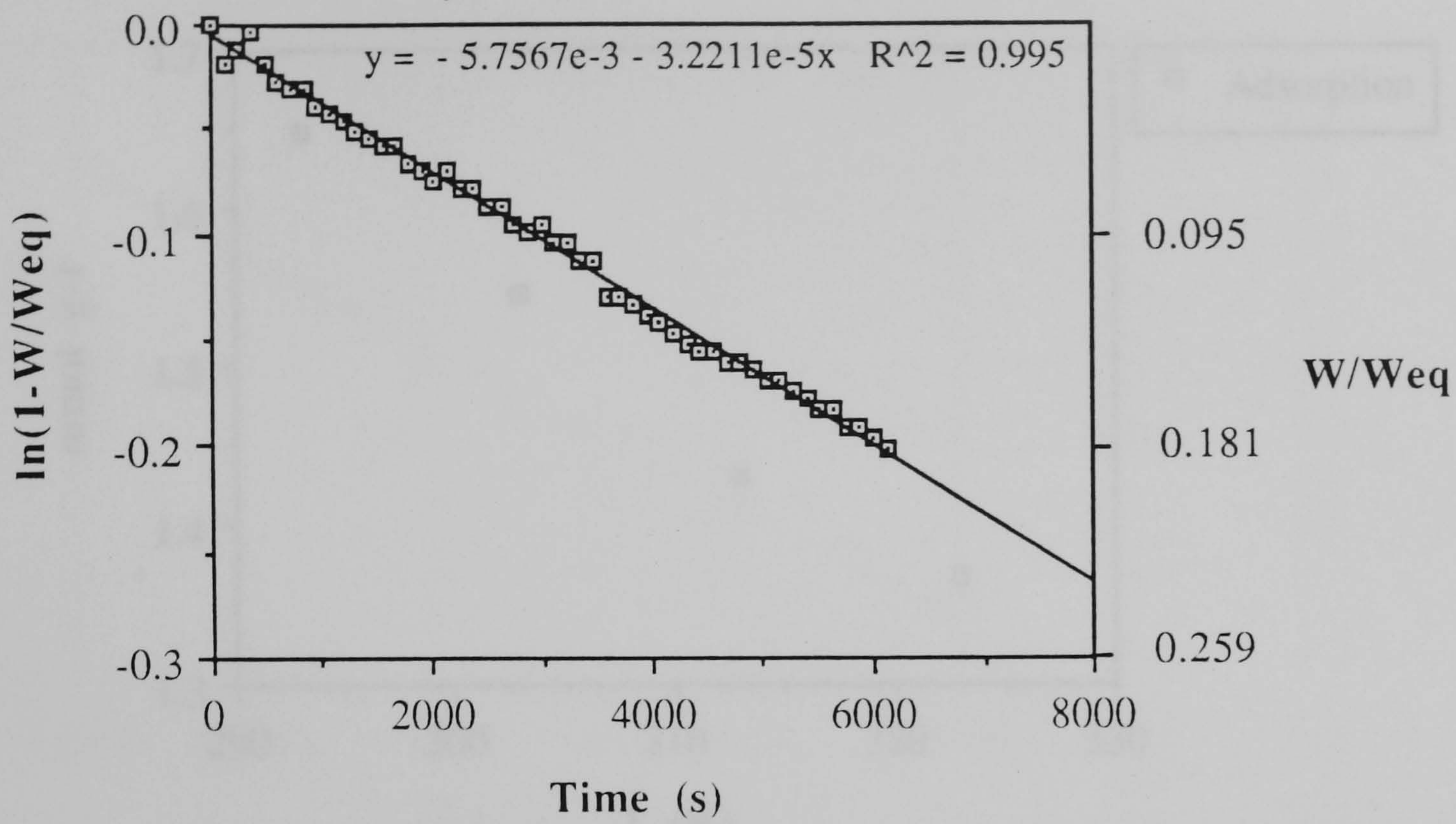

Figure 5.42 A graph of ln(1-W/Weq) against time for desorption of ethene on CMS A3 at 313 K for first 19%.

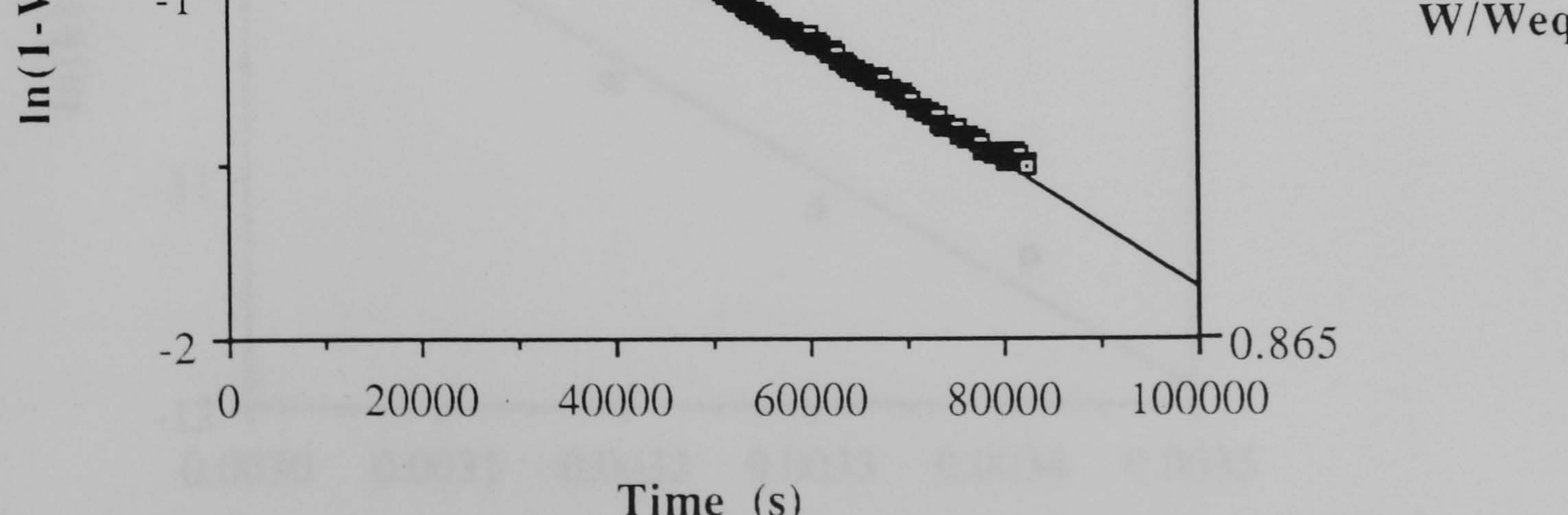

Figure 5.43 A graph of ln(1-W/Weq) against time for desorption of ethene on CMS A3 at 313 K for first 80%.

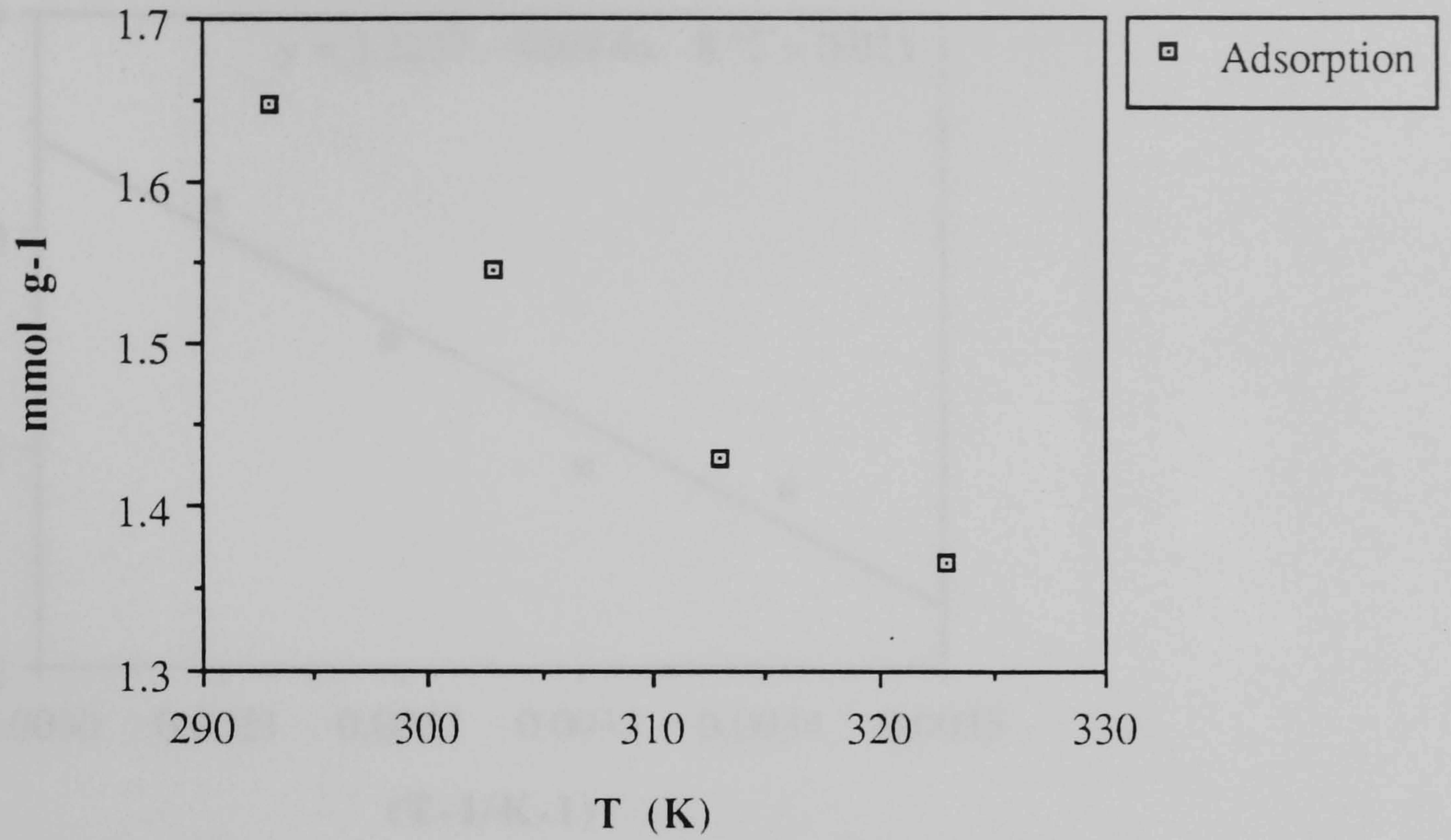

Figure 5.44 A graph of adsorption capacities of ethene against increasing temperature for CMS A3.

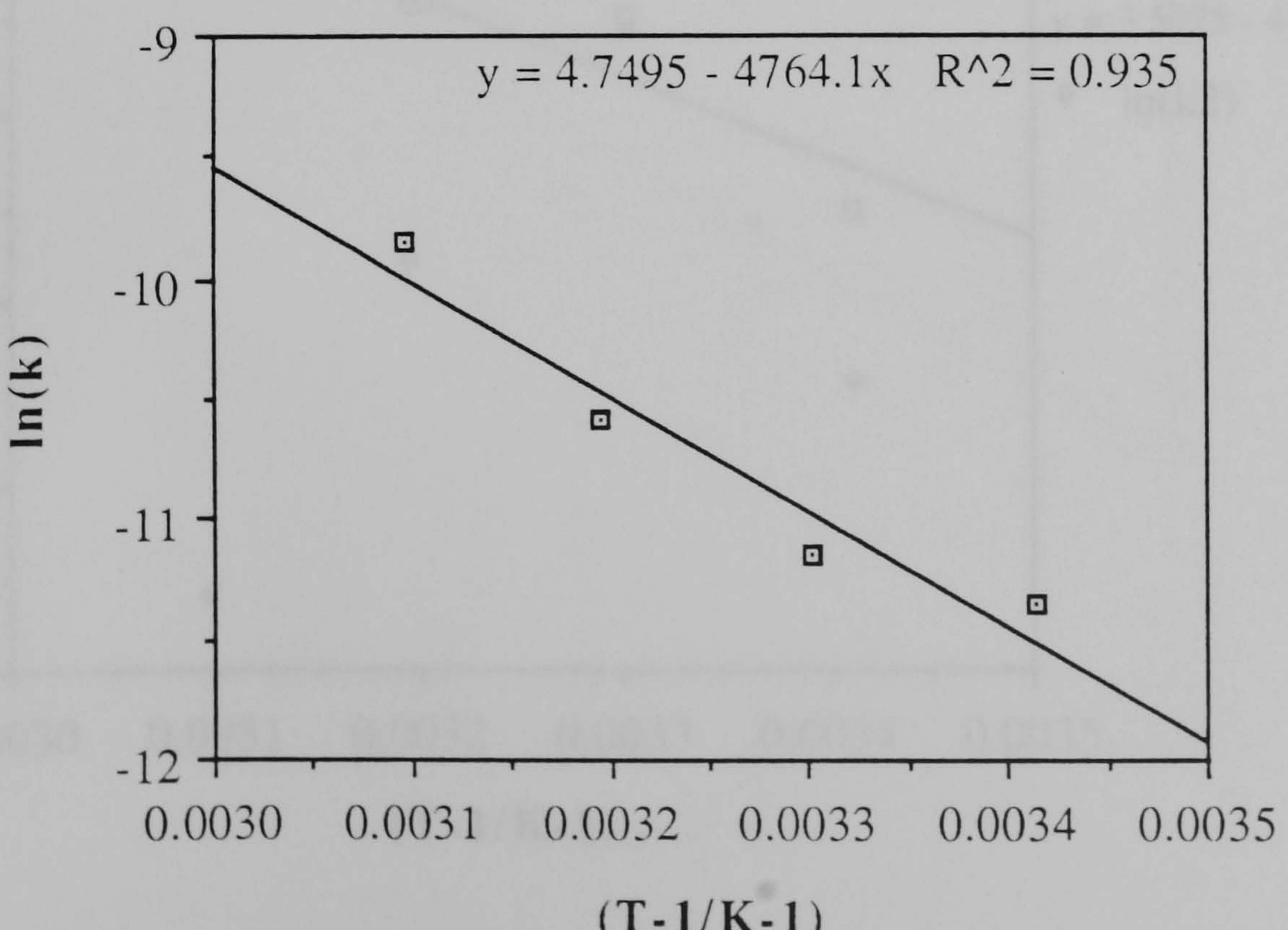

Figure 5.45 Arrhenius graph for adsorption of ethene on CMS A3 for first 9.5% data.

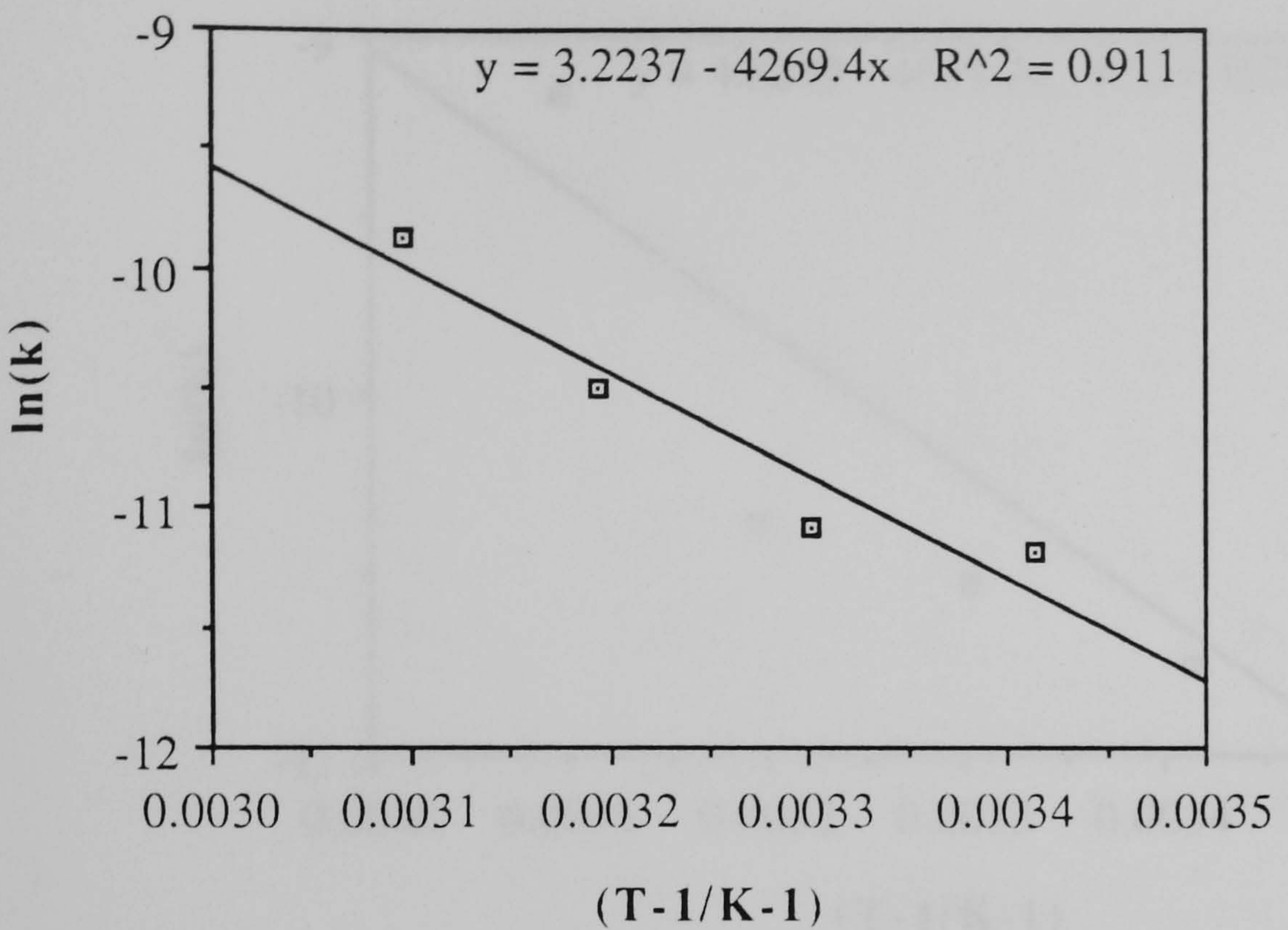

Figure 5.46 Arrhenius graph for adsorption of ethene on CMS A3 for first 19% data.

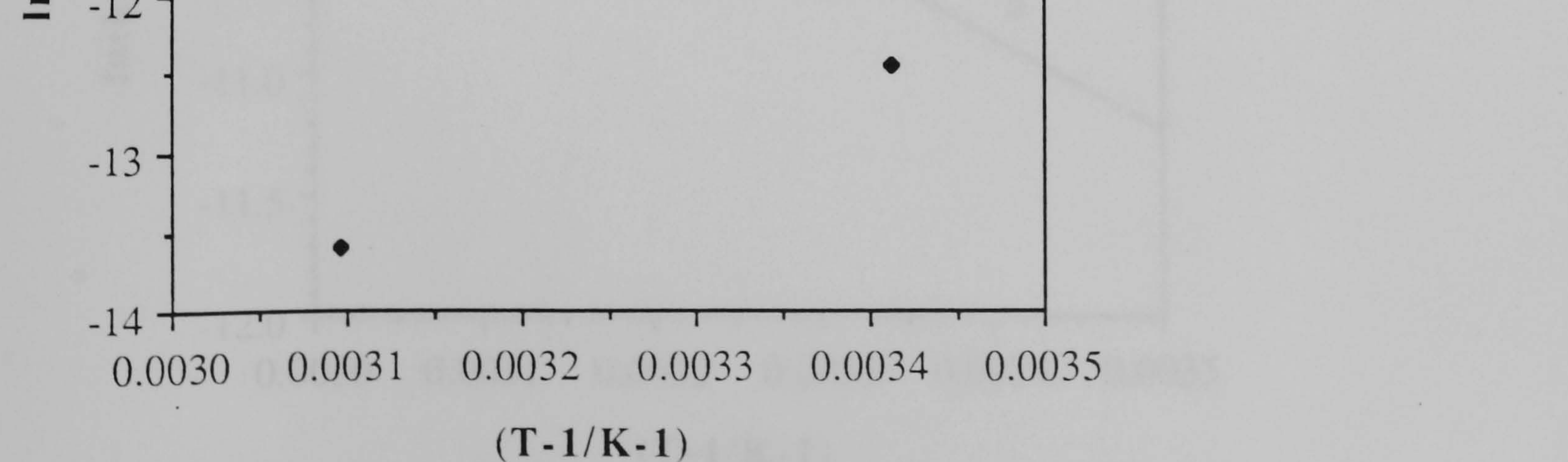

Figure 5.47 Arrhenius graph for k_1 and k_2 from the mathematical model for adsorption of ethene on CMS A3.

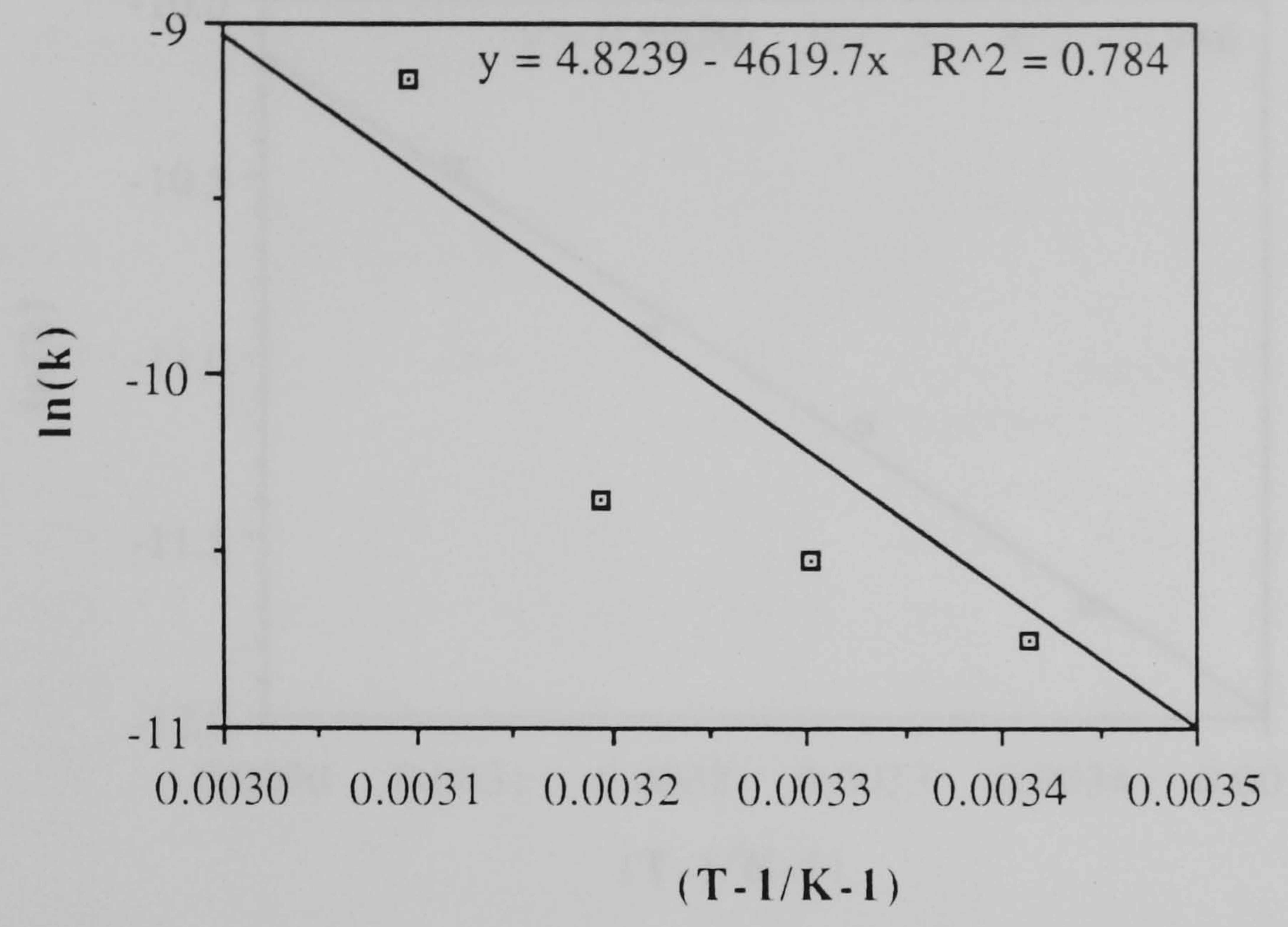

Figure 5.48 Arrhenius graph for desorption of ethene on CMS A3 for first 9.5% data.

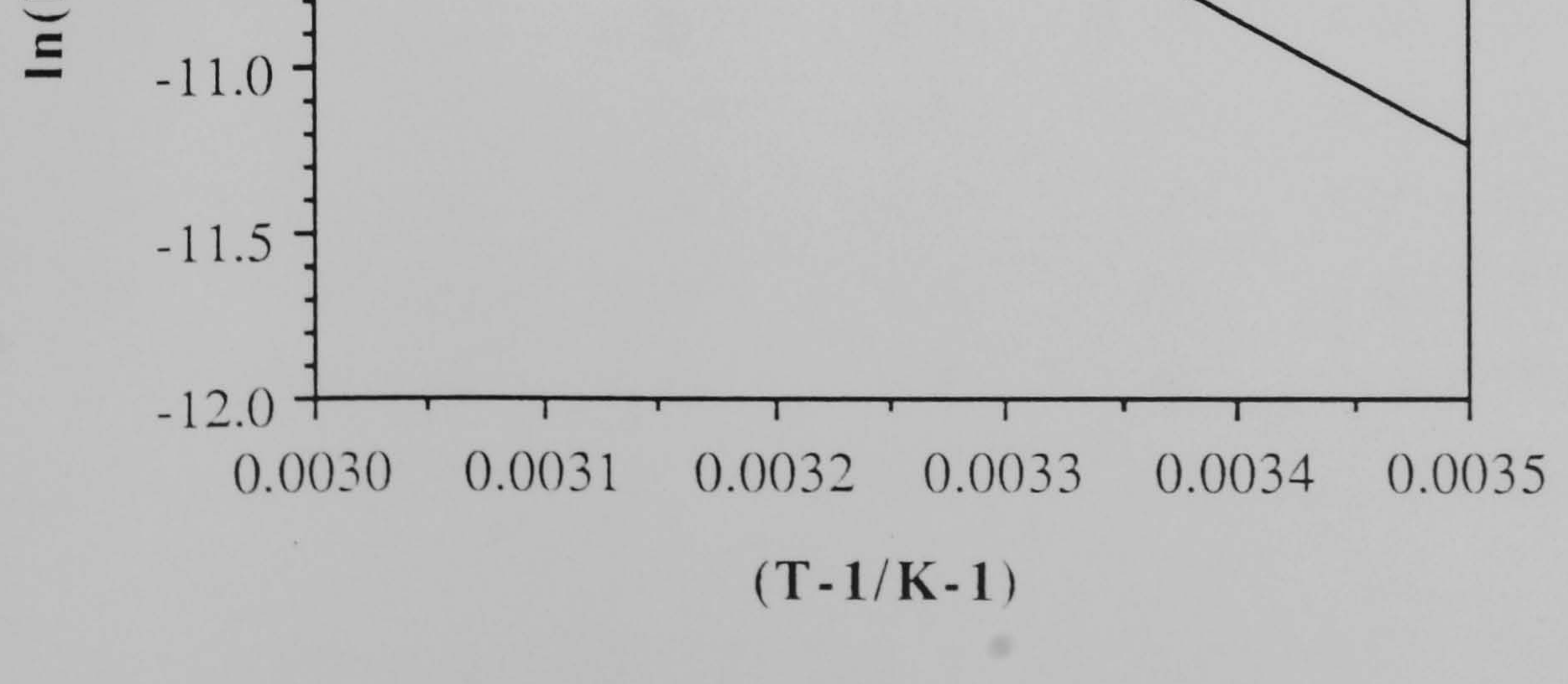

Figure 5.49 Arrhenius graph for desorption of ethene on CMS A3 for first 19% data.

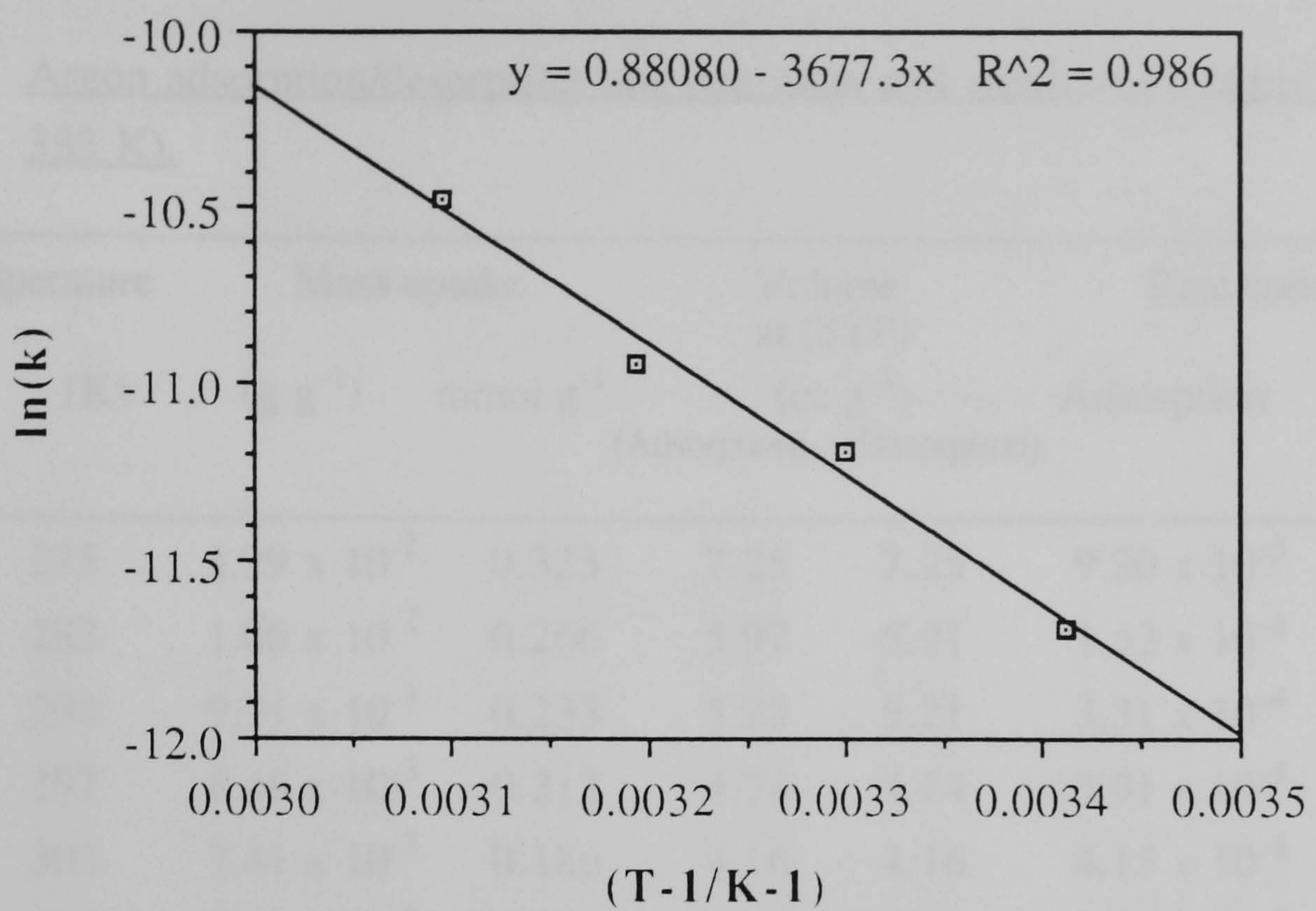

Figure 5.50 Arrhenius graph for desorption of ethene on CMS A3 for 80% data.

Table 5.5

The adsorption/desorption kinetics and capacity parameters for CMS A3.

(1) Argon adsorption/desorption rate constants and equilibrium capacities (275 - 333 K).

Temperature	Mass uptake		Volume at (STP)		Rate constant (s^{-1})	
(K)	($g\ g^{-1}$)	mmol g^{-1}	($cc\ g^{-1}$) (Adsorption)	($cc\ g^{-1}$) (Desorption)	Adsorption	Desorption
275	1.29×10^{-2}	0.323	7.25	7.25	9.30×10^{-5}	4.84×10^{-5}
283	1.06×10^{-2}	0.266	5.97	5.91	1.52×10^{-4}	7.60×10^{-5}
294	9.31×10^{-3}	0.233	5.22	5.21	3.31×10^{-4}	2.36×10^{-4}
297	8.46×10^{-3}	0.212	4.74	4.74	3.91×10^{-4}	4.57×10^{-4}
303	7.41×10^{-3}	0.186	4.16	4.16	4.15×10^{-4}	4.29×10^{-4}
313	7.03×10^{-3}	0.176	3.94	3.94	9.14×10^{-4}	7.53×10^{-4}
323	6.46×10^{-3}	0.162	3.62	3.52	1.14×10^{-3}	1.18×10^{-3}
333	5.70×10^{-3}	0.143	3.20	3.04	1.86×10^{-3}	1.27×10^{-3}

(2) Oxygen adsorption/desorption rate constants and equilibrium capacities (275 - 313 K).

Temperature	Mass uptake		Volume at (STP)		Rate constant (s^{-1})	
(K)	($g\ g^{-1}$)	mmol g^{-1}	($cc\ g^{-1}$) (Adsorption)	($cc\ g^{-1}$) (Desorption)	Adsorption	Desorption
275	1.17×10^{-2}	0.365	8.18	8.18	4.64×10^{-3}	1.94×10^{-3}
283	9.41×10^{-3}	0.294	6.58	6.52	6.48×10^{-3}	4.59×10^{-3}
292	7.79×10^{-3}	0.243	5.45	5.39	1.23×10^{-2}	7.54×10^{-3}
303	6.56×10^{-3}	0.205	4.59	4.59	1.64×10^{-2}	1.26×10^{-2}
313	5.51×10^{-3}	0.172	3.86	3.86	2.33×10^{-2}	2.15×10^{-2}

Table 5.5 continued

(3) Nitrogen adsorption/desorption rate constants and equilibrium capacities (275 - 333 K).

Temperature (K)	Mass uptake ($g\ g^{-1}$)	Mass uptake (mmol g^{-1})	Volume at (STP) ($cc\ g^{-1}$) (Adsorption)	Volume at (STP) ($cc\ g^{-1}$) (Desorption)	Rate constant (s^{-1}) Adsorption	Rate constant (s^{-1}) Desorption
275	8.65×10^{-3}	0.309	6.91	6.91	1.83×10^{-4}	1.03×10^{-4}
283	7.51×10^{-3}	0.268	6.00	6.00	2.03×10^{-4}	1.10×10^{-4}
298	6.46×10^{-3}	0.231	5.17	5.17	4.32×10^{-4}	3.47×10^{-4}
303	6.18×10^{-3}	0.220	4.94	4.94	7.29×10^{-4}	5.28×10^{-4}
313	5.61×10^{-3}	0.200	4.48	4.26	1.46×10^{-3}	7.19×10^{-4}
323	4.85×10^{-3}	0.173	3.87	3.87	1.66×10^{-3}	9.81×10^{-4}
333	4.09×10^{-4}	0.146	3.27	3.27	1.87×10^{-3}	1.43×10^{-3}

(4) Carbon dioxide adsorption rate constants and equilibrium capacities (275 - 333 K).

Temperature (K)	Mass uptake ($g\ g^{-1}$)	Mass uptake (mmol g^{-1})	Volume at (STP) ($cc\ g^{-1}$) (Adsorption)	Rate constant (s^{-1}) Adsorption
275	9.02×10^{-2}	2.051	45.96	3.94×10^{-3}
293	7.60×10^{-2}	1.727	38.70	6.07×10^{-3}
303	6.67×10^{-2}	1.516	33.96	7.52×10^{-3}
313	5.90×10^{-2}	1.341	30.04	8.92×10^{-3}
323	5.21×10^{-2}	1.183	26.51	9.52×10^{-3}
333	4.43×10^{-2}	1.006	22.54	9.54×10^{-3}

Table 5.5 continued

(5) Carbon dioxide rate constants for desorption from the mathematical model.

Temperature (K)	Rate constants (s^{-1})				
	A_1	A_2	k_1	k_2	χ^2
275	0.55	0.47	1.57×10^{-3}	2.44×10^{-4}	6×10^{-5}
293	0.67	0.31	2.80×10^{-3}	6.13×10^{-4}	2×10^{-5}
303	0.74	0.29	3.59×10^{-3}	8.42×10^{-4}	3×10^{-5}
313	0.95	0.09	3.53×10^{-3}	1.65×10^{-4}	7×10^{-5}
323	0.93	0.03	3.09×10^{-3}	5.44×10^{-5}	9×10^{-5}
333	0.93	0.07	4.03×10^{-3}	4.07×10^{-4}	7×10^{-5}

(6) Nitrous oxide adsorption rate constants and equilibrium capacities (275 - 333 K).

Temperature	Mass uptake		Volume at (STP)	Rate constant (s^{-1})
(K)	($g\ g^{-1}$)	mmol g^{-1}	($cc\ g^{-1}$) (Adsorption)	Adsorption
275	9.45×10^{-2}	2.148	48.11	6.22×10^{-3}
283	9.32×10^{-2}	2.116	47.43	6.93×10^{-3}
301	8.02×10^{-2}	1.822	40.81	8.76×10^{-3}
303	7.63×10^{-2}	1.733	38.83	9.77×10^{-3}
313	6.88×10^{-2}	1.563	35.01	1.25×10^{-2}
323	6.16×10^{-2}	1.399	31.33	1.33×10^{-2}

Table 5.5 continued

(7) Nitrous oxide rate constants for desorption from the mathematical model.

Temperature (K)	Rate constants (s^{-1})				
	A1	A2	k1	k2	χ^2
275	0.52	0.39	2.51×10^{-3}	4.67×10^{-4}	2×10^{-5}
283	0.60	0.36	2.61×10^{-3}	3.87×10^{-4}	3×10^{-5}
301	0.68	0.30	3.20×10^{-3}	7.29×10^{-4}	3×10^{-5}
303	0.73	0.20	3.88×10^{-3}	8.60×10^{-4}	4×10^{-5}
313	0.94	0.08	3.43×10^{-3}	5.38×10^{-5}	9×10^{-5}
323	0.93	0.07	4.42×10^{-3}	5.80×10^{-4}	10×10^{-5}

(8) Ethyne adsorption rate constants and equilibrium capacities for adsorption (283 - 323 K).

Temperature (K)	Mass uptake ($g\ g^{-1}$)	Mass uptake mmol g^{-1}	Volume at (STP) ($cc\ g^{-1}$) (Adsorption)	Rate constant (s^{-1}) Adsorption (0 to 22.5%)
283	5.35×10^{-2}	2.056	46.05	7.47×10^{-5}
301	4.97×10^{-2}	1.910	42.78	1.17×10^{-4}
303	4.46×10^{-2}	1.713	38.36	1.43×10^{-4}
308	4.26×10^{-2}	1.636	36.65	1.58×10^{-4}
313	4.19×10^{-2}	1.610	36.07	1.90×10^{-4}
323	3.89×10^{-2}	1.494	33.46	2.73×10^{-4}

Table 5.5 continued

(9) Ethyne adsorption rate constants for from the mathematical model.

Temperature (K)	Rate constant (s^{-1})				
	A_1	A_2	k_1	k_2	χ^2
283	1.23	- 0.22	6.87×10^{-5}	2.40×10^{-5}	2.9×10^{-4}
301	1.14	- 0.12	1.32×10^{-4}	1.59×10^{-5}	3.7×10^{-4}
303	1.03	0.25	1.55×10^{-4}	5.32×10^{-6}	2.8×10^{-4}
308	1.16	- 0.12	1.86×10^{-4}	5.29×10^{-5}	2.9×10^{-4}
313	1.05	- 0.05	2.35×10^{-4}	1.28×10^{-5}	2.4×10^{-4}
323	1.04	-0.03	3.36×10^{-4}	6.65×10^{-5}	1.3×10^{-4}

(10) Ethyne rate constants for desorption from the mathematical model.

Temperature (K)	Rate constants (s^{-1})				
	A_1	A_2	k_1	k_2	χ^2
283	0.30	0.52	9.51×10^{-5}	1.05×10^{-5}	2×10^{-5}
301	0.29	0.57	1.01×10^{-4}	1.21×10^{-5}	4×10^{-5}
303	0.37	0.62	1.78×10^{-4}	2.43×10^{-5}	3×10^{-5}
308	0.36	0.59	2.58×10^{-4}	3.45×10^{-5}	0.9×10^{-5}
313	0.30	0.60	3.50×10^{-4}	4.13×10^{-5}	11×10^{-5}
323	0.40	0.53	4.04×10^{-4}	6.10×10^{-5}	1×10^{-5}

(11) Ethene adsorption/desorption rate constants for first 9.5%, 19% of the data and equilibrium capacities for adsorption (293 - 323 K).

Temperature (K)	Mass uptake $(g\ g^{-1})$	Mass uptake mmol g^{-1}	Volume at (STP) $(cc\ g^{-1})$ (Adsorption)	Rate constant (s^{-1}) Adsorption (For first 9.5% data)	Rate constant (s^{-1}) Adsorption (For first 19% data)
293	4.62×10^{-2}	1.647	36.89	1.17×10^{-5}	1.39×10^{-5}
303	4.33×10^{-2}	1.545	34.61	1.44×10^{-5}	1.53×10^{-5}
313	4.01×10^{-2}	1.430	32.03	2.51×10^{-5}	2.77×10^{-5}
323	3.83×10^{-2}	1.365	30.59	5.53×10^{-5}	5.21×10^{-5}

(12) Ethene desorption rate constants for first 9.5%, 19% and 80% of the data (293 - 323 K).

Temperature (K)	Rate constant (s^{-1}) Desorption (For first 9.5% data)	(For first 19% data)	(For 80% data)
293	2.15×10^{-5}	2.15×10^{-5}	8.39×10^{-6}
303	2.69×10^{-5}	2.36×10^{-5}	1.38×10^{-5}
313	3.19×10^{-5}	3.22×10^{-5}	1.77×10^{-5}
323	1.06×10^{-4}	7.29×10^{-5}	2.82×10^{-5}

(13) Ethene rate constants for adsorption from the mathematical model.

Temperature (K)	A_1	A_2	Rate constants (s^{-1}) k_1	k_2	χ^2
293	1.41	0.60	9.95×10^{-6}	3.96×10^{-6}	3×10^{-5}
303	0.76	0.32	2.86×10^{-5}	2.59×10^{-5}	325×10^{-5}
313	1.33	- 0.27	3.06×10^{-5}	7.70×10^{-6}	40×10^{-5}
323	1.04	- 0.23	4.42×10^{-5}	1.24×10^{-6}	18×10^{-5}

Table 5.6
Activation energy data for commercial carbon molecular sieve CMS A3.

Gas		Adsorption		Desorption	
Spherical					
Ar	$Ea/kJmol^{-1}$	**39.1**	**± 1.7**	**45.4**	**± 4.9**
	A/s^{-1}	2592		25084	
	ln A	7.86	± 0.69	10.13	± 1.96
Linear diatomic					
O_2	$Ea/kJmol^{-1}$	**30.9**	**± 2.6**	**43.2**	**± 3.5**
	A/s^{-1}	3905		369535	
	ln A	8.27	± 1.07	12.82	± 1.44
N_2	$Ea/kJmol^{-1}$	**34.6**	**± 3.1**	**36.3**	**± 3.3**
	A/s^{-1}	646		796	
	ln A	6.47	± 1.25	6.68	± 1.33
Linear triatomic				(From the mathematical model) (Fast stage)	
CO_2	$Ea/kJmol^{-1}$	**12.6**	**± 1.3**	**10.7**	**± 2.9**
	A/s^{-1}	1.03		0.2	
	ln A	2.87×10^{-2}	± 0.53	-1.61	± 1.18
				(From the mathematical model) (Fast stage)	
N_2O	$Ea/kJmol^{-1}$	**11.6**	**± 1.3**	**8.4**	**± 1.7**
	A/s^{-1}	0.99		0.095	
	ln A	-9.02×10^{-5}	± 0.5	-2.35	± 0.67

Table 5.6 continued

Gas		Adsorption		Desorption	
Linear tetratomic					
C_2H_2		(Initial rate 22.5% mass uptake)			
	$Ea/kJmol^{-1}$	**24.5**	± **2.0**		
	A/s^{-1}	2.33			
	ln A	0.845	± 0.8		
		(From the mathematical model)			
C_2H_2		(Fast)		(Fast stage)	
	$Ea/kJmol^{-1}$	**30.4**	± **1.2**	**31.0**	± **7.9**
	A/s^{-1}	27.46		41.06	
	ln A	3.31	± 0.49	3.71(5)	± 3.13
				(Slow stage)	
C_2H_2	$Ea/kJmol^{-1}$			**36.1**	± **7.9**
	A/s^{-1}			38.63	
	ln A			3.65(4)	± 3.16
Planar					
C_2H_4		(For first 9.5% of the data)			
	$Ea/kJmol^{-1}$	**39.6**	± **7.4**	**38.4**	± **14.25**
	A/s^{-1}	115.58		124.5	
	ln A	4.75	± 2.9	4.82(4)	± 5.58
C_2H_4		(For first 19% of the data)			
	$Ea/kJmol^{-1}$	**35.5**	± **7.8**	**30.9**	± **9.8**
	A/s^{-1}	25.12		5.92	
	ln A	3.22(4)	± 3.1	1.78	± 3.83

Gas		Adsorption		Desorption	
C_2H_4				(For 80% of the data)	
	Ea/kJmol^{-1}			**30.6**	**± 2.6**
	A/s^{-1}			2.41	
	ln A			0.88	± 0.10
		(From the mathematical model)			
C_2H_4		(Fast stage)		(Fast stage)	
	Ea/kJmol^{-1}	**36.1**	**± 1.1**	-	
	A/s^{-1}	33.20		-	
	ln A	3.5	± 0.41	-	

5.2.3 *Partial pressures for probe molecules*

Comparison of the adsorption capacities for the gases studied is difficult because many of the gas adsorption experiments are carried out above the critical temperature and, hence, a true saturated vapour pressure does not exist. Two approaches were considered for comparison of the capacities of the CMS for the gases studied. These approaches are as follows (1) extrapolation of the equation used for calculating p_0 below the critical temperature to above the critical temperature thereby providing a hypothetical p_0 value and (2) calculation of the monolayer surface coverage assuming that the isotherm follows the Langmuir equation. In this study the former has been used. The limitation of this approach is that the extrapolations are long for argon, nitrogen and oxygen. Table 5.7 below shows the partial pressure of the gases used and the results of adsorption and desorption kinetics and capacity of different gases in temperature range of 275-333 K on commercial carbon molecular sieve CMS A3. The hypothetical saturated vapour pressure has been calculated by extrapolation of equations applicable up to the critical pressure[2].

Table 5.7

Relative pressures (p/p_0) and hypothetical relative pressures for probe molecules

Probe molecule	Temperature/K	Relative pressure p/p_0
Argon	275	13.53×10^{-4}
Critical temperature	283	12.37×10^{-4}
150.8 K	294	11.01×10^{-4}
	297	10.69×10^{-4}
	303	10.08×10^{-4}
	313	91.93×10^{-5}
	323	84.31×10^{-5}
	333	77.72×10^{-5}
Oxygen	275	16.31×10^{-4}
(Atmospheric pressure)	283	14.91×10^{-4}
Critical temperature	292	13.29×10^{-4}
154.58 K	303	12.16×10^{-4}
	313	11.09×10^{-4}

Table 5.7 continued

Probe molecule	Temperature/K	p/p_o
Oxygen	275	65.22×10^{-4}
(High pressure)	293	53.70×10^{-4}
(0.4 MPa)	303	48.66×10^{-4}
	313	44.37×10^{-4}
	323	40.69×10^{-4}
	333	37.51×10^{-4}
Nitrogen	275	10.33×10^{-4}
Critical temperature	283	95.65×10^{-5}
126.2 K	298	86.62×10^{-5}
	303	80.30×10^{-5}
	313	74.20×10^{-5}
	323	68.90×10^{-5}
	333	64.26×10^{-5}
Carbon dioxide	275	2.90×10^{-2}
Critical temperature	293	1.80×10^{-2}
304 K	303	1.40×10^{-2}
	313	1.00×10^{-2}
	323	5.00×10^{-3}
	333	2.00×10^{-3}
Nitrous oxide	275	23.28×10^{-3}
Critical temperature	283	18.20×10^{-3}
309.5 K	301	10.97×10^{-3}
	303	10.40×10^{-3}
	313	80.81×10^{-4}
	323	63.76×10^{-4}

Table 5.7 continued

Probe molecule	Temperature/K	p/p_o
Ethyne	283	25.03×10^{-3}
Critical temperature	301	15.24×10^{-3}
308.5 K	303	14.47×10^{-3}
	308	12.76×10^{-3}
	313	11.30×10^{-3}
	323	89.59×10^{-4}
Ethene	301	11.83×10^{-3}
Critical temperature	303	98.51×10^{-4}
282.9 K	313	82.95×10^{-4}
	323	70.58×10^{-4}

The CO_2 273 K isotherm for the CMS A3 is also given in Table 5.8. The results clearly show that the isotherm follows a Langmuir equation closely and this is shown in Figure 5.51. The surface area obtained from the gradient of the Langmuir graph is a monolayer coverage of 2.37 mmol g^{-1} which corresponds to a surface area of 243 m^2 g^{-1} assuming a surface area of 1.7×10^{-19} m^2 for the area of a CO_2 molecule.

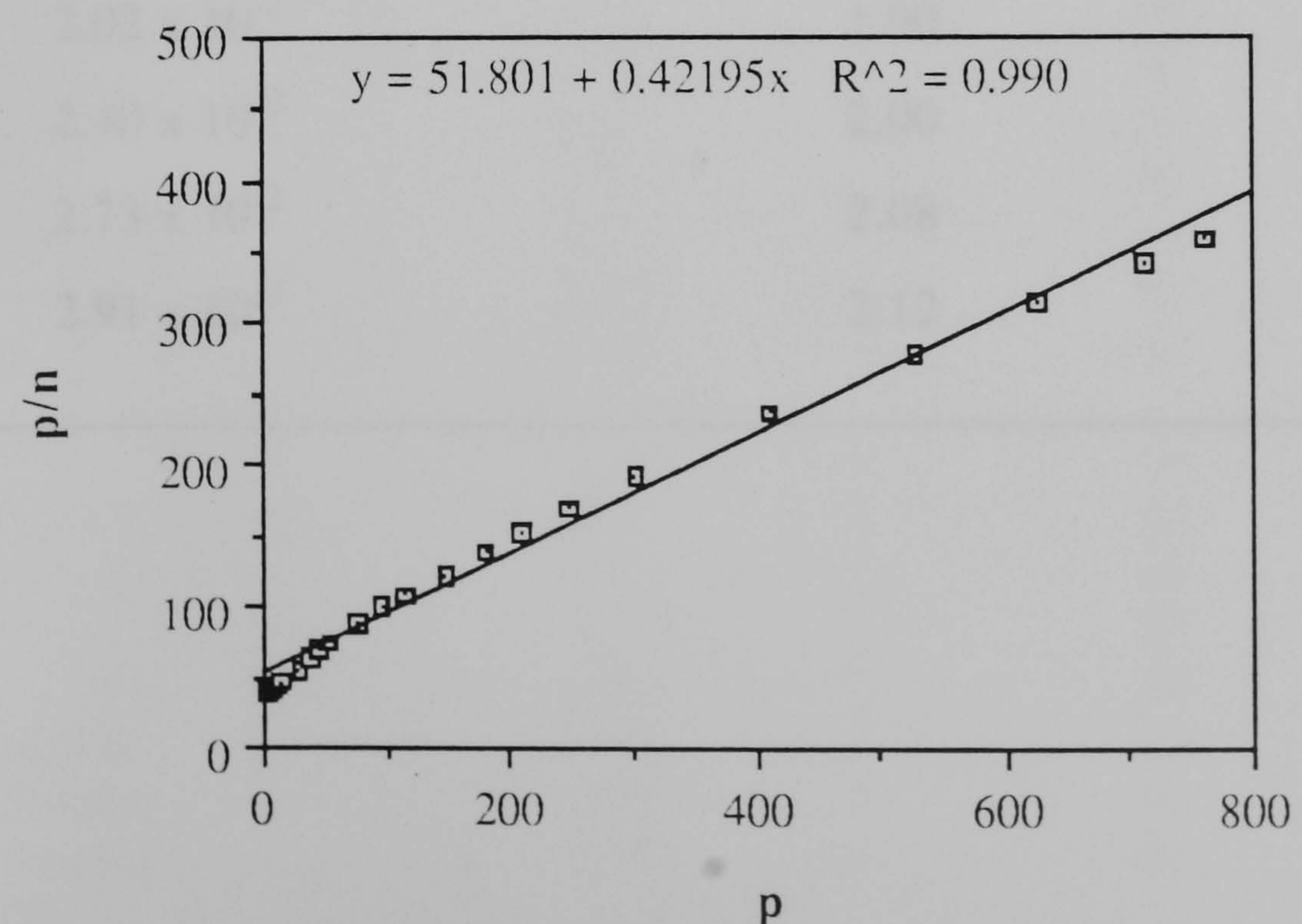

Figure 5.51 Langmuir graph for CMS A3.

Table 5.8 continued

CO_2 273 K isotherm for CMS A3

Relative pressure (p/p_o)	mmol g^{-1}
5.30×10^{-4}	2.95×10^{-1}
1.08×10^{-3}	5.06×10^{-1}
1.44×10^{-3}	6.02×10^{-1}
1.75×10^{-3}	6.65×10^{-1}
2.14×10^{-3}	7.33×10^{-1}
2.93×10^{-3}	8.69×10^{-1}
3.70×10^{-3}	9.80×10^{-1}
4.42×10^{-3}	1.066
5.58×10^{-3}	1.18
6.87×10^{-3}	1.29
7.95×10^{-3}	1.36
9.43×10^{-3}	1.45
1.15×10^{-3}	1.56
1.57×10^{-2}	1.75
2.02×10^{-2}	1.90
2.40×10^{-2}	2.00
2.73×10^{-2}	2.08
2.91×10^{-2}	2.12

5.3 Characterisation of Carbons

5.3.1 Preparation Conditions of Carbon

Table 5.9 gives a summary of preparation conditions of all carbons synthesised.

Table 5.9

Summary of preparation conditions of carbons produced.

(1) Polymer and resin based carbons.

Materials used	Weight fraction Aromatic	HTT (K)	Heating rate ($K\ min^{-1}$)	Soak time (min)	Pressure (MPa)
PVDC	-	873	1	60	0.1
PVDC	-	973	1	60	0.1
PVDC	-	1073	1	60	0.1
PVDC	-	1173	1	60	0.1
PVDC	-	1173	15 ($K\ h^{-1}$)	60	0.1
PVDC	-	873	1	60	7.5
PVDC	-	1173	1	60	0
PVDC-CH_4 (10min)	-	1173	1	60	0.1
PVDC-CH_4 (20min)	-	1173	1	60	0.1
PVDC-CH_4 (30min)	-	1173	1	60	0.1
PVDC:Acridine	0.25	873	1	60	0.1
PVDC:Acridine	0.50	873	1	60	0.1
PVDC:Acridine	0.75	873	1	60	0.1
PVDC:Carbazole	0.25	873	1	60	0.1
PVDC:Carbazole	0.50	873	1	60	0.1
PVDC:Carbazole	0.75	873	1	60	0.1
PVDC:Novolak	0.50	873	1	60	0.1
PVDC:Acenaphthylene	0.25	1173	1	60	0.1
PVDC:Dibenzofuran	0.25	1173	1	60	0.1
PVDC:Dihydroxy-naphthalene	0.25	1173	1	60	0.1
PVDF	-	1173	1	60	0.1
PEEK	-	873	1	60	0.1
PEEK	-	1073	1	60	0.1
PEEK	-	1173	1	60	0.1
PFA	-	1173	5	60	0.1
PFA + 1% Sulphur	-	1173	5	60	0.1
PFA + 10% Sulphur	-	1173	5	60	0.1
PFA + 20% Sulphur	-	1173	5	60	0.1

0.1 MPa ≡ Atmospheric pressure   0 = Vacuum < 5×10^{-4} MPa

Table 5.9 continued

(2) Coconut and wood based carbons.

Materials used	Weight fraction Aromatic	HTT (K)	Heating rate (K min^{-1})	Soak time (min)	Pressure (MPa)
C1	-	873	1	60	0.1
C2	-	1023	1	60	0.1
C3	-	1173	1	60	0.1
C4	-	873	50	60	0.1
C5	-	973	50	60	0.1
C6	-	1073	50	60	0.1
C7	-	1173	50	60	0.1
C8	-	873	1	60	0
C9	-	1073	1	60	0
C10	-	1173	1	60	0
C11	-	873	50	60	0
C12	-	973	50	60	0
C13	-	1073	50	60	0
C14	-	1173	50	60	0
C15	-	873	1	60	6.6
C16	-	873	1	60	10.2
C17	-	873	1	60	12.24
C18	-	873	50	60	6.6
C19	-	873	50	60	10.2
C20	-	873	50	60	12.24
C21	-	1173	1 (K h^{-1})	60	0
C21 + Pitch	0.50	1173	1 (K h^{-1})	60	0
C22	-	1173	15 (K h^{-1})	60	0
Cellulose-tri-acetate	-	1173	15(K h^{-1})	60	0
Teak	-	873	50	60	7.5
Beech	-	873	50	60	7.5
Beech	-	873	1	60	0.1
Beech	-	1173	1	60	0.1

0.1 MPa ≡ Atmospheric pressure   0 = Vacuum < 5 x 10^{-4} MPa

5.3.2 Surface Area

Table 5.10 shows the total surface area measurement for the different carbons obtained from carbon dioxide adsorption at 273 K. Each sample was measured in duplicate. The repeatability of the surface area measurements was ~ ± 10 $m^2 g^{-1}$. Surface area gives an estimation of the acessible microporosity. The higher the surface area more microporous is the carbon

The results show that the commercial CMS materials and active carbons have a high surface area indicating presence of microporosity. In comparison the carbons synthesised in the laboratory show higher surface area for carbons like pure PVDC and coconut shell carbons. Addition of aromatics to pure PVDC led to a decrease in surface area. PVDC carbons prepared by methane pyrolysis also tend to show a decrease in surface area with increasing methane pyrolysis time. The surface area of PVDF carbon was slightly low compared with that of pure PVDC carbon. The PEEK carbons also had lower surface areas compared with the pure PVDC carbons. PFA carbons showed a decrease in surface area with addition of sulphur. Coconut shell carbons obtained under high pressure conditions showed low surface area as compared to those obtained under atmospheric pressure and vacuum carbonisation.

Table 5.10

(1) The apparant surface area (CO_2,273 K) of commercial samples.

Sample	Apparant surface area (m^2g^{-1}) min.	max.*
CMS A	250	360
CMS B	355	450
EP 1	265	345
EP 2	341	495
EP 3	295	335
EP 4	315	435
Chemviron	355	735
Sutcliffe	250	500

* From the extrapolation of the D-R plot.

Table 5.10 continued

(2) Apparant surface area (CO_2,273 K) of polymer and resin based carbons.

Materials used	Weight fraction Aromatic	HTT (K)	Heating rate (K min^{-1})	Soak time (min)	Pressure (MPa)	Apparant surface area (m^2g^{-1}) min.	max.
PVDC	-	873	1	60	0.1	460	900
PVDC	-	1173	1	60	0.1	650	1670
PVDC	-	873	1	60	7.5	230	320
PVDC	-	1173	1	60	0	575	1160
PVDC-CH_4(10 min)	-	1173	1	60	0.1	180	770
PVDC-CH_4(20 min)	-	1173	1	60	0.1	287	778
PVDC-CH_4(30 min)	-	1173	1	60	0.1	150	650
PVDC:Acridine	0.25	873	1	60	0.1	300	430
PVDC:Acridine	0.50	873	1	60	0.1	355	480
PVDC:Acridine	0.75	873	1	60	0.1	215	300
PVDC:Carbazole	0.25	873	1	60	0.1	250	460
PVDC:Carbazole	0.50	873	1	60	0.1	260	420
PVDC:Carbazole	0.75	873	1	60	0.1	245	415
PVDC:Acenaphthylene	0.25	1173	1	60	0.1	390	600
PVDC:Dibenzofuran	0.25	1173	1	60	0.1	460	780
PVDC:Dihydroxy-napthalene	0.25	1173	1	60	0.1	315	510
PVDC:Novolak	0.50	873	1	60	0.1	420	655
PVDF	-	1173	1	60	0.1	550	1450
PEEK	-	873	1	60	0.1	300	507
PEEK	-	1073	1	60	0.1	480	716
PEEK	-	1173	1	60	0.1	115	200
PFA	-	1173	5	60	0.1	250	430
PFA + 1% sulphur	-	1173	5	60	0.1	265	430
PFA + 10% sulphur	-	1173	5	60	0.1	230	335

0.1 MPa ≡ Atmospheric pressure   0 = Vacuum < 5 x 10^{-4} MPa

Table 5.10 continued

(3) Apparant surface area (CO_2,273 K) of coconut, wood and cellulose based carbons.

Materials used	Weight fraction aromatic	HTT (K)	Heating rate (K min^{-1})	Soak time (min)	Pressure (MPa)	Apparant surface area ($m^2 g^{-1}$) min.	max.
C1	-	873	1	60	0.1	145	270
C2	-	1023	1	60	0.1	320	495
C3	-	1173	1	60	0.1	420	510
C4	-	873	50	60	0.1	180	345
C5	-	973	50	60	0.1	335	480
C6	-	1073	50	60	0.1	340	500
C7	-	1173	50	60	0.1	370	520
C8	-	873	1	60	0	340	525
C9	-	1073	1	60	0	430	660
C10	-	1173	1	60	0	425	600
C11	-	873	50	60	0	300	445
C12	-	973	50	60	0	380	550
C13	-	1073	50	60	0	370	510
C14	-	1173	50	60	0	435	605
C15	-	873	1	60	6.6	115	215
C16	-	873	1	60	10.2	130	222
C17	-	873	1	60	12.24	135	248
C18	-	873	50	60	6.6	110	150
C19	-	873	50	60	10.2	140	285
C20	-	873	50	60	12.2	153	165
C21	-	1173	1 (K h^{-1})	60	0	430	590
C21 + pitch		1173	1 (K h^{-1})	60	0	100	400
Cellulose triacetate		1173	15 (K h^{-1})	60	0	125	535
Beech	-	873	1	60	0.1	340	615
Teak	-	873	1	60	7.5	200	480

C=Coconut shell 0.1 MPa ≡ Atmospheric pressure 0 = Vacuum < 5 x 10^{-4} MPa

5.3.3 Helium Density

Table 5.11 gives the helium density of high capacity and high surface area carbons which were measured using a Micromeritics AccuPyc 1330 instrument. This was carried out in order to assess the closed porosity for these carbon and to determine if there was any scope for further activation.

The commercial samples have helium densities close to that of graphite indicating that these samples do not have any scope for substantial further activation. However, the active carbons (Chemviron and Sutcliffe) show high helium densities. Thermogravimetric analysis, Section 5.3.4 indicates the presence of mineral matter which could be the reason for high helium densities for these two carbons. The helium density values for all laboratory based carbons are quite close to that of graphite. Hence, they do not have any scope for further activation.

Table 5.11

(1) Helium density results for commercial samples.

Sample	Helium density ($g\ cc^{-1}$)
CMS A	1.99
CMS	2.02
EP 1	1.96
EP 2	1.94
EP 3	1.97
EP 4	2.28
Chemviron	2.33
Sutcliffe	2.41

Table 5.11 continued

(2) Helium density of polymer and resin based carbons.

Materials used	Weight fraction aromatic	HTT (K)	Heating rate (K min^{-1})	Soak time (h)	Pressure (MPa)	Helium density (g cc^{-1})
PVDC	-	873	1	60	0.1	1.53
PVDC	-	973	1	60	0.1	1.78
PVDC	-	1073	1	60	0.1	1.73
PVDC	-	1173	1	60	0.1	1.89
PVDC	-	873	1	60	7.5	1.64
PVDC	-	1173	15(K h^{-1})	60	0.1	2.18
PVDC-CH_4(10 min)	-	1173	1	60	0.1	2.09
PVDC-CH_4(20 min)	-	1173	1	60	0.1	2.19
PVDC-CH_4(30 min)	-	1173	1	60	0.1	1.48
PVDC:Acridine	0.25	873	1	60	0.1	1.66
PVDC:Acridine	0.50	873	1	60	0.1	1.64
PVDC:Acridine	0.75	873	1	60	0.1	1.63
PVDC:Acenaphthylene	0.25	1173	1	60	0.1	2.04
PVDC:Dibenzofuran	0.25	1173	1	60	0.1	2.06
PVDC:Dihydroxy -naphthalene	0.25	1173	1	60	0.1	1.97
PVDC:Novolak	0.50	873	1	60	0.1	1.45
PVDF	-	1173	1	60	0.1	2.13
PEEK	-	873	1	60	0.1	1.41
PEEK	-	873	1	60	0.1	1.93
PEEK	-	1173	1	60	0.1	2.02
PFA	-	1173	5	60	0.1	1.79
PFA + 1% sulphur	-	1173	5	60	0.1	1.39
PFA + 10% sulphur	-	1173	5	60	0.1	1.40

0.1 MPa ≡ Atmospheric pressure 0 = Vacuum < 5 x 10^{-4} MPa

Table 5.11 continued

(3) Helium density results for coconut, cellulose and wood based carbons.

Materials used	Weight fraction aromatic	HTT (K)	Heating rate ($K\ min^{-1}$)	Soak time (min)	Pressure (MPa)	Helium density ($g\ cc^{-1}$)
C1	-	873	1	60	0.1	1.42
C2	-	1023	1	60	0.1	1.77
C3	-	1173	1	60	0.1	2.04
C4	-	873	50	60	0.1	1.41
C5	-	973	50	60	0.1	1.56
C6	-	1073	50	60	0.1	1.79
C7	-	1173	50	60	0.1	1.98
C8	-	873	1	60	0	1.51
C9	-	1073	1	60	0	1.96
C10	-	1173	1	60	0	2.02
C11	-	873	50	60	0	1.49
C12	-	973	50	60	0	1.67
C13	-	1073	50	60	0	1.87
C14	-	1173	50	60	0	1.80
C15	-	873	1	60	6.6	1.40
C16	-	873	1	60	10.2	1.79
C17	-	873	1	60	12.24	1.68
C18	-	873	50	60	6.6	1.44
C20	-	873	50	60	12.24	1.43
C21	-	1173	1 ($K\ h^{-1}$)	60	0	1.64
C21 + pitch	-	1173	1 ($K\ h^{-1}$)	60	0	1.83
Cellulose triacetate	-	1173	15 ($K\ h^{-1}$)	60	0	2.27
Beech	-	873	50	60	7.5	1.57
Teak	-	873	50	60	7.5	1.62
Beech	-	873	1	60	0.1	1.87
Beech	-	1173	1	60	0.1	2.21

0.1 MPa ≡ Atmospheric pressure   0 = Vacuum < 5×10^{-4} MPa

5.3.4 Thermogravimetric Analysis

Table 5.12 shows the thermogravimetric temperature data for polymers and resins. DTG analysis was carried out to assess the suitability of the polymers for blending in co-carbonisation studies. Polymers with similar decomposition temperatures were used because reaction/fusion during carbonisation would influence the nature of the carbon.

Table 5.12

Thermogravimetric data for the polymers and resin at heating rate 5 K/min to maximum temperature of 1073 K.

Polymer/Resin	Maximum weight loss temperature /K	Decomposition start of weight loss/K
PVDC	528	417
PEEK	783	473
PES	789	729
Novolak	591	393

Proximate analysis was carried out on activated carbons showing unusually high densities. The results for moisture content, volatile matter and ash percentages are shown in Table 5.13. Results indicate the presence of mineral matter which could have attributed to high helium densities for the two active carbons, Chemviron and Sutcliffe.

Table 5.13

Results obtained from TGA analysis.

Sample content (%)	Moisture matter (%)	Volatile (%)	Ash
Sutcliffe	3.12	6.2	20.03
Chemviron	0.58	1.2	11.83

5.3.5 *Gravimetric Capacities and Kinetics of Different Carbons and Capacities of all Carbons Synthesised*

The equilibrium capacities for oxygen and nitrogen of carbons obtained from the co-carbonisation of PVDC with polynuclear aromatics or Novolak in different ratios, coconut shell carbons, PEEK, PFA etc. using gravimetric uptake technique and are shown in Table 5.14. Pure PVDC carbons show maximum capacity for oxygen and nitrogen. Addition of aromatics to pure PVDC led to a decrease in the capacity. PVDF carbon possessed similar capacity as that of pure PVDC carbon. PEEK carbons did not have high capacities for oxygen or nitrogen compared with pure PVDC carbons, and the addition of sulphur to PFA led to a decrease in oxygen and nitrogen adsorption capacity. Coconut shell carbonised under vacuum conditions had slightly lower capacity compared with that of pure PVDC. Coconut shell carbons obtained by high pressure carbonisation possessed lower capacity compared with those obtained under atmospheric pressure and vacuum carbonisation conditions.

Table 5.14

(1) The equilibrium capacities for oxygen and nitrogen for carbons derived from PVDC:Aromatics/resin etc.

Sample	Weight fraction aromatic	HTT (K)	Rate ($K\ min^{-1}$)	Soak (min)	Pressure (MPa)	Capacity ($cc\ g^{-1}$) O_2	N_2
PVDC	-	873	1	60	0.1	8.46	7.60
PVDC	-	973	1	60	0.1	7.42	8.09
PVDC	-	1073	1	60	0.1	9.93	9.76
PVDC	-	1173	1	60	0.1	10.22	11.31
PVDC	-	1173	15($K\ h^{-1}$)	60	0.1	10.70	11.30
PVDC	-	873	1	60	7.5	3.29	3.50
PVDC	-	1173	1	60	0	10.53	11.91
PVDC-CH_4(10 min)	-	1173	1	60	0.1	9.02	10.62
PVDC-CH_4(20 min)	-	1173	1	60	0.1	9.01	9.63
PVDC-CH_4(30 min)	-	1173	1	60	0.1	7.54	8.43

Table 5.14 continued

Sample	Weight fraction aromatic	HTT (K)	Rate ($K\ min^{-1}$)	Soak (min)	Pressure (MPa)	Capacity ($cc\ g^{-1}$) O_2	N_2
PVDC:Acridine	0.25	873	1	60	0.1	3.76	3.18
PVDC:Acridine	0.50	873	1	60	0.1	3.30	2.76
PVDC:Acridine	0.75	873	1	60	0.1	2.28	2.07
PVDC:Carbazole	0.25	873	1	60	0.1	3.65	1.69
PVDC:Carbazole	0.50	873	1	60	0.1	4.32	4.12
PVDC:Carbazole	0.75	873	1	60	0.1	2.28	2.87
PVDC:Acenaphthylene	0.25	1173	1	60	0.1	5.58	6.05
PVDC:Dibenzofuran	0.25	1173	1	60	0.1	8.05	8.48
PVDC:Dihydroxyl-napthalene	0.25	1173	1	60	0.1	5.50	4.00
PVDC:Novolak	0.50	873	1	60	0.1	5.02	4.43
PVDF	-	1173	1	60	0.1	9.00	10.30
PEEK	-	873	1	60	0.1	3.5	3.60
PEEK	-	1073	1	60	0.1	8.84	9.74
PEEK	-	1173	1	60	0.1	7.45	6.92
PFA	-	1173	5	60	0.1	3.16	1.07
PFA + 1% sulphur	-	1173	5	60	0.1	0.66	-
PFA + 10% sulphur	-	1173	5	60	0.1	0.10	0.22

(2) Oxygen and nitrogen equilibrium capacities for coconut , wood and cellulose based carbons.

Sample	HTT (K)	Heating rate ($K\ min^{-1}$)	Soak time (min)	Gauge Pressure (MPa)	Capacity ($cc\ g^{-1}$) O_2	N_2
C1	873	1	60	0.1	1.70	0.80
C2	1023	1	60	0.1	6.20	6.30
C3	1173	1	60	0.1	8.20	7.40

Table 5.14 continued

Sample	HTT (K)	Heating rate ($K\ min^{-1}$)	Soak time (min)	Gauge Pressure (MPa)	Capacity ($cc\ g^{-1}$) O_2	N_2
C4	873	50	60	0.1	3.60	3.31
C7	1173	50	60	0.1	6.70	7.10
C8	873	1	60	0	4.80	3.80
C9	1073	1	60	0	9.00	9.70
C10	1173	1	60	0	8.91	10.65
C11	873	50	60	0	5.13	4.30
C12	973	50	60	0	8.30	8.30
C13	1073	50	60	0	10.15	10.50
C14	1173	50	60	0	11.77	11.65
C15	873	1	60	6.60	1.20	0.98
C17	873	1	60	12.24	1.00	0.96
C18	873	50	60	6.60	0.61	0.41
C20	873	50	60	12.24	2.20	1.00
C21	1173	1 ($K\ h^{-1}$)	60	0	9.00	10.30
C21 +pitch	1173	1 ($K\ h^{-1}$)	60	0	5.90	7.00
C22	1173	15 ($K\ h^{-1}$)	60	0	2.20	3.70
Cellulose-triacetate	1173	15 ($K\ h^{-1}$)	60	0	10.70	11.30
Beech	873	50	60	7.5	2.59	2.98
Teak	873	50	60	7.5	2.95	3.58
Beech	873	1	1	0.1	4.91	5.12
Beech	1173	1	1	0.1	5.14	6.23

C=coconut shell   0.1 MPa ≡ Atmospheric pressure   0 = Vacuum < 5 x 10^{-4} MPa

Table 5.15. shows the gas uptake rates for the carbons derived from the carbonisation of PVDC, PEEK, PFA, mixtures of PVDC and Aromatics and coconut shell carbons etc. The rates were calculated using the pseudo-first order method see Section 4.2.2 in Chapter Four for details. Pure PVDC carbons do not show any

selectivity. Carbons obtained by pyrolysis of methane over pure PVDC show selectivity, which decreases as the contact time increases. Carbons obtained by co-carbonisation of pure PVDC and aromatics do not show any marked selectivity. PEEK and PFA carbons do not show any selectivity. Carbons obtained by carbonisation of coconut shell under different conditions do not indicate presence of any selectivity either.

Table 5.15

The rates of gas uptake for carbons obtained by the carbonisation of different polymers, resins coconut shell and wood.

Sample	Weight fraction aromatic	HTT (K)	Pressure (MPa)	Rate constant (s^{-1}) O_2	Rate constant (s^{-1}) N_2	Selectivity
(Heating rate 1 K min^{-1}, 60 min soak time)						
PVDC	-	873	0.1	7.93×10^{-2}	6.18×10^{-2}	1.3
PVDC	-	973	0.1	6.01×10^{-2}	5.26×10^{-2}	1.1
PVDC	-	1073	0.1	8.03×10^{-2}	6.55×10^{-2}	1.2
PVDC	-	1173	0.1	5.84×10^{-2}	3.61×10^{-2}	1.6
PVDC	-	873	7.5	21.25×10^{-2}	14.48×10^{-2}	1.5
PVDC	-	1173	0	11.75×10^{-2}	4.25×10^{-2}	2.76
PVDC-CH_4(10 min)	-	1173	0.1	7.96×10^{-3}	1.31×10^{-3}	6.08
PVDC-CH_4(20 min)	-	1173	0.1	1.85×10^{-3}	4.03×10^{-4}	4.59
PVDC-CH_4(30 min)	-	1173	0.1	2.92×10^{-3}	9.59×10^{-4}	3.05
PVDC:Acridine	0.25	873	0.1	3.32×10^{-3}	3.73×10^{-3}	0.9
PVDC:Acridine	0.50	873	0.1	2.09×10^{-3}	3.39×10^{-3}	0.6
PVDC:Acridine	0.75	873	0.1	3.45×10^{-3}	2.22×10^{-3}	1.6
PVDC:Carbazole	0.25	873	0.1	12.55×10^{-2}	6.51×10^{-2}	1.9
PVDC:Carbazole	0.50	873	0.1	9.13×10^{-2}	5.69×10^{-2}	1.6
PVDC:Carbazole	0.75	873	0.1	10.63×10^{-2}	6.24×10^{-2}	1.7

Table 5.15 continued

Sample	Weight fraction aromatic	HTT (K)	Pressure (MPa)	Rate constant (s^{-1}) O_2	N_2	Selectivity
(Heating rate 1 K min^{-1}, 60 min soak time)						
PVDC:Acenaph -thylene	0.25	1173	0.1	3.46×10^{-3}	2.02×10^{-3}	1.7
PVDC:Dibenzofuran	0.25	1173	0.1	5.15×10^{-3}	3.13×10^{-3}	1.7
PVDC:Dihydroxy-napthalene	0.25	1173	0.1	2.12×10^{-3}	2.41×10^{-3}	0.9
PVDC:Novolak	0.50	873	0.1	3.83×10^{-2}	7.52×10^{-2}	0.5
PVDF	-	1173	0.1	1.10×10^{-3}	1.20×10^{-3}	0.9

Sample	Weight fraction aromatic	HTT (K)	Pressure (MPa)	Rate constant (s^{-1}) O_2	N_2	Selectivity
(Heating rate 1 K min^{-1}, 60 min soak time)						
PEEK	-	873	0.1	1.16×10^{-2}	4.21×10^{-3}	2.8
PEEK	-	1073	0.1	4.87×10^{-3}	4.33×10^{-3}	1.1
PEEK	-	1173	0.1	5.26×10^{-3}	2.23×10^{-3}	2.4

Sample	Weight fraction aromatic	HTT	Pressure (MPa)	Rate constant (s^{-1}) O_2	N_2	Selectivity
(Heating rate 5 K min^{-1}, 60 min soak time)						
PFA	-	1173	0.1	1.48×10^{-3}	1.79×10^{-3}	0.8
PFA + 1% sulphur	-	1173	0.1	0.85	0.92	0.9
PFA + 10% sulphur	-	1173	0.1	0.14	0.13	1.1

Sample	HTT (K)	Heating rate (K min^{-1})	Soak time (min)	Pressure (MPa)	Rate constant (s^{-1}) O_2	N_2	Selectivity
C1	873	1	60	0.1	3.80×10^{-3}	3.50×10^{-3}	1.01
C2	1023	1	60	0.1	8.90×10^{-3}	9.10×10^{-3}	1.0
C3	1173	1	60	0.1	5.80×10^{-3}	4.10×10^{-3}	1.41

Table 5.15 continued

Sample	HTT (K)	Heating rate (K min^{-1})	Soak time (min)	Pressure (MPa)	Rate constant (s^{-1}) O_2	N_2	Selectivity
C4	873	50	60	0.1	3.21×10^{-3}	2.09×10^{-3}	1.5
C5	973	50	60	0.1	1.14×10^{-3}	8.31×10^{-3}	1.41
C6	1073	50	60	0.1	6.98×10^{-3}	9.61×10^{-3}	0.72
C7	1173	50	60	0.1	1.14×10^{-3}	8.31×10^{-3}	1.40
C8	873	1	60	0	1.10×10^{-2}	7.80×10^{-3}	1.40
C9	1073	1	60	0	1.70×10^{-3}	9.04×10^{-4}	1.8
C10	1173	1	60	0	7.40×10^{-3}	1.0×10^{-3}	1.2
C11	873	50	60	0	2.10×10^{-2}	1.90×10^{-2}	1.10
C12	973	50	60	0	2.70×10^{-2}	1.70×10^{-2}	1.5
C13	1073	50	60	0	1.00×10^{-2}	8.60×10^{-2}	1.3
C14	1173	50	60	0	8.30×10^{-3}	3.5×10^{-3}	2.3
C15	873	1	60	6.6	0.20	0.19	1.1
C17	873	1	60	12.24	0.12	0.10	1.2
C18	873	50	60	6.60	0.28	0.32	0.87
C20	873	50	60	12.24	1.3×10^{-3}	7.6×10^{-3}	1.70
C21	1173	1 (K h^{-1})	60	0	7.4×10^{-3}	7.7×10^{-3}	0.8
C21 +pitch	1173	1 (K h^{-1})	60	0	1.6×10^{-3}	1.2×10^{-3}	1.3
C22	1173	15 (K h^{-1})	60	0	1.7×10^{-2}	2.4×10^{-3}	7.2
Beech	873	50	60	7.5	6.59×10^{-3}	3.85×10^{-3}	1.70
Teak	873	50	60	7.5	2.15×10^{-3}	7.38×10^{-3}	0.29
Beech	873	1	60	0.1	4.89×10^{-3}	3.04×10^{-3}	1.61
Beech	1173	1	60	0.1	3.11×10^{-3}	1.36×10^{-3}	2.3
Cellulose-triacetate	1173	15 (K h^{-1})	60	0	1.3×10^{-3}	4.56×10^{-3}	2.85

C=coconut 0.1 MPa ≡ Atmospheric pressure 0 = Vacuum < 5×10^{-4} MPa

5.3.6 Probe Molecule Analysis

Probe molecule studies were carried out in order to study the effect of pore size distribution with increasing carbonisation pressure. Hence a similar HTT of 873 K was chosen with different carbonisation pressures ranging from vacuum to 10.2 MPa. The pore size distribution of carbons decreased as carbonisation pressure increased.

The effect of varying HTT in the range of 873-1173 K on the pore size distribution for coconut shell vacuum carbons and PVDC carbons obtained by carbonisation under atmospheric carbonisation pressure was also studied. The pore size distribution tended to decrease with increasing carbonisation temperature and the pore size distribution became sharp near 0.4 nm.

The pore size distribution of carbons obtained by carbon vapour deposition was also determined. The pore size distribution tended to decrease with increasing carbon deposition time. Lastly the pore size distribution of carbons obtained by co-carbonisation of PVDC with polynuclear aromatics and some high capacity carbons was also assessed. The pore size distribution of the carbons was found to have shifted to smaller pore sizes with addition of polynuclear aromatics.

Table 5.16

Molecular probe analysis results

Material	Aromatic ratio	HTT (K)	Heating rate ($K\ min^{-1}$)	Soak time (min)	Pressure (MPa)	Methylene chloride (0.4 nm) (At 301 K)	Butane (0.43 nm) (At 275 K)	Chloroform (0.46 nm) (At 301 K)	Isopentane (0.49 nm) (At 301 K)	Carbon tetrachloride (0.6 nm) (At 301 K)
	Probe molecule					Capacity of different probe molecules used				
C1	-	873	1	60	0.1	0.163	0.033	0.053	0.023	0.018
C8	-	873	1	60	0	0.157	0.122	0.103	0.034	0.007
C15	-	873	1	60	6.6	0.125	0.029	0.014	0.000	0.007
C16	-	873	1	60	10.2	0.126	0.052	0.044	0.017	0.005
C11	-	873	50	60	0	0.159	0.037	0.031	0.023	0.027
C12	-	973	50	60	0	0.160	0.035	0.026	0.030	0.009
C13	-	1073	50	60	0	0.167	0.004	0.017	0.009	0.020
C14	-	1173	50	60	0	0.135	0.000	0.002	0.009	0.001
PVDC	-	873	1	60	0.1	0.295	0.309	0.275	0.272	0.200
PVDC	-	973	1	60	0.1	0.145	0.267	0.268	0.238	0.144
PVDC	-	1073	1	60	0.1	0.291	0.309	0.272	0.265	0.009
PVDC	-	1173	1	60	0.1	0.282	0.284	0.266	0.106	0.001
PVDC	-	1173	15	60	0.1	0.261	0.247	0.227	0.035	0.016

Table 5.16 continued

Material	Aromatic ratio	HTT (K)	Heating rate (K min^{-1})	Soak time (min)	Pressure (MPa)	Capacity of different probe molecules used: Methylene chloride (0.4 nm) (At 301 K)	Butane (0.43 nm) (At 275 K)	Chloroform (0.46 nm) (At 301 K)	Isopentane (0.49 nm) (At 301 K)	Carbon tetrachloride (0.6 nm) (At 301 K)
PVDC-CH_4 (10 minCH_4)	-	1173	1	60	0.1	0.262	0.073	0.068	0.045	0.005
PVDC-CH_4 (20 minCH_4)	-	1173	1	60	0.1	0.286	0.050	0.005	0.014	0.014
PVDC-CH_4 (30 min-CH_4)	-	1173	1	60	0.1	0.176	0.001	0.015	0.029	0.021
PVDC:Acridine	0.25	1173	1	60	0.1	0.132	0.112	0.052	0.035	0.000
PVDC:Acridine	0.50	1173	1	60	0.1	0.140	0.088	0.049	0.080	0.003
PVDC:Acridine	0.75	1173	1	60	0.1	0.073	0.042	0.014	0.018	0.000
PVDC:Acenap -thylele	0.25	1173	1	60	0.1	0.136	0.000	0.019	0.042	0.004
PVDC:Dibenzofuran	0.25	1173	1	60	0.1	0.206	0.000	0.019	0.015	0.002
PFA	-	1173	5	60	0.1	0.028	0.020	0.002	0.011	0.002
Cellulose triacetate	-	1173	15	60	0	0.259	0.249	0.170	0.182	0.092
CMS A3	-	-	-	-	-	0.141	0.037	0.028	0.044	0.016

C=Coconut 0=Vacuum CMS A3=Commercial carbon molecular sieve

References

(1) Sykes M.L., Chagger H.K. and Thomas K.M., *Carbon*, **31**, 827 (1993)

(2) *CRC Handbook of Chemistry and Physics, 66th Edition*,Eds. Weast, R.C., Astle, M.J. and Beyer, W.H., CRC Press, Florida (1986).

Chapter 6

Discussion

6.1 Introduction

Numerous physical and chemical techniques are available for the characterisation of microporous carbons. However, it is not possible to obtain a complete and unequivocal description of the structure of these carbons. Most of the techniques available are based on gas adsorption methods. The physisorption of molecules on a solid surface has an associated heat of adsorption. It is possible to follow the adsorption process by monitoring the evolution of heat. However the sites are not equivalent in energy since the surface may be heterogeneous and interactions exist between neighbouring adsorbed molecules. Active carbons and carbon molecular sieves have a complex porous structure. In addition, they contain functionality and inorganic material. Therefore, a wide variety of techniques are required in order to characterise the carbon structure. These methods include gas adsorption studies, calorimetry, probe molecule studies, helium density measurements and mercury porosimetry etc..

6.1.1 Background to the Use of FMC

The development of thermistors has made it possible to construct a compact flow microcalorimeter (FMC) having high sensitivity and ease of operation. FMC has been used in evaluating the surface properties of coals, active carbons, zeolites etc.[1]. FMC as a technique also gives as an insight into[1]:

(1) heats of adsorption and desorption,

(2) rates of adsorption and desorption,

(3) degree of reversibility of surface interactions,

(4) adsorption of several components, competitive adsorption and synergistic effects,

(5) preferential adsorption on specific surface sites and
(6) effects of temperature on heats of adsorption.

The idea behind using this technique was to assess the surface properties of the material by recording the heat of adsorption of a gas or a liquid on the particular adsorbent. This requires the use of an appropriate calibration factor[2].

FMC has been used in the past to determine the surface areas of a variety of materials. The total heat evolved, when an adsorbate was covered with a monolayer, multiplied by a calibration factor was taken as a measure of its surface area. This technique was applied with the assumption that firstly a close packed monolayer was formed when a selected polar solute was adsorbed from a dilute solution and secondly, the preferential heat of adsorption of solute per unit area was the same for different solid surfaces when the monolayer was formed. The surface area, S_A is directly proportional to the integral heat of adsorption per gram of solid ΔH, and can be written as[2]:

$$S_A = k\ \Delta H$$

where, k is the proportionality constant having dimensions of m^2/J and ΔH is the total heat produced in joules, when n-butanol forms a close-packed monolayer on the surface. For all solids studied the adsorption of n-butyl alcohol adsorbed from a 0.2% solution in n-heptane, was found to have a closely packed monolayer[2]. A close relationship was found between the surface areas estimated from the magnitude of integral heat of adsorption of n-butanol (obtained from FMC) and the nitrogen BET method[2].

FMC has also been used as a technique where the heats of adsorption have been used to provide information regarding the relative surface acidities and hydrophobicities of the coals[3]. The surface properties of coals were determined by studying the surface interactions with specific solutes. The surface area of polar sites can be estimated by determination of integral heats of adsorption of n-butanol from n-heptane. The polar surface area was obtained using the following calibration:

$$1\ J\ g^{-1} = 11.5\ m^2\ g^{-1}$$

The hydrophobicity was determined by taking the ratio of the heats of adsorption of n-butanol from water and n-heptane onto the coal samples. The acidity was assessed by measuring preferential adsorption of ammonium hydroxide from solution in water. Silica was chosen as a model solid as it possesses a surface with weak acidic sites. The weakness of acidic sites in silica was indicated by relatively low heats of ammonia adsorption and the complete reversibility, unlike coal samples which showed high heats of ammonia adsorption and mostly irreversible adsorption.

Heats of adsorption by selected solutes, like n-butanol and t-butanol from n-heptane were used for rapid evaluation of 'internal' and more accessible 'external' surface sites in zeolites. The heats of adsorption of n-butanol from n-heptane were found to be higher compared with the tertiary alcohol, as a large portion of the internal surface in zeolites were not accessible to large branched alcohols. Hence, it was concluded that the sites occupied by t-butanol were relatively polar in nature, as compared with sites within internal surface accessible to n-butanol. The heats of 1 J g^{-1} was taken to equivalent to 11.5 m^2 g^{-1} of the surface. The drawback of this technique was that the resulting surface areas were found to be higher than the corresponding BET nitrogen adsorption surface areas. This was attributed to the enhanced overlapping fields of surface forces acting on n-butanol within the micropore which consequently gave rise to enhanced heats of adsorption[4].

Basal planes and polar sites exist in active carbons and carbon molecular sieves. These can be considered separately as far as adsorption is concerned. The basal plane sites can be studied using heats of adsorption of n-dotriacontane for basal planes. Integral heats of adsorption were found to increase with solute concentration in a similar manner to those of the adsorption isotherm. Since the concentration of adsorbate in the carrier can be varied, it is possible to obtain isotherms, hence a conversion from J g^{-1} to m^2 g^{-1} can be calculated as explained previously. These integral heats of adsorption for amounts of n-dotriacontane were also found to be directly proportional to the number of surface sites capable of adsorbing n-dotriacontane. The heat of 1 J g^{-1} was found to correspond area covered by 8.1 mg of n-dotriacontane adsorbate consisting of close-packed horizontally oriented molecules, i.e. 19.3 $m^2\ g^{-1}$. Consequently n-dotriacontane from n-heptane was used as a measure of basal plane area in graphites.

This observation was found to be analogous to that concerning the adsorption of n-butanol. The method for comparing polar sites involves the determination of the integral heats of adsorption of n-butanol from dilute solution in n-heptane. In this case the n-butanol is adsorbed mainly on the polar sites. The calibration factor for the polar surface area was taken as: 1 J g^{-1} = 6.7 $m^2\ g^{-1}$.

In order to obtain measurements of graphiticity and polarity in terms of the total surface area of the material the resulting graphitic indices and the surface polarity indices were divided by total surface area of the carbons measured by the nitrogen BET method. The technique as found to be useful as it provides a quantitative measure of the affinity of the accessible carbon surfaces for non-polar and polar substances. This also gives an indication for hydrophilic/hydrophobic nature of carbons. The disadvantage was that the surface area estimated from the heats of adsorption measurements related only to the surface accessible to n-butanol or n-dotriacontane and excludes surfaces present in micropores with in diameters of less than 0.6 nm[5].

FMC has also been used to predict the performance of various microporous carbons in various selective adsorption processes. They were assessed by rapid evaluation of the patterns of heat evolution occurring by adsorption of gas/liquid on the adsorbent. The length of time to reach equilibrium differed for the specific probe molecule, depending upon its size and shape. The heat of preferential adsorption for the probe gave an estimation of the rate of adsorption[6]. Groszek *et. al.*[7] have established a correlation between the heats of adsorption of carbon dioxide and nitrogen BET surface area for several non-porous solids. However for microporous solids there is no direct correlation between the heats of adsorption of carbon dioxide and nitrogen BET surface area.

However, in this project for the first time the FMC technique has been exploited in terms of the measurements of the rate of gas uptake. The kinetic rate constants were calculated for gases such as oxygen and nitrogen on commercial CMS materials and active carbons. The results of which have been discussed below.

6.1.1.1 Assessment of Capacity and Selectivity of Commercial Materials using FMC and Gravimetric Uptake.

The kinetics of gas uptake measured using the FMC were calculated at the usual FMC flow rate (3 $cm^3 min^{-1}$) and a higher flow rate (14 $cm^3 min^{-1}$). The results obtained from the analysis of six CMS and two activated carbons were compared. They were related in terms of their capacities, rates and selectivity to that obtained by the gravimetric technique. This was done in order to assess the correlation between the two techniques for gas adsorption characteristics. The comparison of the rates and capacity data between the two techniques showed a limited degree of correlation.

The equilibrium capacities showed a close relationship between the two techniques with correlation of ($R^2 = 0.986$) for nitrogen capacity as measured with the FMC gas flow rate of $3 cm^3 min^{-1}$ and shown in Figure 6.1.

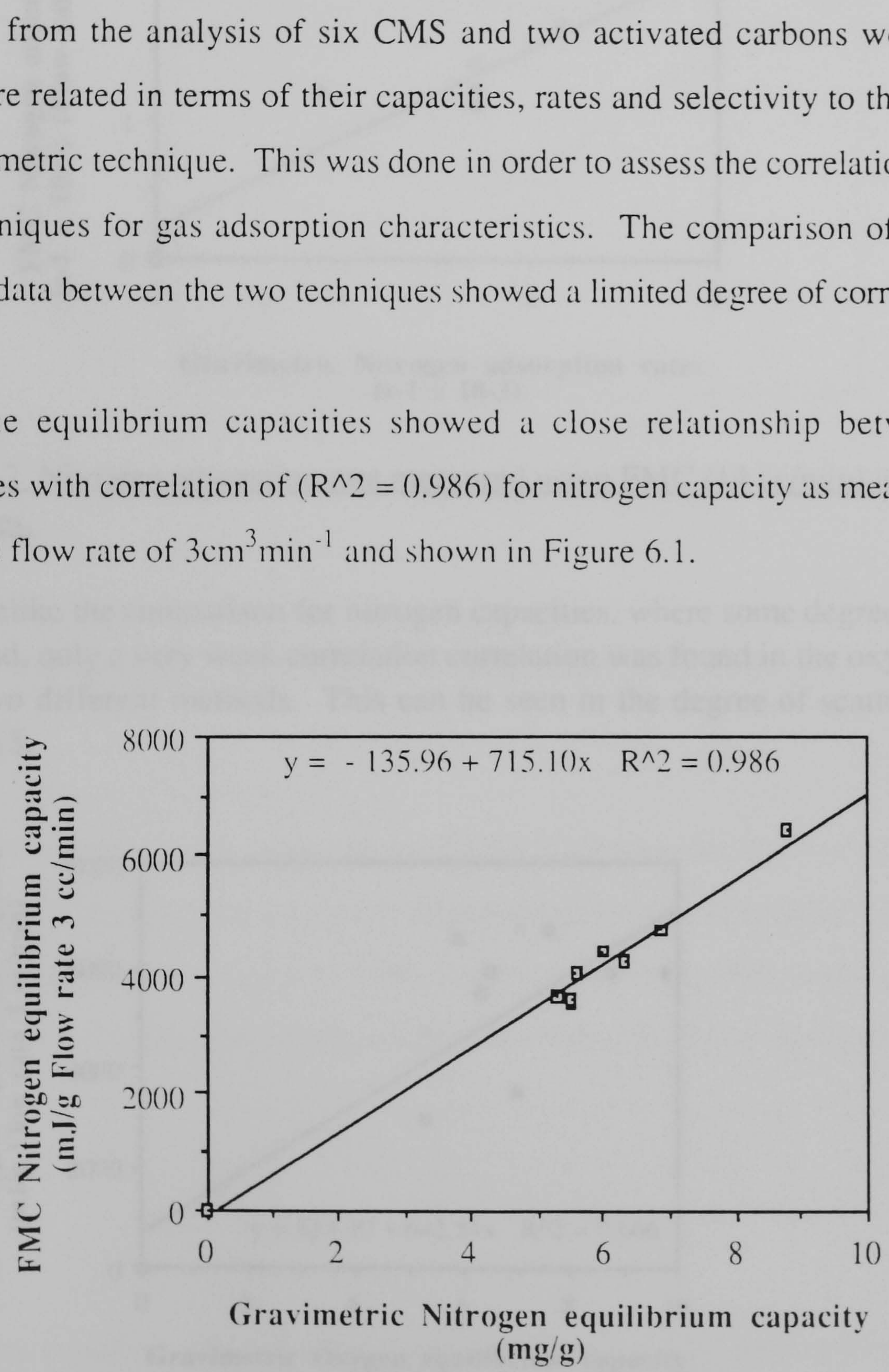

Figure 6.1 Nitrogen equilibrium capacities obtained using FMC (3 cc/min) and gravimetric technique.

A comparison of the nitrogen rates obtained by the two techniques is shown in Figure 6.2. The FMC flow rate was 14 $cm^3 min^{-1}$. A good correlation was observed but the observation that the correlation does not pass close to origin is probably indicative of a non-linear relationship between the rates measured by the two methods.

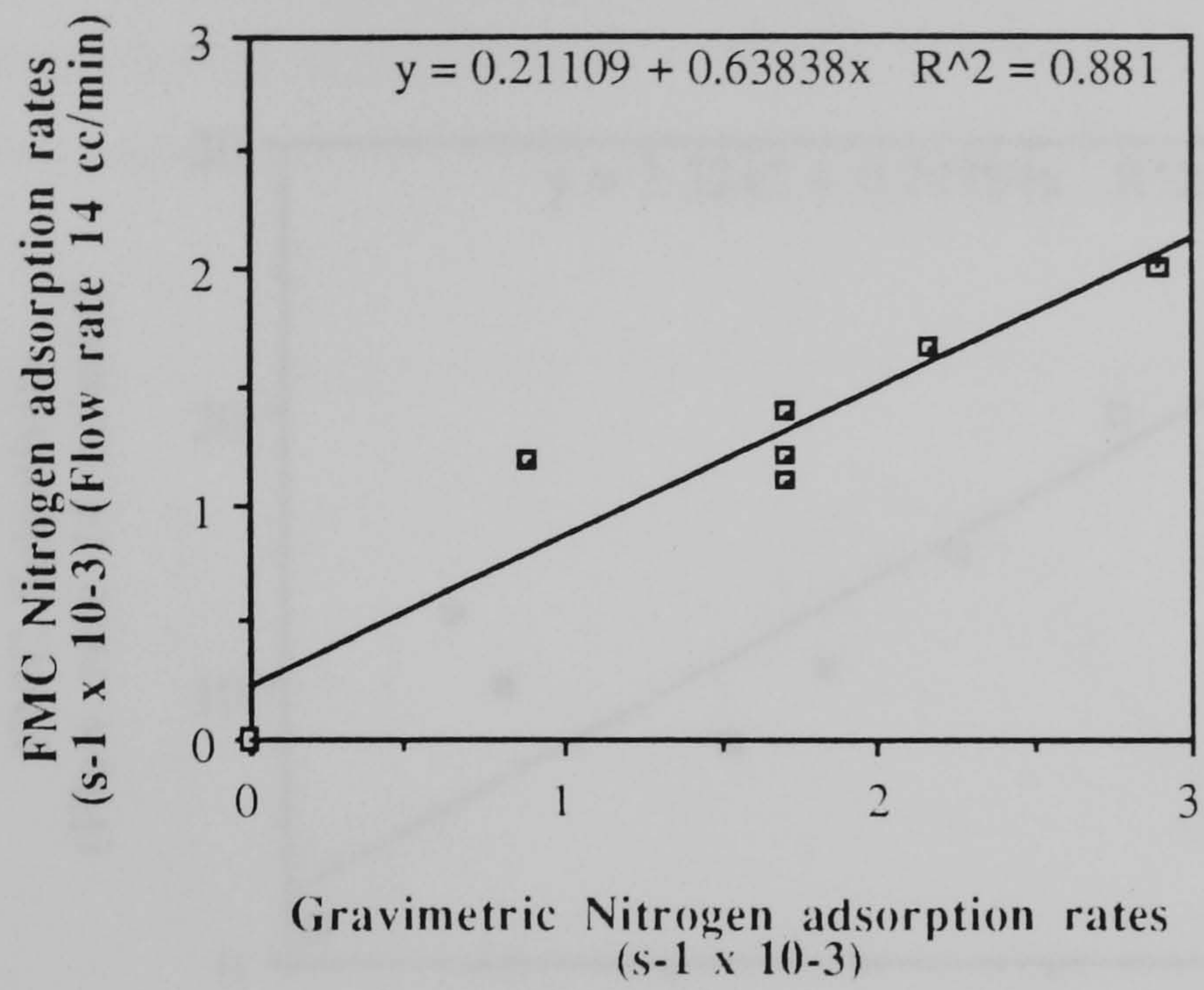

Figure 6.2 Nitrogen adsorption rate measured using FMC (14 cc/min) and gravimetric techniques.

Unlike the comparison for nitrogen capacities, where some degree of correlation was found, only a very weak correlation correlation was found in the oxygen capacities of the two different methods. This can be seen in the degree of scatter as shown in Figure 6.3.

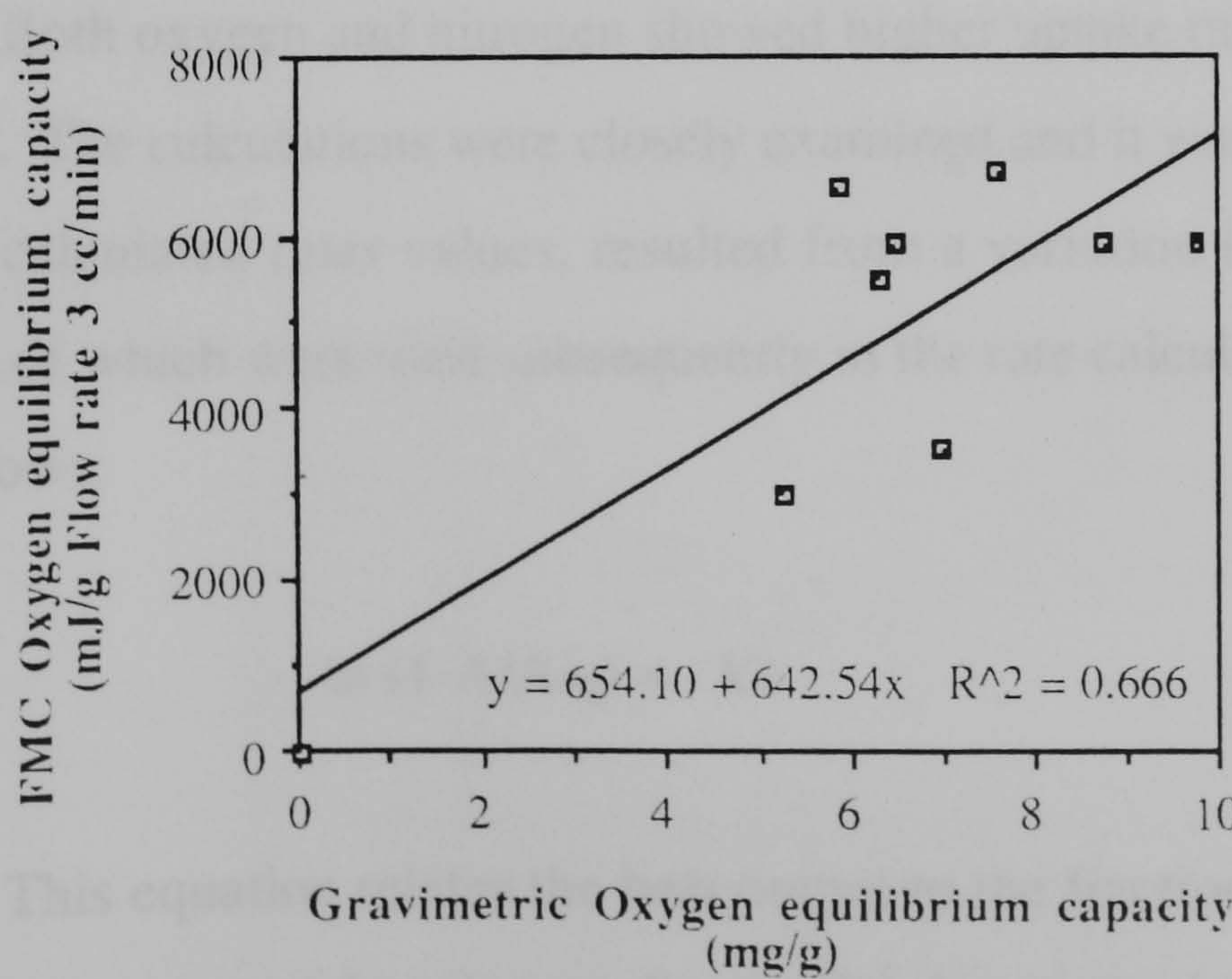

Figure 6.3 Oxygen equilibrium capacities obtained using FMC (3cc/min) and gravimetric techniques.

The selectivity factor calculated as the ratio of the oxygen rate constant to the corresponding nitrogen rate constant indicated that there was some degree of correlation between the two techniques. FMC experiments at 14 cm^3min^{-1} flow rate gave the closest approximation to gravimetric data (R^ 2 = 0.766), as shown in Figure 6.4.

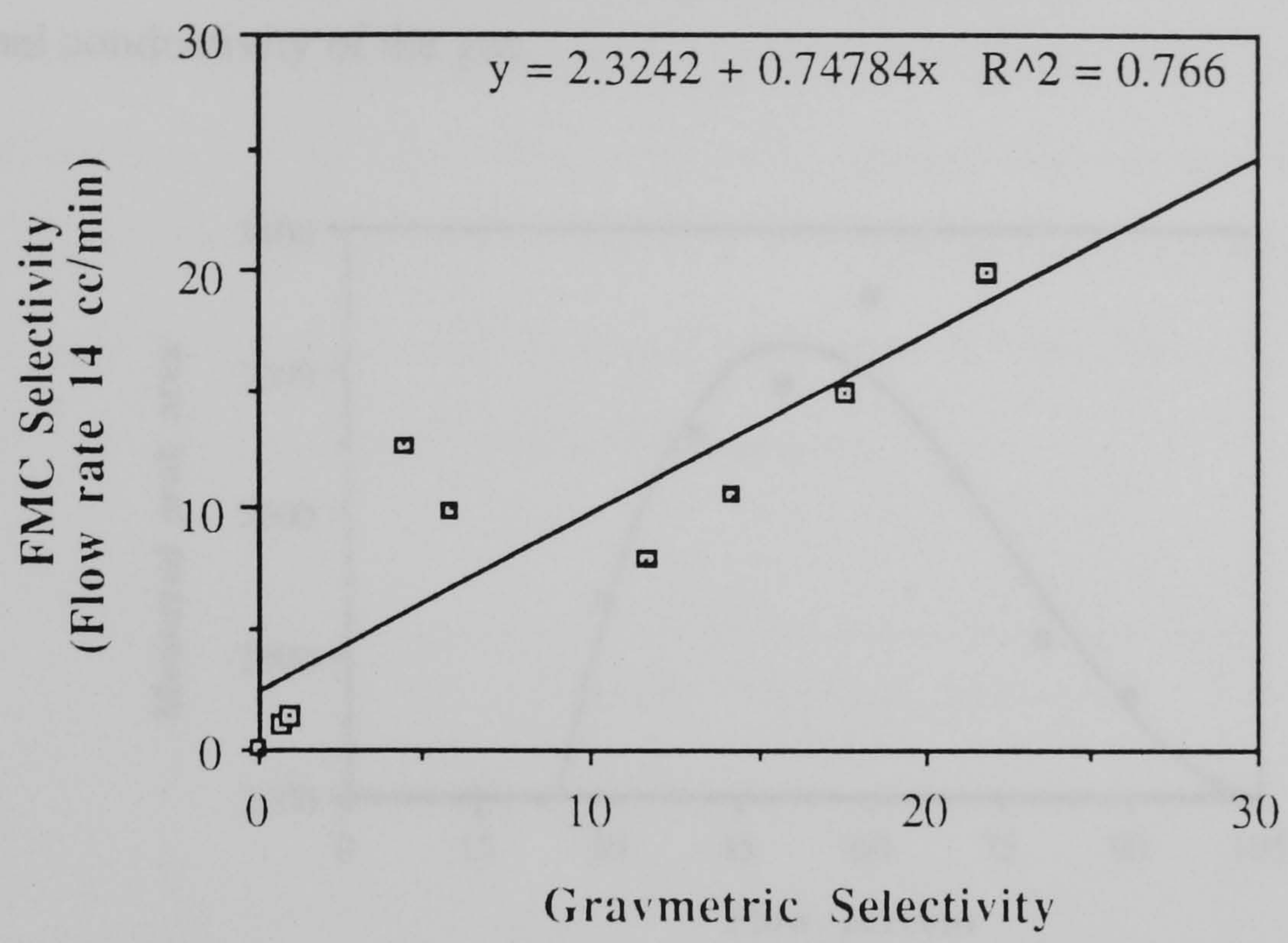

Figure 6.4 Selectivity measured using FMC (Flow rate 14 cc/min) and gravimetric technique.

Both oxygen and nitrogen showed higher uptake rates for slow flow rates (3 $cm^3 min^{-1}$). The calculations were closely examined and it was concluded that the reduction in the calculated rates values, resulted from a variation in the overall peak area. The values of which were used subsequently in the rate calculation equation which is given as follows:

$$\ln (1-A/A_{eq}) = - k't$$

This equation relates the heat output to the fractional peak area remaining. The greater the measured peak area the smaller the proportional change in the A/A_{eq} term with time in the part of the peak used for the measurement. This means that in the ln $(1-A/A_{eq})$ term, the rate may decrease with an increase in the measured value of A_{eq}.

This relationship was tested experimentally using Sutcliffe Speakman carbon which was analysed at different flow rates between 3 and 14 cm^3min^{-1}. Oxygen adsorption was followed using the FMC, and the rate of uptake calculated and peak area measured, the results of which are shown in Table 5.4. The uncalibrated peak areas showed variation with gas flow rate, as shown in Figure 6.5. The noted variation was not consistent but depended upon the shape of the heat output peak being studied and the thermal conductivity of the gas.

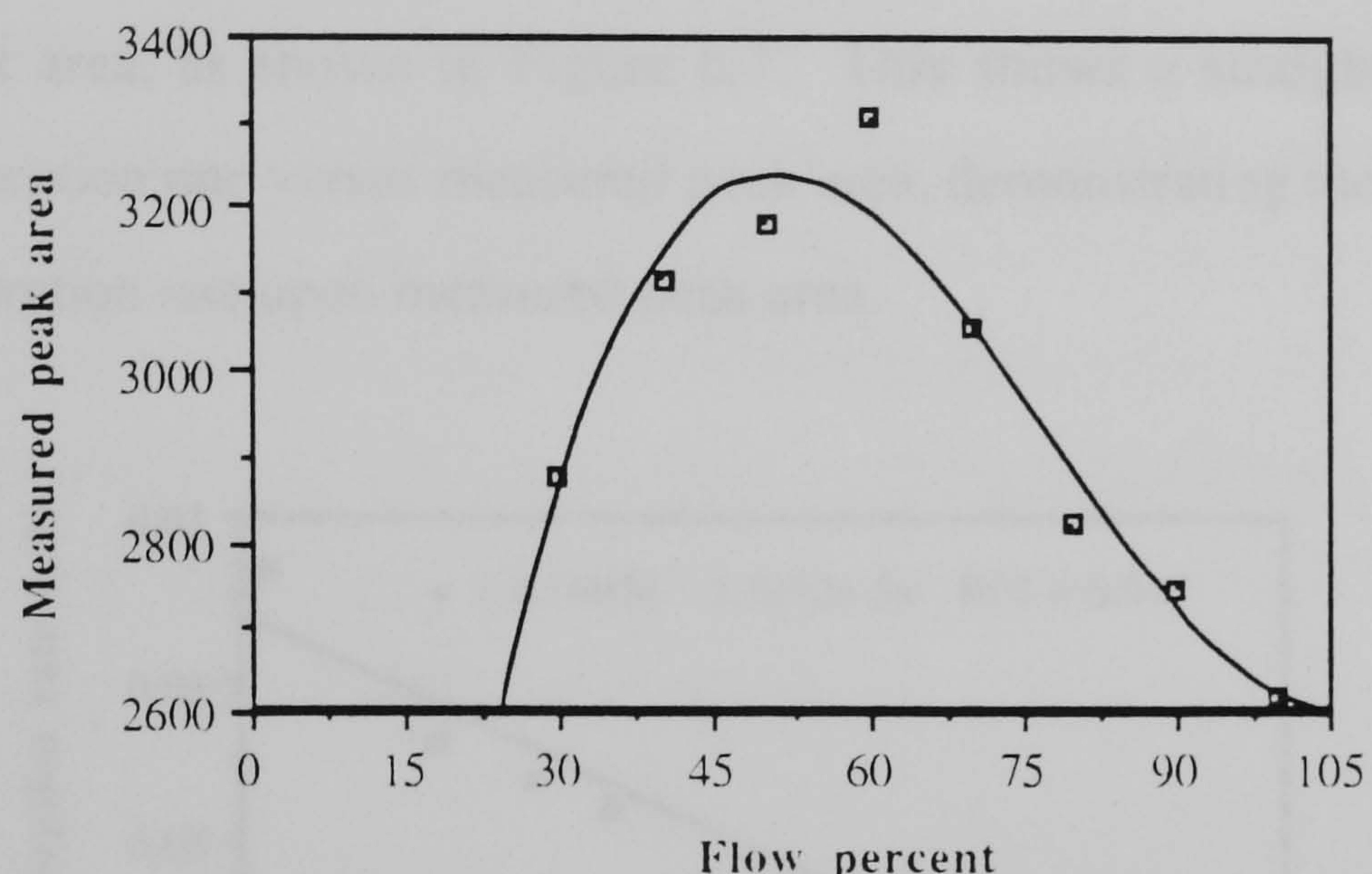

Figure 6.5 Graph of peak area versus gas flow percent.

Figure 6.6 obtained from the results in Table 5.4 shows a graph of calculated adsorption rate versus flow percent.

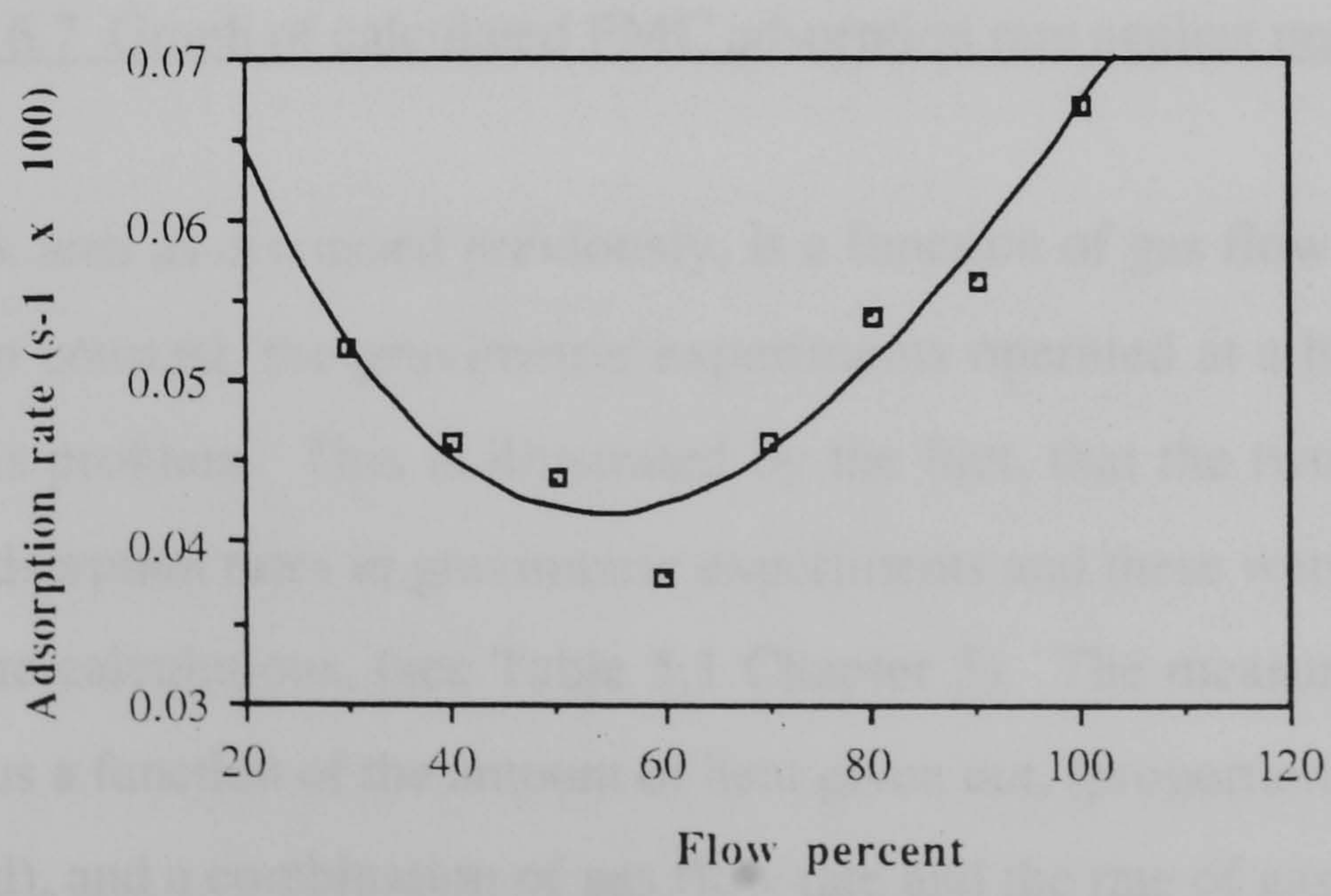

Figure 6.6 Graph of calculated adsorption rate versus gas flow rate.

This was thought to be due a large fraction of heat output being transferred away by the gas and not being measured by the FMC thermistors. In other words, the greater the flow, the greater sample cooling effects. At very low flow rates however, the peak area was very small. This was because the flow rate was limiting the rate of gas uptake, giving a more elongated peak resulting in a larger percentage of heat output being lost to the gas. The largest measured peak areas were in the mid-range of the flow rate variation. The adsorption rates were seen to vary systematically with the measured peak area, as shown in Figure 6.7. This shows a straight line graph of calculated adsorption rate versus measured peak area, demonstrating the dependence of calculated adsorption rate upon measured peak area.

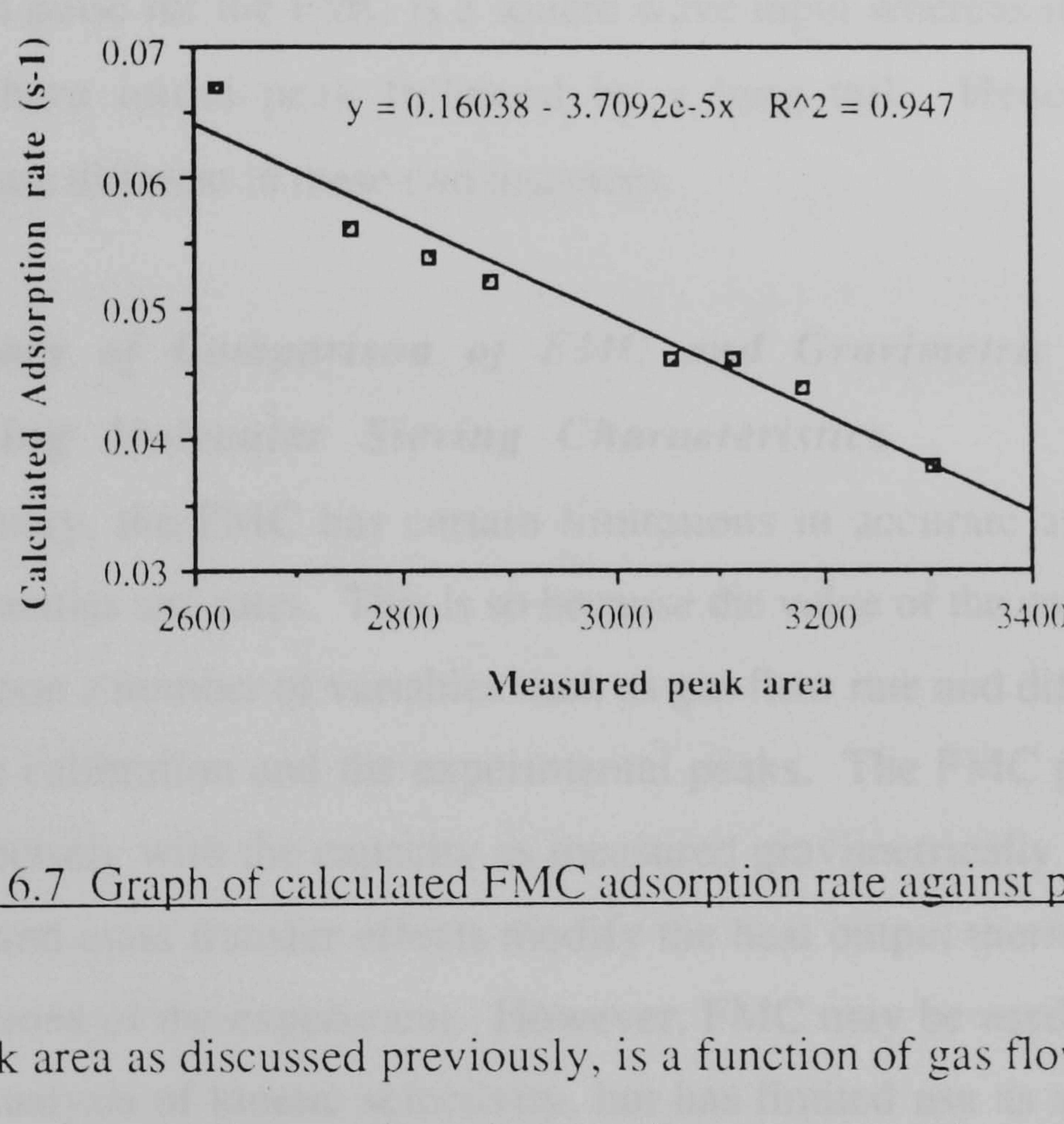

Figure 6.7 Graph of calculated FMC adsorption rate against peak area.

The peak area as discussed previously, is a function of gas flow rate and rate of heat output. In contrast, the gravimetric experiments operated at a higher flow rate, eliminating this problem. This is illustrated by the fact, that the two active carbons showed high adsorption rates in gravimetric experiments and these were vastly reduced in the FMC rate calculations, (see Table 5.1 Chapter 5). The measured uncalibrated peak area is thus a function of the amount of heat given out, (proportional to the amount of gas adsorbed), and a combination of gas flow rate and the rate of gas adsorption.

The calibrated values of the FMC peak area at different flow rates, as shown in

Table 5.2, generally showed a decrease in measured and calibration FMC peak areas, with increased FMC gas flow rate. This could be interpreted on the basis of a proportion of the heat being lost to the flowing gas. The heat loss increased as the gas flow rate increased. However, another disadvantage was that the calibrated energy peaks were not of precisely the same shape and size as that of the experimental heat output peak which would have resulted in an equal amount of heat loss to the flowing gas. Hence, the calibrated experimental peak areas would have shown no variation with gas flow rate. It was the difference in heat loss characteristics of the calibration peak and experimental peak, which gave rise to observed differences in calibrated peak areas at different flow rates. The greater the difference in size or shape of the peak, the greater the difference in the calibrated experimental peak values with gas flow rates. The calibration pulse for the FMC is a square wave input whereas the gas adsorption profile is a sharp initial peak followed by a long tail. Hence, the heat loss characteristics are different in these two instances.

6.1.2. Summary of Comparison of FMC and Gravimetric Technique for Assessing Molecular Sieving Characteristics

In summary, the FMC has certain limitations in accurate assessment of gas adsorption capacities and rates. This is so because the value of the calibrated peak area is dependent upon a number of variables such as gas flow rate and differences in shape and size of the calibration and the experimental peaks. The FMC peak areas do not correspond precisely with the capacity as measured gravimetrically. Besides this the complex heat and mass transfer effects modify the heat output thermogram under the specific conditions of the experiment. However, FMC may be used as a tool for fast approximate analysis of kinetic selectivity, but has limited use as a measurement of fundamental scientific properties. The problems associated with FMC can be minimised by addition of computer control for peak calibration. Also, the addition of PTFE as a dilutant in the sample cell will minimise the problems arising due to the rate limiting effects of the gas supply to the cell. In contrast, the gravimetric technique is more efficient as it can be operated at relatively high flow rates although some difficulty may be encountered due to buoyancy effects. The problems of buoyancy are easier to correct and are straightforward to apply. Hence, the gravimetric technique has been used as an overall technique for the assessment of kinetics and selectivity for all laboratory and commercial samples.

6.2 *Diffusion in Porous Carbons*

CMS are used in large scale industrial processes for gas separation using the pressure swing adsorption method. High adsorption capacities are required for economic viability. These CMS/adsorbents, in general, have a bimodal pore size distribution consisting of macropores for efficient gas transport and an extensive microporous structure for high capacity. The CMS materials are tailored in such a fashion that the selective part of the porous structure has molecular dimensions similar to those of adsorbates. It is believed that the molecule diffusing through the selective porosity experiences a net repulsive force upon entering the micropores, and thus, must pass over an energy barrier to gain entry into these pores. The rate of adsorption depends upon the pore size and the size, shape and length of the adsorbate molecule used. It has been found that the micropore diffusion of different gases varies markedly, although their adsorption equilibrium capacities might be similar. Hence, there is a kinetic selectivity which may be utilised by the pressure swing adsorption technique.

The purpose of this work was to develop an improved understanding of the fundamentals of the kinetic selective process in CMS materials. In this investigation, the adsorption/desorption kinetics of gases of varying molecular shapes and dimensions on a CMS material have been studied. The gases used were argon which is a spherical molecule: oxygen and nitrogen which are linear diatomic gases: carbon dioxide and nitrous oxide representing linear triatomic molecules: ethyne representing a long linear molecule and ethene representing a longer planar molecule were studied. The rates of adsorption and desorption of various gases at different temperatures on commercial CMS material were determined for a range of temperatures and the activation energies for all the adsorption/desorption processes. The nature of selectivity occurring in this material was assessed.

6.2.1 Pore size distribution

The pore size distribution of microporous materials can be estimated by the adsorption of molecules of varying sizes[8,9]. The pore size distribution of commercial CMS A3 material indicates that the bulk of pore volume begins between 0.4 and 0.43 nm and has very little volume between 0.46 and 0.65 nm, as shown graphically in Figure 6.8 and numerically in Table 5.14.

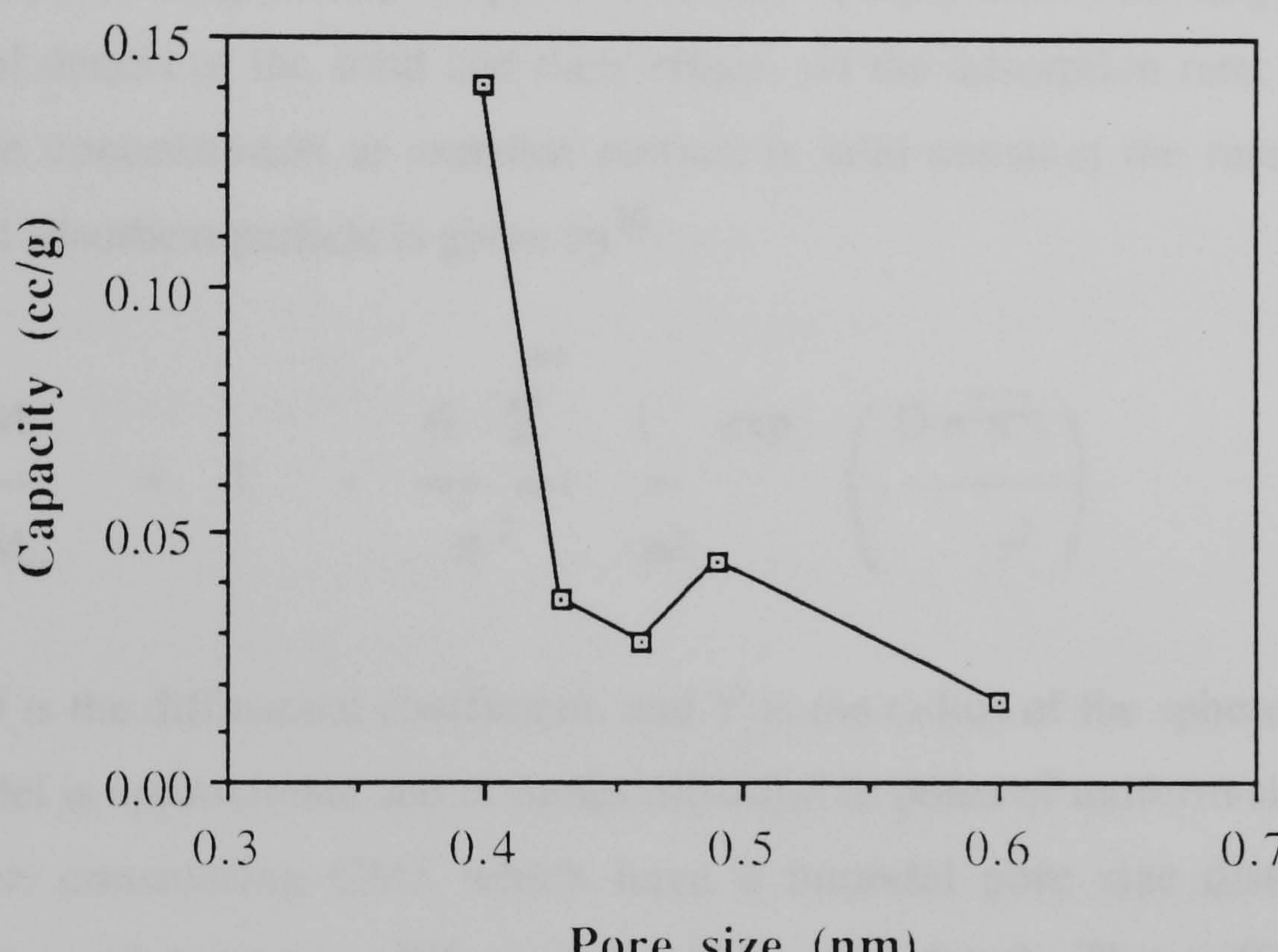

Figure 6.8 Probe molecule capacities for commercial material CMS A3.

6.2.2 Nature of porosity

The selective porosity of the CMS material is slit-shaped since it adsorbs ethene and has a similar equilibrium capacity as that of carbon dioxide and ethyne. In contrast methane is not adsorbed to any significant extent. The kinetic measurements indicate that the ethene adsorption is very slow. This is expected from the steric requirements for the ethene to obtain the correct orientation to pass through the selective porosity. The results indicate that the nature of porosity which gives rise to kinetic selectivity is slit-shaped.

6.2.3 Diffusion in micropores

In recent years most research has been focused on the microporous nature of the CMS and on the related physisorption mechanism. The description of transport process in CMS is difficult to assess owing to complex and largely unknown pore network. Depending upon the dimensions of the pores the mechanisms of mass transfer may be due to bulk diffusion, Knudsen diffusion and surface diffusion. As a result, most models for diffusion in porous solids are approximate. In general the sorption of gases on CMS occurs by the unsteady state diffusion which is rate limiting. Rate data have been analysed using the time dependant diffusion equation which largely ignores the structural details of the solid and their effects on the adsorption rate. For example, when the concentration at external surface is held constant the rate of uptake by spherical adsorbent particle is given by[10]:

$$\frac{M_t}{M_\infty} = 1 - \frac{6}{\pi^2} \sum_{n=1}^{\infty} \frac{1}{n^2} \exp\left(-\frac{D n^2 \pi^2 t}{r^2}\right)$$

where D is the diffusional coefficient, and 'r' is the radius of the sphere. This type of rate model is approximate and assumes diffusion in pores of uniform size is involved. However, considering CMS which have a bimodal pore size distribution, both macropore and micropore diffusion should be considered. These effects have been observed by Roberts and York[11] for adsorption of liquid normal paraffins on 0.5 nm molecular sieve. Antonson and Dranoff[12] for fixed bed sorption of ethane also for Linde 0.5 nm molecular sieve. These authors have used an additive series model to account for macro/micropore effects.

As stated previously the CMS have pores with restrictions of certain sizes, which allow small molecules to pass through more rapidly than larger molecules. The differences in gas diffusivities reflects the 'sieving' action of the restrictions present along the particle pore[13,14], and the selectivity of CMS has been found to depend on the differences in adsorption kinetics as observed by several workers[13,14,15,16]. In all the cases the adsorbents were kinetically selective to oxygen as compared to nitrogen and were weakly adsorbed. In contrast LaCava *et al.*[17,18] concluded that the adsorption dynamics in some CMS were depicted by a non-Fickian behaviour. The rate of gas uptake by non-Fickian CMS (with selectivity introduced by carbon deposition) was described by Langmuir rate model; and the selective porosity was considered to be slit-shape where the slit-molecule interaction potential controls the rate of entrance into the cavity. The slit potential was found to be greater for nitrogen; hence nitrogen was adsorbed slowly compared with oxygen. Work carried out by Chagger *et al.*[19] concluded that the CMS prepared by direct carbonisation follow a Fickian mechanism. The reason for this was attributed to the homogeneous structure of the CMS prepared by direct carbonisation and the selectivity was effective throughout the microporous region. In comparison, when the CMS selectivity is produced by carbon deposition, the pyrolysis gas cannot penetrate all the structure and, therefore, only deposits in the accessible regions which are primarily meso and macropore surfaces thereby introducing selectivity in a heterogeneous manner. This heterogeneous carbon deposition was confirmed by the particle size studies which showed that the selectivity decreased with decreased particle size.

The microporosity can be sub-divided into two regions, i.e. ultramicropores (< 0.7 nm) and supermicropores (0.7-1.5 nm); these can be distinguished by the different filling mechanisms involved. In ultramicropores the mechanism of adsorption occurs by micropore filling whereas in supermicropores cooperative filling effects may occur. The mechanism of pore filling is dependent on the nature of the adsorption system and the ratio of pore width (d_p) to molecular diameter (σ), i.e. d_p/σ rather than the absolute value of d_p. Pores of molecular dimensions (i.e. d_p/σ = 1-2) are filled preferentially at very low p/p_0, whilst the wider micropores (d_p/σ = 2-5) are filled by a cooperative process at higher p/p_0[20]. The process of 'micropore filling' is associated with enhanced adsorbate-adsorbent interaction, as compared to cooperative effects which occur at high p/p_0 and the enhancement of interaction energy is relatively small. The nature of this process has been explained in detail on the basis of a simplified slit shaped model (see Chapter One, Section 1.5). Although in the cooperative effect, the phenomena of monolayer formation and condensation occurring in rapid succession are said to constitute a single process.

To date, the authors mentioned above have reported rates and diffusivities of various gases in micro/macropores by chromatographic, gravimetric and volumetric techniques. In this work the gas adsorption and desorption uptake rate measurements were made using gravimetric technique. A new model has been developed which is based on Langmuir kinetics. This allows the rate constants for adsorption and desorption to be assessed. This model is based on the study of the gas adsorption kinetics and capacities for molecules of varying size and shape of the adsorbate (i.e the probe molecules).

The experimental data on the adsorption rates of gases show that the probe molecules with small molecular diameter (minimum cross-sectional area) enter the pores more easily than larger molecules. Firstly the simplest molecule studied, argon, follows Langmuir pseudo-first order kinetics for adsorption. However, the rates of adsorption are slow in the temperature range of 275-333 K. The linear diatomic gases follow Langmuir first order kinetics for the adsorption process. This is indicated by straight line graphs for ln(1-W/Weq) against time, for adsorption in case of argon, oxygen and nitrogen. In the case of the linear triatomic molecules, carbon dioxide and nitrous oxide the adsorption kinetics also follow the same kinetic laws. The adsorption capacities for carbon dioxide and nitrous oxide are significantly higher than argon, oxygen and nitrogen. This is due to the higher p/p_0. However, ethyne and ethene adsorption kinetics deviate from Langmuir first order kinetics at low temperatures. The linear molecule, ethyne, which is relatively long, has a slow adsorption rate but high adsorption capacities due to the high relative pressures (p/p_0). Similarly, for ethene, which has a rectangular cross-sectional shape the adsorption rate is very slow but the adsorption capacity is high due to the high relative pressure (p/p_0). The rates of adsorption for ethene and ethyne for the fast stage process show an increase as the temperature increases. This is contrast to the rates for the slow stage process which did not show any trend. For comparison purposes it is probably most appropriate to compare the initial uptake rate constants since these refer to the low surface coverage region. Above this surface coverage there is a marked deviation from the ln(1-W/Weq) against time graph from linearity. The mathematical model involving two exponential terms fits the data fairly well for observed and calculated values for the adsorption of ethyne and ethene.

In comparison the desorption behaviour can be quite different from that of adsorption for some gases especially at high surface coverage. In the case of argon, oxygen and nitrogen the rate plots for desorption are straight line graphs for ln(1-W/Weq) against time, indicating a pseudo-first order kinetics. This also signifies the absence of diffusional resistance in the macro and mesopores in the temperature range studied. The desorption is a two staged process at high surface coverage. This may be associated with the desorption from different sizes of microporosity with varying extents of volume filling and multilayer formation. As the temperature increases the processes merge into a single stage process. Although an excellent fit to the desorption curve was obtained for $W/Weq = A_1 e^{-k1T} + A_2 e^{-k2T}$ there are likely to be difficulties with comparison because each temperature has different levels of surface coverage. In the case of gases associated with high surface coverage like carbon dioxide, nitrous oxide, ethyne and ethene the desorption can be described by a model based on two exponentials. Carbon dioxide and nitrous oxide show only one distinct process i.e. the fast process. The reason for this phenomenon is that the contribution for the slow process is very low leading to errors in estimation of rate constants for the slower rate term in the model. In the case of ethyne the contribution from the two exponential terms in the mathematical model are similar and hence the kinetic parameters are more accurate. It is interesting to note that the activation energies for the two processes are fairly similar whereas the pre-exponential factors are quite different.

6.2.3.1 Adsorption capacities

Virtually all the previous studies on adsorption capacities have been carried out below the critical temperatures. In this investigation the adsorption /desorption of the majority of the probe molecules was studied above the critical temperatures of the gas. In order to plot an isotherm the saturation pressure of the gas has to be taken into account, but in this work a hypothetical p/p_0 was determined by extrapolation of equations applicable below the critical temperature. These hypothetical pressures are subject to some degree of error as relatively large extrapolation were required for some gases. The alternative is to apply the Langmuir isotherm to estimate the monolayer coverage for gases such as argon, oxygen and nitrogen etc. The extrapolations of the saturated vapour pressure data were carried out in order to compare the different isobars in terms of isotherms at their relative pressure (p/p_0). The isotherms of all gases at their respective partial pressures were compared with the carbon dioxide isotherm as, shown in Figure 6.9. It was observed that the argon, nitrogen and oxygen isotherms cover a low p/p_0 range. These gases lie along the steep part of the isotherm with low p/p_0 and are associated with micropore filling, monolayer formation and low surface coverage. The adsorption kinetics for these gases are straight lines, as shown in Figure 5.4 etc. in

Chapter Five. In comparison, the carbon dioxide, nitrous oxide, ethyne and ethene isotherms cover a higher p/p_o range. These gases lie close to the plateau of the isotherm. The adsorption rate plot for ethyne and ethene deviated from linearity at low temperatures. It is proposed that the deviation is associated with cooperative adsorption effects. Marsh and O'Hair[21] concluded that both adsorbates, carbon dioxide and nitrous oxide behave similarly, although nitrous oxide takes longer than carbon dioxide to reach equilibrium. Adsorption experiments conducted at higher pressure (4 bars) for oxygen increased the equilibrium capacities of the gas. This is expected from the change in p/p_o. Figure 6.9 shows a graph of the amount of gas adsorbed in the kinetic measurements as a function of the hypothetical p/p_o or actual p/p_o as appropriate with the carbon dioxide, 273 K adsorption isotherm.

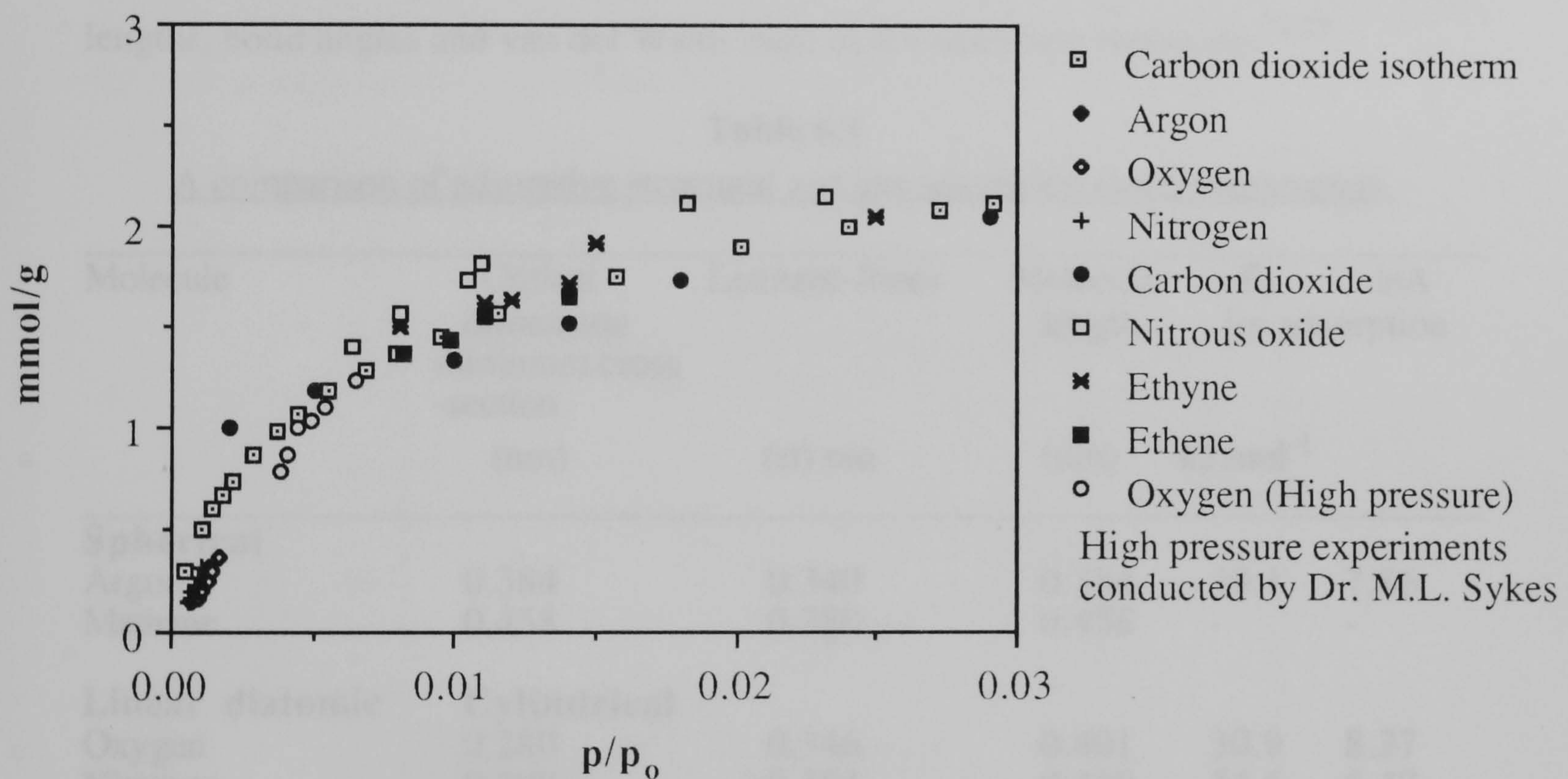

Figure 6.9 Isobars of probe molecules as compared with carbon dioxide isotherm against relative pressure.

It is apparent that the adsorption capacities for all the gases studied follow the CO_2, 273 K isotherm closely despite the differences in sizes of the molecules. It is apparent that the CO_2, 273 K isotherm is a guide line to the capacity of the CMS material.

6.2.3.2 *The relationship between adsorptive structural parameters and Arrhenius parameters for the probe molecules*

Diffusion in micropores occurs by surface or activated diffusion as stated previously. In this kind of diffusion the molecule or atom hops from one site to another across the energy barrier which separates adjoining sites. The value of rate constants (k) was plotted for different temperatures according to the following Arrhenius equation:

$$k = A \exp^{-E_a/RT}$$

where A is pre-exponential factor, E_a is the activation energy, R is the gas constant and T is the temperature.

Table 6.1, below, gives the critical dimensions, estimated diameter from Lennard-Jones and molecular diameter in terms of the length of the probe molecule. The critical diameter and molecular lengths were calculated on the basis of the bond lengths, bond angles and van der Waals radii of the adsorbate molecules[22,23].

Table 6.1

A comparison of adsorptive structural and gas adsorption kinetic parameters.

Molecule	Critical dimension minimum cross -section (nm)	Lennard-Jones (σ) nm	Molecular length (nm)	E_a for adsorption kJ mol^{-1}	lnA
Spherical					
Argon	0.384	0.340	0.384	39.1	7.86
Methane	0.458	0.380	0.458	-	-
Linear diatomic	**Cylindrical**				
Oxygen	0.280	0.346	0.401	30.9	8.27
Nitrogen	0.300	0.364	0.410	34.6	6.47
Linear triatomic	**Cylindrical**				
Carbon dioxide	0.280	0.352	0.513	12.6	0.029
Nitrous oxide	0.300	0.388	0.521	11.6	-9.02×10^{-5}
Linear tetratomic	**Cylindrical**				
Ethyne	0.335!	0.422	0.572	24.5	0.85
Planar	**Rectangular**				
Ethene	0.387*	0.423	0.489	39.6	4.75

! Distance between the graphite layers: actual value (0.352)

* Average of length and cross-section of the molecule: actual value (0.352 x 0.425)

The activation energy for adsorption was found to be complex function of both length and cross-section of the probe molecules. The activation energies of adsorption for the gases studied have been compared. Figure 6.10 shows a graph of activation energy against the cross-section of probe the molecules. The activation energy for adsorption tends to show an increase as the cross-section of the molecule increases. Large molecules require higher energy to pass over the energy barrier into the CMS. A similar trend was observed for the spherical and linear diatomic gases when compared against their Lennard-Jones diameter. Conversely, there is a decrease in the activation energy value for adsorption for oxygen at a high pressure (0.4 MPa). The activation energies of adsorption for ethyne and ethene obtained from rate constants using Langmuir kinetics and the mathematical model based on two exponential terms are of similar magnitude for both contribution terms, indicating the validity of the mathematical model. A comparison of activation energies of the probe molecules like oxygen and nitrogen show that they are quite similar, oxygen being slightly lower than nitrogen as expected from the differences in the size of these molecules.

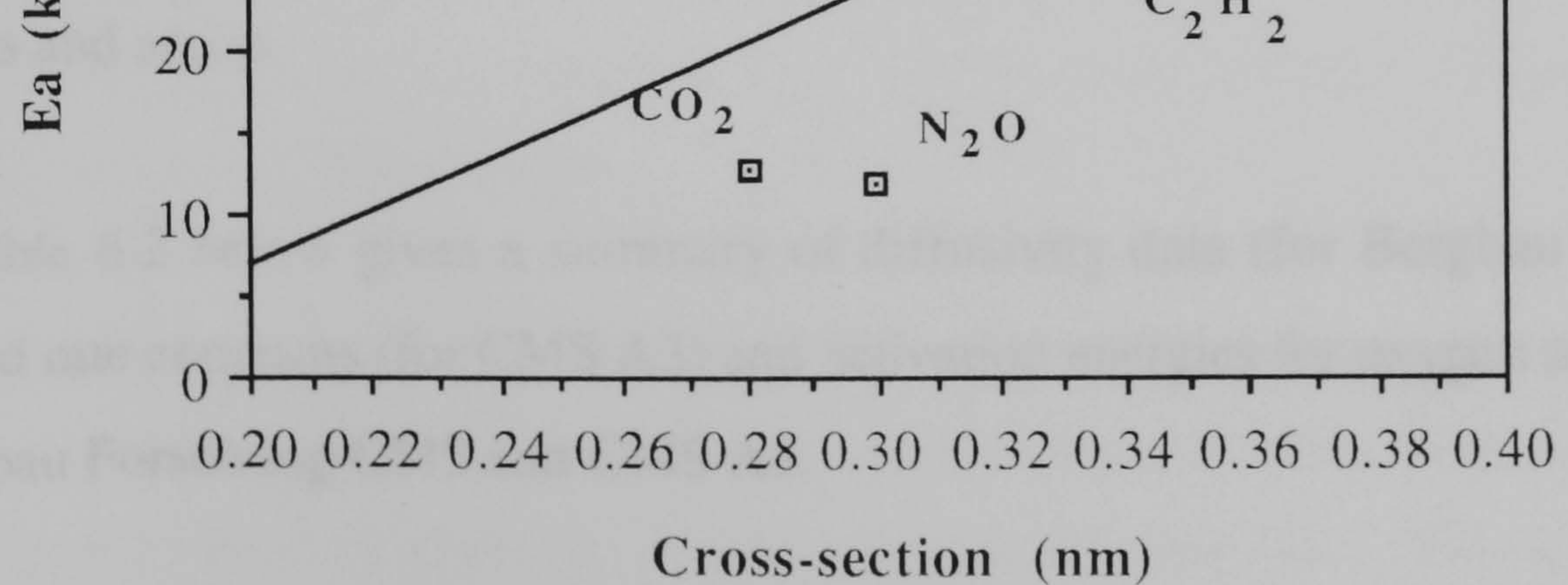

Figure 6.10 A graph of activation energy of adsorption against cross-section of the probe molecules.

In contrast the activation energy of adsorption decreases with increasing length of the probe molecules as shown in Figure 6.11.

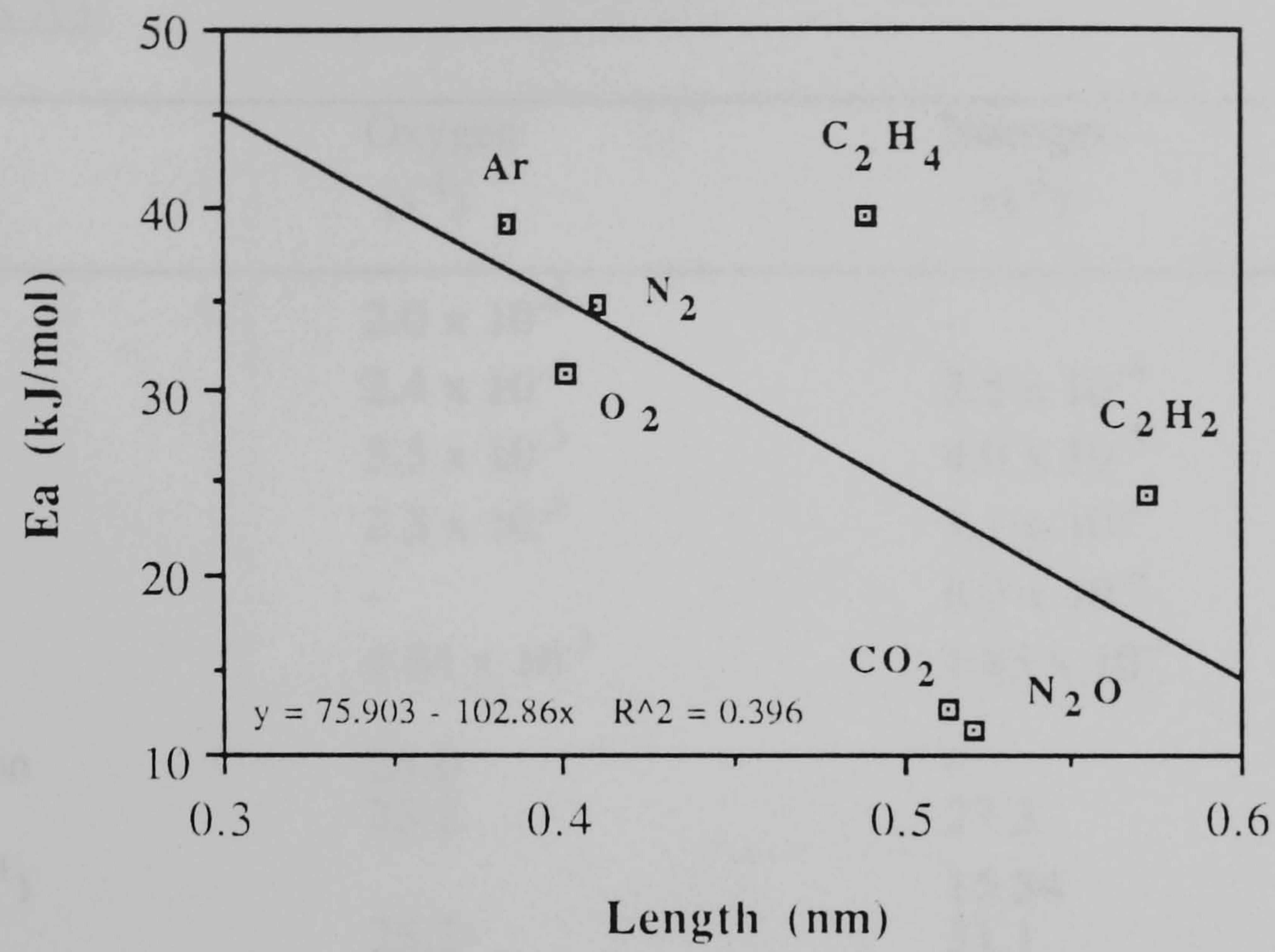

Figure 6.11 A graph of activation energy of adsorption against the length of probe molecules.

The activation energies for desorption of the probe molecules cannot be compared and contrasted directly to those obtained for the adsorption process. This is because the activation energies for desorption in case of linear triatomic, tetra-atomic linear and planar molecules refer to higher surface coverages than the diatomic molecules and argon.

Table 6.2 below gives a summary of diffusivity data (for Bergbau Forschung CMS) and rate constants (for CMS A3) and activation energies for oxygen and nitrogen for Bergbau Forschung CMS and CMS A3.

Table 6.2

Summary of diffusivity data (for Bergbau Forschung CMS) and rate constants (for CMS A3) and activation energies for oxygen and nitrogen for Bergbau Forschung CMS and CMS A3.

T(K)	Oxygen (s^{-1})	Nitrogen (s^{-1})	References
193	2.0×10^{-6}	-	13
273	2.4×10^{-4}	3.5×10^{-6}	13
300	3.5×10^{-3}	4.0×10^{-5}	12
300	2.3×10^{-3}	1.1×10^{-4}	12
333	-	6.0×10^{-6}	24
275	4.64×10^{-3}	1.83×10^{-4}	This work
Activation	26.0	-	13
energies	25.2	27.3	12
($kJ\ mol^{-1}$)		15.54	15
	25.2	31.1	16
	30.9	34.6	This work

The activation energies for CMS A3 are slightly higher as compared to Bergbau CMS. Similarly activation energies for carbon dioxide[25], ethene[26] and ethyne[27] are quite close to those as obtained by other researchers. In the case of ethyne the activation energy observed by Ghosh and Agnew[27] has been obtained at extreme temperatures. As this study was carried out on CMS A3 and some variation between samples is expected, the results are consistent with those of other researchers. It is possible that the rates might differ for different CMS as these materials might have been pre-treated differently and activated in the manufacturing process. Hence they may show different rate limiting kinetics.

The accessibility is also related to the length of the molecule. Figure 6.12 illustrates a graph of pre-exponential factor against length of probe molecules. As the length of probe molecule increases the frequency factor decreases. This correlation is much better than the correlation between the activation energy and minimum cross-section.

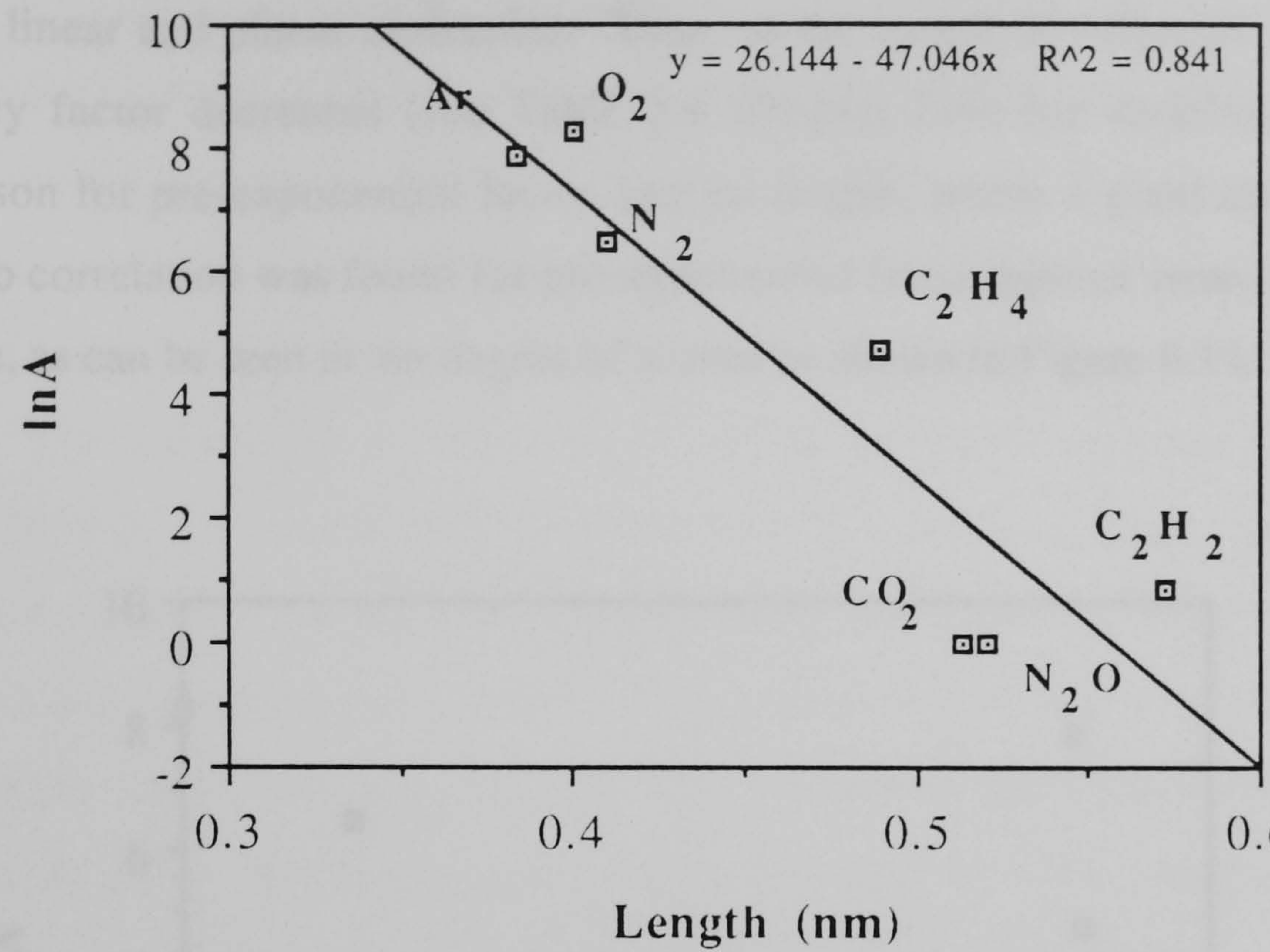

Figure 6.12 A graph of pre-exponential factor against increasing length of probe molecules used.

The reason for the decrease in the frequency factor with the length of the molecule is that the spherical molecules are able to pass through the pore neck in the porous network more easily unlike the larger linear molecules as shown in Figure 6.13 where the orientation required to enter the pore mouth is more critical.

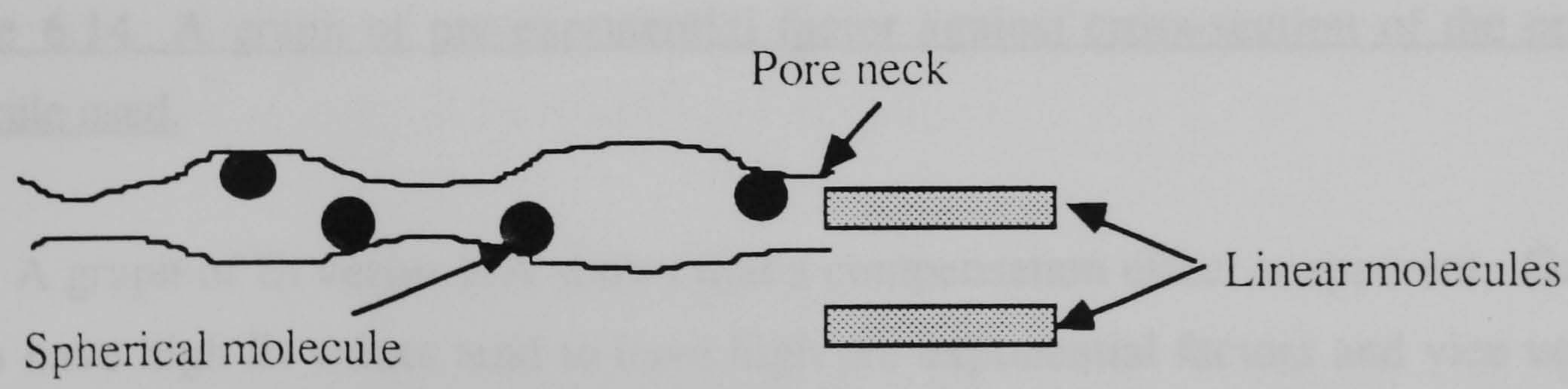

Figure 6.13 Diffusion of molecules into CMS micropores.

It is more difficult for the orientation to be achieved for a longer molecule compared with a short molecule. This will result in differences in the frequency factor with longer molecules having smaller frequency factors. In addition to being a long molecule ethene has a rectangular cross-section and therefore the correct orientation will also have to be achieved for the rectangular shaped molecule to pass through the slit shaped selective porosity. Thus, ethene has a very low pre-exponential factor compared with argon, oxygen etc. Hence, argon possesses a very high frequency factor compared with the linear and planar molecules. Thus, as the length of molecule increases the frequency factor decreases (see Table 5.6 Chapter Five for details). Unlike the comparison for pre-exponential factor against length, where a good correlation was found, no correlation was found for pre-exponential factor against cross-section of the molecule, as can be seen in the degree of scatter as shown in Figure 6.14.

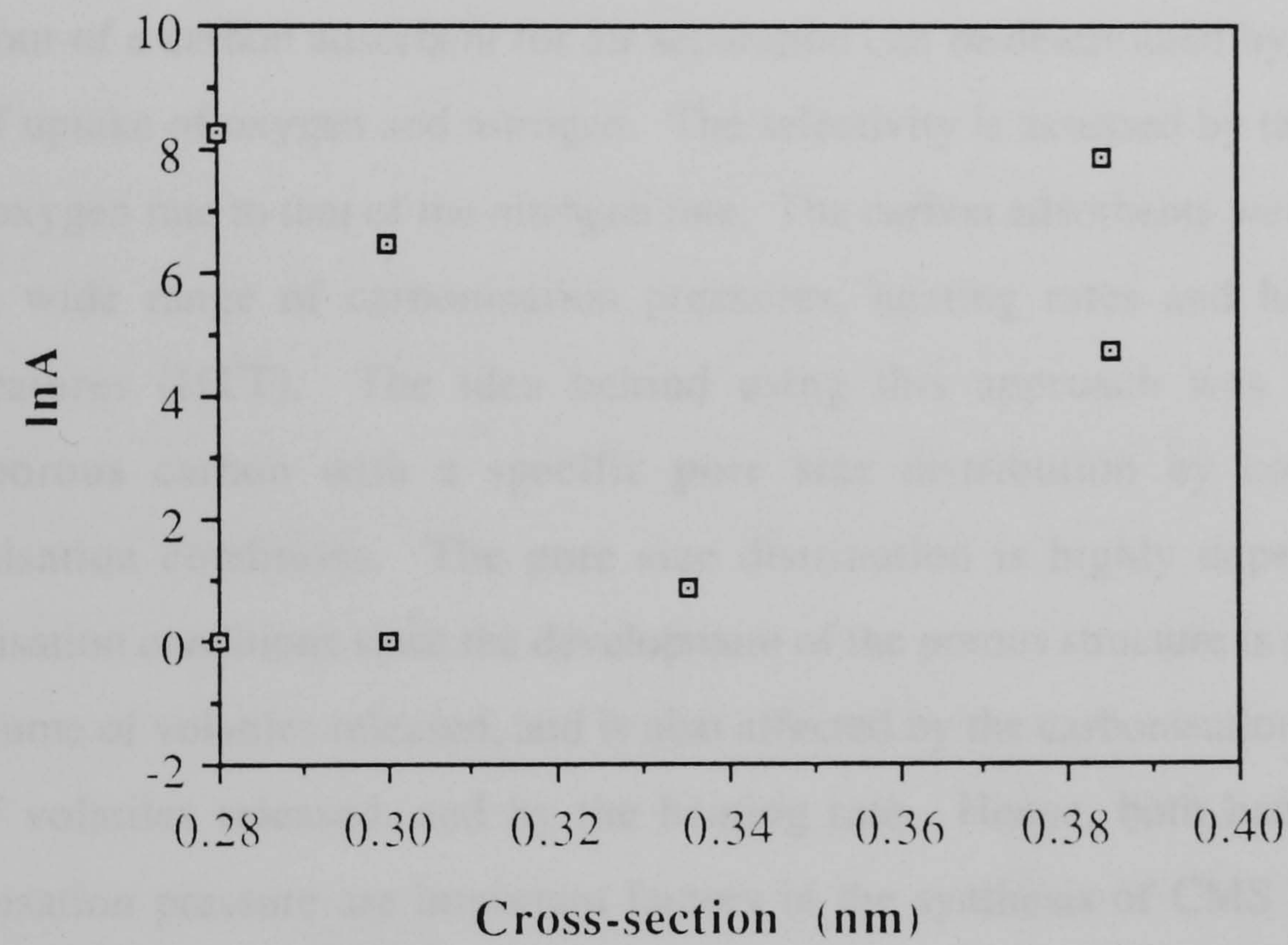

Figure 6.14 A graph of pre-exponential factor against cross-section of the probe molecule used.

A graph of E_a versus lnA shows that a compensation effect is apparent. Gases which have high E_a values tend to have high pre-exponential factors and vice versa. The comparison is subject to limitations due to different levels of surface coverage and the comparison should exclude ethene which has a rectangular cross-section which has to pass through the selective porosity.

6.3 *Assessment of Capacity and Selectivity of Carbons Synthesised in Laboratory.*

In this work carbons were synthesised using different precursor materials which can basically be divided into two categories: (1) polymer and resin based carbons and (2) lignocellulosic materials (coconut shell, hard-wood and cellulose triacetate). The aim of this part of the project was to make high capacity carbon adsorbents from a variety of host materials and to introduce molecular sieving characteristics into these carbons. The capacity of an adsorbent can be defined as the volume or mass of gas taken up by a given volume or mass of the carbon adsorbent. The molecular sieving behaviour of a carbon adsorbent for air separation can be determined by assessing the rates of uptake of oxygen and nitrogen. The selectivity is assessed by taking the ratio of the oxygen rate to that of the nitrogen rate. The carbon adsorbents were synthesised over a wide range of carbonisation pressures, heating rates and heat treatment temperatures (HTT). The idea behind using this approach was to prepare a microporous carbon with a specific pore size distribution by controlling the carbonisation conditions. The pore size distribution is highly dependent on the carbonisation conditions since the development of the porous structure is determined by the volume of volatiles released, and is also affected by the carbonisation pressure, the rate of volatiles released, and by the heating rate. Hence, both heating rate and carbonisation pressure are important factors in the synthesis of CMS materials and techniques which make use of these factors enable the synthesis of CMS material in one step, thereby, making the manufacturing process cost-effective by cutting down the number of stages required in the manufacturing process.

6.3.1 Polymer and resin based carbons

Several cross-linked polymers, including PVDC, PEEK, PES and PFA etc. were chosen as precursor materials because they were known to give rise to microporous carbons. The carbonisation of polymers with a range of structural characteristics over a range of carbonisation pressures, HTTs and heating rates were studied in order to assess the suitability for producing microporous carbons with high capacity and a suitable pore size distribution for the production of CMS materials.

6.3.1.1 Effect of HTT on properties of pure PVDC and PEEK carbons

Pure PVDC carbons were produced at atmospheric conditions (0.1 MPa) under a variety of HTTs ranging from 873 to 1173 K and heating rate of 1 K min^{-1}. The capacities of these carbons (at 293 K) increased with increasing HTT from 8.46 to 10.22 cc g^{-1} for oxygen and 7.60 to 11.31 cc g^{-1} for nitrogen as shown in Table 5.14. The CO_2, 273 K surface area of these carbons also followed the same trend increasing from 460 m^2g^{-1} to 650 m^2 g^{-1} with increasing HTT. The rates of uptake of oxygen and nitrogen of the above mentioned carbons reached a maximum for carbon produced at a HTT of 1073 K and showed a decrease for carbon obtained at a HTT of 1173 K (see Table 5.15 for details). The pore size distribution of these carbons was also measured using the probe molecule technique as discussed in Section 4.2.7. The results are shown numerically in Table 5.16 and represented graphically in Figure 6.15. Figure 6.15 illustrates that the pure PVDC carbons synthesised at low HTT had a wide pore size distribution compared with the pure PVDC carbon obtained at a HTT 1173 K which had a narrow pore size distribution. This carbon showed a sharp cut-off in capacity which came at between 0.47 to 0.5 nm.

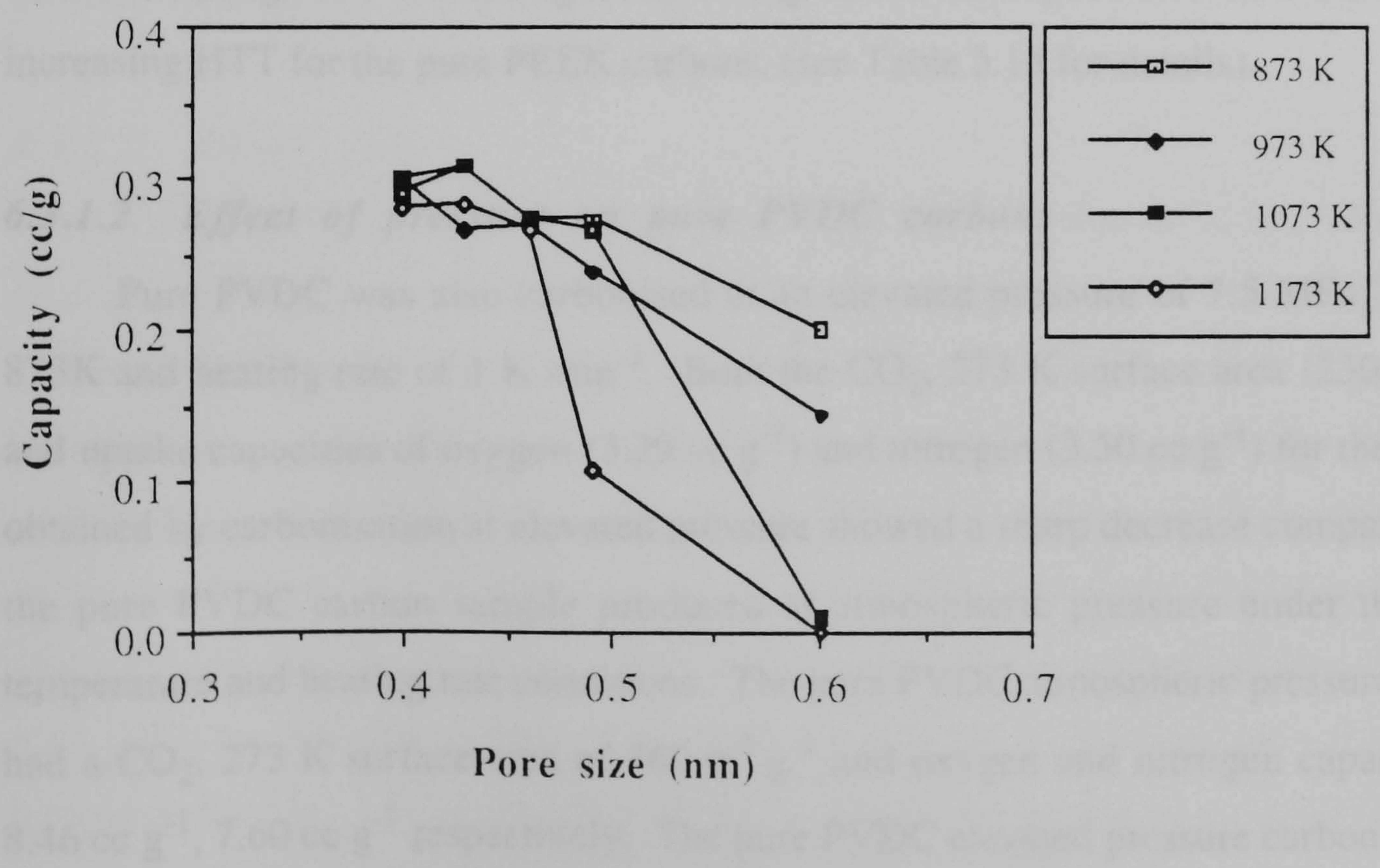

Figure 6.15 Probe molecule capacity graphs for pure PVDC carbons synthesised at a heating rate 1 K/min and 1 hour soak time.

The pure PVDC carbons did not show any selectivity for air separation. Therefore, the apparant pore size distribution needs to be shifted from 0.47 nm to ~ 0.4 nm which could make these materials selective between oxygen and nitrogen[8]. A comparison with the pore size distribution for coconut derived carbons showed that the coconut carbons (C11-C14) had a sharper pore size cut-off near to 0.4 nm compared with pure PVDC carbons.

Pure PEEK carbons were also produced under atmospheric conditions at a temperature range of 873 to 1173 K and heating rate of 1 K min^{-1}. In this case both the oxygen and nitrogen capacities and the CO_2, 273 K surface area increased to a maximum at HTT of 1073 K (CO_2, 273 K surface area of 480 m^2 g^{-1}) before reducing on further heating to 1173 K (CO_2, 273 K surface area of 115 m^2 g^{-1}). The maximum capacities for pure PEEK carbon was obtained at a HTT of 1073 K (9.74 cc g^{-1} for nitrogen and 7.45 cc g^{-1} for oxygen). These were lower than for the corresponding pure PVDC carbon (synthesised at HTT of 1073 K and heating rate of 1 K min^{-1}), the uptake equilibrium capacities for pure PVDC carbon being 9.93 cc g^{-1} for oxygen and 9.76 cc g^{-1} for nitrogen. The rates of uptake of oxygen tend to show a sharp decrease with increasing HTT indicating a narrowing of the micropore size distribution with increasing HTT for the pure PEEK carbons, (see Table 5.15 for details).

6.3.1.2 Effect of pressure on pure PVDC carbons

Pure PVDC was also carbonised at an elevated pressure of 7.5 MPa, HTT of 873K and heating rate of 1 K min^{-1}. Both the CO_2, 273 K surface area (230 m^2 g^{-1}) and uptake capacities of oxygen (3.29 cc g^{-1}) and nitrogen (3.50 cc g^{-1}) for the carbon obtained by carbonisation at elevated pressure showed a sharp decrease compared with the pure PVDC carbon sample produced at atmospheric pressure under the same temperature and heating rate conditions. The pure PVDC atmospheric pressure carbon had a CO_2, 273 K surface area of 460 m^2 g^{-1} and oxygen and nitrogen capacities of 8.46 cc g^{-1}, 7.60 cc g^{-1} respectively. The pure PVDC elevated pressure carbon showed an increased rate for adsorption (21.25 x 10^{-2} s^{-1} for oxygen and 14.48 x 10^{-2} s^{-1} for nitrogen) compared with those for the pure PVDC atmospheric carbon (7.93 x 10^{-2} s^{-1} for oxygen and 6.18 x 10^{-2} s^{-1} for nitrogen). This could be accounted for by the available microporosity being reduced in the case of the high pressure carbons leading to a faster rate of uptake.

A pure PVDC carbon was also produced by carbonisation under vacuum conditions at HTT of 1173 K and heating rate of 1 K min^{-1}. The CO_2, 273 K surface area and the oxygen and nitrogen uptake capacities of this carbon were compared to pure PVDC carbon synthesised at atmospheric conditions under similar HTT and heating rate conditions. The results showed a slight increase in nitrogen uptake (11.91 cc g^{-1}) and oxygen uptake capacity (10.53 cc g^{-1}) as compared with pure PVDC atmospheric carbon which had uptake capacities of 11.31 cc g^{-1} for nitrogen and 10.22 cc g^{-1} for oxygen.. The corresponding CO_2, 273 K surface area values are 575 m^2 g^{-1} for pure PVDC carbon produced at reduced pressure and 650 m^2g^{-1} for pure PVDC carbon synthesised at atmospheric pressure. The corresponding rates of adsorption were also measured and these showed that the pure PVDC vacuum carbon had higher rates of uptake, 11.75 x 10^{-2} s^{-1} for oxygen and 4.25 x 10^{-2} s^{-1} for nitrogen compared with rates for pure PVDC carbon obtained at atmospheric pressure conditions at same HTT and heating rate (5.84 x 10^{-2} s^{-1} for oxygen and 3.61 x 10^{-2} s^{-1} for nitrogen). The increase in the rate of uptake for the vacuum carbon can be attributed to the production of more uniform microporous structure with unobstructed transport porosity.

6.3.1.3 PVDF carbon

Pure PVDF the fluorine analogue of PVDC was carbonised under atmospheric pressure at temperature of 1173 K and heating rate of 1 K min^{-1}. The CO_2, 273 K surface area (550 m^2g^{-1}) and uptake capacities at 293 K (10.30 cc g^{-1} for nitrogen and 9.0 cc g^{-1} for oxygen) for this PVDF carbon were slightly less than the corresponding pure PVDC carbon (CO_2, 273 K surface area 575 m^2g^{-1}), and uptake capacities (11.31 cc g^{-1} for nitrogen and 10.22 cc g^{-1} for oxygen). The rates of uptake of oxygen and nitrogen were considerably slower than corresponding PVDC carbon as shown in Table 5.15. These results are possibly due to differences in the liberation of the volatiles (e.g. hydrogen halides - HF compared with HCl). Since the release of a smaller molecule leads to a more constricted microporosity with a narrower pore size distribution and hence leading to a reduction in capacity and gas uptake.

6.3.1.4 PVDC and aromatic carbons

The carbons obtained by co-carbonisation of polymer PVDC and acridine showed a reduction in capacity with increasing aromatic ratio. The pore size distribution shifts to lower pore size with increasing aromatic ratio as shown in Figure 6.16 (see Table 5.16 for numerical values).

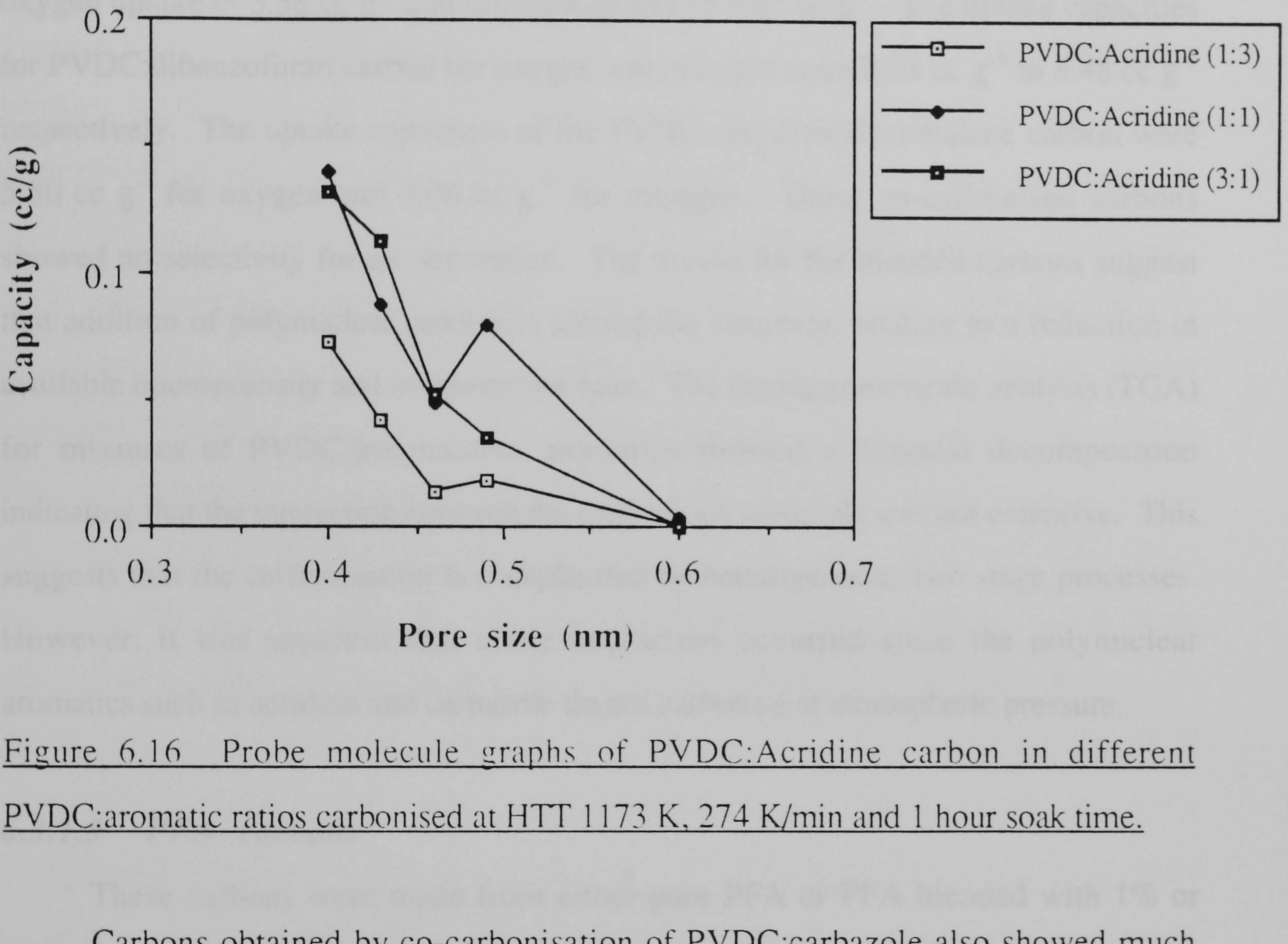

Figure 6.16 Probe molecule graphs of PVDC:Acridine carbon in different PVDC:aromatic ratios carbonised at HTT 1173 K, 274 K/min and 1 hour soak time.

Carbons obtained by co-carbonisation of PVDC:carbazole also showed much lower oxygen (varying from 2.28 to 3.65 cc g^{-1}) and nitrogen (varying from 1.69 to 2.87 cc g^{-1}) uptake capacities at 293 K than pure PVDC carbon synthesised at HTT of 873 K and heating rate of 1 K min^{-1} for which the oxygen and nitrogen capacities were 8.46 cc g^{-1} and 7.60 cc g^{-1} respectively. The CO_2, 273 K surface area for the co-carbonised carbons i.e. PVDC:carbazole also followed the same trend. The CO_2, 273 K surface area decreased from 250 to 245 m^2 g^{-1} with the increasing aromatic ratio in comparison with pure PVDC atmospheric carbon which had a CO_2, 273 K surface area value of 460 m^2 g^{-1}. Neither set of carbons (PVDC:acridine or PVDC:carbazole) showed any increase in selectivity.

The PVDC:polynuclear aromatics carbons (aromatic compounds used were acenaphthylene, dibenzofuran and dihydronaphthalene) also showed lower gas uptake capacities at 293 K compared with pure PVDC atmospheric carbon obtained at HTT of 1173 K and heating rate 1 K min^{-1} which had uptake capacity (at 293 K) of 10.22cc g^{-1} for oxygen and 11.31 cc g^{-1} for nitrogen.. The PVDC:acenapthylene carbon had oxygen uptake of 5.58 cc g^{-1} and nitrogen uptake of 6.05 cc g^{-1}. The uptake capacities for PVDC:dibenzofuran carbon for oxygen and nitrogen were 8.05 cc g^{-1} to 8.48 cc g^{-1} respectively. The uptake capacities of the PVDC:dihydroxylnapthalene carbon were 5.50 cc g^{-1} for oxygen and 4.00 cc g^{-1} for nitrogen. These co-carbonised carbons showed no selectivity for air separation. The results for the blended carbons suggest that addition of polynuclear aromatics altered the structure, leading to a reduction in available microporosity and in adsorption rates. The thermogravimetric analysis (TGA) for mixtures of PVDC:polynuclear aromatics showed a bimodal decomposition indicating that the interaction between the carbonising materials was not extensive. This suggests that the carbonisation is complicated by heterogeneous two stage processes. However, it was apparent that some interaction occurred since the polynuclear aromatics such as acridine and carbazole do not carbonise at atmospheric pressure.

6.3.1.5 PFA carbons

These carbons were made from either pure PFA or PFA blended with 1% or 10% of sulphur at HTT of 1173 K and heating rate of 5 K min^{-1}. These carbons were also analysed in terms of their capacities and rates of adsorption. The pure PFA carbon had lower uptake capacities for both oxygen (3.16 cc g^{-1}) and nitrogen (1.07 cc g^{-1}) in comparison with pure PVDC atmospheric carbon synthesised at similar conditions but at heating rate of 1 K min^{-1}. The pure PVDC carbon had uptake capacities of 10.22 cc g^{-1} for oxygen and 11.31 cc g^{-1} for nitrogen. The pure PFA carbons had a slower rates of uptake 1.48 x 10^{-3} s^{-1} for oxygen and 1.79 x 10^{-3} s^{-1} for nitrogen in contrast the with pure PVDC atmospheric carbon which had rates of 5.84 x 10^{-2} s^{-1} for oxygen and 3.61 x 10^{-2} s^{-1} for nitrogen. The addition of sulphur resulted in loss of uptake capacity at 293 K (oxygen uptake capacity was 0.66 cc g^{-1} for PFA:1% sulphur carbon; and 0.10 cc g^{-1} for the PFA:10% sulphur carbon) although the CO_2, 273 K surface area did not change significantly. The addition of sulphur also led to an increase in adsorption rates (see Table 5.15 for details) this could be due to filling or blocking up of micropores by sulphur leading to a reduction in microporosity.

6.3.1.6 Helium density

The porosity of chars is not always accessible, as it becomes filled or blocked by disorganised carbon resulting from deposition and decomposition of tars. The closed porosity of all chars was estimated by measuring their helium densities. The PVDC carbon synthesised under atmospheric pressure at HTT of 1173 K and heating rate 1 K min^{-1} had a helium densities of 1.89 g cc^{-1}, while the pure PEEK carbon synthesised under similar conditions had a slightly higher value of 2.02 g cc^{-1}. Carbons prepared by co-carbonisation of PVDC and polynuclear aromatics showed higher helium densities between 1.97 and 2.06 g cc^{-1} in comparison with the pure PVDC carbon. Carbons obtained by co-carbonisation of PVDC with acridine (HTT 873 K) had helium densities between 1.63 to 1.66 g cc^{-1} compared with 1.53 g cc^{-1} for pure PVDC carbon under similar carbonisation conditions. This indicates that the closed porosity is being reduced with addition of polynuclear aromatics. In general the helium densities for pure PVDC carbons synthesised at atmospheric conditions increased with increasing HTT (873-1173 K) from 1.53 to 1.89 cc g^{-1}. Similarly the pure PEEK carbons showed a corresponding increase from 1.41 to 2.02 cc g^{-1}. This indicates that the closed porosity decreases with increasing HTT. The highest capacity carbons showed little or no scope for further activation.

6.3.1.7 Methane pyrolysis on PVDC carbons

The carbons obtained by methane pyrolysis over the PVDC chars were characterised by the probe molecule technique. It was found that carbon deposited from methane leads to a narrower pore size distribution with increasing pyrolysis time as shown in Figure 6.17.

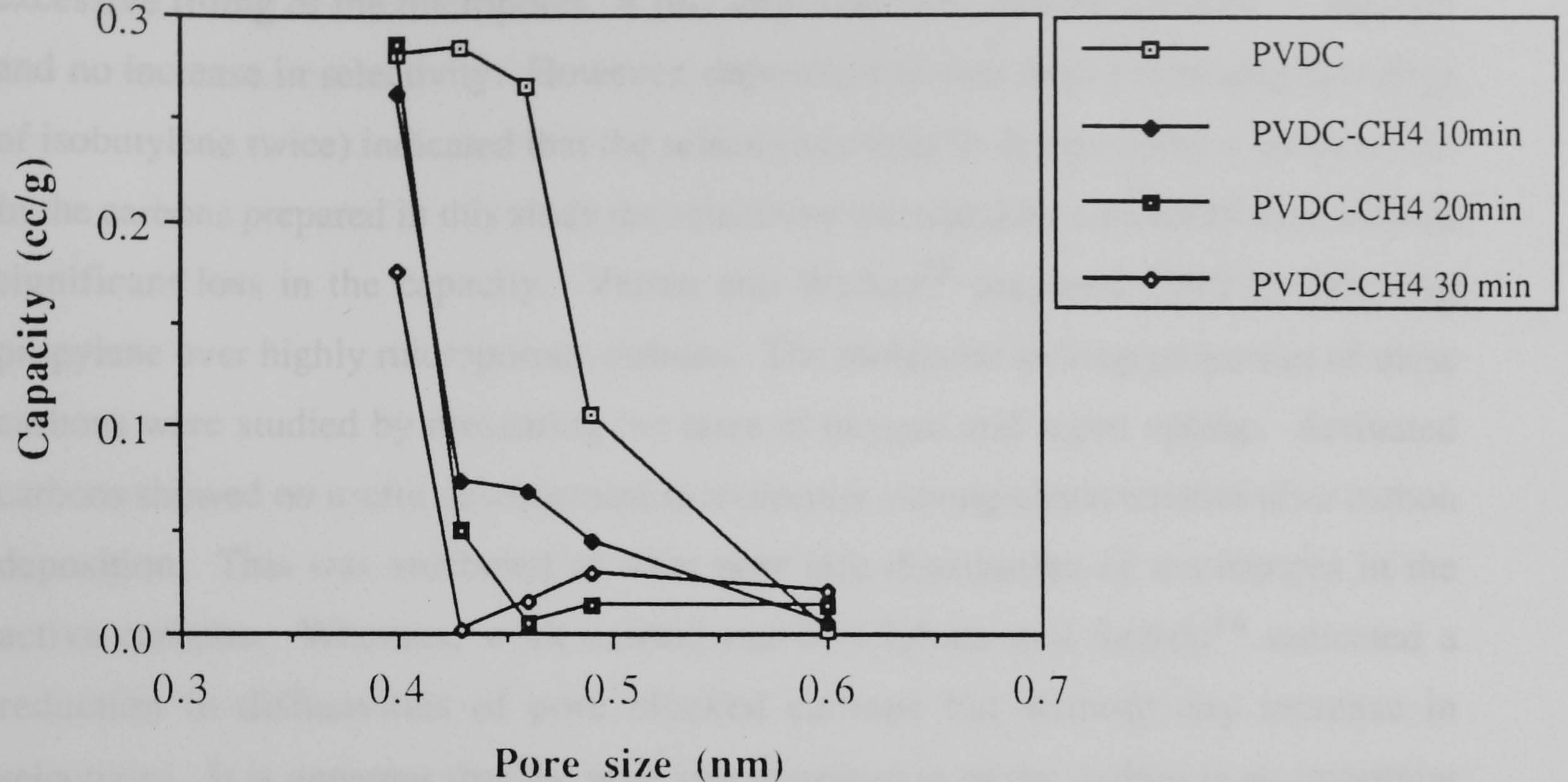

Figure 6.17 Probe molecule capacity graphs for pure PVDC carbons carbonised under atmospheric conditions and carbon deposited from methane at different contact times at heating rate 1 K/min, HTT 1173 K and 1 hour soak time.

The narrowing of the pore size distribution led to a decrease in the capacity for both oxygen (from 10.22 to 7.54 cc g^{-1}) and nitrogen (11.31 to 8.43 cc g^{-1}). This decrease corresponded to decreasing total surface area (carbon dioxide, 273 K, from 650 to 150 m^2 g^{-1}) with increasing pyrolysis time. The rates of adsorption for both oxygen and nitrogen for the pore blocked carbons decreased with increasing methane pyrolysis time; this was due to narrowing in the pore size distribution of the carbons as shown in Figure 6.17. The selectivity of the pore blocked carbons was determined by taking the ratio of rates of oxygen and nitrogen adsorption. The selectivity of the methane deposited carbons was higher than the pure PVDC carbon (1.6) with a four fold increase for the 10 min pyrolysis carbon. However, the pore blocked carbons showed a decrease in selectivity for oxygen and nitrogen with increasing contact time (6.08 to 3.05). It appeared that the pore network was reduced due to excessive pore filling. Hence, there was a loss in capacity and adsorption rates became too slow. Cabrera *et al.*[8] synthesised CMS by using a two-step process in which the sieve was contacted with two different concentrations of isobutylene. The concentration used in the first step was larger than the second step, so that the pore openings of the micropores of the support became successively narrower in two distinct steps without excessive filling of the micropores A one step treatment showed 6% loss in capacity and no increase in selectivity. However, deposition in two steps (involving pyrolysis of isobutylene twice) indicated that the selectivity could be increased by a factor of 10. In the carbons prepared in this study the selectivity increased by a factor of four without significant loss in the capacity. Verma and Walker[28] prepared CMS by cracking propylene over highly microporous carbons. The molecular sieving properties of these carbons were studied by measuring the rates of oxygen and argon uptake. Activated carbons showed no useful development in molecular sieving characteristics after carbon deposition. This was attributed to wide pore size distribution of micropores in the active carbons. Whereas, work carried out by Chihara and Suzuki[16] indicated a reduction in diffusivities of pore blocked carbons but without any increase in selectivity. It is apparent that the pore size distribution of the carbon is an important structural consideration when blocking pores by carbon deposition to introduce kinetic selectivity.

6.3.2 Lignocellulosic materials

Various carbons were synthesised using coconut shell, hard-wood and cellulose triacetate. The advantages of using hard woods or coconut shell as precursor materials lie in their high strength, stiffness and density, and their low cost. These materials were selected as starting materials because they give rise to highly microporous carbons. The cell structure of the plant material influences the pore size distribution and the shapes of the pores. Upon carbonisation the precursor material undergoes overall shrinkage of walls, vessels and fibers and releases small gas molecules like methane, carbon monoxide, carbon dioxide and water leaving voids. The structure collapses on cooling creating fissures and cracks which give rise to pores. The results indicated that the carbons obtained by subjecting the precursor materials to different carbonisation pressures and a range of HTTs were microporous and the gas adsorption isotherms for CO_2 at 273 K followed a Type I isotherm shape. The effect of carbonisation pressure, heat treatment and heating rates on the adsorption capacities and rates is discussed in the following section.

6.3.2.1 Influence of pressure on CO_2, 273 K surface area and equilibrium capacity

The CO_2, 273 K surface areas of carbons produced at different carbonisation pressures, HTTs and heating rates are shown in Table 5.9. The carbon samples were synthesised under different carbonisation pressures ranging from vacuum to elevated pressure up to 12.24 MPa, HTT of 873 K to 1173 K and heating rates of either 1 K min^{-1} or 50 K min^{-1}. These carbon were compared and contrasted in terms of their CO_2, 273 K surface areas, adsorption capacities (see Tables 5.10 and 5.14).

For the group of carbons (C1, C8, C15 and C17) prepared with HTT 873 K and heating rate 1 K min^{-1} there seemed to be little significant change in the CO_2, 273 K surface areas or oxygen and nitrogen capacities with increase of pressure above atmospheric pressure. Carbons (C1, C15 and C17), had CO_2, 273 K surface areas which varied between 145 and 135 $m^2\ g^{-1}$. However, for low pressure (5×10^{-4} MPa) carbonisation under vacuum the CO_2, 273 K surface area was considerably higher, 340 $m^2\ g^{-1}$. The oxygen and nitrogen uptake capacities for the carbons C1, C8, C15 and C17 [(1.70, 4.80, 1.20 and 1.00 cc g^{-1}) and (0.80, 3.80, 0.98 and 0.96 cc g^{-1}) respectively] exhibit the same phenomenon of little change for high pressure carbonisation but a large increase for low pressure carbon (C8).

A similar trend was observed for the series of carbons produced at a standard HTT of 873 K and heating rate of 50 K min^{-1}. These carbons C4, C11, C18 and C20 also showed little change in surface area or uptake capacity for higher pressure carbonisation but significant increases for the carbonisation under vacuum.

The carbons obtained under similar HTT but different heating rates had slightly different uptake capacities. The uptake capacities for both oxygen and nitrogen for carbons (C4, C18-C20 and C11) obtained at the high heating rate were found to be higher than those obtained under the slow heating rate (C1, C15-C17 and C8), for example, the uptake capacities of the vacuum carbon C11 synthesised at a heating rate of 50 K min^{-1} (5.13 cc g^{-1} for oxygen and 4.30 cc g^{-1} for nitrogen) were found to be slightly higher than C8 (4.80 and 3.80 cc g^{-1} for oxygen and nitrogen), the corresponding carbon synthesised at a slow heating rate of 1 K min^{-1}. In comparison the CO_2, 273 K surface area of the high heating rate vacuum carbon C11 (300 $m^2 g^{-1}$) was found to be slightly lower than the corresponding vacuum carbon C8 (340 $m^2 g^{-1}$) which was synthesised at a slow heating rate 1 K min^{-1}.

The fact that carbonisation at low heating rates gave carbons with higher CO_2, 273 K surface areas than the high heating rates carbons can be explained by the gradual release of volatile matter at low heating rate leading to more developed pore structure, whereas, high heating rate tends to break the carbon structure.

Figure 6.11 illustrates the effect of carbonisation pressure on the CO_2, 273 K surface area for both sets of carbons. There is a clear increase in the surface areas for the carbons produced by vacuum carbonisation. The log scale has been used for clarity.

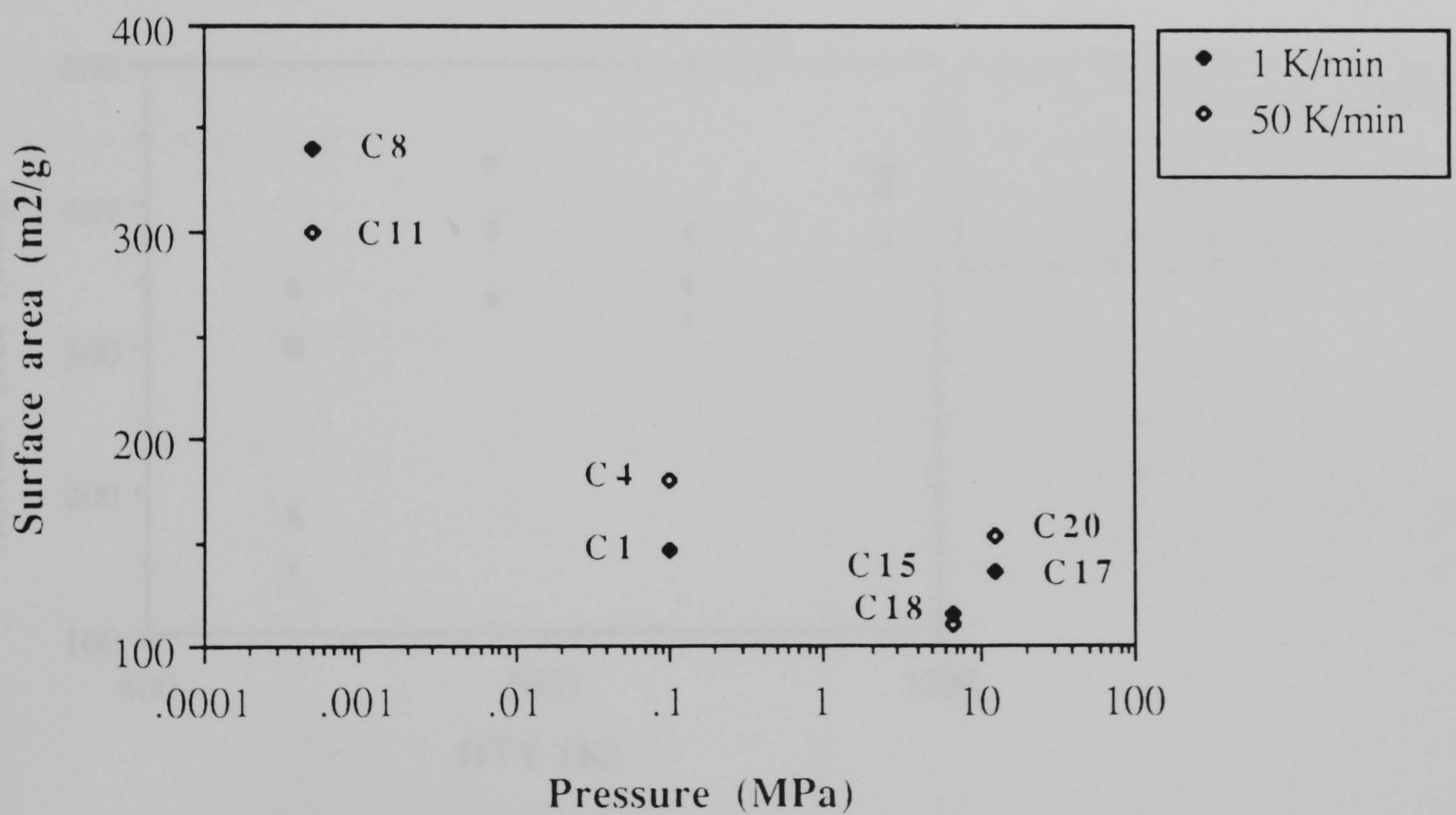

Figure 6.11 Graph showing the effect of increasing carbonisation pressure against CO_2, 273 K surface area for carbons produced at standard HTT 873 K and heating rates of either 1 K/min and 50 K/min.

This could be due to an increase in accessibility to the pore structure for the low pressure carbonisation carbons. However, the helium density measurements, are inconclusive and vary between 1.40 g cc^{-1} (C15) to 1.68 g cc^{-1} (C17) for the carbons under consideration as shown in Table 5.11.

6.3.2.2 *Effect of HTT on CO_2, 273 K surface area and capacity*

Yinrui[29] reported that the carbonisation is complete at 823 K for the production of activated carbon from coconut shell. However, it is apparent that the pore structure development still occurs above this temperature. Armor[9] has indicated advantages of using higher temperatures which agrees with the findings in this work.

The carbons sets produced at atmospheric pressure [(C1-C3) (C4-C7)] and vacuum carbonisation condition [(C8-C10) (C11-C14)] at heating rates of either 1 K min^{-1} or 50 K min^{-1}, were also treated to a variety of HTTs in the range of 873 - 1173 K. All carbons showed an increase in CO_2, 273 K surface area with HTT as illustrated in Figure 6.12 and given numerically in Table 5.10.

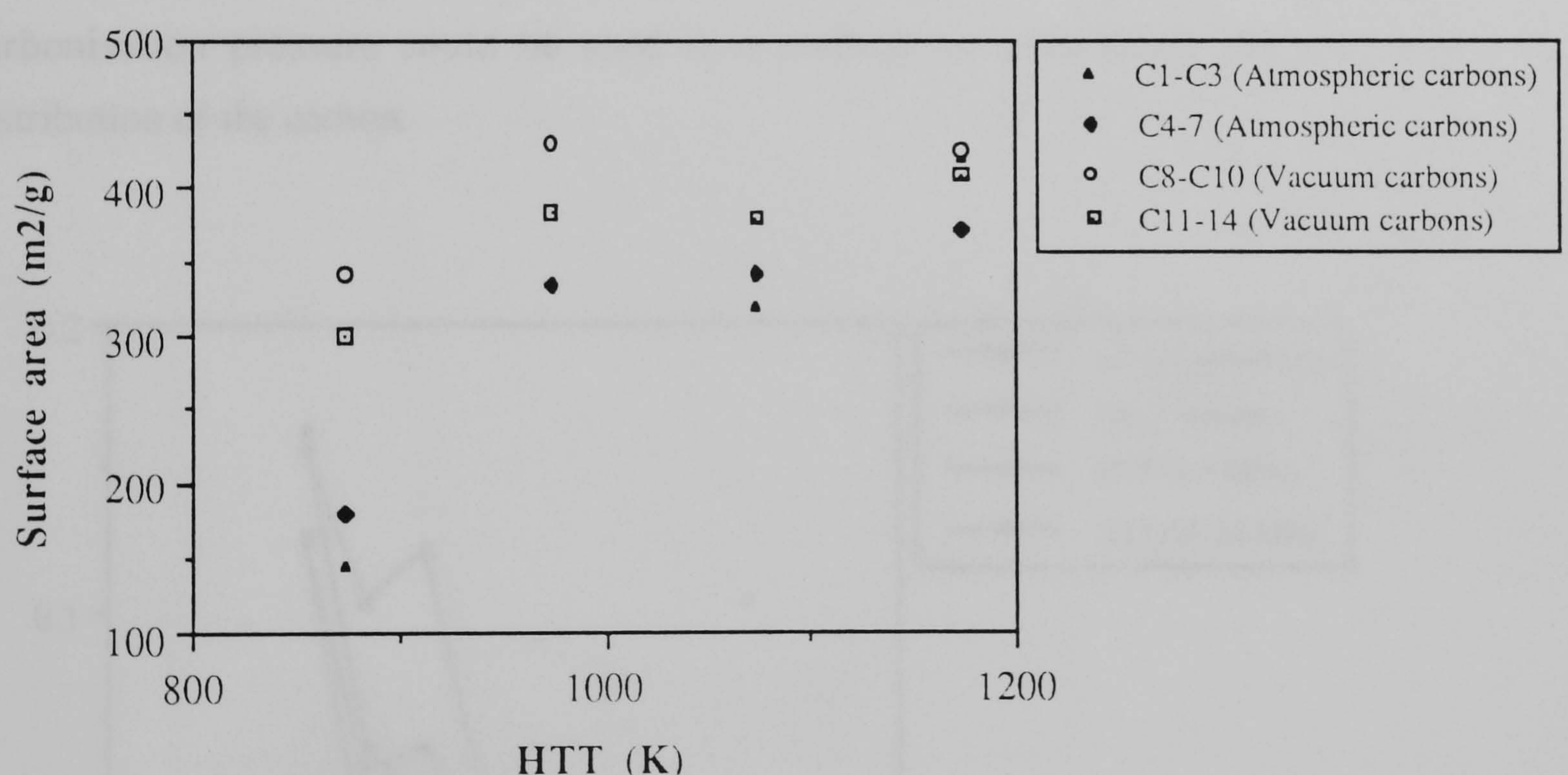

Figure 6.12 The effect of increasing heat treatment temperature (HTT) on CO_2, 273 K surface area of carbons obtained by carbonising coconut shell under atmospheric conditions and vacuum conditions at heating rates of 1 K/min and 50 K/min.

This increase in the CO_2, 273 K surface area was accompanied by an increase in the helium density with increasing heat treatment temperature. The helium density of the carbons series C4 to C7 synthesised under atmospheric pressure conditions showed an increase from 1.41 to 1.98 g cc^{-1}. A similar trend was observed for the carbons C11-C14, obtained under vacuum carbonisation conditions where the helium density increases from 1.49 to 1.80 g cc^{-1}. Carbons C1-C3 (1.42 to 2.04 g cc^{-1}) and C8-C10 (1.51 to 2.02 g cc^{-1}) also show the same trends for the helium density with heat treatment temperature. Hence, it is evident that closed porosity is becoming accessible with increasing heat treatment.

6.3.2.3 Pore size distribution of lignocellulose carbons

The pore size distribution of the lignocellulose carbons was measured using the probe molecule adsorption method as detailed in Section 4.2.7. The probe molecule results for different carbons are shown in Table 5.16. The pore size distribution for carbons C1, C8, C15 and C17, which were produced under different carbonisation pressures ranging from vacuum to elevated pressure of 12.24 MPa, HTT of 873 K and heating rate of 1 K min^{-1} are shown in Figure 6.13. An increase in carbonisation pressure resulted in narrowing the pore size distribution of the carbons. Hence, the carbonisation pressure could be used as a method for controlling the pore size distribution of the carbon.

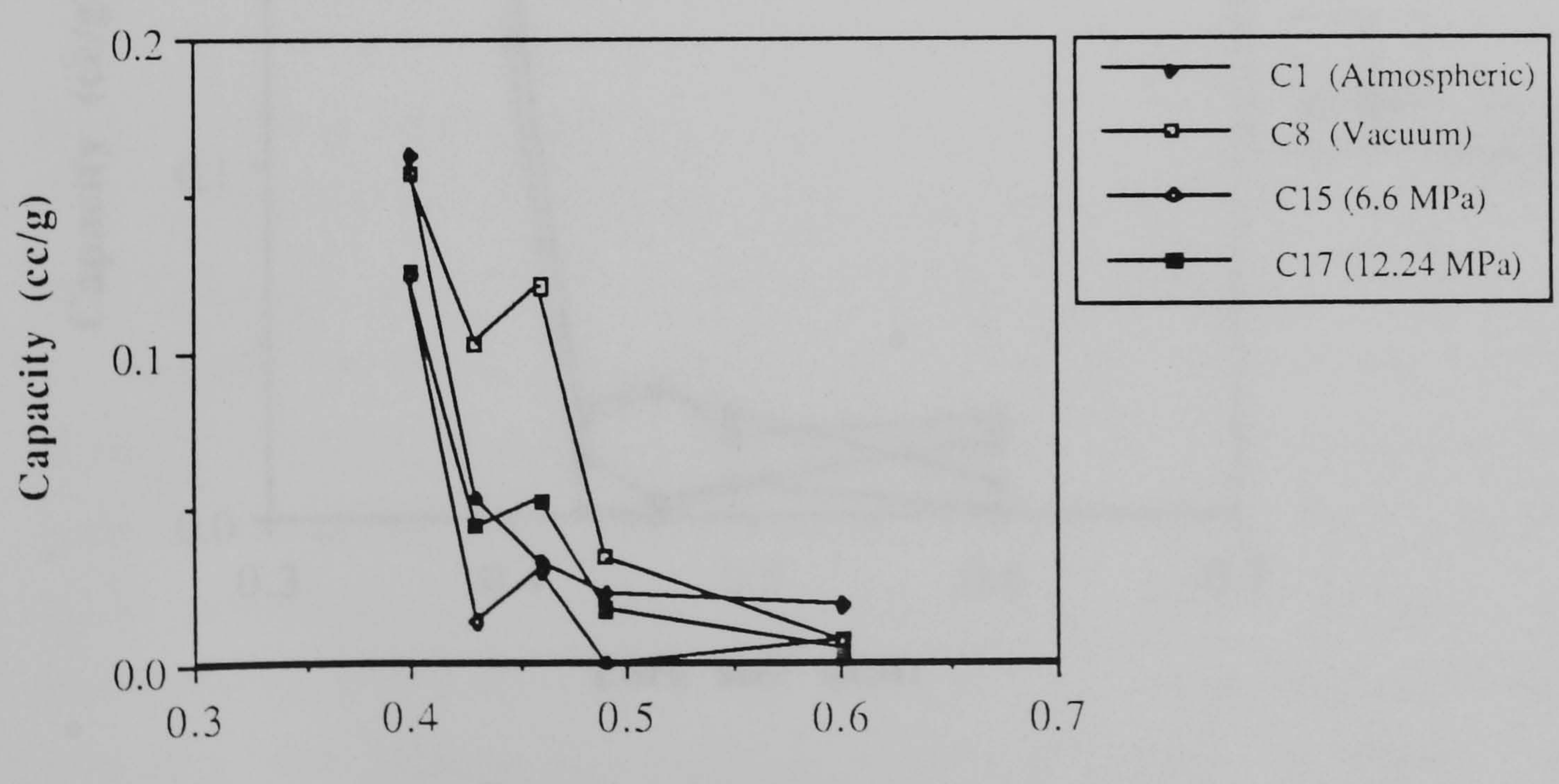

Figure 6.13 Probe molecule capacity graphs for coconut shell carbons produced at various carbonisation pressure and HTT 873 K at heating rate 1 K/min and soak time 1 hour.

The rates of uptake for both oxygen and nitrogen tend to show an increase with increasing carbonisation pressure and these carbons do not show much selectivity for oxygen relative to nitrogen.

The pore size distribution for series of carbons C11 to C14 produced under vacuum carbonisation conditions with HTTs in the range of 873 to 1173 K at a heating rate of 50 K min^{-1}, indicated that the bulk of pore volume began between 0.4 and 0.43 nm and had very little capacity in pore sizes between 0.43 and 0.6 nm. Examination of the 0.46 nm region shows that the major reduction in adsorption came about between HTT of 973 K and 1073 K. Thus, up to a HTT of 1173 K, the effect of increasing carbonisation temperature is to reduce the amount of the porosity above 0.4 nm and to sharpen the cut-off point near 0.4 nm and increase the capacity. Thus, the micropore size distribution has been decreased. This is represented numerically in Table 5.16 and presented graphically in Figure 6.14.

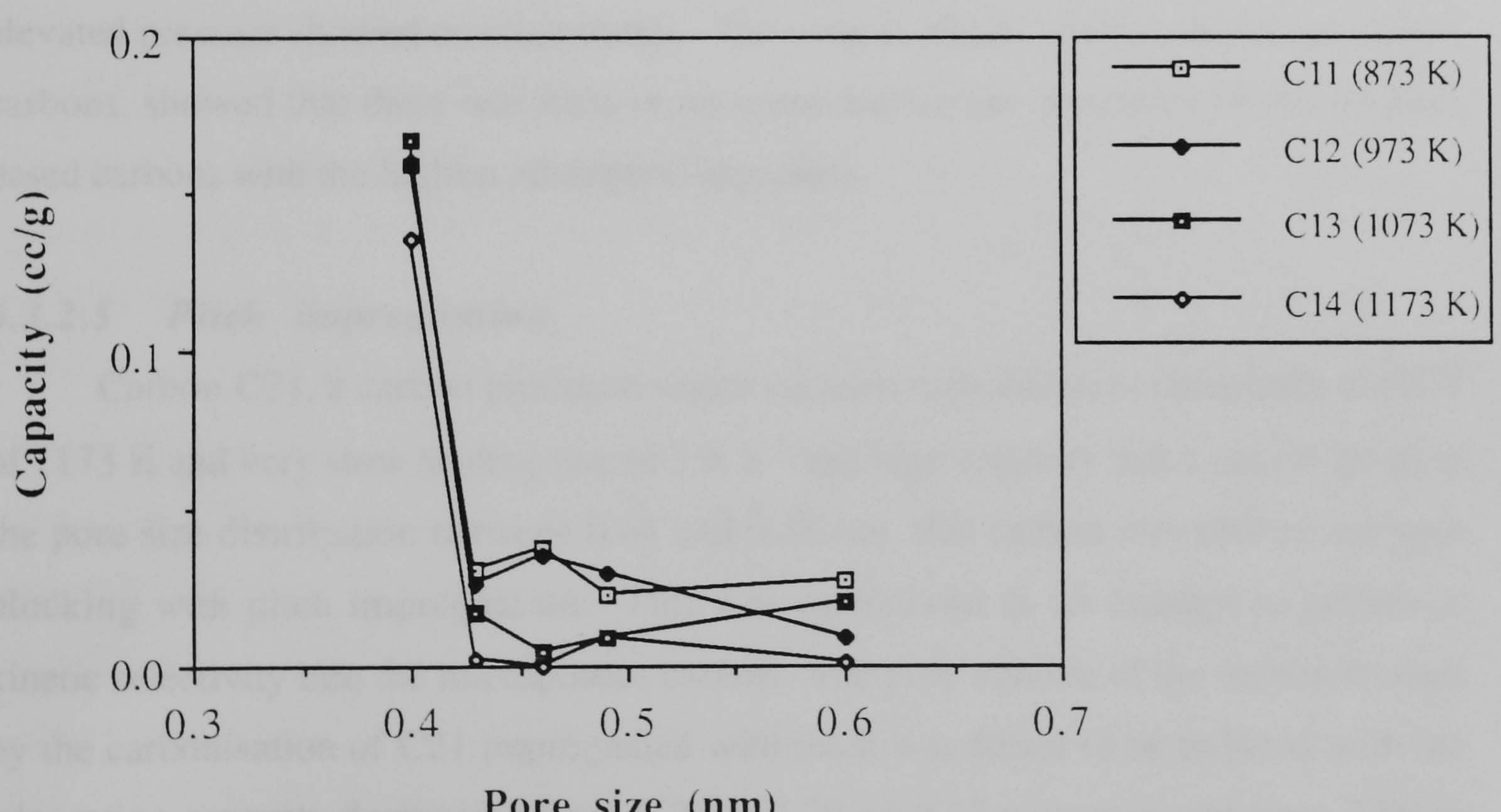

Figure 6.14 Probe molecule capacity graphs for vacuum carbonised coconut samples at heating rate 50 K/min and soak time 1 hour.

The rates of uptake for both oxygen and nitrogen tend to show a decrease with reduction in the pore size distribution. The rates for C11-C14 showed a decrease from

2.10×10^{-2} to 8.30×10^{-3} s^{-1} for oxygen adsorption and from 1.90×10^{-2} to 3.5×10^{-3} s^{-1} for nitrogen adsorption. In contrast the selectivity i.e. the ratio of oxygen rate to nitrogen rate showed a slight increase, the selectivity ratio increased from 1.10 (for C11 carbon) to 2.30 (for C14 carbon).

6.3.2.4 Helium density of lignocellulose carbons

The helium density was determined for all the carbons in order to assess the closed porosity. The helium density for carbons synthesised by carbonisation under vacuum at a variety of HTTs between from 873-1173 K and at a fast or slow heating rate (C8 to C10 were synthesised at heating rate of 1 K min^{-1}, carbons C11-C14 produced at heating rate of 50 K min^{-1}) showed an increase in helium density with increasing HTT. The carbons produced at atmospheric conditions were also subjected to HTTs in the range 873-1173 K, carbons C1-C3 were produced at a heating rate of 1 K min^{-1}, and carbons C4-C7 were synthesised at heating rate of 50 K min^{-1}. These carbons also followed the same trend. This implies that the closed porosity was being made accessible with increasing heat treatment temperature. Carbons produced at elevated pressure showed no clear trends. The overall results, for the above mentioned carbons, showed that there was little or no scope for further activation of the coconut based carbons with the highest adsorption capacities

6.3.2.5 Pitch impregnation

Carbon C21, a carbon produced under vacuum carbonisation conditions at HTT of 1173 K and very slow heating rate of 1 K h^{-1} had high capacity and a cut-off point in the pore size distribution between 0.44 and 0.48 nm, this carbon was chosen for pore blocking with pitch impregnation. This was carried out in an attempt to introduce kinetic selectivity into the microporous carbon. The pore volume of the carbon formed by the carbonisation of C21 impregnated with pitch was found to be reduced with the adsorption capacity decreasing from 5.90 to 2.20 cc g^{-1} for oxygen and from 7.00 to 3.70 cc g^{-1} for nitrogen after impregnation of C21 carbon with pitch. The pitch impregnated carbon also showed a reduction in the adsorption rates for both oxygen and nitrogen. In contrast the kinetic selectivity [the selectivity was calculated by taking the ratio of rates of oxygen to nitrogen adsorption] was found to be slightly higher for the pitch impregnated carbon (1.3) in comparison with C21 (0.8). Studies carried out by Kitawage and Yuki[30] on the modification of Saran waste carbon with the addition of coal tar pitch also showed a reduction in pore volume and effective diameter with increase in coal tar pitch addition.

Coconut shell carbon C22, was also carbonised at HTT of 1173 K and a slow heating rate of 15 K h^{-1}. This carbon showed a large reduction in the uptake capacities of both oxygen (2.20 cc g^{-1}) and nitrogen (3.70 cc g^{-1}) as compared to C14 (11.77 cc g^{-1} for oxygen uptake capacity and 11.65 cc g^{-1} for nitrogen uptake capacity) which was produced under vacuum carbonisation conditions at HTT of 1173 K and at a fast heating rate of 50 K min^{-1}. This sample, C22 also showed a high selectivity (7.2) compared with C14 (2.3) indicating that a greater portion of microporosity could have been formed in a more uniform manner resulting in a narrower pore size distribution.

6.3.2.6 Cellulose triacetate and wood based carbons

The cellulose triacetate carbon synthesised at HTT of 1173 K and at a heating rate of 15 K h^{-1} had relatively higher capacities for oxygen (10.70 cc g^{-1}) and nitrogen (11.30 cc g^{-1}) compared with hard-wood derived carbons. For example Beech carbons prepared under atmospheric conditions at a HTT of 1173 K at a heating rate of 1 K min^{-1} had an oxygen uptake capacity of 5.14 cc g^{-1} and nitrogen uptake capacity of 6.23 cc g^{-1}. Both the carbons lacked selectivity. The uptake capacity of the cellulose triacetate carbon was not as high as the highest capacity coconut carbon C14 (synthesised at HTT of 1173 K and heating rate of 50 K min^{-1}). Beech-wood carbons obtained by carbonisation under atmospheric conditions at HTTs of either 873 or 1173 K and heating rate of 1 K min^{-1} did not show any significant increase in equilibrium gas uptake capacities or selectivity with increasing HTT. The CO_2, 273 K apparant surface area value of (340 m^2g^{-1}) beech carbon obtained under atmospheric conditions at a HTT of 873 K and at a heating rate of 1 K min^{-1} was comparable to that obtained for a beech carbon by Ehrburger *et al.*[31] (the carbon synthesised under atmospheric conditions with a HTT of 735K had a CO_2, 273 K apparant surface area of 320 m^2g^{-1}). Beech carbon obtained at elevated pressure carbonisation (7.5 MPa) showed uptake capacity of 2.59 cc g^{-1} for oxygen and 2.98 cc g^{-1} for nitrogen. These uptake capacities were low compared with Beech carbons synthesised at atmospheric pressure (4.91 cc g^{-1} for oxygen and 5.12 cc g^{-1} for nitrogen). The reason for the decreased capacity for the high pressure beech carbon could be due to the smaller volumes of gases evolved under high pressure or the cracking of pyrolysis compounds leading to a greater amount of closed porosity. This was supported by the helium density measurements; the elevated pressure beech carbon has a helium density of 1.57 implying a great deal of closed porosity, whereas, beech carbon produced at atmospheric pressure carbonisation conditions had a helium density of 2.12 g cc^{-1}. Hence, the microporosity in the carbonised product of elevated pressure carbon may not be accessible to the oxygen or nitrogen gas molecule.

6.2.3 Overall comparison between the two sets of carbon:lignocellulose and polymer based

The pore size distribution of CMS precursor is the most important factor for producing a CMS carbon by 'pore' blocking techniques. The type of porosity is dictated by the type of raw material employed and carbonisation conditions used. Table 6.3 shows the capacity and selectivity of the samples synthesised in the laboratory and commercial CMS synthesised from various precursor materials. The manufacturing details for the CMS are given in Table 2.4 in Chapter Two.

Table 6.3

Precursor	Use	O_2 Capacity	Selectivity	Reference/ (Patent No.)
Coconut shell char	O_2/N_2 separation	8.0 cc g^{-1}	21	8
Coconut shell char	O_2/N_2 separation	4.0 cc cc^{-1}	43.3	32 (EP 119925)
Coconut shell char	O_2/N_2 separation	4-6 cc cc^{-1}	6.68	33 (EP 102902)
Coconut shell char	O_2/N_2 separation	7 cc g^{-1}	35	34 (JP 62176908)
Phenol resin	O_2/N_2 separation	11.4 cc g^{-1}	4.3	35 (EP 282053)
		2.87 cc g^{-1} (N_2)		35 (EP 282053)
Phenolic resins	O_2/N_2 separation	11.6 cc g-1		36 (JP 63201008)
Coconut shell (C14)	O_2/N_2 separation	11.8 cc g^{-1}	2.3	This work
		11.7 cc g^{-1} (N_2)		This work
PVDC (Vacuum)	O_2/N_2 separation	10.7 cc g^{-1}	2.45	This work
		11.3 cc g^{-1} (N_2)		This work
PVDC(CH_4-10 min)	O_2/N_2 separation	10.70 cc g^{-1}	6.08	This work
		11.30 cc g^{-1} (N_2)		This work

Coconut shell char is a suitable precursor material for preparation of CMS materials but there is very little in the literature about the variables critical to the preparation of a CMS material. This work provides an insight into possible ways for optimising the properties of the host material by using different carbonisation pressures, heating rates and heat treatment temperature to obtain a high capacity microporous carbons. Coconut shell was found to be the best precursor material amongst all materials studied. Although the PVDC carbon obtained by carbonisation under atmospheric conditions at HTT 1173 K has the highest capacity, the coconut shell carbon had the a suitable pore size distribution and highest density. The carbons obtained under vacuum carbonisation for coconut shell also showed an improved capacity whilst maintaining a suitable pore size distribution for 'pore blocking' for the introduction of kinetic selectivity. Clearly vacuum carbonisation is a method by which carbon adsorption capacity can be enhanced significantly, and forms a route to increasing the capacity of CMS materials.

References

(1) Groszek A.J, *Materials Science Forum*, **25**, 483 (1988).

(2) Groszek A.J., *Chem. and Indusrty*, 1754 (1966).

(3) Groszek A.J. and Templer C.E., *Fuel*, **67**, 1658 (1988).

(4) Groszek A.J., *Poster Presentation at IUPAC Symposium of Porous Solids*, Badseder, Germany, April 26-29 (1987).

(5) Groszek A.J., *Carbon*, **25**, 717 (1987).

(6) Groszek A.J., *Carbon*, **27**, 33 (1989).

(7) Groszek A.J., unpublished work

(8) Cabrera A.L., Zehner J.E., Coe C.G., Gaffney T.R., Farris T.S. and Armor J.N., *Carbon*, **31**, 969 (1993).

(9) Armor J., *Separation Technology*, 163 (1994).

(10) Crank J., *The Mathematics of Diffusion*, Oxford, London (1957).

(11) Roberts P.V. and York R., *Ind. Engng. Chem. Process Develop.*, **6**, 516 (1967).

(12) Antonson C.R. and Dranoff J.S., *Chem. Engn. Prog. Sypm., Series No. 96*, **65**, 27 (1969).

(13) Ruthven D.M., Raghavana N.S. and Hassan N.S., *Chem. Engn. Sci.*, **41**, 1325 (1986).

(14) Ruthven D.M., *Chem. Engng. Sci.*, **47**, 4305 (1992).

(15) Kawazoe K. and Suzuki M., *J. Chem. Engn. Japan*, **7**, 151 (1974).

(16) Chihara K. and Suzuki M., *Carbon*, **17**, 339 (1979).

(17) Dominguez J.A., Psaris D. and LaCava A.I., *AIChE Symp. Ser.*, **84(264)**, 73 (1988).

(18) LaCava A.I., Koss V.A. and Wickens D., *Gas Separation and Purification*, **3(4)**, 180 (1989).

(19) Chagger H.K., Ndaji F.E., Sykes M.L. and Thomas K.M. *Carbon* (submitted for publication)

(20) Atkinson D., Carrott P.J.M., Griller Y., Rouqerol J. and Sing K.S.W., in *Fundamentals of Adsorption*, Ed. Liapis A.I., Engineering Foundation, N.Y., p. 89, (1987).

(21) Marsh H. and O'Hair T.E., *Fuel*, **65**, 301 (1966).

(22) Breck D.W., Eversole W.G., Milton R.M., Reed T.B. and Thomas T.L., *J. Am. Chem. Soc.*, **78**, 5963 (1956)

(23) Rao M.B. and Jenkins R.G., *Carbon*, **25**, 445 (1987).

(24) Farooq S. and Ruthven D.M., *Chem. Engn. Sci.*, **46**, 2213 (1991).

(25) Nandi S.P. and Walker P.L.Jr., *Fuel*, **43**, 385 (1964).

(26) Chihara K,.Suzuki M and Kawazoe K., *J. Coll. Intf. Sc.*, **64(3)**,584 (1978).

(27) Ghosh A.K. and Agnew J.B., *Chem. Eng. Commun.*, **40**, 169 (1986).

(28) Verma S.K. and Walker P.L.Jr., *Carbon*, **30**, 829 (1982).

(29) Yinrui S., *Carbonisation of Coconut Shells*, Forest Products Chemistry and Industry Institute, Chinese Academy of Forestry, **6**, 23 (1982).

(30) Kitawaga H. and Yuki N., *Kogai*, **18**, 373 (1983).

(31) Ehrburger P., Lahaye J. and Wozniak E., *Carbon*, **20**, 433 (1982).

(32) Sutt R.F. Jr., *E.P. Patent 119925* (1984).

(33) Sutt R.F. Jr., *E.P. Patent 102902* (1984).

(34) Takao O., *J.P. Patent 62176908* (1987).

(35) Marumo C., Hayata E. and Shiomi N., *E.P. Patent 282053* (1988).

(36) Marumo C., Hayata E. and Shiomi N., *J.P. Patent 63201008* (1988).

Chapter 7

Conclusions

7.1 Overall Conclusions

7.1.1 A Comparison on Flow Microcalorimetry (FMC) and Gravimetric Methods for Characterising CMS Materials

Six commercial CMS samples were assessed using both the FMC and gravimetric techniques. The results showed that the two techniques had similar trends for adsorption capacities and selectivity ratios but the results for the latter showed some scatter. The gravimetric method is preferred to the FMC method because the corrections for buoyancy are more straight forward than the corrections for the heat and mass transfer effects on the FMC.

7.1.2 Adsorption/Desorption Kinetics on Commercial CMS A3

Various probe molecules were used to study the fundamentals of kinetics of adsorption/desorption on commercial CMS A3. The nature of the porosity which gave rise to selectivity was found to be slit-shaped. The adsorption kinetics rate laws differed from the desorption kinetics at the higher surface coverages. This can be attributed to the different mechanisms of adsorption and desorption. The activation energy was found to be a complex function of the shape and size of the molecule, the extent of surface coverage and the relative pressure.

7.1.3 Carbon Synthesised in the Laboratory

Carbons were obtained from a variety of precursor materials. PVDC carbons had slightly higher adsorption capacities compared with the coconut shell carbons. The pore size distribution of carbons can be controlled to some extent by adjustment of the carbonisation pressures. Adsorption capacity tends to decrease with increasing carbonisation pressure. Hence the highest adsorption capacities were obtained for carbonisation under vacuum. Coconut shell derived carbons were found to be the most suitable for the production of CMS because of their narrow micropore size distribution and relatively high density. Kinetic selectivity for oxygen and nitrogen can be introduced by gas phase pyrolysis of methane at 1173 K.

7.2 Specific Conclusions

7.2.1 Comparison of Flow Microcalorimetry and Gravimetric Methods for Characterising CMS Materials

FMC has been used for the first time to assess the kinetics, capacity and the molecular sieving abilities of CMS materials. The heat output thermograms for adsorption were modelled and the heat output curves were found to follow a first order kinetic rate law. This enabled an assessment of the selectivity ratios to be carried out. The equilibrium capacities were related to the total heat output obtained from the peak of the thermogram area. This technique (FMC) provides a rapid analysis for the molecular sieving characteristics of the material. However, it is subject to complex mass transfer and heat loss corrections.

7.2.2 Adsorption/Desorption Kinetics on Commercial CMS A3

The fundamentals of adsorption/desorption of various gases on CMS A3 used for air separation was studied over the temperature range of 275-333 K.

(1) The shape of the selective porosity

It was found that ethene was taken up by the CMS material whereas methane was not taken up to any significant extent. This indicates that the nature of selectivity is slit-shaped.

(2) Adsorption studies

The rates for adsorption were generally faster in comparison to desorption rates.

The gas uptake follow first order Langmuir kinetics at low surface coverage. The rate plots for adsorption deviated from linearity in some cases at high surface coverage indicating a cooperative adsorption mechanism. The rates for adsorption/desorption showed an increase with increasing temperature and the variation in kinetic parameters are related by the Arrhenius equation.

(3) Surface coverage

The results suggested that when the surface coverage is high, cooperative effects influence the kinetics. This is clearly indicated in the study of the adsorption kinetics of ethene and ethyne where the rates of adsorption at high surface coverage are higher than predicted from the rate law for the initial gas adsorption.

(4) Desorption studies

Desorption kinetics followed a similar kinetic rate law to the adsorption studies for spherical and linear diatomic gas molecules. In comparison, for linear triatomic, C_2H_2 and planar C_2H_4 gas molecules where the surface coverage was higher, the desorption can be described as a mathematical model with two exponential terms. The variation of the desorption kinetics with temperatures follows an Arrhenius equation.

(5) Probe molecules

(i) Kinetics studies

The gas molecules are transferred through the selective porosity with the minimum dimension being the critical parameter. As a result the end-on molecule dimensions are also related to the Arrhenius activation energies for adsorption. The pre-exponential factor or the frequency factor is related to the length of the molecule. As the length of the molecule increased the frequency factor decreased. In addition, the frequency factor for the adsorption of ethene is very slow because the planar molecule has to have the correct orientation to enter the porous structure in addition to having a similar length to ethyne.

(ii) Capacity studies

Comparison of the gas uptake of the probe molecules over a range of temperatures is difficult because many of the experiments are carried out above the critical temperature and hence, a saturated vapour pressure (p_0) does not exist. A hypothetical p_0 value was calculated by extrapolation of the equations fitting the variation of p_0 with temperature. In addition, the equilibrium uptake of the molecules used in this study and the real and hypothetical p/p_0 values have been shown to follow the shape of carbon dioxide isotherm. Hence, the optimization of these adsorbents for capacity can be simplified by using a carbon dioxide isotherm adsorption to describe the equilibrium characteristics of pure vapours.

7.2.3 Carbon Molecule Sieve Precursors

A wide range of precursor materials were subjected to a variety of carbonisation conditions and the following conclusions regarding the variation of carbonisation conditions have been made.

(1) Vacuum carbonisation gives rise to increase in equilibrium capacities compared with other carbons obtained under atmospheric or high pressure carbonisation pressures. The adsorption capacity decreased with increasing carbonisation pressure. The pore size distribution of the carbons can be be modified by careful control of the carbonisation pressures.

(2) Carbons were obtained from a variety of host materials, pure PVDC carbons showed slightly higher adsorption capacities on a weight basis compared with the coconut shell carbons. PVDF showed slightly lower capacities and rates in comparison to PVDC carbon (carbonised at 1173 K under atmospheric conditions). The addition of polynuclear aromatics led to a shift in the pore size distribution to smaller dimensions. This was accompanied by a reduction in available microporosity and adsorption rates.

(5) PFA carbons had low capacities and rates compared with pure PVDC carbons.

The addition of sulphur resulted in loss of capacity and increased adsorption rates. The capacity and surface area of PEEK carbons increased to a maximum before decreasing on further heating to 1173 K. The maximum capacity of PEEK carbons was found to be less than pure PVDC carbon.

(6) Amongst all the precursor materials studied coconut shell was found to be the most suitable precursor material for the production of CMS because of its high density and pore size distribution consisting of a narrow micropore distribution combined with a macroporous structure for effective gas transport

(7) Kinetic selectivity can be introduced by carbon deposition. Carbons obtained by methane pyrolysis over PVDC chars showed an increase in selectivity but possessed slightly lower capacities. This is a reliable method of introducing kinetic selectivity into microporous carbons with a suitable micropore distribution.

Publications

List of Publications

(1) *Adsorption kinetics and diffusion characteristics of carbon molecular sieve.* H.K. Chagger, F. Ndaji, M.L. Sykes, K.M. Thomas, paper submitted to **Carbon** accepted for publication (1994).

(2) *Kinetic selectivity in carbon molecular sieves,* H.K. Chagger, F. Ndaji, M.L. Sykes, K.M. Thomas, **Carbon 94, International Conf. on Carbon, July 3rd - 5th** Granada, Spain (1994).

(3) *Adsorption kinetics and diffusion characteristics of carbon molecular sieve,* M.L. Sykes, H. Chagger, K.M. Thomas, **Gas Separation Conf., American Institute of Chemical Engineers, Seattle, U.S.A.** (1993).

(4) *Assessment of kinetics, selectivity and capacity in carbon molecular sieves by flow microcalorimetry,* M.L. Sykes, H. Chagger, K.M. Thomas, **Carbon**, vol. 31, No. 5, p. 827 (1993)

(5) *Fundamental studies of the physical properties of carbon molecular sieves,* M.L. Sykes, H. Chagger, K.M. Thomas, presented at the **21st Biennial Conf. on Carbon**, June 13 - 18. Buffalo,p 436 U.S.A. (1993)

(6) *Flow microcalorimetry as a technique for assessing kinetics and equilibrium capacities in carbon molecular sieves,* M.L. Sykes, H. Chagger, K.M. Thomas, **Ext. Abs. Carbon 92, International Conf. on Carbon, Essen, Germany, p 263** (1992).

(7) *Adsorption on active carbons.* M.L. Sykes, H. Chagger, K.M. Thomas, presented in the **Proc. Envt. Aspects of Coal Utilization and Carbon Science, 31 March, The University of Newcastle upon Tyne.** (1992).